

DESIGN, ANALYSIS AND OPTIMIZATION OF THIN WALLED SEMI-MONOCOQUE WING STRUCTURES USING DIFFERENT STRUCTURAL IDEALIZATIONS IN THE PRELIMINARY DESIGN PHASE

A THESIS SUBMITTED TO
THE GRADUATE SCHOOL OF NATURAL AND APPLIED SCIENCES
OF
MIDDLE EAST TECHNICAL UNIVERSITY

BY

ODEH DABABNEH

IN PARTIAL FULFILLMENT OF THE REQUIREMENTS
FOR
THE DEGREE OF MASTER OF SCIENCE
IN
AEROSPACE ENGINEERING

AUGUST 2011

Approval of the thesis:

DESIGN, ANALYSIS AND OPTIMIZATION OF THIN WALLED SEMI-MONOCOQUE WING STRUCTURES USING DIFFERENT STRUCTURAL IDEALIZATIONS IN THE PRELIMINARY DESIGN PHASE

Submitted by **ODEH DABABNEH** in partial fulfillment of the requirements for the degree of **Master of Science in Aerospace Engineering Department, Middle East Technical University** by,

Prof. Dr. Canan Özgen
Dean, Graduate School of **Natural and Applied Sciences**

Prof. Dr. Ozan Tekinalp
Head of Department, **Aerospace Engineering**

Prof. Dr. Altan Kayran
Supervisor, **Aerospace Engineering Dept., METU**

Examining Committee Members:

Prof. Dr. Turgut Tokdemir
Engineering Science Dept., METU

Prof. Dr. Altan Kayran
Aerospace Engineering Dept., METU

Assist. Prof. Dr. Demirkan Çoker
Aerospace Engineering Dept., METU

Assist. Prof. Dr. Ercan Gürses
Aerospace Engineering Dept., METU

Mustafa Ekren, M.Sc.
Turkish Aerospace Industry (TAI)

Date: 25.08.2011

I hereby declare that all information in this document has been obtained and presented in accordance with academic rules and ethical conduct. I also declare that, as required by these rules and conduct, I have fully cited and referenced all material and results that are not original to this work.

Name, Last name : Odeh DABABNEH

Signature :

ABSTRACT

DESIGN, ANALYSIS AND OPTIMIZATION OF THIN WALLED SEMI-MONOCOQUE WING STRUCTURES USING DIFFERENT STRUCTURAL IDEALIZATIONS IN THE PRELIMINARY DESIGN PHASE

Dababneh, Odeh

M.Sc., Department of Aerospace Engineering

Supervisor : Prof. Dr. Altan Kayran

August 2011, 283 pages

This thesis gives a comprehensive study on the effect of using different structural idealizations on the design, analysis and optimization of thin walled semi-monocoque wing structures in the preliminary design phase. In the design part, wing structures are designed by employing two different structural idealizations that are typically used in the preliminary design phase. In the structural analysis part, finite element analysis of one of the designed wing configurations is performed using six different one and two dimensional element pairs which are typically used to model the sub-elements of semi-monocoque wing structures. The effect of using different finite element types on the analysis results of the wing structure is investigated. During the analysis study, depending on the mesh size used, conclusions are also inferred with regard to the deficiency of certain element types in handling the true external load acting on the wing structure. Finally in the optimization part, wing structure is optimized for minimum weight by using finite element models which have the same six different element pairs used in the analysis phase. The effect of using different one and two dimensional element pairs on the final optimized

configurations of the wing structure is investigated, and conclusions are inferred with regard to the sensitivity of the optimized wing configurations with respect to the choice of different element types in the finite element model. Final optimized wing structure configurations are also compared with the simplified method based designs which are also optimized iteratively.

Based on the results presented in the thesis, it is concluded that with the simplified methods, preliminary sizing of the wing structures can be performed with enough confidence, as long as the simplified method based designs are also optimized. Results of the simplified method of analysis showed that simplified method is applicable to be used as an analysis tool in performing the preliminary sizing of the wing structure before moving on to more refined finite element based analysis.

Keywords: Wing Torque Box, Aerospace Structural Design, Structural Optimization, Finite Element Analysis

ÖZ

ÖN TASARIM SÜRECİNDE İNCE ET KALINLIKLIL GÜÇLENDİRİLMİŞ KANAT YAPILARININ FARKLI YAPISAL İDEALLEŞTİRME YÖNTEMLERİ KULLANARAK TASARIM, ANALİZ VE OPTİMİZASYONU

Dababneh, Odeh

Yüksek Lisans, Havacılık ve Uzay Mühendisliği Bölümü

Tez Yöneticisi : Prof. Dr. Altan Kayran

Ağustos 2011, 283 sayfa

Bu tezde değişik yapısal idealleştirme yöntemlerinin ince et kalınlıklı, güçlendirilmiş tipik bir kanat tork kutusunun tasarımı, analizi ve yapısal optimizasyonu üzerindeki etkileri üzerine kapsamlı bir çalışma sunulmaktadır. Yapısal tasarım fazında, uçak ön tasarım sürecinde tipik olarak kullanılan iki farklı yapısal idealleştirme yöntemi kullanılmıştır. Yapısal analiz kısmında genellikle güçlendirilmiş kanat yapılarının alt elemanlarını modellemek için kullanılan altı farklı bir ve iki boyutlu eleman çiftleri kullanılarak, tasarlanan kanat yapılarının sonlu elemanlar analizi gerçekleştirilmiştir. Değişik sonlu eleman tiplerinin kullanılmasının kanat yapısının analiz sonuçları üzerindeki etkisi incelenmiştir. Analiz çalışması sırasında, bazı eleman tiplerinin kanat yapısı üzerine etki eden harici yükü tam olarak yapıya aktarmada yetersiz kaldığı durumlar üzerinde de sonuçlar çıkarılmıştır. Optimizasyon kısmında ise analiz çalışması sırasında kullanılan altı farklı sonlu eleman çifti kullanılarak kanat yapısı en az ağırlık amacına yönelik olarak optimize edilmiştir. Sonlu elemanlar modelinde değişik bir ve iki boyutlu sonlu eleman çiftlerinin kullanılmasının,

optimum kanat konfigürasyonları üzerindeki etkisi incelenmiştir. Bu sayede, farklı sonlu eleman tipi seçimi ile optimum kanat yapısı arasındaki ilişki hakkında çıkarımlar yapılmıştır. Optimum tork kutusu konfigürasyonları, el hesabına dayalı tekrarlama yöntemi kullanarak elde edilmiş olan en iyi kanat tork kutusu konfigürasyonları ile kıyaslanmıştır.

Tezde sunulan sonuçlara dayanarak, basitleştirilmiş yöntem dayalı tasarımlarda optimize edildiği takdirde, basitleştirilmiş yöntem ile kanat yapılarının ilk boyutlandırmalarının güvenilirlikle yapılabileceği sonucuna varılmıştır. Basitleştirilmiş yöntem ile elde edilen sonuçlar, sonlu elemanlar analizi gibi daha hassas metodlara gerek kalmadan, ilk boyutlandırmada basitleştirilmiş yöntemin uygulanabilir olduğunu göstermiştir.

Anahtar Kelimeler: Kanat Tork Kutusu, Havacılık ve Uzay Yapısal Tasarım, Yapısal Optimizasyon, Sonlu Elemanlar Analizi

dedicated to my parents
&
my beloved fiancé Linute
for their never fading support and love
over years

ACKNOWLEDGEMENTS

I would like to express my deepest thanks to my supervisor Prof. Dr. Altan Kayran and I offer my sincerest gratitude to him for his encouragement, guidance and support from the initial to the final level of thesis work. This thesis would not have been completed without his expert advice and unfailing patience.

I would like also to deeply thank my parents for their support throughout the studying and completion time of my thesis. A special thank to my mother Amira Maayah for her unwavering support throughout my studies.

TABLE OF CONTENTS

ABSTRACT.....	iv
ÖZ.....	vi
ACKNOWLEDGEMENTS	ix
TABLE OF CONTENTS.....	x
LIST OF TABLES.....	xvi
LIST OF FIGURES.....	xxii
LIST OF SYMBOLS	xxxiv
LIST OF ABBREVIATIONS	xxxvi
CHAPTERS	
1. BACKGROUND TO THE STUDY.....	1
1.1 INTRODUCTION.....	1
1.2 PURPOSE OF THE STUDY.....	1
1.3 LITERATURE SURVEY.....	2
1.4 SCOPE OF THE STUDY.....	3
2. WING TORQUE BOX STRUCTURAL DESIGN	5
2.1 INTRODUCTION.....	5
2.2 WING DESCRIPTION AND REQUIREMENTS.....	5
2.2.1 Applicability of FAR Part 23 Appendix A.....	6
2.3 AERODYNAMIC LOADS CALCULATION PROCEDURE.....	7
2.3.1 Calculation of Wing Planform Area and Wing Loading.....	7
2.3.2 Calculation of Limit Load Factors and Minimum Speeds	8
2.3.3 Constructing the V-N Diagram	11

2.3.4	Calculation of Angles of Attack	12
2.3.5	NACA 2412 Mean Camber Line Calculation.....	14
2.3.6	External Aerodynamic Load Calculation by ESDU	15
2.3.7	Calculation of Internal Loads	17
2.4	WING STRUCTURAL DESIGN AND ANALYSIS METHODOLOGY.....	22
2.4.1	Wing Geometry and Structural Layout	23
2.4.2	Material Selection and Properties	23
2.4.3	Analysis and Programming Tool	24
2.5	FLOWCHART OF THE DESIGN STEPS	25
2.5.1	Initial Sizing, Design Parameters and Design Criteria.....	26
2.5.2	Axial Stresses Calculation	28
2.5.3	Shear Flow and Shear Stress Calculations	30
2.5.4	Local Buckling Analysis	34
2.5.5	Determination of Shear Center	35
2.5.6	Determination of Locations of the Spars and Stringers for Minimum Weight Wing Structure	36
2.5.7	Calculation of Divergence Speed.....	36
2.6	DESIGN RESULTS OVERVIEW	37
2.6.1	Iteration Results for Spar – Stiffener Locations and Minimum weight ...	37
2.6.2	Final Spars - Stiffeners and Ribs Locations	39
2.6.3	Final Minimum Wing Weight Results and Weight Breakdown.....	41
2.6.4	Results of Flange Areas for the First and the Second Idealization	43
2.6.5	Results of Skin and Spar Web Thicknesses for the First and the Second Structural Idealizations	49
2.6.6	Results of Rib Thicknesses for the First and the Second Idealization	56
2.6.7	Divergence Speed Results of the Design Determined by the First and the Second Idealization.....	58
3.	FINITE ELEMENT ANALYSIS OF WING TORQUE BOXES	60
3.1	INTRODUCTION	60
3.2	WING CONFIGURATION SELECTION	60
3.2.1	Wing Structural Lay-Out	62
3.2.2	Material Properties	62

3.2.3	Aerodynamic Loading and Boundary Conditions Acting On the Wing Torque Box.....	63
3.3	SELECTION OF ELEMENT TYPES	64
3.4	CASE STUDY ON THE USE OF SHELL AND MEMBRANE ELEMENTS.....	64
3.4.1	Tip Moments Producing Pure Torsion	65
3.4.2	Uniform Pressure on the Lower and Upper Skin.....	67
3.4.3	Tip Force Loading.....	77
3.4.4	Tip Moments Producing Pure Torsion – Box Beam Model with Flanges.....	84
3.4.5	Distributed Line Force Loading – Box Beam Model with Flanges and Ribs.....	86
3.4.6	Distributed Line Pitching Moment Loading.....	90
3.5	FINITE ELEMENT MODELING OF WING TORQUE BOXES.....	95
3.5.1	Structural Model	96
3.5.2	Mesh Convergence Study.....	98
3.6	ANALYSIS OF WING TORQUE BOX FINITE ELEMENT MODELS	101
3.6.1	Analysis Results of Rod – Shell Finite Element Model.....	101
3.6.2	Analysis Results of Beam – Shell Finite Element Model	106
3.6.3	Analysis Results of Rod – Shell-R Finite Element Model.....	110
3.6.4	Analysis Results of Beam – Shell-R Finite Element Model	115
3.6.5	Analysis Results of Rod – Membrane-R Finite Element Model	119
3.6.6	Analysis Results of Beam – Membrane-R Finite Element Model.....	122
3.7	FINITE ELEMENT ANALYSIS STUDY WITH SHEAR AND MEMBRANE ELEMENTS.....	125
3.7.1	Wing Torque Box Case Study Using Rod-Membrane Model.....	125
3.7.2	Wing Torque Box Case Study Using Rod-Membrane-R Model.....	127
3.7.3	Wing Torque Box Case Study Using Rod-Shear Panels Model.....	128
3.7.4	Overview of Maximum Displacement, Von Mises Stress and Axial Stress Determined by Different Element Pairs.....	132
3.8	COMPARISON OF THE RESULTS OF FINITE ELEMENT ANALYSIS AND HAND CALCULATIONS	136
3.8.1	Comparison of Axial Stresses in Spar Caps and Stiffeners.....	137
3.8.2	Comparison of Axial Stress in Skins and Spar Webs	141

3.8.3	Comparison of the Von Mises Stresses in the Wing Skins and Spar Webs.....	145
4.	STRUCTURAL OPTIMIZATION OF WING TORQUE BOXES USING DIFFERENT TYPES OF FINITE ELEMENTS.....	149
4.1	INTRODUCTION.....	149
4.2	OPTIMIZATION IN STRUCTURAL DESIGN.....	149
4.2.1	Requirements for Structural Design.....	150
4.2.2	Structural Optimization Problem.....	150
4.3	MSC.NASTRAN DESIGN OPTIMIZATION.....	151
4.3.1	Optimization Process in MSC.NASTRAN.....	151
4.3.2	Steps of Performing Optimization Task.....	156
4.3.2.1	Creating an Input BDF-File.....	156
4.3.2.2	MSC.NASTRAN Run.....	157
4.3.2.3	MSC.NASTRAN Post Processing.....	157
4.3.3	Continuous and Discrete Optimization in MSC.NASTRAN.....	157
4.3.3.1	Round-Up and Round-Off Discrete Variable Processing Methods.....	158
4.3.3.2	Conservative Discrete Design (CDD) Variable Processing Method.....	158
4.3.3.3	Design of Experiments (DOE) Variable Processing Method.....	159
4.4	WING TORQUE BOX USED IN STRUCTURAL OPTIMIZATION.....	159
4.5	AERODYNAMIC LOADING ACTING ON THE WING STRUCTURE.....	160
4.6	FINITE ELEMENT TYPES USED IN THE WING TORQUE BOX STRUCTURAL OPTIMIZATION.....	162
4.7	DEFINITION OF THE WING TORQUE BOX OPTIMIZATION PROBLEM DEFINITION.....	163
4.8	OPTIMIZATION STUDIES USING DIFFERENT DISCRETE OPTIMIZATION METHODS AND DIFFERENT STARTING POINTS FOR DESIGN VARIABLES.....	168
4.8.1	Optimization Study Using Different Starting Values for Design Variables.....	169
4.8.2	Optimization Study Using Different Discrete Optimization Methods...	172
4.9	STRUCTURAL OPTIMIZATION OF WING TORQUE BOXES USING SIX DIFFERENT FINITE ELEMENTS COMBINATIONS.....	173

4.9.1	Wing Torque Box Optimization Including All Design Constraints	174
4.9.1.1	Optimization Results of Model One (Rod/Shell Model)	175
4.9.1.2	Optimization Results of Model Two (Beam/Shell Model)	183
4.9.1.3	Optimization Results of Model Three (Rod/Shell-R Model)	188
4.9.1.4	Optimization Results of Model Four (Beam/Shell-R Model)	194
4.9.1.5	Optimization Results of Model Five (Rod/Membrane-R Model) ..	200
4.9.1.6	Optimization Results of Model Six (Beam/Membrane-R Model)..	204
4.9.1.7	Summary of the Optimization Results of the Wing Torque Box Modeled with Different Element Combinations	209
4.9.2	The Effect of Design Constraints on Optimum Wing Torque Box Configurations	212
4.9.2.1	Optimization of the Wing Torque Box with Stress Constraints Only – Rod/Shell Model	212
4.9.2.2	Optimization of the Wing Torque Box with Stress and Tip Displacement Constraints – Rod/Shell Model.....	217
4.9.2.3	Wing Rod/Shell Model Optimization with Stress and Buckling Constraints	223
4.9.3	Wing Torque Box Optimization Study with Shear Panel and Membrane Elements	228
4.9.3.1	Wing Torque Box Optimization Study using Rod/Shear Panel Elements	229
4.9.3.2	Wing Torque Box Optimization Study using Rod/Membrane Elements	236
4.9.3.3	Results and Discussions on the Use of Shear and Membrane Elements in the Optimization	240
4.10	Comparison of Minimum Wing Torque Box Mass Determined by the Analytical and Finite Element Optimization Solution	241
5.	CONCLUSION AND RECOMMENDATIONS	245
5.1	CONCLUSIONS	245
5.2	RECOMMENDATIONS FOR FUTURE WORKS	248
	REFERENCES	249
	APPENDICES	

A. SAMPLE CALCULATION FOR THE SECOND IDEALIZATION CASE OF THE ANALYTICAL SOLUTION OF WING TORQUE BOX DESIGN.....	253
B. ORGANIZATION OF THE NASTRAN BDF INPUT FILE.....	265
C. SAMPLE BDF-FILE FOR WING TORQUE BOX OPTIMIZATION.....	267
D. EXAMPLES OF VARIATIONS OF SOME OF THE DESIGN VARIABLES AND THE MAXIMUM CONSTRAINT WITH THE DESIGN ITERATIONS....	277
E. STANDARD THICKNESSES AND FLANGE AREAS VALUES.....	283

LIST OF TABLES

TABLES

Table 2.1: Criteria per FAR Part 23 Appendix A 23.1	6
Table 2.1: Criteria per FAR Part 23 Appendix A 23.1 - (continues).....	7
Table 2.2: Limit Flight Load Factors Table in Appendix A 23.1.....	8
Table 2.3: Minimum Designed and Checked Speeds	9
Table 2.4: Limit Load Factors	11
Table 2.5: NACA 2412 Mean Camber Line Ordinates	14
Table 2.6: Sectional Internal Loads results at Point A.....	18
Table 2.7: Sectional Internal Loads results at Point D.....	20
Table 2.8: Material Properties of Al 2024 T3 used in Wing Design	24
Table 2.9: Percentage Change in Spars and Stiffeners Locations during Iterations...	38
Table 2.10: Effect of Spar – Stiffener Location on the Minimum Weight and Average Shear Center Location for the 1st Idealization	38
Table 2.11: Effect of Spar – Stiffener Location on the Minimum Weight and Average Shear Center Location for the 2nd Idealization.....	39
Table 2.12: Location of the Spars and Stiffeners along the Span of the Final Wing Design	40
Table 2.13: Location of the Ribs along the Span of the Final Wing Design	40
Table 2.14: Minimum Mass of the Wing Structure Determined Using the 1 st Structural Idealization.....	41
Table 2.15: Minimum Mass of the Wing Structure Determined Using the 2 nd Structural Idealization.....	42
Table 2.16: Standard Flange Areas Determined Using the 1 st Idealization - Point A	44
Table 2.17: Standard Flange Areas Determined Using the 1 st Idealization - Point D	44
Table 2.18: Standard Flange Areas Determined Using the 2 nd Idealization - Point A	45
Table 2.19: Standard Flange Areas Determined Using the 2 nd Idealization - Point D	45

Table 2.20: Standard Thicknesses Determined Using the 1 st Idealization - Point A..	50
Table 2.21: Standard Thicknesses Determined Using 1 st Idealization - Point D	51
Table 2.22: Standard Thicknesses Determined Using 2 nd Idealization - Point A	51
Table 2.23: Standard Thicknesses Determined Using 2 nd Idealization - Point D.....	51
Table 2.24: Standard Rib Thicknesses of 1 st Idealization - Points A and D	56
Table 2.25: Standard Rib Thicknesses of 2 nd Idealization - Point A and D.....	57
Table 2.26: Divergence Speed Calculated Using the 1 st Idealization.....	58
Table 2.27: Divergence Speed Calculated Using the 2 nd Idealization.....	59
Table 3.1: Standard Flange Areas of 2 nd Idealization - Point A.....	61
Table 3.2: Standard Thicknesses of 2 nd Idealization - Point A	61
Table 3.3: Standard Rib Thicknesses of 2 nd Idealization - Point A.....	61
Table 3.4: Box Beam Dimensions and Properties	65
Table 3.5: Shell Element Stresses at Node 308.....	69
Table 3.6: Membrane Element Stresses at Node 308	70
Table 3.7: Shell Element Stresses at Node 308.....	79
Table 3.8: Membrane Element Stresses at Node 308	80
Table 3.9: Combination of Element Types Used in Modeling the Wing Torque Box	95
Table 3.10: Comparisons of Maximum Tip Displacement and Von Mises Stress – Six Mesh Cases.....	100
Table 3.11: Comparison of Von Mises Stress on the Top Middle Skin of the Rod/Shell Model.....	104
Table 3.12: Comparison of Von Mises Stress on the Top Middle Skin of the Beam/Shell Model	108
Table 3.13: Comparison of Von Mises Stresses on the Top Middle Skin of the Rod/Shell-R Model.....	113
Table 3.14: Comparison of Von Mises Stress on the Top Middle Skin of Beam/Shell-R Model.....	117
Table 3.15: Von Mises Stress on the Top Middle Skin of the Rod/Membrane-R Model	120
Table 3.16: Von Mises Stress on the Top Middle Skin of the Beam/Membrane-R Model	123

Table 3.17: Comparison of Maximum Tip Displacement, Maximum Von Mises Stress and Von Mises Stress at the Mid Span for the Coarse Mesh Wing Torque Box Models.....	132
Table 3.18: Comparison of Maximum Tip Displacement, Maximum Von Mises Stress and Von Mises Stress at the Mid Span for the Fine Mesh Wing Torque Box Models.....	133
Table 3.19: Comparison of Maximum Axial Stress and Mid Span Axial Stress for the Coarse Mesh Wing Torque Box Models.....	135
Table 3.20: Comparison of Maximum Axial Stress and Mid Span Axial Stress for the Fine Mesh Wing Torque Box Models	135
Table 3.21: Analytical Solution of Axial Stress in the Spars and Stiffeners	137
Table 3.22: Finite Element Analysis Solution of Axial Stresses in the Spars and Stiffeners for the Rod/Shell Coarse Mesh Model of the Wing	138
Table 3.23: Finite Element Analysis Solution of Axial Stresses in the Spars and Stiffeners for the Rod/Membrane-R Coarse Mesh Model of the Wing.....	138
Table 3.24: Finite Element Analysis Solution of Axial Stresses in the Spars and Stiffeners for the Beam/Shell Coarse Mesh Model of the Wing.....	138
Table 3.25: Finite Element Analysis Solution of Axial Stresses in the Spars and Stiffeners for the Beam/Shell Fine Mesh Model of the Wing.....	139
Table 3.26: Finite Element Analysis Solution of Axial Stresses in the Spars and Stiffeners for the Rod/Shell Fine Mesh Model of the Wing	140
Table 3.27: Analytical Solution of Axial Stress in the Wing Skins	141
Table 3.28: Finite Element Analysis Solution of Axial Stress in the Wing Skins for the Rod/Shell Coarse Mesh Model of the Wing.....	142
Table 3.29: Finite Element Analysis Solution of Axial Stress in the Wing Skins for the Rod/Membrane-R Coarse Mesh Model of the Wing	142
Table 3.30: Finite Element Analysis Solution of Axial Stress in the Wing Skins for the Rod/Shell Fine Mesh Model of the Wing.....	143
Table 3.31: Von Mises Stress in the Wing Skins-Analytical results	146
Table 3.32: Finite Element Analysis Solution o of Von Mises Stress in the Wing Skins of the Rod/Shell Coarse Mesh Model of the Wing	146
Table 3.33: Finite Element Analysis Solution of Von Mises Stress in the Wing Skins for the Rod/Membrane-R Coarse Mesh Model of the Wing.....	146

Table 3.34: Finite Element Analysis Solution of Von Mises Stress in the Wing Skins for the Rod/Shell Fine Mesh Model of the Wing	147
Table 4.1: Combination of FE Types Used in Different Models	162
Table 4.2: Summary of Standard Flange Areas of the 2 nd Idealization - Point A	171
Table 4.3: Summary of Standard Thicknesses of the 2 nd Idealization - Point A.....	171
Table 4.4: Summary of Standard Rib Thicknesses of the 2 nd Idealization - Point A	171
Table 4.5: Mass of the Optimized Wing Torque Box (kg) Using Different Starting Values for the Design Variables	172
Table 4.6: Mass of the Optimized Wing Torque Box (kg) Using Discrete Optimization Methods of MSC.NASTRAN®	173
Table 4.7: Initial and Final Optimized Mass of the Wing - Rod/Shell Model.....	178
Table 4.8: Cross Sectional Areas of the Front Spar of the Wing – Rod/Shell Model	181
Table 4.9: Cross Sectional Areas of the Rear Spar of the Wing - Rod/Shell Model	181
Table 4.10: Thicknesses of the Upper Middle Skin of the Wing - Rod/Shell Model	182
Table 4.11: Initial and Final Optimized Mass of Wing Beam/Shell Model	184
Table 4.12: Cross Sectional Areas of the Front Spar of the Wing – Beam/Shell Model	187
Table 4.13: Cross Sectional Areas of the Rear Spar of the Wing – Beam/Shell Model	187
Table 4.14: Thicknesses of the Upper Middle Skin of the Wing - Beam/Shell Model	188
Table 4.15: Initial and Final Optimized Mass of the Wing – Rod/Shell-R Model ..	190
Table 4.16: Cross Sectional Areas of the Front Spar of the Wing- Rod/Shell-R Model	193
Table 4.17: Cross Sectional Areas of the Rear Spar of the Wing – Rod/Shell-R Model	193
Table 4.18: Thicknesses of the Upper Middle Skin of the Wing - Rod/Shell-R Mode	194
Table 4.19: Initial and Final Optimized Mass of the Wing – Beam/Shell-R Model	196

Table 4.20: Cross Sectional Areas of the Front Spar of the Wing – Beam/Shell-R Model.....	198
Table 4.21: Cross Sectional Areas of the Rear Spar of the Wing – Beam/Shell-R Model.....	199
Table 4.22: Thicknesses of the Upper Middle Skin of the Wing - Beam/Shell-R Model.....	199
Table 4.23: Initial and Final Optimized Masses of the Wing - Rod/Membrane-R Model.....	201
Table 4.24: Cross Sectional Areas of the Front Spar of the Wing – Rod/Membrane-R Model.....	202
Table 4.25: Cross Sectional Areas of the Rear Spar of the Wing – Rod/Membrane-R Model.....	203
Table 4.26: Thicknesses of the Upper Middle Skin of the Wing - Rod/Membrane-R Model.....	203
Table 4.27: Initial and Final Optimized Mass of the Wing – Beam/Membrane-R Model.....	205
Table 4.28: Cross Sectional Areas of the Front Spar of the Wing – Beam/Membrane-R Model.....	207
Table 4.29: Cross Sectional Areas of the Rear Spar of the Wing – Beam/Membrane-R Model.....	208
Table 4.30: Thicknesses of the Upper Middle Skin of the Wing - Beam/Membrane-R Model.....	208
Table 4.31: Optimized Masses of the Wing Structure - Coarse Mesh Results – Coarse Mesh.....	209
Table 4.32: Optimized Masses of the Wing Structure - Fine Mesh Results.....	210
Table 4.33: Optimized Masses of the Wing - Rod/Shell Model under Stresses Constraints Only.....	212
Table 4.34: Optimized Masses of the Wing – Rod/Shell Model under Stress and Displacement Constraints.....	218
Table 4.35: Optimized Masses of the Wing – Rod/Shell Model under Stress and Buckling Constraints.....	223
Table 4.36: Optimized Mass (kg) of the Wing Structure – Rod/Shear Panel Model.....	229

Table 4.37: Optimized Mass (kg) of Wing Structure – Rod/Shear Panel Model with the 30 cm Tip Displacement Constraint.....	230
Table 4.38: Cross Sectional Areas of the Front Spar of the Wing for the 20 cm Tip Displacement Constraint- Rod/Shear Panel Model	235
Table 4.39: Cross Sectional Areas of the Front Spar of the Wing for the 30 cm Tip Displacement Constraint- Rod/Shear Panel Model	235
Table 4.40: Optimized Mass (kg) of Wing Structure – Rod/Membrane Model with the 30 cm Tip Displacement Constraints	237
Table 4.41: Cross Sectional Areas of the Front Spar of the Wing- Rod/Membrane Model	239
Table 4.42: Summary of Optimized Masses of the Wing Torque Box for the Rod/Shear and the Rod/Membrane Models	240
Table 4.43: Mass (kg) of the Wing Torque Box Obtained By Using the First and Second Idealization in the Analytical Solution – Point A.....	242
Table 4.44: Review of Mass (kg) Optimization Results of the Wing Torque Box Models – Coarse Mesh.....	243
Table 4.45: Review of Mass (kg) Optimization Results of the Wing Torque Box Models – Fine Mesh.....	243
Table A.1: Average Axial Stress Acting on Skins and Spar Webs Panels (MPa) ...	255
Table A.2: Flange Areas Determined Using the 2 nd Idealization - Point A.....	258
Table A.3: Standard Flange Areas Determined Using the 2 nd Idealization - Point A	258
Table E.1: Standard Thicknesses and Flange Areas	283

LIST OF FIGURES

FIGURES

Figure 2.1: NACA 2412 Wing Cross-section	6
Figure 2.2: Figure A1 in FAR Part 23 Appendix A	10
Figure 2.3: Figure A2 in FAR Part 23 Appendix A	10
Figure 2.4: V-N Diagram	11
Figure 2.5: Span-wise Variation of Normalized Aerodynamic Lift Distribution at Minimum Maneuvering Speed – Point A	15
Figure 2.6: Span-wise Variation of Normalized Aerodynamic Pitching Moment Distribution at Minimum Maneuvering Speed – Point A	16
Figure 2.7: Span-wise Variation of Normalized Aerodynamic Lift Distribution at the Dive Speed - Point D	16
Figure 2.8: Span-wise Variation of Normalized Aerodynamic Pitching Moment Distribution at the Dive Speed – Point D.....	17
Figure 2.9: Span-wise Sectional Shear Force Distribution at Point A.....	18
Figure 2.10: Span-wise Sectional Bending Moment Distribution at Point A	19
Figure 2.11: Span-wise Sectional Pitching Moment Distribution at Point A	19
Figure 2.12: Span-wise Sectional Shear Force Distribution at Point D.....	20
Figure 2.13: Span-wise Sectional Bending Moment Distribution at Point D	21
Figure 2.14: Span-wise Sectional Pitching Moment Distribution at Point D	21
Figure 2.15: Structural Idealization # 1	22
Figure 2.16: Spars and Stiffeners Locations as a Function of (x) % of the Chord.....	23
Figure 2.17: Flow Chart of Design Steps for Idealization Case # 1	25
Figure 2.17: Flow Chart of Design Steps for Idealization Case # 1 - (continues).....	26
Figure 2.18: Axial Stresses Acting On Spar Caps & Stringers of 1 st Idealization	28
Figure 2.19: Axial Stresses Acting on Skins and Spar webs of 2 nd Idealization.....	28
Figure 2.20: Seconds Moment of Inertia and Product of Inertia Calculation of Inclined Thin Sections	29
Figure 2.21: Parallel Axis Theorem.....	29

Figure 2.22: Shear Flow (q), Thickness (t), and Curvature Length (s) in the 1 st Structural Idealization.....	30
Figure 2.23: Shear Flow (q), Thickness (t), and Curvature Length (s) in the 2 nd Structural Idealization.....	31
Figure 2.24: Double Walled Structure.....	37
Figure 2.25: Structural Lay-Out of the Wing Structure.....	40
Figure 2.26: Mass Breakdown of the Wing Configurations Designed Using Structural Idealizations 1 and 2 – External Loading Calculated at Point A.....	43
Figure 2.27: Wing Spars and Stiffeners Definitions.....	44
Figure 2.28: Spanwise Variation of the Area of Spar Cap 1 Determined by Using the 1 st and the 2 nd Structural Idealization.....	46
Figure 2.29: Spanwise Variation of the Area of Spar Cap 2 Determined by Using the 1 st and the 2 nd Structural Idealization.....	47
Figure 2.30: Spanwise Variation of the Area of Spar Cap 3 Determined by Using the 1 st and the 2 nd Structural Idealization.....	47
Figure 2.31: Spanwise Variation of the Area of Spar Cap 4 Determined by Using the 1 st and the 2 nd Structural Idealization.....	48
Figure 2.32: Spanwise Variation of the Area of Stringer 1 Determined by Using the 1 st and the 2 nd Structural Idealization.....	48
Figure 2.33: Spanwise Variation of the Area of Stringer 2 Determined by Using the 1 st and the 2 nd Structural Idealization.....	49
Figure 2.34: Thickness Definitions of the Wing.....	50
Figure 2.35: Spanwise Variation of the Nose Skin Thickness for the 1 st and 2 nd Structural Idealization.....	52
Figure 2.36: Spanwise Variation of the Mid-Upper Skin Thickness for the 1 st and 2 nd Structural Idealization.....	52
Figure 2.37: Spanwise Variation of the Mid-Lower Skin Thickness for the 1 st and 2 nd Structural Idealization.....	53
Figure 2.38: Spanwise Variation of the Right-Upper Skin Thickness for the 1 st and 2 nd Structural Idealization.....	53
Figure 2.39: Spanwise Variation of the Right-Lower Skin Thickness for the 1 st and 2 nd Structural Idealization.....	54
Figure 2.40: Spanwise Variation of the Front Spar Web Skin Thickness for the 1 st and 2 nd Structural Idealization.....	54

Figure 2.41: Spanwise Variation of the Rear Spar Web Skin Thickness for the 1 st and 2 nd Structural Idealization	55
Figure 2.42: Nose Rib Thickness Variation of the 1 st and 2 nd Structural Idealization – Point A	57
Figure 2.43: Mid Rib Thickness Variation for the 1st and 2nd Structural Idealization - Point A	58
Figure 3.1: Structural Lay-Out of the Wing	62
Figure 3.2: External Aerodynamic Load Distribution and Boundary Conditions	63
Figure 3.3: Element Types and Definitions	64
Figure 3.4: Tip Moment Loading on Box Beam Model	65
Figure 3.5: Shell Shear Stress Results	66
Figure 3.6: Uniform Pressure Loading on the Box Beam Model.....	67
Figure 3.7: Shell Elements 238, 239, 242 and 243	68
Figure 3.8: Membrane Elements 238, 239, 242 and 243	70
Figure 3.9: Deformation Plot of the Shell Model - Four Shell Elements in the Width Direction.....	71
Figure 3.10: Deformation Plot of the Membrane Model - Four Membrane Elements in the Width Direction.....	72
Figure 3.11: Axial Stresses Obtained by the Shell Elements at the Center of the Box Beam	73
Figure 3.12: Axial Stresses Obtained by the Membrane Elements at the Center of the Box Beam.....	74
Figure 3.13: Deformation Plot of the Shell Model - One Shell Element in the Width Direction.....	74
Figure 3.14: Deformation Plot of the Membrane Model - One Membrane Element in the Width Direction	75
Figure 3.15: Membrane Elements Taken from the Top Skin of the Box Beam - Coarse and Fine Mesh.....	76
Figure 3.16: Tip Force Loading on Box Beam Model.....	77
Figure 3.17: Shell Elements 238, 239, 242 and 243 and the Stress Monitor Point	78
Figure 3.18: Deformation Plot of the Shell Model - Four Shell Elements in the Width Direction.....	80

Figure 3.19: Deformation Plot of the Membrane Model - Four Shell Elements in the Width Direction	81
Figure 3.20: Axial Stresses Obtained by the Shell Elements at the Center of the Box Beam	82
Figure 3.21: Axial Stresses Obtained by the Membrane Elements at the Center of the Box Beam.....	83
Figure 3.22: Deformation Plot of the Shell Model - One Shell Element in the Width Direction.....	83
Figure 3.23: Deformation Plot of the Shell Model - One Membrane Element in the Width Direction	84
Figure 3.24: Tip Moment Loading on Box Beam Model with Flanges and No Ribs	85
Figure 3.25: Deformation Plot of the Membrane - Beam Model - One Membrane Element in the Width Direction.....	86
Figure 3.26: Distributed Line Force on the Box Beam Model.....	86
Figure 3.27: Deformation Plot of the Membrane Model Under Distributed Line Force – One Element in the Width Direction.....	87
Figure 3.28: Deformation Plot of the Shell Model Under Distributed Line Force - One Element in the Width Direction	88
Figure 3.29: Deformation Plot of the Membrane Model Under Distributed Line Force - Four Elements in the Width Direction and Between the Ribs	89
Figure 3.30: Deformation Plot of the Membrane – R Model Under Distributed Line Force - Four Elements in the Width Direction and Between the Ribs	89
Figure 3.31: Distributed Line Pitching Moment Acting on the Box Beam Model ...	90
Figure 3.32: Deformation Plot of the Membrane Model Under Distributed Line Pitching Moment - One Element in the Width Direction	91
Figure 3.33: Deformation Plot of the Membrane - R Model Under Distributed Line Pitching Moment - One Element in the Width Direction	91
Figure 3.34: Deformation Plot of the Membrane Model Under Distributed Line Pitching Moment - Four Elements in the Width Direction	92
Figure 3.35: Deformation Plot of the Membrane - R Model Under Distributed Line Pitching Moment - Four Elements in the Width Direction	93
Figure 3.36: Surface Model of the Wing	96
Figure 3.37: Surface Model of the Internal Structure of the Wing.....	97
Figure 3.38: Upper and Lower Surfaces of the Wing Structure.....	97

Figure 3.39: Surface Model of the Ribs	98
Figure 3.40: 1 st and 2 nd Mesh Models of the Wing Structure.....	99
Figure 3.41: 3 rd and 4 th Mesh Models of the Wing Structure.....	99
Figure 3.42: 5 th and 6 th Mesh Models of the Wing Structure.....	100
Figure 3.43: Deformation Plot of the Wing for the Coarse Mesh Case Rod/Shell Model	101
Figure 3.44: Deformation Plot of the Wing for the Fine Mesh Case Rod/Shell Model	102
Figure 3.45: Von Mises Stress Distribution on the Shell Elements for the Fine Mesh Case - Rod/Shell Model	103
Figure 3.46: Von Mises Stress Distribution on the Shell Elements for the Fine Mesh Case - Rod/Shell Model	103
Figure 3.47: Axial Stress Distribution on the Front Spar Upper Flange for the Coarse and the Fine Mesh Cases – Rod/Shell Model.....	105
Figure 3.48: Axial Stress Distribution on the Upper Middle Stiffener for the Coarse and the Fine Mesh Cases – Rod/Shell Model.....	105
Figure 3.49: Deformation Plot of the Wing for the Coarse Mesh Case Beam/Shell Model	106
Figure 3.50: Deformation Plot of the Wing for the Fine Mesh Case Beam/Shell Model	106
Figure 3.51: Von Mises Stress Distribution on the Shell Elements for the Coarse Mesh Case - Beam/Shell Model	107
Figure 3.52: Von Mises Stress Distribution on the Shell Elements for the Fine Mesh Case - Beam/Shell Model.....	107
Figure 3.53: Axial Stress Distribution on the Front Spar Upper Flange for the Coarse and the Fine Mesh Cases – Beam/Shell Model	109
Figure 3.54: Axial Stress Distribution on the Upper Middle Stiffener for the Coarse and the Fine Mesh Cases – Beam/Shell Model	109
Figure 3.55: Deformation Plot of the Wing for the Coarse Mesh Case Rod Shell-R Model	111
Figure 3.56: Deformation Plot of the Wing for the Fine Mesh Case Rod Shell-R Model	111
Figure 3.57: Von Mises Stress Distribution on the Shell-R Elements for the Coarse Mesh Case - Rod/Shell-R Model.....	112

Figure 3.58: Von Mises Stress Distribution on the Shell-R Elements for the Fine Mesh Case - Rod/Shell-R Model.....	112
Figure 3.59: Axial Stress Distribution on the Upper Flange of the Front Spar for the Coarse and the Fine Mesh Case – Rod/Shell-R Model.....	114
Figure 3.60: Axial Stress Distribution on the Upper Middle Stiffener for the Coarse and the Fine Mesh Case – Rod/Shell-R Model	114
Figure 3.61: Deformation Plot of the Wing for the Coarse Mesh Case Beam/Shell-R Model.....	115
Figure 3.62: Deformation Plot of the Wing for the Fine Mesh Case Beam/Shell-R Model.....	115
Figure 3.63: Von Mises Stress Distribution on the Shell-R Elements for the Coarse Mesh Case - Beam/Shell-R Model	116
Figure 3.64: Von Mises Stress Distribution on the Shell-R Elements for the Fine Mesh Case - Beam/Shell-R Model	116
Figure 3.65: Axial Stress Distribution on the Upper Flange of the Front Spar for the Coarse and the Fine Mesh Case – Beam/Shell-R Model.....	118
Figure 3.66: Axial Stress Distribution on the Upper Middle Stiffener for the Coarse and the Fine Mesh Case – Beam/Shell-R Model.....	118
Figure 3.67: Deformation Plot of the Wing for the Coarse Mesh Case Rod/Membrane-R Model	119
Figure 3.68: Von Mises Stress Distribution on the Membrane-R Elements for the Coarse Mesh Case - Rod/Membrane-R Model	120
Figure 3.69: Axial Stress Distribution on the Upper Flange of the Front Spar for the Coarse Mesh Case – Rod/Membrane-R Model.....	121
Figure 3.70: Axial Stress Distribution on the Upper Middle Stiffener for the Coarse Mesh Case – Rod/Membrane-R Model	121
Figure 3.71: Deformation Plot of the Wing for the Coarse Mesh Case Beam/Membrane-R Model.....	122
Figure 3.72: Von Mises Stress Distribution on the Membrane-R Elements for the Coarse Mesh Case - Rod/Membrane-R Model	123
Figure 3.73: Axial Stresses Distribution of the Upper Front Spar for the Coarse Mesh Case – Beam/Membrane-R Model.....	124
Figure 3.74: Axial Stresses Distribution of the Middle Upper Stiffener for the Coarse Mesh Case – Beam/Membrane-R Model	124

Figure 3.75: Deformation Plot of the Rod/Membrane Model of the Wing Structure under Pure Line Pitching Moment Loading	126
Figure 3.76: Deformation Plot of the Rod/Membrane Model of the Structure under Pure Line Lift Force Loading	126
Figure 3.77: Deformation Plot of the Rod/Membrane-R Model of the Wing Torque Box under Pure Pitching Moment Loading.....	127
Figure 3.78: Deformation Plot of the Rod/Membrane-R Model of the Wing Torque Box under Pure Lift Force Loading	128
Figure 3.79: Extensional Areas for the Shear Panel	129
Figure 3.80: Extensional Rod Areas for Rod/Shear Panel of the Wing Torque Box	130
Figure 3.81: Deformation Plot of the Rod/Shear Model of the Wing Torque Box under Pure Pitching Moment Loading	131
Figure 3.82: Deformation Plot of the Rod/Shear Model of the Wing Torque Box under Pure Lift Force Loading	131
Figure 3.83: FE Axial Stress results in the Spar Flanges and Stiffeners at the Center Bays of the Wing Determined by the Finite Element Analysis- Beam/Shell Coarse Mesh Model.....	139
Figure 3.84: FE Axial Stress results in the Spar Flanges and Stiffeners at the Center Bays of the Wing Determined by the Finite Element Analysis- Beam/Shell Fine Mesh Model.....	140
Figure 3.85: Axial Stress results in the Wing Upper Skins at the Center Bays of the Wing Determined by the Finite Element Analysis- Rod/Shell Coarse Mesh Model	143
Figure 3.86: Axial Stress results in the Wing Upper Skins at the Center Bays of the Wing Determined by the Finite Element Analysis- Rod/Shell Fine Mesh Model ...	144
Figure 3.87: Von Mises Stress Monitor Points on the Wing Skins and Spar webs of the 2 nd Idealization	145
Figure 3.88: Wing Skins and Spar Webs Definition	145
Figure 4.1: Traditional Optimization Approach.....	152
Figure 4.2: Coupling finite element analysis and optimization using approximate design model [23]	154
Figure 4.3: MSC.NASTRAN® Implementation of Structural Optimization	155
Figure 4.4: Wing Model Used in the Optimization Study	160

Figure 4.5: Span-wise Variation of the Aerodynamic Lift Distribution –Point A ...	161
Figure 4.6: Span-wise Variation of the Aerodynamic Pitching Moment Distribution - Point A	161
Figure 4.7: Distribution of the External Aerodynamic Loading	162
Figure 4.8: Wing Model Showing the Spar, Stiffener and Rib Locations	166
Figure 4.9: Rendered Finite Element Model of the Wing.....	167
Figure 4.10: Variation of the Mass of Wing with Respect to Design Cycles - Coarse Mesh Rod/Shell Model	177
Figure 4.11: Variation of the Mass of Wing with Respect to Design Cycles - Fine Mesh Rod/Shell Model	177
Figure 4.12: Thickness Scalar Plots of Upper Skin Panels in the Optimized Wing Torque Box- Coarse Mesh- Rod/Shell Model.....	179
Figure 4.13: Thickness Scalar Plots of Upper Skin Panels in the Optimized Wing Torque Box - Fine Mesh – Rod/Shell Model.....	179
Figure 4.14: Thickness Scalar Plots of Lower Skin, Spar Web and Rib Panels in the Optimized Wing Torque Box- Coarse Mesh- Rod/Shell Model.....	180
Figure 4.15: Thickness Scalar Plots of Lower Skin, Spar Web and Rib Panels in the Optimized Wing Torque Box - Fine Mesh- Rod/Shell Model.....	180
Figure 4.16: Variation of the Mass of Wing with Respect to Design Cycles - Coarse Mesh Beam/Shell Model.....	183
Figure 4.17: Variation of the Mass of Wing with Respect to Design Cycles – Fine Mesh Beam/Shell Model.....	184
Figure 4.18: Thickness Scalar Plots of Upper Skin Panels in the Optimized Wing Torque Box - Coarse Mesh Beam/Shell Model	185
Figure 4.19: Thickness Scalar Plots of Upper Skin Panels in the Optimized Wing Torque Box - Fine Mesh Beam/Shell Model	185
Figure 4.20: Thickness Scalar Plots of Lower Skin, Spar Web and Rib Panels in the Optimized Wing Torque Box - Coarse Mesh Beam/Shell Model.....	186
Figure 4.21: Thickness Scalar Plots of Lower Skin, Spar Web and Rib Panels in the Optimized Wing Torque Box - Fine Mesh Beam/Shell Model.....	186
Figure 4.22: Variation of the Mass of Wing with Respect to Design Cycles - Coarse Mesh Rod/Shell-R Model	189
Figure 4.23: Variation of the Mass of Wing with Respect to Design Cycles - Fine Mesh Rod/Shell-R Model	189

Figure 4.24: Thickness Scalar Plots of Upper Skin Panels in the Optimized Wing Torque Box - Coarse Mesh Rod/Shell-R Model	191
Figure 4.25: Thickness Scalar Plots of Upper Skin Panels in the Optimized Wing Torque Box - Fine Mesh Rod/Shell-R Model	191
Figure 4.26: Thickness Scalar Plots of Lower Skin, Spar Web and Rib Panels in the Optimized Wing Torque Box - Coarse Mesh Rod/Shell-R Model	192
Figure 4.27: Thickness Scalar Plots of Lower Skin, Spar Web and Rib Panels in the Optimized Wing Torque Box - Fine Mesh Rod/Shell-R Model	192
Figure 4.28: Variation of the Mass of the Wing with Respect to Design Cycles - Coarse Mesh Beam/Shell-R Model	195
Figure 4.29: Variation of the Mass of the Wing with Respect to Design Cycles - Fine Mesh Beam/Shell-R Model	195
Figure 4.30: Thickness Scalar Plots of Upper Skin Panels in the Optimized Wing Torque Box - Coarse Mesh Beam/Shell-R Model.....	196
Figure 4.31: Thickness Scalar Plots of Upper Skin Panels in the Optimized Wing Torque Box - Fine Mesh Beam/Shell-R Model	197
Figure 4.32 Thickness Scalar Plots of Lower Skin, Spar Web and Rib Panels in the Optimized Wing Torque Box - Coarse Mesh Beam/Shell-R Model.....	197
Figure 4.33: Thickness Scalar Plots of Lower Skin, Spar Web and Rib Panels in the Optimized Wing Torque Box - Fine Mesh Beam/Shell-R Model.....	198
Figure 4.34: Variation of the Mass of the Wing with Respect to the Design Cycle - Coarse Mesh Rod/Membrane-R Model	200
Figure 4.35: Thickness Scalar Plot of Upper Skin Panels in the Optimized Wing Torque Box - Coarse Mesh Rod/Membrane-R Model	201
Figure 4.36: Thickness Scalar Plot of Lower Skin, Spar Web and Rib Panels in the Optimized Wing Torque Box - Coarse Mesh Rod/Membrane-R Model.....	202
Figure 4.37: Variation of the Mass of Wing with Respect to the Design Cycle - Coarse Mesh Beam/Membrane-R Model.....	205
Figure 4.38: Thickness Scalar Plot of Upper Skin Panels in the Optimized Wing Torque Box - Coarse Mesh Beam/Membrane-R Model.....	206
Figure 4.39: Thickness Scalar Plot of Lower Skin, Spar Web and Rib Panels in the Optimized Wing Torque Box - Coarse Mesh Beam/Membrane-R Model	207
Figure 4.40: Variation of Upper Middle Skin Thickness of the Optimized Wing Torque Boxes - Coarse Mesh Models.....	211

Figure 4.41: Variation Upper -Flange Cap Areas of the Front Spar in the Optimized Wing Torque Boxes - Coarse Mesh Models	211
Figure 4.42: Variation of the Mass of the Wing With Design Iterations – Rod/Shell Coarse Mesh Model under Stress Constraints Only	213
Figure 4.43: Variation of the Mass of the Wing With Design Iterations – Rod/Shell Fine Mesh Model under Stress Constraints Only	214
Figure 4.44: Thickness Scalar Plots of Upper Skin Panels in the Optimized Wing Rod/Shell for Coarse Mesh Model under Stresses Constraints.....	214
Figure 4.45: Thickness Scalar Plots of Upper Skin Panels in the Optimized Wing Rod/Shell for Fine Mesh Model under Stresses Constraints.....	215
Figure 4.46: Thickness Scalar Plots of Interior Panels in the Optimized Wing Rod/Shell for Coarse Mesh Model under Stresses Constraints.....	215
Figure 4.47: Thickness Scalar Plots of Upper Skin Panels in the Optimized Wing – Rod/Shell Fine Mesh Model under Stress Constraint Only	216
Figure 4.48: Variation of the Front Spar Upper Flange Areas of the Wing - Rod Shell Model under Stress Constraint Only.....	216
Figure 4.49: Variation of the Upper Middle Skin Thicknesses of the Wing – Rod/Shell Model under Stress Constraint Only	217
Figure 4.50: Variation of the Mass of Wing With the Design Cycles – Rod/Shell Coarse Mesh Model under Stress and Displacement Constraints	219
Figure 4.51: Variation of the Mass of the Wing With the Design Cycle – Rod/Shell Fine Mesh Model under Stress and Displacement Constraints	219
Figure 4.52: Thickness Scalar Plots of the Upper Skin Panels in the Optimized Wing – Rod/Shell Coarse Mesh Model under Stress and Displacement Constraints.....	220
Figure 4.53: Thickness Scalar Plots of the Upper Skin Panels in the Optimized Wing – Rod/Shell Fine Mesh Model under Stress and Displacement Constraints.....	220
Figure 4.54: Thickness Scalar Plots of Interior Panels in the Optimized Wing – Rod/Shell Coarse Mesh Model under Stress and Displacement Constraints.....	221
Figure 4.55: Thickness Scalar Plots of Interior Panels in the Optimized Wing – Rod/Shell Fine Mesh Model under Stress and Displacement Constraints.....	221
Figure 4.56: Variation of the Front Spar Upper Flange Areas of the Wing – Rod/Shell Model under Stress and Displacement Constraints	222
Figure 4.57: Variation of the Upper Middle Skin Thicknesses of the Wing – Rod/Shell Model under Stress and Displacement Constraints	222

Figure 4.58: Variation of the Mass of Wing With the Design Cycles – Rod/Shell Coarse Mesh Model under Stress and Buckling Constraints	224
Figure 4.59: Variation of the Mass of Wing With the Design Cycles – Rod/Shell Fine Mesh Model under Stress and Buckling Constraints	225
Figure 4.60: Thickness Scalar Plots of the Upper Skin Panels in the Optimized Wing – Rod/Shell Coarse Mesh Model under Stress and Buckling Constraints	225
Figure 4.61: Thickness Scalar Plots of the Upper Skin Panels in the Optimized Wing – Rod/Shell Fine Mesh Model under Stress and Buckling Constraints	226
Figure 4.62: Thickness Scalar Plots of Interior Panels in the Optimized Wing Rod/Shell for Coarse Mesh Model under Stress and Buckling Constraints	226
Figure 4.63: Thickness Scalar Plots of Interior Panels in the Optimized Wing Rod/Shell for Fine Mesh Model under Stress and Buckling Constraints	227
Figure 4.64: Variation of the Upper Flange Areas of the Front Spar of the Wing – Rod/Shell Model under Stress and Buckling Constraints	227
Figure 4.65: Variation of the Upper Middle Skin Thickness of the Wing – Rod/Shell Model under Stress and Buckling Constraints	228
Figure 4.66: Lift Force Load Distribution and Boundary Conditions Acting on the Wing - Rod/Shear Panel Model.....	229
Figure 4.67: Variation of the Mass of Wing With the Design Cycle for the 20 cm Tip Displacement Constraint – Rod/Shear Panel Coarse Mesh Model	231
Figure 4.68: Variation of the Mass of Wing With the Design Cycle for the 30 cm Modified Displacement Constraint – Rod/Shear Panel Coarse Mesh Model	231
Figure 4.69: Thickness Scalar Plots of the Upper Skin Panels in the Optimized Wing – Rod/Shear Panel Coarse Mesh Model- 20 cm Tip Deflection Constraint	232
Figure 4.70: Thickness Scalar Plots of the Interior Panels in the Optimized Wing – Rod/Shear Panel Coarse Mesh Model-20 cm Tip Deflection Constraint	233
Figure 4.71: Thickness Scalar Plots of the Upper Skin Panels in the Optimized Wing – Rod/Shear Panel Coarse Mesh Model with the Modified 30 cm Displacement Constraint	233
Figure 4.72: Thickness Scalar Plots of Interior Panels in the Optimized Wing Rod/Shear Panel Coarse Mesh Model with Modified 30 cm Displacement Constraint	234
Figure 4.73: Variation of Front Upper Spar Caps Area of Wing Rod/Shear Panel Model	236

Figure 4.74: Variation of the Mass of Wing With the Design Cycle - Rod/Membrane Coarse Mesh Model	237
Figure 4.75: Thickness Scalar Plot of the Upper Skin Panels in the Optimized Wing Structure – Rod/Membrane Coarse Mesh Model	238
Figure 4.76: Thickness Scalar Plot of Interior Panels in the Optimized Wing Structure - Rod/Membrane Coarse Mesh Model.....	238
Figure 4.77: Variation of the Upper Flange Area of the Front Spar of the Wing – Rod/Membrane Model	239
Figure 4.78: Comparison of the Upper Flange Area of the Front Spar of the Wing – Rod/Shear Panel and Rod/Membrane Model.....	240
Figure 4.79: Comparison of Upper Middle Skin Thicknesses of the Wing Rod/Shear Panel and the Rod/Membrane Model	241
Figure A.1: Axial Stresses Acting On Spar Caps & Stiffeners	254
Figure A.2: Axial Stresses Acting on Skins and Spar webs of 2 nd Idealization.....	254
Figure A.3: Wing Skins and Spar Webs Definition	254
Figure A.4 : Shear Flow (q), Thickness (t), and Curvature Length (s) in 2 nd Structural Idealization	256
Figure A.5: Compressive Buckling Coefficient K _c Graph	260
Figure A.6: Bending Buckling Coefficient K _b Graph.....	261
Figure A.7: Shear Buckling Coefficient K _s Graph.....	262
Figure A.8: Nose and Middle Rib Shear Flows, Thicknesses a and Curvature Length Definitions	263
Figure B.1: Organaization of Nastran Input File	265
Figure D.1: History of Front Upper Spar Cap Area at Bay 4.....	277
Figure D.2: History of Front Lower Spar Cap Area at Bay 4	278
Figure D.3: History of Rear Front Spar Cap Area at Bay 3	278
Figure D.4: History of Rear Lower Spar Cap Area at Bay 3	279
Figure D.5: History of Nose Skin Thickness at Bay 2.....	279
Figure D.6: History of Right Upper Skin Thickness at Bay 2	280
Figure D.7: History of Nose Skin Thickness at Bay 2.....	280
Figure D.8: History of Middle Upper Skin Thickness at Bay 4.....	281
Figure D.9: History of Rear Spar Web Thickness at Bay 3	281
Figure D.10: Variation of the Mass of Wing with Respect to Design Cycles - Coarse Mesh Rod/Shell Model	282

LIST OF SYMBOLS

NOMENCLATURE

a	Speed of sound
b	Wing span
c	Wing chord length
AOA	Angle of attack
M	Mach number
MTOW	Maximum Take-Off Weight
MOW	Minimum Operating Weight
S	Wing planform area
V	Speed, Velocity
W	Weight
W/S	Wing Loading
E	Young's Modulus
G	Shear Modulus
L	Lift Force
n	Load Factor
R	Reynolds Number
J	Torsion Stiffness
U_D	Divergence Speed
SF	Safety Factor

GREEK LETTERS

α	Angle of Attack
μ	Absolute Viscosity Coefficient
ρ	Density
ν	Poisson's Ratio

SUBSCRIPTS

A	Maneuvering Speed Point
C	Cruise Speed point
D	Diving Speed point

CONVERSION FACTORS

$$1 \text{ lb} = 0.4536 \text{ kg}$$

$$1 \text{ ft} = 0.3048 \text{ m}$$

$$1 \text{ kts} = 0.5144 \text{ m/s}$$

$$1 \text{ kts} = 1.689 \text{ ft/sec}$$

STANDARD ATMOSPHERE SEA LEVEL VALUES

$$\text{Absolute Viscosity Coefficient } \mu = 1.7894 \times 10^{-5} \text{ kg/m.s}$$

$$\text{Density } \rho = 1.225 \text{ kg/m}^3$$

$$\text{Speed of sound } a = 340 \text{ m/s}$$

LIST OF ABBREVIATIONS

1D	One Dimension
2D	Two Dimensions
FE	Finite Element
DOE	Design of Experiments
CDD	Conservative Discrete Design
FEM	Finite Element Method
N/A	Not Applicable
DOT	Design Optimization Tools

CHAPTER 1

BACKGROUND TO THE STUDY

1.1 Introduction

The major focus of structural design in the early development and manufacturing of flight vehicles was strength. Nowadays the use of lighter structures in aerospace structural design is becoming an important issue which can be achieved by using reinforced thin wall members, multi-cell box beam configuration and semi-monocoque construction. Examples of thin walled substructures reinforced by stiffeners are lifting surfaces like aircraft wing and horizontal stabilizer.

In modeling an aircraft wing, structural idealizations are often employed in hand calculations to simplify the structural analysis. In real applications of structural design and analysis, finite element methods are used because of the complexity of the geometry, combined and complex loading conditions.

In recent years, structural optimization has been combined with finite element analysis to determine component gauges that may minimize weight subjected to a number of constraints.

1.2 Purpose of the Study

Weight saving in aerospace structures is becoming ever more significant. Sustainability issues and green environment quest is putting pressure on the designers to reduce weight in aerospace structures. Thin walled lifting surfaces are regions where substantial weight savings can be achieved if optimizations techniques are used early in the design phase.

This study investigates the finite element analysis results of a wing torque box model which is designed by hand calculation method using two different idealization approaches. Also it will have a close look into the effect of using different element types on the designed wing torque box model results while performing finite element analysis and finite element optimization.

1.3 Literature Survey

In the literature there are a large number of references in the area of structural design, analysis and optimization. Stephen A. Bunis, P.E. presented on March 1994 a fundamental approach for aircraft wing torque box design [1]. The study employed also analysis methods that could be performed without the aid of a finite element routine or extensive computer programming knowledge. J. Ampofo and F. Ferguson presented in 2002 a study that focus on the preliminary design of aircraft wing structure with optimized weight by using a computer aided design method [2]. In this study, the design concept is based on the optimal arrangement of the major force-carrying components within the aircraft. The study reveals that optimum locations of the wing spars results in a minimum shear flows in spar webs and wing skins and also, minimum axial stresses in the stringers of the wing spars. The net effect is an aircraft with minimum weight.

A motivating work on the correct use of finite element models for stress analysis of an aircraft is given by Vaughan and Daniel [3]. In this study the authors presented examples on the correct and incorrect structural analysis by means of finite element method.

A number of key studies were carried out in the field of optimization methods and their use in structural engineering areas. An introduction to engineering optimization, optimum design and an overview of modern optimization methods was provided by Singiresu S. Rao in 2009 [4]. One review article is the work of Wasiutynski and Brandt who conducted a study in the field of optimum design of structures in 1960s [5]. In the area of optimum structural design concepts for aerospace vehicles Gerard presents a generalized approach for optimum design theory and preferred methods of

presenting optimum design results [6]. The paper by Ashley gives an excellent review on the use of optimization in aeronautical engineering [7].

Another study on the subject of optimization of wing structures presented by Richard Butler provides an overview of some of the existing optimization methods which may be applied at various stages during the design of wing structures. An indication of the variety of design variables, constraints and objective functions available within these methods is given [8]. Many commercial finite element programs have built-in optimization modules which work in conjunction with their finite element solvers. For instance, optimization module of MSC Nastran utilizes the DOT optimization algorithms from Vanderplaats Research and Development Inc. [9].

A trail analysis study of MSC.NASTRAN[®] optimization capability was presented by T. Miki, M. Kondo, F. Mizuguchi and Y. Ogino. The Study demonstrates the effectiveness of MSC.NASTRAN[®] optimization capability in achieving satisfactory results while saving much of the designer time [10]. A study on discrete optimization approaches in MSC.NASTRAN[®] was carried out by Xiaoming Yu, Erwin H. Johnson, and Shenghua Zhang. In their study they gave a brief background, theoretical discussions and some illustrative examples on the new discrete optimization feature in SOL 200 [11].

1.4 Scope of the Study

The organization of this thesis begins with a short introductory part that highlights the background to the study.

The process of wing structural design is given in Chapter 2. The main goal of the design phase is to give concise information on the design procedure using structural idealizations that are typically employed in the design phase, and also come up with a reasonably sized torque box which will be used in the analysis and optimization phases and make comparative study of the finite element based analysis and optimization studies with the hand calculation based design and analysis.

In Chapter 3, MSC[®]/PATRAN is used to develop the finite element model of the wing torque box structure using different element types and structural analysis are performed using MSC.NASTRAN[®]. In the analysis phase, one of the designed wing

configuration is modeled by using MSC[®]/PATRAN software program and structural analysis of the designed wing configuration is performed by the finite element analysis software MSC.NASTRAN[®] using six different element combinations, which represent different structural idealizations that are typically used in practice. In the finite element analysis part the effect of using different finite element types on the analysis results of a wing torque box, which is designed by hand calculation method using two different idealization approaches, is investigated. Comparisons are made between the analysis results of finite element solution and hand calculation. In this section, conclusions are also inferred with regard to the deficiency of certain element types in handling the true external load acting on the wing structure.

In Chapter 4, structural optimization is carried out by the MSC.NASTRAN[®] optimization module for the six different element configurations. In the optimization phase the effect of using different one and two dimensional element pairs on the final optimized configuration of wing torque box is investigated. Conclusions are inferred with regard to the sensitivity of the optimized wing configuration with respect to the choice of different element types in the finite element model. Final optimized torque box configurations are also compared with the hand calculation based designs which are also optimized using iterations.

A general conclusion of the study and several follow-on topics are presented for future thesis work in Chapter 5.

CHAPTER 2

WING TORQUE BOX STRUCTURAL DESIGN

2.1 Introduction

This chapter describes the preliminary structural design process of a typical aircraft wing torque box by hand calculation. During the structural design process, iterations are performed using the standard size components, which are selected from the related catalogs, to come up with designs with minimum weight. The process of structural design starts from the external aerodynamic load estimation, internal structural loads calculations, structural sizing and layout. Two different structural idealization approaches are used to design the wing torque box. The goal is to come up with an acceptable design based on material strength, stiffness requirements and local buckling with the objective of achieving minimum weight wing configuration.

2.2 Wing Description and Requirements

The basic wing design is assumed to be for a single utility aircraft having a maximum takeoff weight of 1460 kg and minimum operating weight of 861 kg. The wing structure is taken as a straight and unswept wing. The design should meet the minimum requirements set forth in the appendix A (Simplified Design Load Criteria) of the Federal Aviation Regulations Part 23.

As shown in Figure 2.1 the wing has a NACA 2412 airfoil profile with a rectangular planform and has a chord length of 1.524 m and semi-span of 4.572 m.

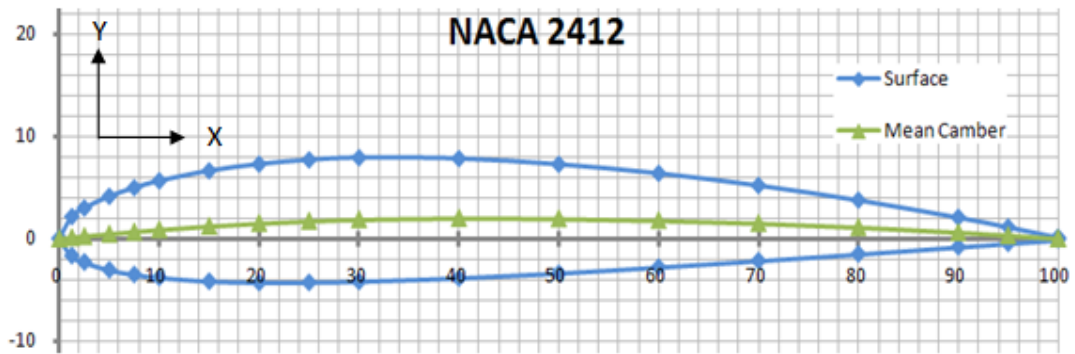


Figure 2.1: NACA 2412 Wing Cross-section

2.2.1 Applicability of FAR Part 23 Appendix A

In order for the design to be acceptable, the criteria defined in Appendix A of FAR Part 23 should be satisfied. Table 2.1 shows the applicability of the criteria satisfying the design requirements [12].

Table 2.1: Criteria per FAR Part 23 Appendix A 23.1

	Criteria per FAR Part 23 Appendix A 23.1 "General":	Value	Check
1	Maximum weight of 6,000 pounds or less	MTOW = 3213 lb	Passed
2	A single engine excluding turbine power plants	Not Applicable (N/A)	
3	A main wing located closer to the airplane's center of gravity than to the aft, fuselage-mounted, empennage	N/A	
4	A main wing that contains a quarter-chord sweep angle of not more than 15 degrees fore or aft	No sweep	Passed
5	A main wing that is equipped with trailing-edge controls (ailerons or flaps, or both)	N/A	
6	A main wing aspect ratio not greater than 7	$b^2/S = 6$	Passed
7	A horizontal tail aspect ratio not greater than 4	N/A	
8	A horizontal tail volume coefficient not less than 0.34	N/A	
9	A vertical tail aspect ratio not greater than 2	N/A	
10	A vertical tail platform area not greater than 10 percent of the wing platform area	N/A	
11	Symmetrical airfoils must be used in both the horizontal and vertical tail designs	N/A	
12	None of canard, tandem-wing, close-coupled, or tailless arrangements of the lifting surfaces	N/A	
13	No biplane or multiplane wing arrangements	No	Passed

Table 2.1: Criteria per FAR Part 23 Appendix A 23.1 - (continues)

14	None of T-tail, V-tail, or cruciform-tail (+) arrangements	N/A	
15	None of highly-swept wing platform (more than 15-degrees of sweep at the quarter-chord), delta planforms, or slatted lifting surfaces	No sweep	Passed
16	None of winglets or other wing tip devices, or outboard fins	No wing tip device	Passed

2.3 Aerodynamic Loads Calculation Procedure

The aerodynamic load is calculated for the steady pull-up maneuver at the positive maximum load factor for both minimum maneuvering speed and dive speed. These conditions correspond to the upper corner points of the V-N diagram for the particular airplane. Based on this information, span-wise lift and pitching moment distribution is calculated in accordance with the ESDU document 95010 which calculates the span-wise loading of wings with camber and twist in subsonic attached flow using the lifting surface theory [13].

2.3.1 Calculation of Wing Planform Area and Wing Loading

1. Wing Planform Area, S :

The given values are:

Wing semi span, $b/2 = 15 \text{ ft} = 4.572 \text{ m}$

Chord length, $c = 5 \text{ ft} = 1.524 \text{ m}$

Therefore,

Wing Span, $b = 30 \text{ ft} = 9.144 \text{ m}$

Wing Planform Area, $S = 150 \text{ ft}^2 = 13.935 \text{ m}^2$

2. Wing Loading, W/S :

The given values of aircraft weights and the converted values in pounds are:

$$W_{MTOW} = 1460 \text{ kg} = 3218.716 \text{ lb}$$

$$W_{MOW} = 861 \text{ kg} = 1898.161 \text{ lb}$$

The calculation of wing loadings is below:

$$W/S_{MTOW} = 21.458 \text{ lb/ft}^2 = 104.769 \text{ kg/m}^2$$

$$W/S_{MOW} = 12.654 \text{ lb/ft}^2 = 61.785 \text{ kg/m}^2$$

2.3.2 Calculation of Limit Load Factors and Minimum Speeds

The load factors limits and minimum speeds are determined by using Table 1 in FAR Part 23 Appendix A [12]. Table 2.2 defines the limit flight load factors for each category of aircrafts.

Table 2.2: Limit Flight Load Factors Table in Appendix A 23.1

Limit Flight Load Factors				
Flight Load Factors		Normal Category	Utility Category	Acrobatic Category
Flaps Up	n_1	3.8	4.4	6.0
	n_2	$-0.5n_1$		
	n_3	Find n_3 from Fig A1		
	n_4	Find n_4 from Fig A2		
Flaps Down	$n_{\text{-flap}}$	$0.5n_1$		
	$n_{\text{-flap}}$	Zero*		
* Vertical wing load may be assumed equal to zero and only the flap part of the wing need to be checked for this condition.				

For an utility aircraft, from Table 2.2 it can be seen that the values of load factors n_1 and n_2 are 4.4 and -2.2 for the positive and negative g conditions. In order to determine the other load factors n_3 and n_4 , which are the positive and negative gust, limit load factors, the minimum design speeds are calculated first by referring to the equations in Figure A3 in FAR Part23 Appendix A. Eqns. 2.1, 2.2 and 2.3 summarize Figure A3 in FAR Part23 Appendix A.

$$V_{C,min} = 17.0 \sqrt{n_1 \frac{W}{S}} \text{ and } V_{C,min} \leq 0.9 V_H \quad (2.1)$$

$$V_{D,min} = 24.0 \sqrt{n_1 \frac{W}{S}} \text{ and } V_{D,min} \leq 1.4 \sqrt{\frac{n_1}{3.8}} V_{C,min} \quad (2.2)$$

$$V_{A,min} = 15.0 \sqrt{n_1 \frac{W}{S}} \text{ and } V_{A,min} \leq V_{C,selected} \quad (2.3)$$

The results are presented in Table 2.3:

Table 2.3: Minimum Designed and Checked Speeds

Speed	In SI Units (m/s)	In Imperial Units (kts)	
	Minimum (converted)	Minimum ¹ (calculated)	Checking Speed ²
V _A	74.975	145.752	180 ³
V _C	84.971	165.185	
V _D	119.959	233.203	248.848

1) Above formula for minimum design speeds give results in knots.
2) The checking speeds are calculated as the right hand side of above inequalities suggest.
3) The selected cruise speed (V_{C, selected}) is chosen as 180 kts.

In order to find the values of n_3 and n_4 , the K value which defines the ratio of the selected cruise speed to the minimum cruise speed must be calculated first as shown in Eqn. (2.4) along with the wing loading which is calculated by Eqn. (2.5).

$$K = \frac{V_{C,selected}}{V_{C,min}} = \frac{180}{165.185} \cong 1.1 \quad (2.4)$$

$$\frac{n_1 W}{S} = 94.415 \text{ lb/ft}^2 \quad (2.5)$$

By referring to Figure 2.2 which defines the chart for finding n_3 load factor at speed V_C , the load factor n_3 is found by using the values of K and the wing loading. From Figure 2.2, the value of n_3 / n_1 ratio is read as 1, and since the value of n_1 which was previously determined as 4.4, n_3 value is also 4.4.

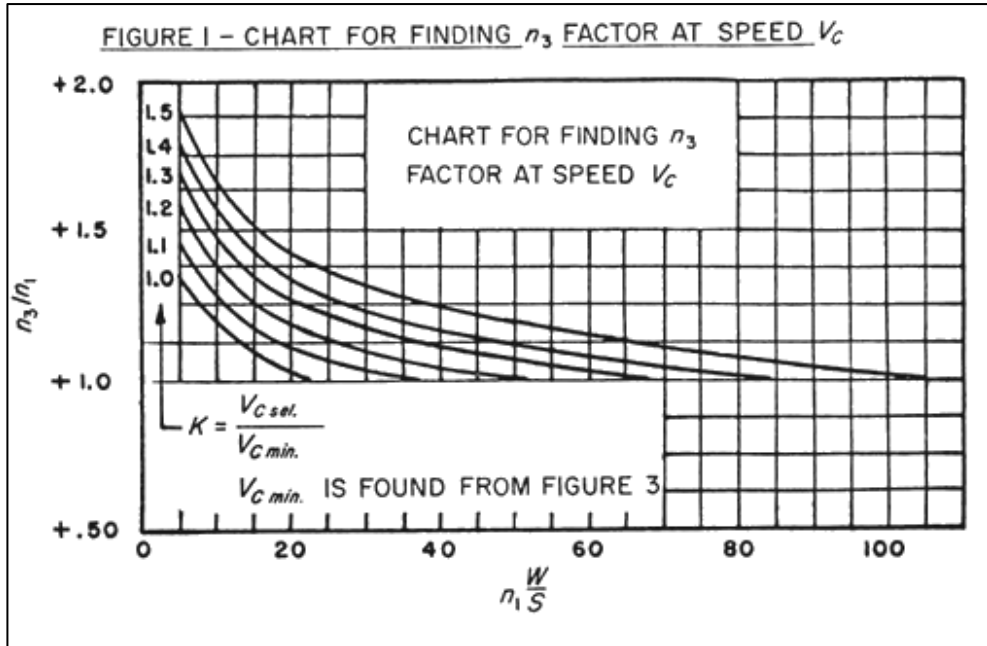


Figure 2.2: Figure A1 in FAR Part 23 Appendix A

In the same manner and by referring to Figure 2.3, which defines the chart for finding n_4 load factor at speed V_C , the load factor n_4 is found by using the values of K and wing loading to read the value of n_4 / n_1 ratio. Since n_4 / n_1 ratio is read as -0.5 and the value of n_1 is 4.4, n_4 value is found as -2.2.

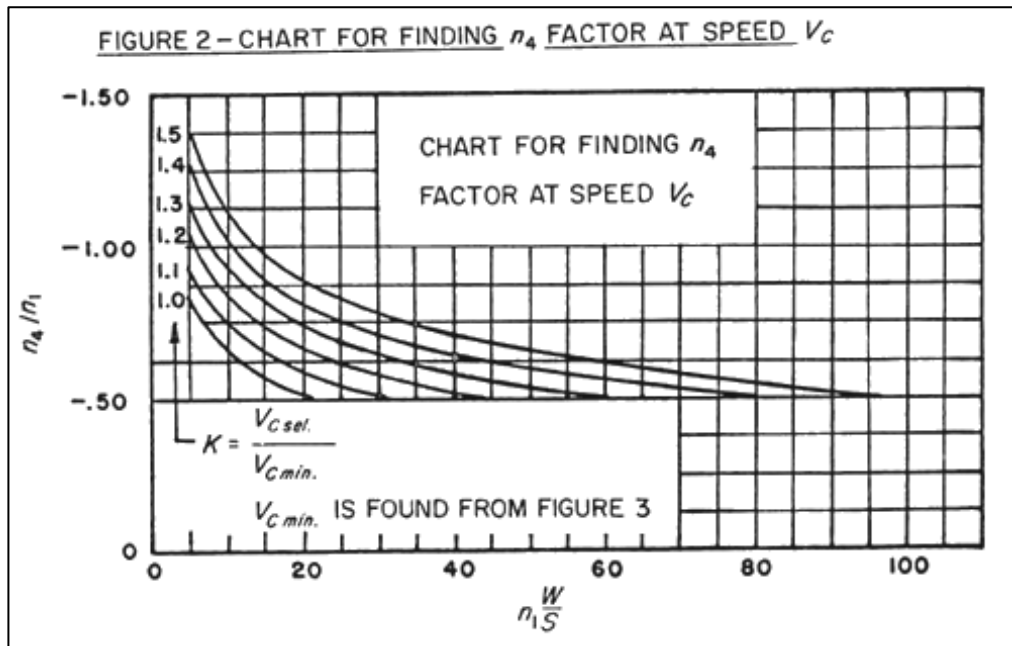


Figure 2.3: Figure A2 in FAR Part 23 Appendix A

The load factor results are tabulated in Table 2.4 below:

Table 2.4: Limit Load Factors

Limit Load Factor Ratio		Limit Load Factor	Value
-	-	n_1	4.4
-	-	n_2	-2.2
n_3/n_1	1.0	n_3	4.4
n_4/n_1	-0.5	n_4	-2.2

2.3.3 Constructing the V-N Diagram

Figure 2.4 shows the V-N diagram, which is constructed based on Appendix A of FAR 23.

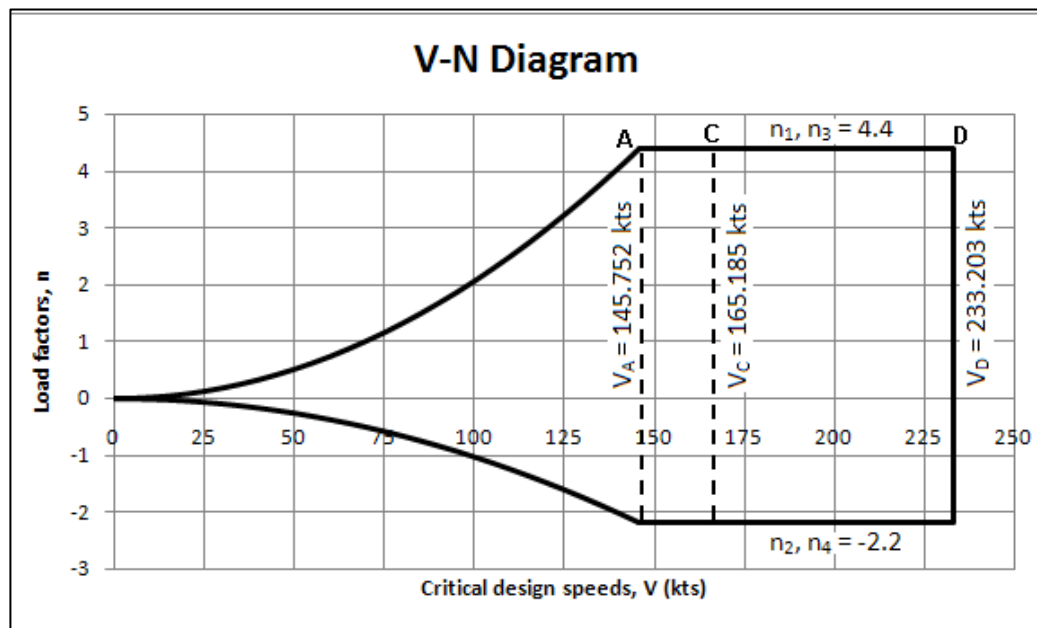


Figure 2.4: V-N Diagram

The upper right and lower right points on the V-N diagram correspond to maximum positive and negative n factors. As it can be seen from Figure 2.2, the positive limit load factor value is 4.4 and the negative limit load factor value is -2.2. Point A

defines the minimum maneuvering speed V_A with a value of 145.8 kts. Point C on defines the minimum cruise speed V_C with a value of 165.2 kts. The minimum dive speed V_D is defined at point D and it has a value of 233.2 kts.

2.3.4 Calculation of Angles of Attack

Angles of attack are calculated at minimum maneuvering speed and dive speed at the corner points of the V-N diagram. These points correspond to limit external aerodynamic loading.

1. AOA at the Minimum Maneuvering Speed:

In order to calculate the angle of attack at minimum maneuvering speed, the maximum angle of attack could be assumed as the highest angle of attack that the NACA2412 airfoil allows before it enters the stall regime. This critical angle of attack is typically around 15 degrees and it may vary significantly depending on Reynolds number. So the calculation of the angle of attack includes calculating the lift coefficient at point A in V-N diagram and then calculating the Reynolds number.

The lift coefficient $C_{L,A}$ is calculated by using Eqn. (2.6)

$$C_{L,A} = \frac{2 \times n_1 \times \left(\frac{w}{s}\right) \times 9.81}{\rho \times V_A^2} = \frac{2 \times 4.4 \times 104.769 \times 9.81}{1.225 \times 74.975^2} \cong 1.313 \quad (2.6)$$

The Reynolds number is calculated using Eqn. (2.7)

$$R = \frac{\rho V c}{\mu} = \frac{1.225 \times 74.975 \times 1.524}{1.7894 \times 10^{-5}} \cong 7.82 \times 10^6 \quad (2.7)$$

where c is the characteristic chord length, ρ is the density at sea level, μ is the absolute viscosity coefficient. Substituting the values into Eqn. (2.7), the Reynolds number is calculated as 7.82×10^6 .

For this value of the Reynolds number and lift coefficient $C_{L,A}$ the angle of attack is approximately 15.5 degrees [14, 15].

2. AOA at the Dive Speed:

In order to calculate the angle of attack at the dive speed, Eqn. (2.8) is used that defines the lift force.

$$L = nW = \frac{1}{2}\rho V^2 (C_{L,0} + C_{L,\alpha}\alpha)S \quad (2.8)$$

From Eqn. (2.8) the angle of attack is determined as:

$$\alpha = \frac{\frac{nW}{S} - \frac{1}{2}\rho V^2 C_{L,0}}{C_{L,\alpha}} \quad (2.9)$$

ESDU 95010 code (A9510) is used to calculate zero-AOA lift coefficient and lift curve slope. For this purpose, the input file is configured with the following values of the related variables:

$$\alpha = 0 \text{ deg}$$

$$M_D = 0.353 \text{ for } V_D = V_{D,\min} = 119.959 \text{ m/s}$$

Zero-AOA lift coefficient and lift coefficient slope results are found as:

$$C_{L,0} = 0.1569$$

$$C_{L,\alpha} = 4.4001 \text{ rad}^{-1}$$

Therefore, substituting the required values at point D into Eqn. (2.9), the angle of attack at point D is calculated as 4.638 degrees.

2.3.5 NACA 2412 Mean Camber Line Calculation

The use of ESDU A9510v12 code requires the input of airfoil camber data in order to calculate the aerodynamic loading associated with the camber of the airfoil. Therefore, the mean camber line of NACA 2412 is calculated and the results are presented in Table 2.5.

Table 2.5: NACA 2412 Mean Camber Line Ordinates

Station	Upper Airfoil Ordinate	Lower Airfoil Ordinate	Airfoil Mean Camber Ordinates
X/C	Y/C	Y/C	
0	0	0	0
0.0125	0.0215	-0.0165	0.00123
0.025	0.0299	-0.0227	0.00242
0.05	0.0413	-0.0301	0.00469
0.075	0.0496	-0.0346	0.00680
0.1	0.0563	-0.0375	0.00875
0.15	0.0661	-0.041	0.01219
0.2	0.0726	-0.0423	0.01500
0.25	0.0767	-0.0422	0.01718
0.3	0.0788	-0.0412	0.01875
0.4	0.078	-0.038	0.02000
0.5	0.0724	-0.0334	0.01944
0.6	0.0636	-0.0276	0.01778
0.7	0.0518	-0.0214	0.01500
0.8	0.0375	-0.015	0.01111
0.9	0.0208	-0.0082	0.00611
0.95	0.0114	-0.0048	0.00319
1	0	0	0

The mean camber line, which is drawn based on the data given in Table 2.5, is shown in Figure 2.1.

2.3.6 External Aerodynamic Load Calculation by ESDU

The external aerodynamic load is calculated in accordance with the ESDU document 95010 which calculates the span-wise loading of wings with camber and twist in subsonic attached flow using the lifting surface theory [13].

The data calculated in the previous sections is used to create the input file for ESDU A9510 v12. Span-wise lift and pitching moment distributions, which are calculated at the minimum maneuvering speed (point A in the V-N diagram), are given in Figures 2.5 and 2.6. By default, span-wise lift and pitching moment distributions are calculated at the 25 % of the chord measured from the leading edge, by ESDU A9510 v12.

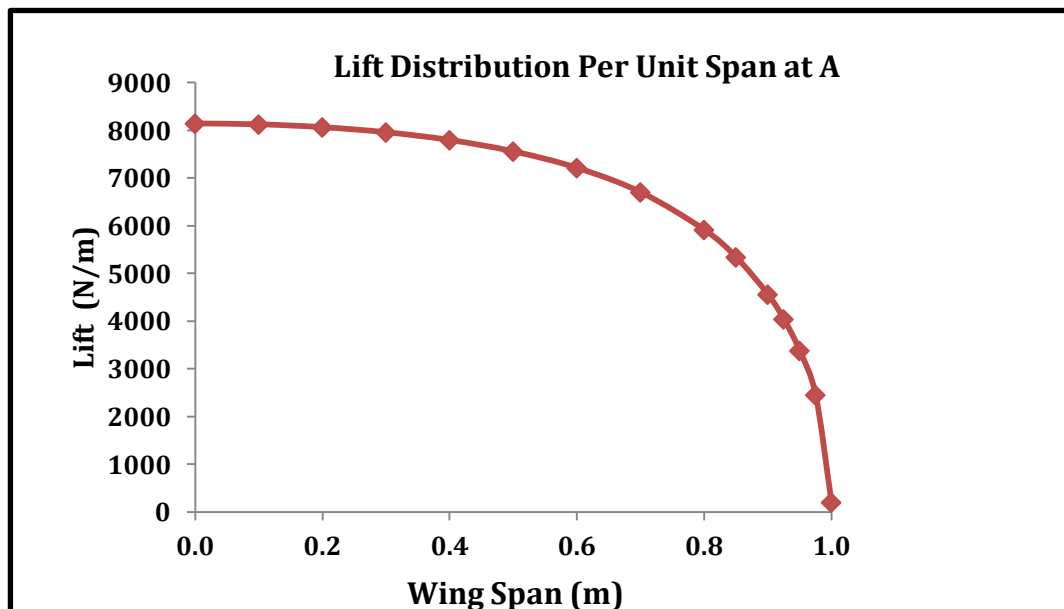


Figure 2.5: Span-wise Variation of Normalized Aerodynamic Lift Distribution at Minimum Maneuvering Speed – Point A

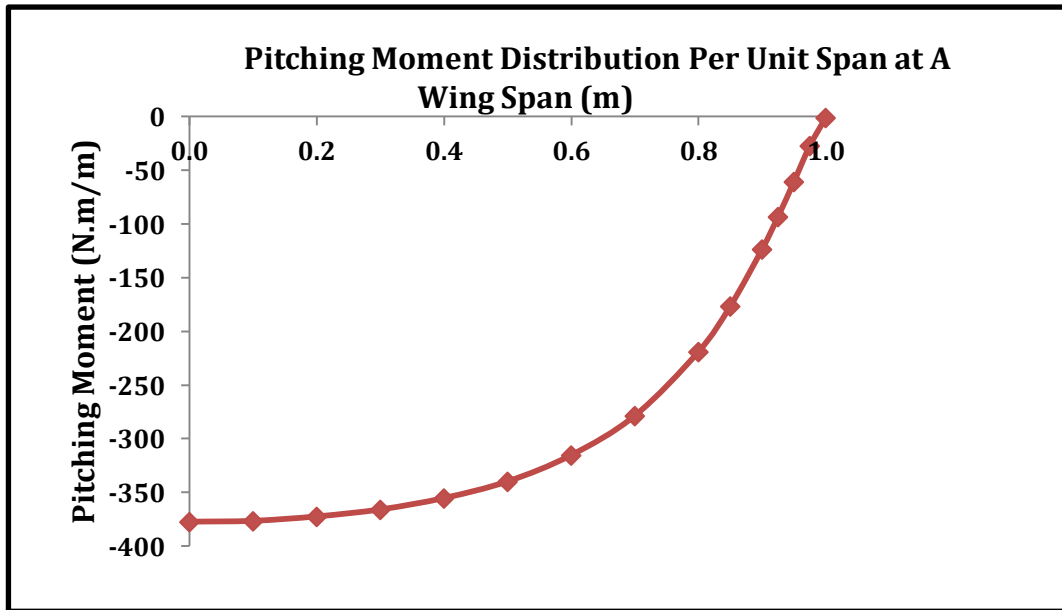


Figure 2.6: Span-wise Variation of Normalized Aerodynamic Pitching Moment Distribution at Minimum Maneuvering Speed – Point A

Similarly, span-wise lift and pitching moment distributions at the dive speed (point D in V-N diagram) at the 25 % of the chord measured from the leading edge are given in Figures 2.7 and 2.8, respectively.

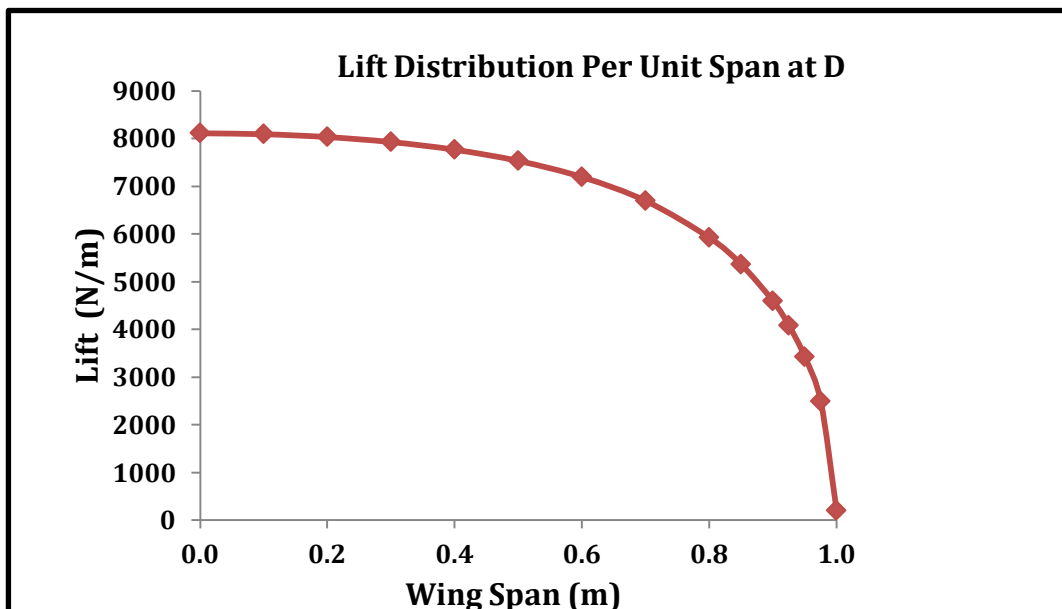


Figure 2.7: Span-wise Variation of Normalized Aerodynamic Lift Distribution at the Dive Speed - Point D

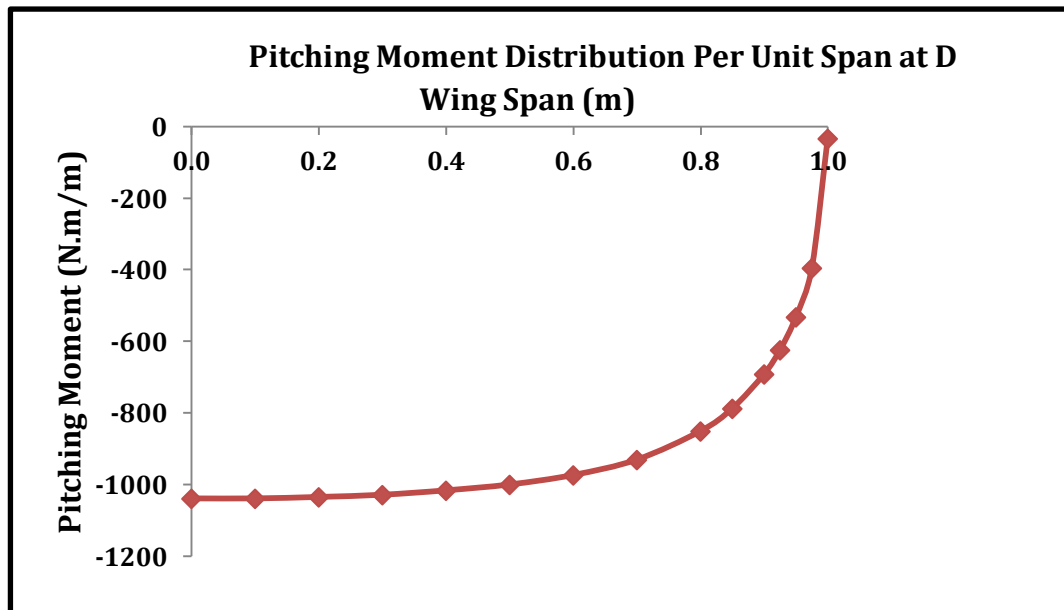


Figure 2.8: Span-wise Variation of Normalized Aerodynamic Pitching Moment Distribution at the Dive Speed – Point D

2.3.7 Calculation of Internal Loads

The sectional shear force, pitching and bending moments are calculated using the method defined by Bruhn where the details of this method and calculation steps are given in details [16]. At the positive limit load factor, the load on half wing has to be half of the total weight of the aircraft which is $(n_l W/2)$ 31510 N. Therefore, the sectional shear force at the wing root has to be very close to 31510 N and this is used as the check of the calculations.

Sectional shear force, pitching and bending moment results at point A in V-N diagram are tabulated in Table 2.6. Based on the values given in Table 2.6, sectional shear force, sectional bending moment and sectional pitching moment versus dimensionless span-wise coordinate plots are given in Figures 2.9 - 2.11 respectively.

Table 2.6: Sectional Internal Loads results at Point A

POINT A						
Spanwise Stations	Y coordinate (m)	Local Lift Coefficient	Local Pitching Moment Coefficient	Sectional Shear Force (N)	Sectional Bending Moment (Nm)	Sectional Pitching Moment (Nm)
0.000	0.000	1.505	-0.046	31478	63786	-1409
0.100	0.457	1.502	-0.046	27756	50245	-1235
0.200	0.914	1.491	-0.046	24052	38403	-1062
0.300	1.372	1.471	-0.045	20386	28247	-890
0.400	1.829	1.441	-0.044	16782	19753	-721
0.500	2.286	1.397	-0.042	13269	12887	-557
0.600	2.743	1.333	-0.039	9890	7599	-400
0.700	3.200	1.239	-0.034	6707	3814	-255
0.800	3.658	1.093	-0.027	3820	1422	-126
0.850	3.886	0.987	-0.022	2533	698	-76
0.900	4.115	0.842	-0.015	1400	252	-35
0.925	4.229	0.747	-0.011	909	120	-21
0.950	4.343	0.625	-0.007	484	41	-10
0.975	4.458	0.453	-0.003	151	6	-3
1.000	4.572	0.036	0.000	0	0	0

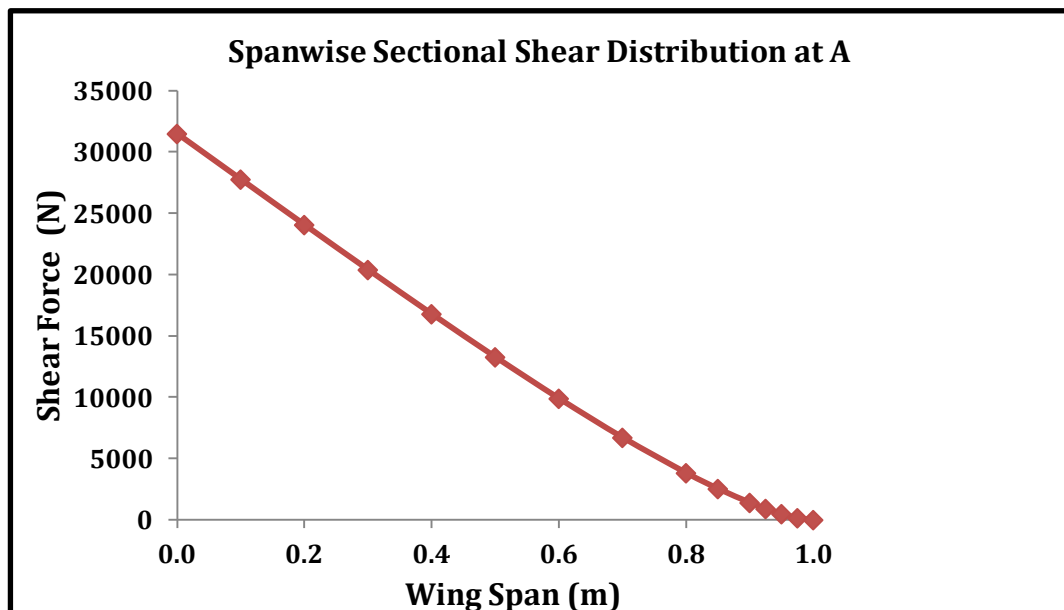


Figure 2.9: Span-wise Sectional Shear Force Distribution at Point A

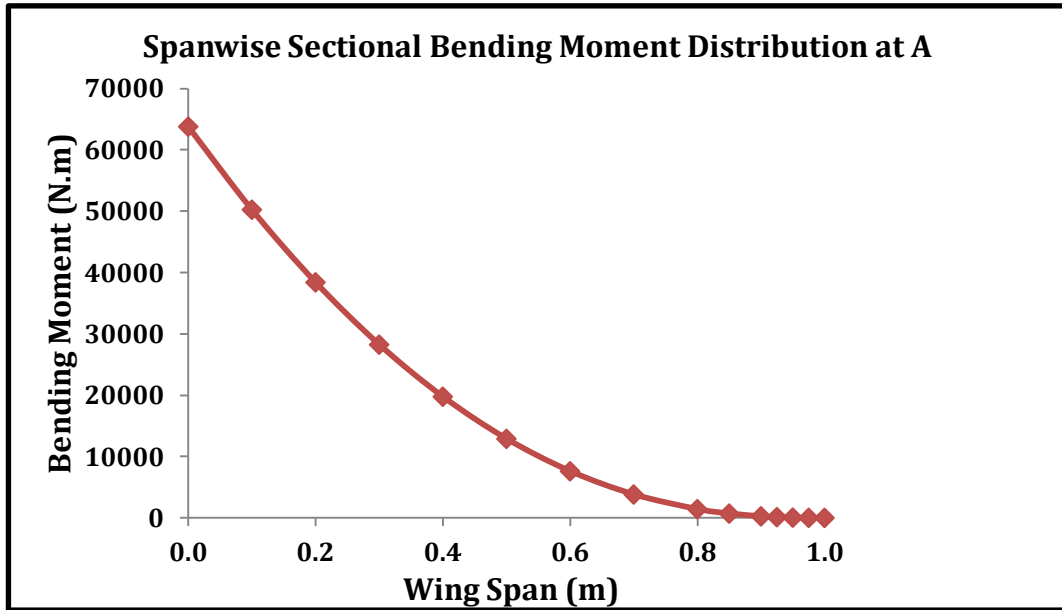


Figure 2.10: Span-wise Sectional Bending Moment Distribution at Point A

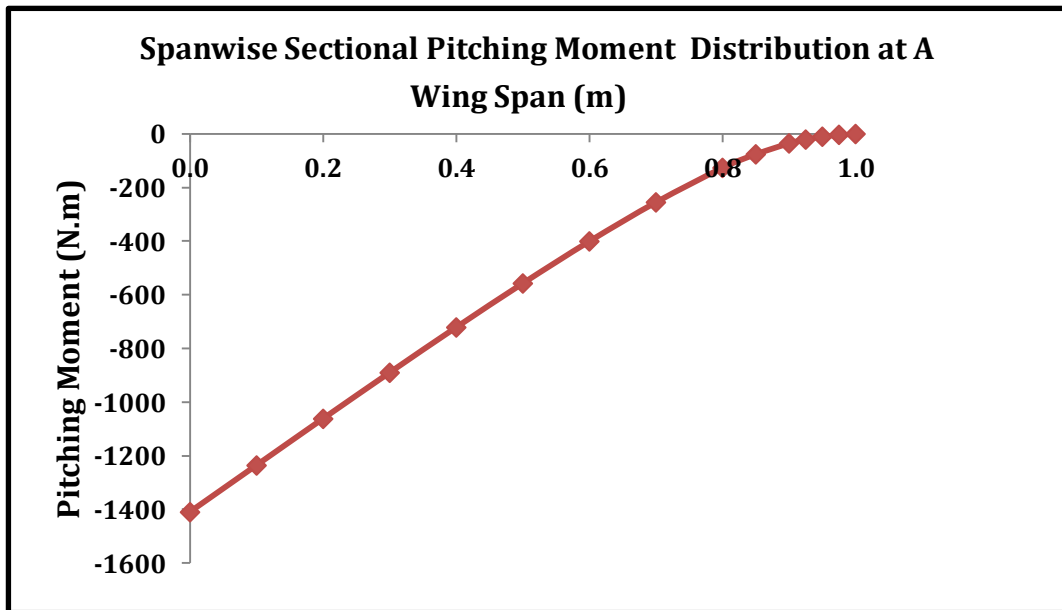


Figure 2.11: Span-wise Sectional Pitching Moment Distribution at Point A

Sectional shear force, pitching and bending moment results at point D in V-N diagram are tabulated in Table 2.7. Based on the values given in Table 2.7, sectional shear force, sectional bending moment and sectional pitching moment versus dimensionless span-wise coordinate plots are given in Figures 2.12 - 2.14, respectively.

Table 2.7: Sectional Internal Loads results at Point D

POINT D						
Spanwise Stations	Y coordinate (m)	Local Lift Coefficient	Local Pitching Moment Coefficient	Sectional Shear Force (N)	Sectional Bending Moment (Nm)	Sectional Pitching Moment (Nm)
0.000	0.000	0.6047	-0.0508	31482	63903	-4316
0.100	0.457	0.6033	-0.0508	27767	50359	-3841
0.200	0.914	0.5988	-0.0506	24070	38510	-3366
0.300	1.372	0.5910	-0.0503	20411	28344	-2893
0.400	1.829	0.5790	-0.0497	16813	19837	-2423
0.500	2.286	0.5615	-0.0489	13305	12956	-1958
0.600	2.743	0.5362	-0.0476	9930	7651	-1501
0.700	3.200	0.4990	-0.0455	6746	3847	-1056
0.800	3.658	0.4415	-0.0416	3854	1438	-630
0.850	3.886	0.3996	-0.0385	2560	707	-436
0.900	4.115	0.3423	-0.0338	1419	256	-256
0.925	4.229	0.3041	-0.0305	923	122	-177
0.950	4.343	0.2551	-0.0260	493	42	-106
0.975	4.458	0.1857	-0.0193	154	6	-45
1.000	4.572	0.0150	-0.0016	0	0	0

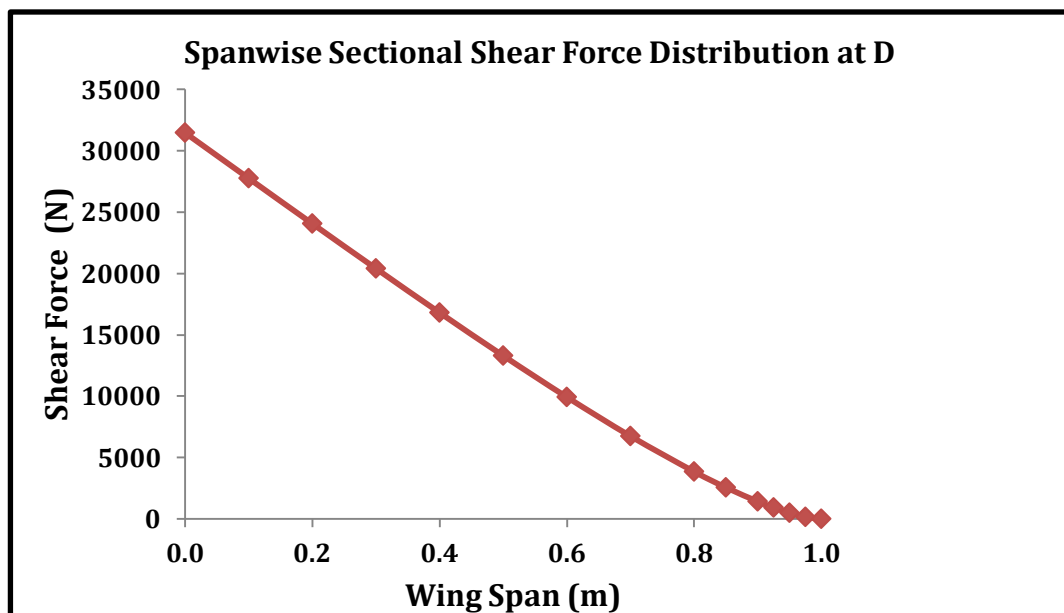


Figure 2.12: Span-wise Sectional Shear Force Distribution at Point D

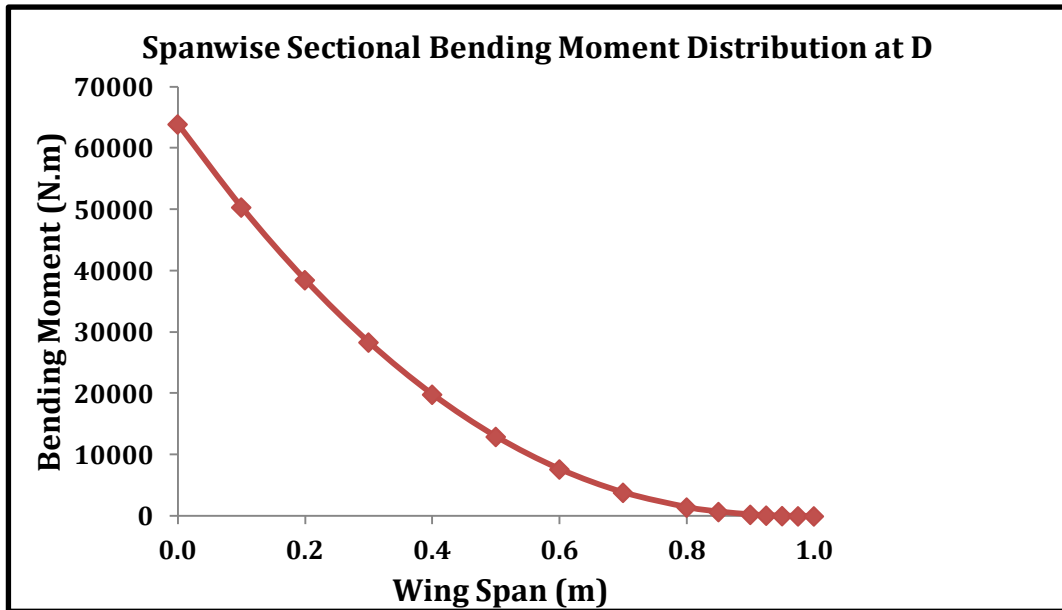


Figure 2.13: Span-wise Sectional Bending Moment Distribution at Point D

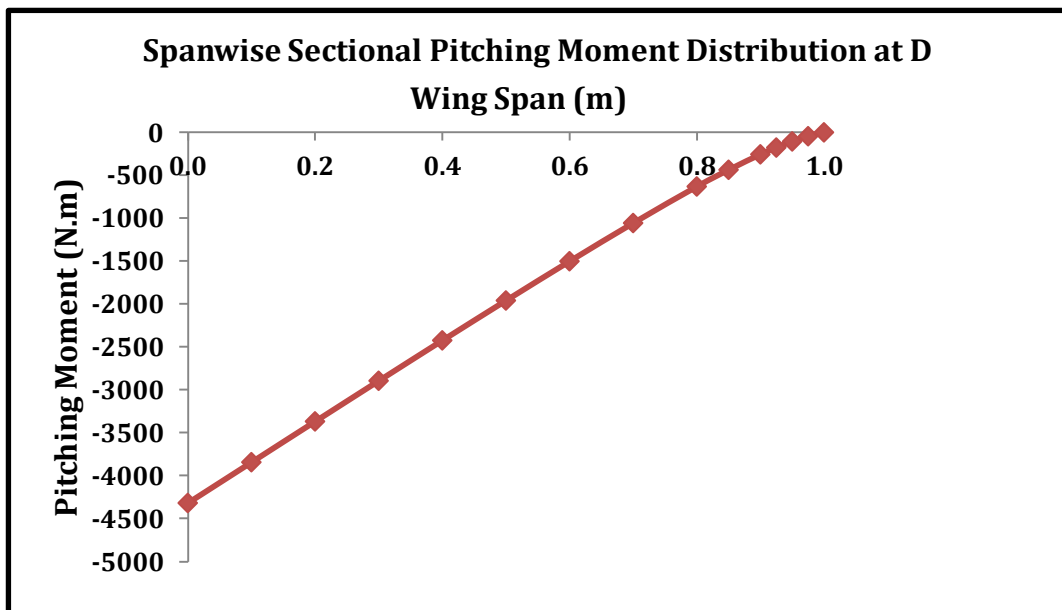


Figure 2.14: Span-wise Sectional Pitching Moment Distribution at Point D

2.4 Wing Structural Design and Analysis Methodology

The structural design and analysis of the wing torque box is carried out by using two different classical idealization methods [16, 17].

- The first idealization assumes that spars and stiffeners carry only axial stress and skin panels and webs carry shear stress only.
- The second idealization assumes that spars and stiffeners carry only axial stress and skin panels and webs carry axial stress and shear stress

In the design process, structural analysis is based on the assumption that wing behaves as beam with axial, bending and torsional stiffness. Therefore, normal stresses in the chordwise direction are neglected. Modeling a wing torque box as a beam is a reasonable approximation especially for high aspect ratio wings. During the preliminary design stage, beam modeling of the wing structure makes the hand calculation possible. In the following, simplified hand calculation based structural analysis methodology is described in more detail.

Figure 2.15 shows the first structural idealization which assumes that one - dimensional members carry axial load only and thin walled skins and webs carry shear load only. In the second idealization skins and spar webs are also assumed to carry axial load.

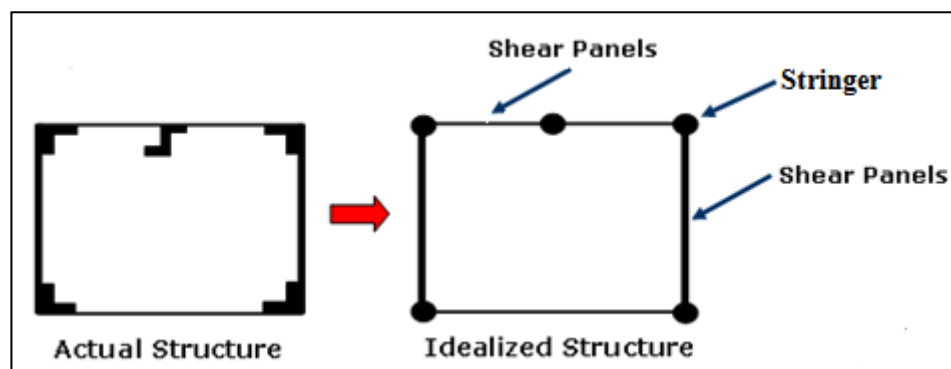


Figure 2.15: Structural Idealization # 1

2.4.1 Wing Geometry and Structural Layout

As mentioned before, the wing has a NACA 2412 airfoil profile with a rectangular planform with a chord length of 1.524 m and semi-span of 4.572 m. In the current study, wing design is done for a two-spar, two-stiffener and seven-rib configuration dividing the wing into 6 equal sections of length 0.762 m. The root extensions of the front and rear spars are taken as 0.5 m in length.

The front spar is located between 20 – 25 % of the chord length and the rear spar is located between 65 – 75 % of the chord length. The upper and lower stiffeners are located between 30 – 50 % of the chord length. Figure 2.16 shows spar and stiffener locations which are also used as design variables in the initial calculations which are performed to see the effect of spar and stringer positions on the final mass of the wing structure.

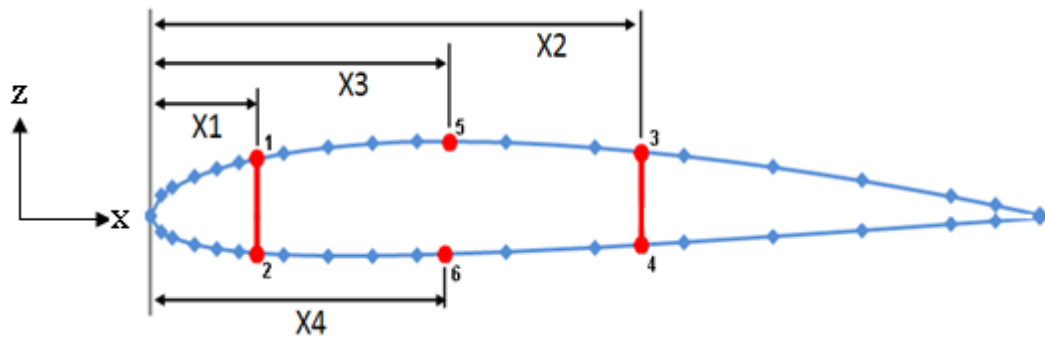


Figure 2.16: Spars and Stiffeners Locations as a Function of (x) % of the Chord

2.4.2 Material Selection and Properties

In the design of the wing structure, Aluminum 2024 T3 is selected considering its following characteristics:

- High strength to density ratio
- Good fatigue resistance
- Moderate formability into required form as sheet or shapes as extrusion.
- The lower price in Aluminum family used in aerospace application.

Table 2.8 defines Aluminum 2024 T3 material properties [18].

Table 2.8: Material Properties of Al 2024 T3 used in Wing Design

Material Properties Al 2024 T3	
Ultimate Tensile Strength	483 MPa
Tensile Yield Strength	345 MPa
Modulus of Elasticity	73.1 MPa
Shear Modulus	28 GPa
Shear Strength	283 MPa
Density	2768 kg/ m ³
Poisson's Ratio	0.3

The allowable stress values used in the wing design are calculated by considering a 1.5 factor of safety. In this case, the allowable stress is calculated by dividing the ultimate tensile strength by 1.5.

$$\sigma_{\text{allowable}} = \frac{\sigma_{\text{ultimate}}}{\text{SF}} = \frac{483 \text{ MPa}}{1.5} = 322 \text{ MPa} \quad (2.10)$$

Similarly, the allowable shear stress is calculated by dividing shear strength by 1.5.

$$\tau_{\text{allowable}} = \frac{\tau_{\text{ultimate}}}{\text{SF}} = \frac{283 \text{ MPa}}{1.5} \cong 188.67 \text{ MPa} \quad (2.11)$$

2.4.3 Analysis and Programming Tool

MATLAB R2006a is selected as the programming tool to perform calculations and to code the procedure of the design because of its capability of carrying out mathematical operations easily, and presenting charts and graphs with less effort.

2.5 Flowchart of the Design Steps

Figure 2.17 illustrates the flowchart which gives the design procedure of wing torque box with the minimum weight requirement. The important steps in the design process are explained in more detailed manner in the next sections. This flowchart describes the design steps for the first idealization case. The same design steps are followed in the second idealization case with some differences like the average axial stress and average shear stress are used for buckling calculations and maximum Von Mises stress is used for the strength check of skin panels and spar webs.

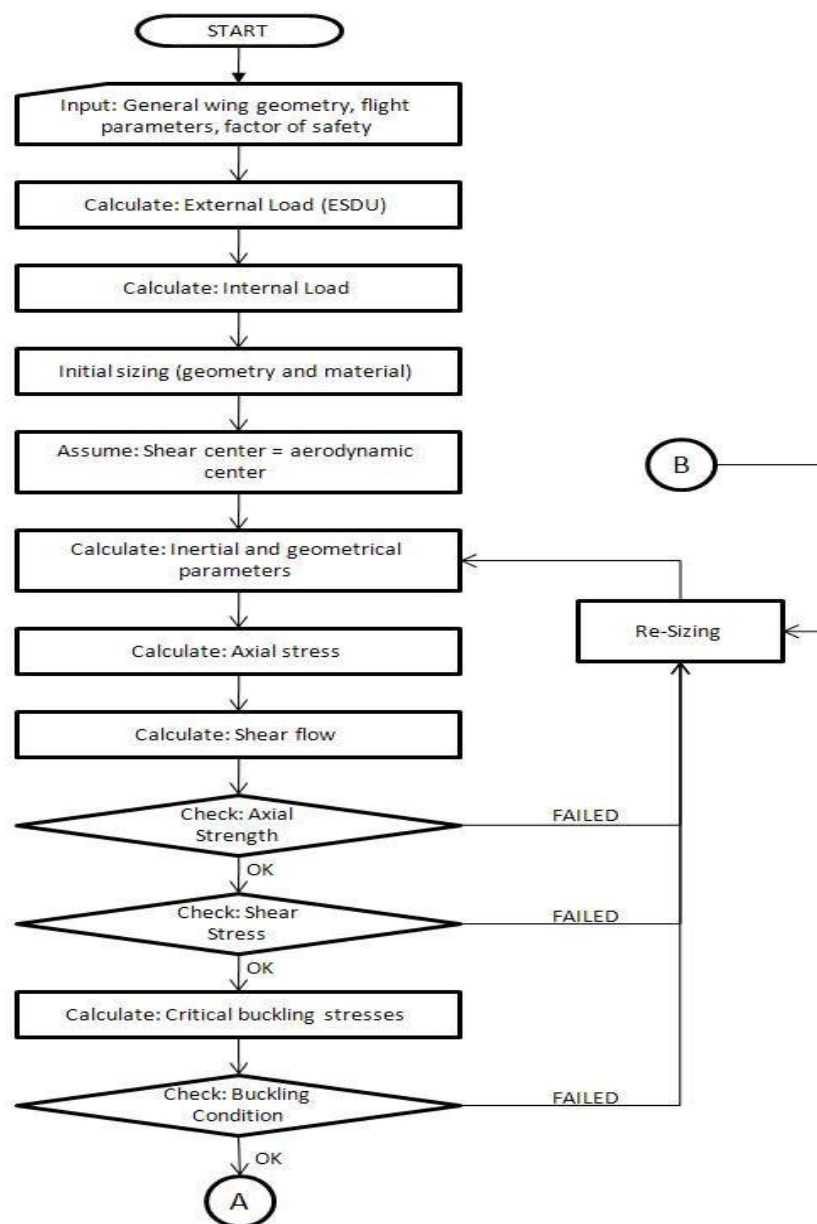


Figure 2.17: Flow Chart of Design Steps for Idealization Case # 1

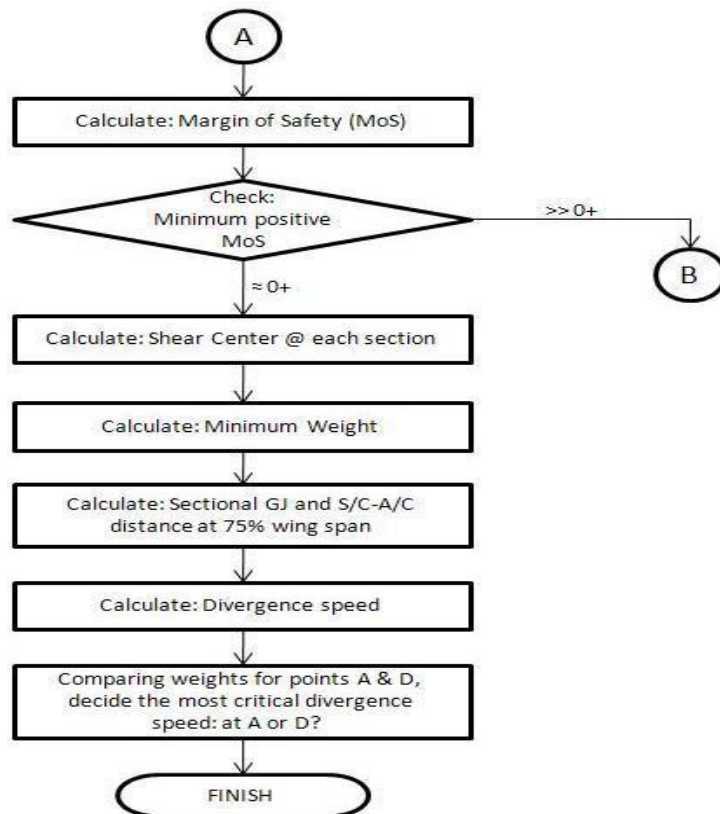


Figure 2.17: Flow Chart of Design Steps for Idealization Case # 1 - (continues)

2.5.1 Initial Sizing, Design Parameters and Design Criteria

The design parameters are first estimated and initialized. These parameters are the number of ribs and their locations, the size and position of spars and stiffeners, thicknesses of skins and spar webs. The mechanical properties of the selected material which include the ultimate tensile strength, tensile yield strength, modulus of elasticity, shear modulus, shear strength and density are also entered here. The shear force, which is calculated by the ESDU code, acts at the aerodynamic center which is at the 25 % of the chord length from the leading edge. Since the shear center location depends on the geometry, during the initial calculations shear center location is assumed to be the same location as the aerodynamic center. However, in both structural idealizations the main assumption about the effect of torque loading is that torque does not generate axial stress in the members (stingers in the structural idealization #1, stringers and skins and spar webs in the structural idealization #2) away from the restraint end, and free warping prevails. Free warping is an acceptable assumption away from the restraint end but near the restraint end torque

also creates axial stress in the members. Therefore, the structural analysis results are more accurate away from the restraint end. However, it is deemed that for the preliminary design stage, sizing based on the beam approximation of the wing torque box is appropriate, because beam approximation makes the hand calculation possible and speeds up the calculations considerably.

In the design process, sheet thicknesses and spar flange and stringer areas are kept constant in each bay and they are allowed to change discretely at the rib stations. design of the wing structure is performed based on the following criteria for the structural idealizations employed in the study.

Design criteria for structural idealization 1 (skins and webs carry shear load only and spar flanges and stringers carry axial stress)

- Maximum shear stresses in the skins and webs of each bay should be less than the shear stress allowable
- Maximum axial stress in the spar flange and stringers should be less than the stress allowable
- Local shear buckling of the wing skins and spar webs in each bay should be prevented

Design criteria for structural idealization 2 (skins and webs carry shear and axial load and spar flanges and stringers carry axial stress)

- Maximum Von Mises stresses in the skins and webs of each bay should be less than the stress allowable
- Maximum axial stress in the spar flange and stringers should be less than the stress allowable
- Combined tension and shear local buckling of the lower wing skins should be prevented
- Combined compression and shear local buckling of the upper wing skins should be prevented
- Combined bending and shear local buckling of the spar webs should be prevented

2.5.2 Axial Stresses Calculation

The axial stresses are calculated using the unsymmetrical bending formula as defined by Eqn. (2.12). A cambered airfoil does not have a plane of symmetry with respect to the chordwise coordinate (x) and the perpendicular coordinate (z), shown in Figure 2.18 which are the convenient axes about which the internal loads are decomposed. In the first idealization, where spars and stringers are assumed to carry axial stresses, the calculated axial stresses are compared to the allowable ones in order to determine the cross sectional areas of spar caps and stringers in an iterative method permitting maximum allowable stress to be carried by them.

$$\sigma_Y = \frac{P}{A} + \left(\frac{M_X I_Z + M_Z I_{XZ}}{I_X I_Z - I_{XZ}^2} \right) Z - \left(\frac{M_Z I_X + M_X I_{XZ}}{I_X I_Z - I_{XZ}^2} \right) X \quad (2.12)$$

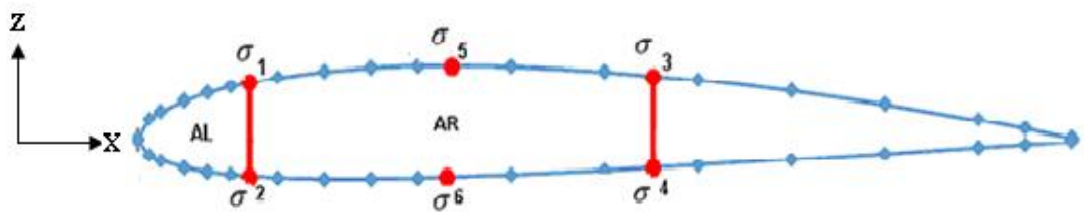


Figure 2.18: Axial Stresses Acting On Spar Caps & Stringers of 1st Idealization

In the second idealization where skins and web panels are also assumed to carry axial stress beside shear stress, two axial stresses are defined just before and just after each spar flange and stringer as shown in Figure 2.19. In this case, the maximum Von Mises stress, which is calculated by Eqn. (2.13), is used for the strength check of the wing skins and web panels. For strength check of the skin and web panels, Von Mises stresses are calculated at the inboard edge of each bay where the maximum loads act for each bay.

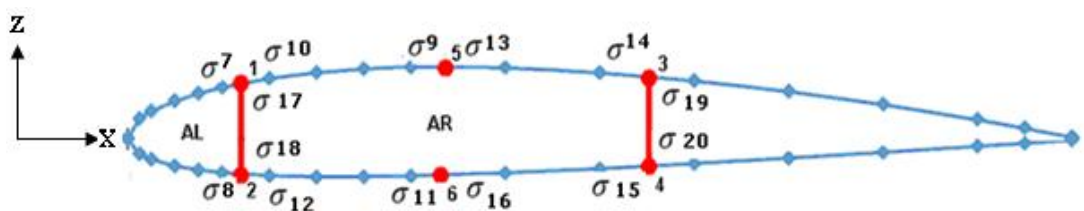


Figure 2.19: Axial Stresses Acting on Skins and Spar webs of 2nd Idealization

$$\sigma_{Von-Mises} = \sqrt{\sigma_x^2 + 3\tau_{xy}^2} \quad (2.13)$$

In the second structural idealization, the second moment of inertia of the skins and spar webs are also taken into account while calculating the axial stresses. Therefore, second moment of inertia and product of inertia of inclined thin walled sections are calculated by the formulas given in Figure 2.20 and the use of parallel axis theorem shown in Figure 2.21 [17].

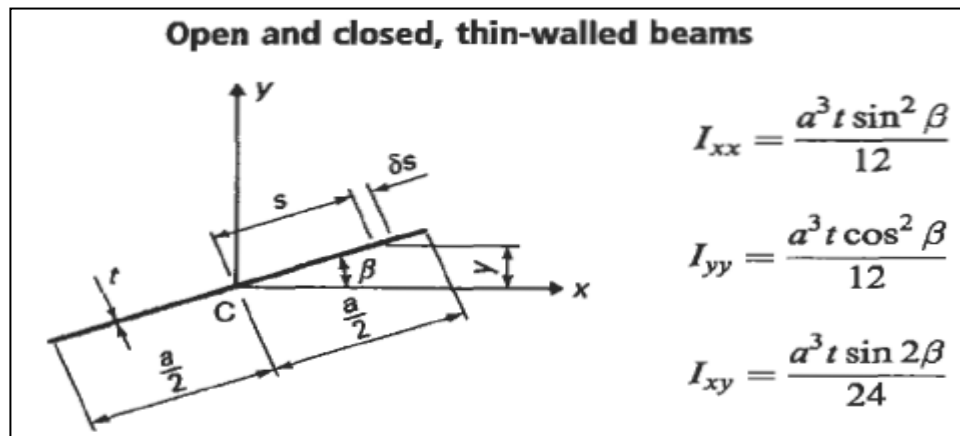


Figure 2.20: Seconds Moment of Inertia and Product of Inertia Calculation of Inclined Thin Sections

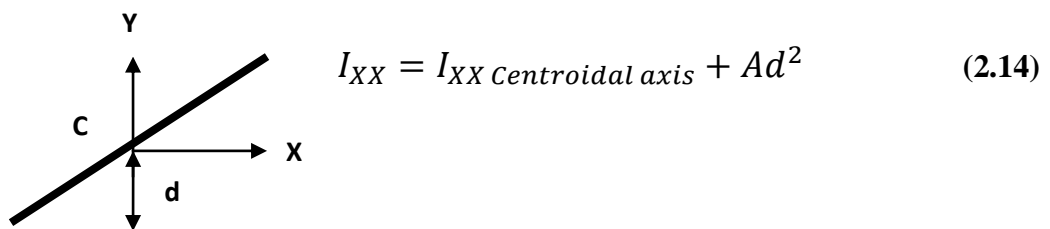


Figure 2.21: Parallel Axis Theorem

2.5.3 Shear Flow and Shear Stress Calculations

Shear flow acting on the skin panels, spar webs and ribs are calculated by solving a system of linear equations in both idealization cases. Shear stresses are calculated at the inboard edge of each bay where the maximum loads act for each bay. Calculated shear stresses are then compared with the allowable ones in order to determine the thickness of each panel that satisfies the maximum allowable shear stress. In the first idealization, the shear flows are constant along the wing skins and spar webs but in the second idealization the shear flow changes along the wing skins and spar webs. Figure 2.22 shows the shear flow distribution in the first structural idealization approach.

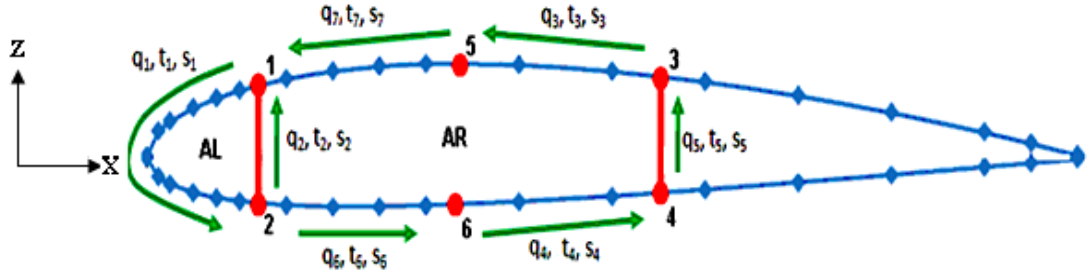


Figure 2.22: Shear Flow (q), Thickness (t), and Curvature Length (s) in the 1st Structural Idealization

The shear flow equality at a joint is derived from the unsymmetrical bending formula as

$$q(s) = q_0 + \frac{(V_Z I_{XZ})Q_Z}{I_{AA}} - \frac{(V_Z I_{ZZ})Q_X}{I_{AA}} \quad (2.15)$$

where $I_{AA} = I_X I_Z - I_{XZ}^2$

Additionally, the equality equation of twist angle between left and right cells is used. The equality of the twists comes from the main requirement of chordwise rigidity of the wing.

$$\theta_{Right} = \theta_{Left} \Rightarrow \frac{1}{2ARG} \sum \left(\frac{q_r s_r}{t_r} \right) = \frac{1}{2ALG} \sum \left(\frac{q_l s_l}{t_l} \right) \quad (2.16)$$

Finally, the external moment about a point should be equal to the moment of the shear flows about the same point. Equality of moment resultants is given by Eqn. (2.17).

$$\sum M_{Y,external} = \sum M_{Y,shear\ flow} \Rightarrow M_Y + V_Z L = \sum 2Aq \quad (2.17)$$

where L is the moment arm about which the moments are calculated.

In the second structural idealization, inertia of the wing skins and spar webs are also taken into consideration, therefore shear flow varies along the wing skins and spar webs. Since the shear flow change along the wing skins and spar webs, two shear flows are defined just before and just after each spar flange and stringer, as shown in Figure 2.23. The system of linear equations is established based on the shear flows defined just before and just after the spar flanges and stringers.

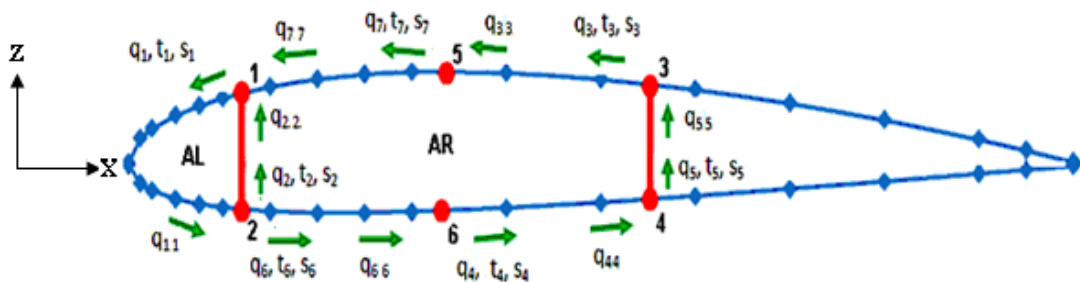


Figure 2.23: Shear Flow (q), Thickness (t), and Curvature Length (s) in the 2nd Structural Idealization

The shear flow equality at a joint or along the curvature can be written in a simple form as:

$$q(s) = q_0 + B$$

$$\text{where } B = \frac{(V_Z I_{XZ}) Q_Z}{I_{AA}} - \frac{(V_Z I_{ZZ}) Q_X}{I_{AA}}$$

For example, the shear flow equality at joint 1, as shown in Figure 2.21, is written as

$$q_1 = q_2 + q_{22} + B_1$$

and the shear flow equality along S_1 curvature, as show in Figure 2.21, is written as

$$q_{11} = q_1 + B_2$$

Accordingly, the rest of shear equality equations can be written in the same way, and they can all be cast in a matrix form as shown below.

$$\text{Shear Flow Equation Set} \rightarrow \begin{Bmatrix} q_1 - q_2 - q_{22} \\ q_{11} - q_1 \\ \cdot \\ \cdot \\ \cdot \\ q_{22} - q_2 \end{Bmatrix} = \begin{Bmatrix} B_1 \\ B_2 \\ \cdot \\ \cdot \\ \cdot \\ B_{13} \end{Bmatrix}$$

By using Eqn. (2.16), the equality of the twist angle between left and right cells is written as:

$$\begin{aligned} \frac{1}{2ALG} \left\{ \frac{(q_1 + q_{11})(S_{1U} + S_{1L})}{2t_1} + \frac{(q_2 + q_{22})S_2}{2t_2} \right\} = \\ \frac{1}{2ARG} \left\{ \frac{(q_6 + q_{66})S_6}{2t_6} + \frac{(q_5 + q_{55})S_5}{2t_5} + \frac{(q_3 + q_{33})S_3}{2t_3} + \frac{(q_4 + q_{44})S_4}{2t_4} \right. \\ \left. + \frac{(q_7 + q_{77})S_7}{2t_7} - \frac{(q_2 + q_{22})S_2}{2t_2} \right\} \end{aligned} \quad (2.18)$$

The external equilibrium of moments around a joint 2 as shown in Figure 2.21 is written by refereeing to Eqn. (2.17) and it equals:

$$\begin{aligned} 2AL \frac{(q_1 + q_{11})}{2} + 2A_{246} \frac{(q_4 + q_{44})}{2} + 2A_{243} \frac{(q_5 + q_{55})}{2} + 2A_{253} \frac{(q_3 + q_{33})}{2} \\ + 2A_{251} \frac{(q_7 + q_{77})}{2} = M_Y + V_Z(e - X_1) \end{aligned} \quad (2.19)$$

where M_Y is the sectional pitching moment, V_Z is the sectional shear force, e is the shear center location measured from leading edge, X_1 defines the location of point 2 measured from leading edge, and A defines the related areas used in the torque calculation due to shear flow.

Finally, the system of linear equations that consists of shear equality equations, equality equation of twist angle and external equilibrium of moment's equation are written in a matrix form, and solved simultaneously for the unknown shear flows.

The contracted form of the final matrix equation is created as follow to solve for the unknown shear flows.

$$\begin{bmatrix}
 1 & 0 & 0 & 0 & 0 & 0 & 0 & 0 & 0 & 0 & 0 & 0 & 0 & 0 \\
 0 & -1 & 0 & 0 & 0 & 0 & 0 & 0 & 0 & 0 & -1 & 0 & -1 & 0 \\
 0 & -1 & 0 & 1 & 0 & 1 & 0 & 0 & 0 & 0 & 0 & 0 & 0 & 0 \\
 -1 & 1 & 0 & 0 & 0 & 0 & 0 & 0 & 0 & 0 & 0 & 0 & 0 & 0 \\
 0 & 0 & 0 & 0 & -1 & 0 & -1 & 0 & 0 & 0 & 0 & 0 & 0 & 0 \\
 0 & 0 & -1 & 0 & 1 & 0 & 1 & 0 & 0 & 0 & 0 & 0 & 0 & 0 \\
 0 & 0 & 1 & 0 & 0 & 0 & 0 & 0 & 0 & 0 & 0 & 0 & 0 & 0 \\
 0 & 0 & 0 & 0 & 0 & -1 & 0 & -1 & 0 & 0 & 0 & 0 & 0 & 0 \\
 0 & 0 & 0 & 0 & 0 & 0 & 0 & 1 & 0 & 1 & 0 & 0 & 1 & 0 \\
 0 & 0 & 0 & 0 & 0 & 0 & 0 & 0 & 0 & 0 & 0 & 0 & 0 & 0 \\
 0 & 0 & 0 & 0 & 0 & 0 & 0 & 0 & -1 & 0 & -1 & 0 & 0 & -1 \\
 0 & 0 & 0 & 0 & 0 & 0 & 0 & 0 & 0 & 1 & 0 & 0 & 0 & 1 \\
 K1 & K2 & K3 & K4 & K5 & K6 & K7 & K8 & K9 & K10 & K11 & K12 & K13 & K14 \\
 H1 & H2 & H3 & H4 & H5 & H6 & H7 & H8 & H9 & H10 & H11 & H12 & H13 & H14
 \end{bmatrix}
 \begin{bmatrix}
 q_1 \\
 q_{11} \\
 q_2 \\
 q_{22} \\
 q_3 \\
 q_{33} \\
 q_4 \\
 q_{44} \\
 q_5 \\
 q_{55} \\
 q_6 \\
 q_{66} \\
 q_7 \\
 q_{77}
 \end{bmatrix}
 =
 \begin{bmatrix}
 B_1 \\
 B_{11} \\
 B_2 \\
 B_{22} \\
 B_6 \\
 B_{66} \\
 B_4 \\
 B_{44} \\
 B_3 \\
 B_{33} \\
 B_5 \\
 B_{55} \\
 KB \\
 HB
 \end{bmatrix}$$

By referring to Eqn. (2.16), which represents the equality equation of the twist angle between left and right cells the following K's values are written:

$$\begin{aligned}
 k1 &= \frac{(S_{1U+} S_{1L})}{Al t_1}, & k2 &= \frac{(S_{1U+} S_{1L})}{Al t_1}, & k3 &= \frac{S_2}{Al t_2} + \frac{S_2}{AR t_2} \\
 k4 &= \frac{S_2}{Al t_2} + \frac{S_2}{AR t_2}, & k5 &= -\frac{S_3}{ARt_3}, & k6 &= -\frac{S_3}{ARt_3} \\
 k7 &= -\frac{S_4}{ARt_4}, & k8 &= -\frac{S_4}{ARt_4}, & k9 &= -\frac{S_5}{ARt_5}, & k10 &= -\frac{S_5}{ARt_5} \\
 k11 &= -\frac{S_6}{ARt_6}, & k12 &= -\frac{S_6}{ARt_6}, & k13 &= -\frac{S_7}{ARt_7}, & k14 &= -\frac{S_7}{ARt_7}
 \end{aligned}$$

$$KB = 0$$

By referring to Eqn. (2.17), that represents the external equilibrium of moments around a joint 2 the following H's values are written as:

$$H1 = Al, \quad H2 = Al, \quad H3 = 0, \quad H4 = 0, \quad H5 = A253, \quad H6 = A253$$

$$H7 = A246, \quad H8 = A246, \quad H9 = A243, \quad H10 = A243, \quad H11 = 0$$

$$H12 = 0, \quad H13 = A251, \quad H14 = A251, \quad HB = M_Y + V_Z(e - X_1)$$

2.5.4 Local Buckling Analysis

A large part of an aircraft structure consists of thin plates and panels stiffened by stringers or longerons. For this type of structures local buckling is the most critical mode of failure and for this reason an early check for critical buckling loads is very important in aircraft design.

In the first idealization approach, buckling is assumed to be due to shear stresses only. Panels are assumed to be simply supported at sides and at the ends. Sides and ends refer to the spar flange, stringer and ribs. Critical thicknesses of skins, ribs and spar webs are determined in such a way that they satisfy the critical buckling constraint. For local buckling checks, average stresses are calculated on the skin and spar web panels for each bay. The thicknesses determined in local buckling analysis are compared with the thicknesses determined due to shear stress strength check, and the larger thickness value is chosen as the minimum required thickness value for the panels to be safe.

$$\tau_{Critical} = K_S E \left(\frac{t}{b}\right)^2 \quad (2.20)$$

Eqn. (2.20) defines the critical shear stress which is used to calculate the thicknesses of skins, ribs and spar webs. The value of K_S , the shear buckling coefficient, is dependent on the support conditions and on aspect ratio (a/b) of the panel in which “b” is the plate width length and “a” is the length. The value of K_S is read directly from the shear buckling coefficient curves which are given for different support conditions, Appendix [A], Figure A.7.

On the other hand, for the second idealization approach, buckling is assumed to be due to combined loading. Panels are again assumed to be simply supported at the sides and the ends. Buckling of wing skins is assumed to be due to combined shear stress and compressive/tensile axial stress, buckling of spar webs is assumed to be due to combined bending and shear stress, and buckling of ribs is assumed to be due to shear stress only. Again, for local buckling checks, average stresses are calculated on the skin and spar web panels for each bay. Under these different buckling conditions, thicknesses of each skin panel, spar web and rib are determined and compared to the thicknesses found due to Von Mises stress constraints, because in

the second idealization, skin panels and spar webs are under combined axial and shear loading. The thicknesses determined in the local buckling analysis are compared with the thicknesses determined due to Von Mises stress constraint, and the larger thickness value is chosen as the minimum required thickness value for the thin walled panels of each bay to be safe.

Buckling due to combined compression axial stress and shear stress is determined by Eqn. (2.21).

$$R_S^2 + R_C \leq 1 \Rightarrow \left(\frac{\tau}{K_S E \left(\frac{t}{b}\right)^2} \right)^2 + \left(\frac{\sigma_{Compression}}{K_C E \left(\frac{t}{b}\right)^2} \right) \leq 1 \quad (2.21)$$

Buckling due to combined shear stress and bending stress is determined by Eqn. (2.22).

$$R_S^2 + R_b^2 \leq 1 \Rightarrow \left(\frac{\tau}{K_S E \left(\frac{t}{b}\right)^2} \right)^2 + \left(\frac{\sigma_{Compression}}{K_b E \left(\frac{t}{b}\right)^2} \right)^2 \leq 1 \quad (2.22)$$

The buckling coefficients K_C and K_b , are defined as axial compressive buckling coefficient and bending buckling coefficient respectively, and they are dependent on support condition and on the aspect ratio (a/b) in which “b” is the plate width length and “a” is the length. The values of K_C and K_b are read directly from the compression buckling coefficient and bending buckling coefficient curves, Appendix [A], Figures A.5 and A.6.

2.5.5 Determination of Shear Center

The shear force, which is calculated by the ESDU code, acts at the aerodynamic center which is at the 25 % of the chord length from the leading edge. Since the shear center location depends on the geometry, during the initial calculations shear center location is assumed to be the same location as the aerodynamic center. However, in both structural idealizations the main assumption about the effect of torque loading is that torque does not generate axial stress in the members (stingers in the structural idealization #1, stringers and skins and spar webs in the structural idealization #2) away from the restraint end, and free warping prevails. Free

warping is an acceptable assumption away from the restraint end but near the restraint end torque also creates axial stress in the members. The corrected value of shear center which is independent of the loading can be calculated by adding a new equation to the system of linear equations which are used to calculate shear flows and shear stresses. The condition of chordwise rigidity requires that angles of twist of all cells of the wing torque box must be equal to each other and they must be identically equal to zero if the external force passes through the shear center. The additional equation to be used for the calculation of shear center location is given by Eqn. (2.23).

$$\theta_{Right} = \theta_{Left} = 0 \Rightarrow \frac{1}{2AR} \sum \left(\frac{q_r s_r}{t_r} \right) = \frac{1}{2AL} \sum \left(\frac{q_l s_l}{t_l} \right) = 0 \quad (2.23)$$

The location of the shear center is calculated to complete the structural design process and also to calculate the torsional divergence speed which can be calculated using the slender beam model.

2.5.6 Determination of Locations of the Spars and Stringers for Minimum Weight Wing Structure

The minimum weight is determined for different spar and stiffener locations in an iterative solution. Standard thicknesses for skins, spar webs and ribs and standard areas for spar caps and stringers are used while calculating the weight of the wing torque box.

2.5.7 Calculation of Divergence Speed

The divergence speed is calculated by using Eqn. (2.24) which defines the torsional divergence for a wing using the slender beam model. [17].

$$U_D = \frac{\pi}{2l} \sqrt{\frac{2GJ}{\rho c e C_{L,\alpha}}} \quad (2.24)$$

where "l" defines the wing semi span, "GJ" is the torsional rigidity, and "e" is the distance between aerodynamic center and shear center. The effective polar moment

of inertia J is approximately calculated at 75 % of the wing semi span length. The value of J is calculated by referring to Figure 2.24, which shows a two cell thin walled airfoil- like cross section, and utilizing Eqn. (2.25).

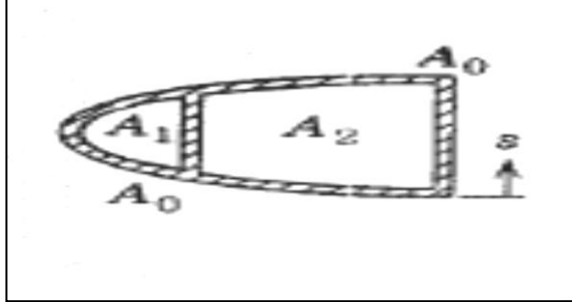


Figure 2.24: Double Walled Structure

In Figure 2.24, A_1 and A_2 defines the inside area of each cell and A_0 defines the outside area.

The torsional stiffness J is defined in Eqn. (2.25) as

$$J = 4 \frac{\alpha_{20}A_1^2 + \alpha_{12}(A_1+A_2)^2 + \alpha_{01}A_2^2}{\alpha_{01}\alpha_{12} + \alpha_{01}\alpha_{20} + \alpha_{12}\alpha_{20}} \quad (2.25)$$

where $\alpha_{ij} = \int \frac{ds}{t}$, is the integral being taken along boundary between A_i and A_j . [19].

2.6 Design Results Overview

The results of the first and second structural idealization for the design of the wing torque box with the minimum weight requirement are presented in detail in the following sections.

2.6.1 Iteration Results for Spar – Stiffener Locations and Minimum weight

Wing design is done for a two-spar, two-stiffener and seven-rib configuration dividing the wing into 6 equal sections of length 0.762 m. The root extensions of the

front and rear spars are taken as 0.5 m in length but in the simplified method of analysis the root extensions are not included in the design process. During the iterations, the location of spars, stiffeners and their effect on minimum weight is calculated for both idealization cases. Table 2.9 shows the percentage change in spar and stiffener locations allowed during the iterations.

Table 2.9: Percentage Change in Spars and Stiffeners Locations during Iterations

	Limits (% of Chord)	Allowable % Change Between Each Iterative Design
Front Spar	$20 \leq X1 \leq 25$	$X1 = 1$
Rear Spar	$65 \leq X2 \leq 75$	$X2 = 1$
Upper Stiffener	$30 \leq X3 \leq 50$	$X3 = 2$
Lower Stiffener	$30 \leq X4 \leq 50$	$X4 = 2$

After each iterative solution, minimum weight design is reached for different spar and stiffener combinations given in Table 2.9. In addition, for each spar/ stiffener location combination, minimum wing torque box weight is reached and for each design average shear center location is calculated as a percentage of chord length. Tables 2.10 and 2.11 give some selected designs which illustrate the effect of spars and stiffeners locations as a percentage of chord length on the minimum wing torque box weight and on the average shear center location for both idealization cases respectively.

Table 2.10: Effect of Spar – Stiffener Location on the Minimum Weight and Average Shear Center Location for the 1st Idealization

Configuration Number	Front Spar	Rear Spar	Upper Stiffener	Lower Stiffener	Weight (kg)	Average Shear Center (% Chord)
1	20	65	30	50	77.63	44.0
2	21	67	40	38	68.84	39.7
3	22	71	36	50	94.42	44.8
4	25	70	48	30	64.60	41.0
5	23	68	38	36	67.13	41.6
6	25	70	50	46	67.69	45.8
7	24	69	42	48	68.97	48.1

Table 2.11: Effect of Spar – Stiffener Location on the Minimum Weight and Average Shear Center Location for the 2nd Idealization

Configuration Number	Front Spar	Rear Spar	Upper Stiffener	Lower Stiffener	Weight (kg)	Average Shear Center (% Chord)
1	20	65	30	50	59.88	25.3
2	21	67	40	38	84.75	19.9
3	22	71	36	50	88.72	23.2
4	25	70	48	30	57.70	29.3
5	23	68	38	36	76.84	25.6
6	25	70	50	46	57.61	33.7
7	24	69	42	48	59.06	34.7

From an engineering point of view not all the iteration results can be considered acceptable. A close look at the arrangement of spar – stiffener locations and the average shear center location can be a key while choosing an acceptable design configuration. The selection of the best configuration is based on the minimum weight and calculation of the shear center location behind the aerodynamic center.

Therefore, configuration 6 in both idealizations is selected as an acceptable design for both structural idealizations. For both idealizations, the front spar is located at 25 %, rear spar is at 70 %, upper stiffener is at 50 % and lower stiffener is at 46 % of chord length. On the other hand, average shear center is calculated as the sum of shear centers location at each wing bay divided by the numbers of bays. For first idealization shear center is at 45.8 % of the chord length, and for the second idealization it is at 33.7 % of the chord length.

2.6.2 Final Spars - Stiffeners and Ribs Locations

Table 2.12 shows the selected position of spars – stiffeners along the span of the wing design configuration.

Table 2.12: Location of the Spars and Stiffeners along the Span of the Final Wing Design

	Limits (% of Chord)	Best location for minimum flange area (% of chord)
Front Spar	$20 \leq X1 \leq 25$	$X1 = 25$
Rear Spar	$65 \leq X2 \leq 75$	$X2 = 70$
Upper Stiffener	$30 \leq X3 \leq 50$	$X3 = 50$
Lower Stiffener	$30 \leq X4 \leq 50$	$X4 = 46$

Table 2.13 shows the location of ribs dividing the wing into 6 equal sections along the span of the wing.

Table 2.13: Location of the Ribs along the Span of the Final Wing Design

	Tip						Root
Station	1	2	3	4	5	6	7
Percent %	0	16.67	33.34	50.01	66.68	83.35	100
Y (m)	0	0.762	1.524	2.286	3.049	3.811	4.572

On the other hand, Figure 2.25 shows the structural lay – out of the wing structure.

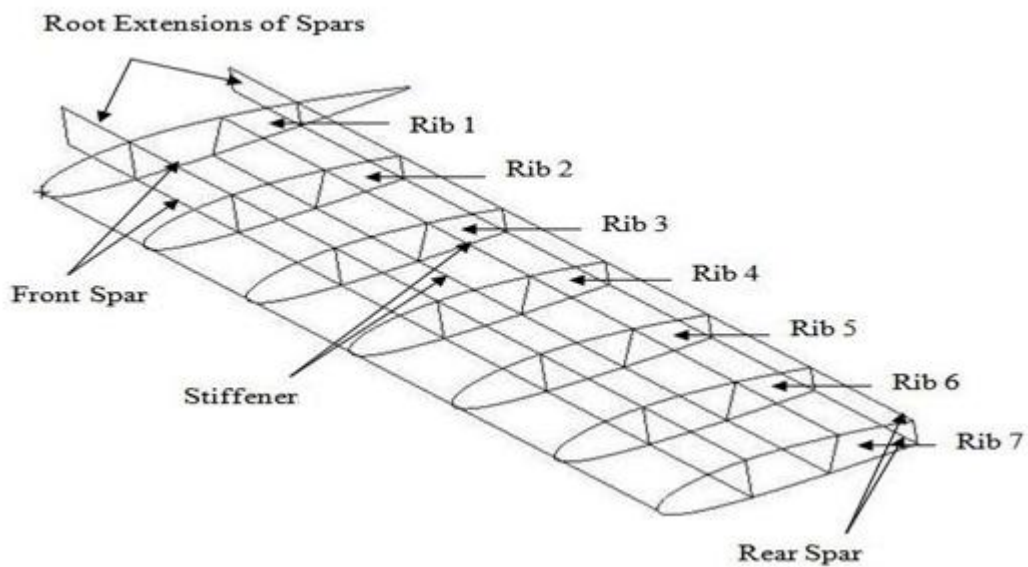


Figure 2.25: Structural Lay-Out of the Wing Structure

2.6.3 Final Minimum Wing Weight Results and Weight Breakdown

Table 2.14 shows the mass of the wing torque box structure and contribution of the elements to the final weight using the first idealization approach which assumes that spars and stringers carry only axial stress; panels and webs carry shear force only. Table 2.14 summarizes the mass breakdown of the wings which are designed based on the external aerodynamic loading calculated at the minimum maneuvering speed/positive load factor (point A) and at the dive speed/positive load factor (point D). The mass of the wing torque box structure is determined using both continuous and discrete solution approaches. In the continuous approach, a minimum initial thickness value of 0.0003 m and a minimum initial flange area of 0.000038 m² are assigned, and two separate factors are selected to increment the sheet thicknesses and flange/stringer areas until all stress and buckling constraints are satisfied in each bay. In the continuous approach, thickness and flange area incremental factors are specified as 1.05 and 1.001, respectively. Iterations are performed to reach to the minimum mass of the wing structure while satisfying all stress and local buckling constraints. In the discrete approach, a set of standard thicknesses and standard flange areas are created to be selected from lists, Appendix [E]. The selections of standard values are carried out by simply rounding up the continuous solution to the closest values of standard thicknesses and areas available in the lists generated. In Table 2.14 mass breakdown is given for the discrete solution.

Table 2.14: Minimum Mass of the Wing Structure Determined Using the 1st Structural Idealization

Method	Mass (kg) at Point A		Mass (kg) at Point D	
Continuous	62.90		64.20	
Discrete	67.69		69.61	
Component	Mass (kg)	% Contribution	Mass (kg)	% Contribution
Skins	43.84	64.33 %	45.79	65.34 %
Spar Webs	5.06	7.43 %	5.02	7.16 %
Flange Areas	14.65	21.65 %	14.67	21.08 %
Ribs	4.12	6.05 %	4.13	5.90 %

Table 2.15 shows the mass of the wing torque box structure and the contributions of the elements on the final discrete weight using the second idealization approach

which assumes that spars and stiffeners carry only direct stress; panels and webs carry direct stress and shear force. Table 2.15 summarizes the mass breakdown of the wings which are designed based on the loading calculated at the minimum maneuvering speed/positive load factor (point A) and at the dive speed/positive load factor (point D).

Table 2.15: Minimum Mass of the Wing Structure Determined Using the 2nd Structural Idealization

Method	Mass (kg) at Point A		Mass (kg) at Point D	
Continuous	52.18		52.51	
Discrete	57.61		58.27	
Component	Mass (kg)	% Contribution	Mass (kg)	% Contribution
Skins	45.29	78.60 %	45.65	78.34 %
Spar Webs	6.56	11.39 %	6.80	11.68 %
Flange Areas	3.34	5.80 %	3.34	5.73 %
Ribs	2.42	4.21 %	2.47	4.25 %

The masses that have been determined in both idealizations using the external loading calculated at point D are slightly higher than the masses determined using the external loading calculated at point A for both structural idealizations. Although the sectional bending moments and shear forces are nearly same for the minimum maneuvering speed and dive speed flight conditions, sectional pitching moments calculated for the dive speed flight condition is higher than the minimum maneuvering speed flight condition. Therefore, the main reason for the higher weight obtained for the dive speed flight condition is higher sectional pitching moment that is calculated at the dive speed condition. Comparison of Tables 2.14 and 2.15 reveal that the use of second structural idealization results in approximately 10 kg lighter mass in the final configuration. Although the second idealization results in lighter weight compared to first one, the percent contribution of skins and spar webs is higher because in the second idealization, skin panels and spar webs are also allowed to carry axial stress beside carrying shear stress.

Figure 2.26 shows the mass breakdown of the wing configurations designed by employing both structural idealizations for the minimum maneuvering speed flight condition. From Figure 2.26, it can be seen that since in the second idealization wing

skins and spar webs are also allowed to carry axial load, total skin and spar web mass obtained by using the second idealization is higher than the total skin and spar web mass obtained by employing the first idealization. On the other hand, since in the first idealization, spar flanges and stringers are assumed to carry all the axial load, the total flange and stringer mass obtained by using the first idealization is considerably higher than the total flange and stringer mass obtained by using the second idealization in the design process. Therefore, it can be concluded that the mass of the spar flanges and the stringers account for the higher mass of the final configuration wing structure, which is designed using the first structural idealization.

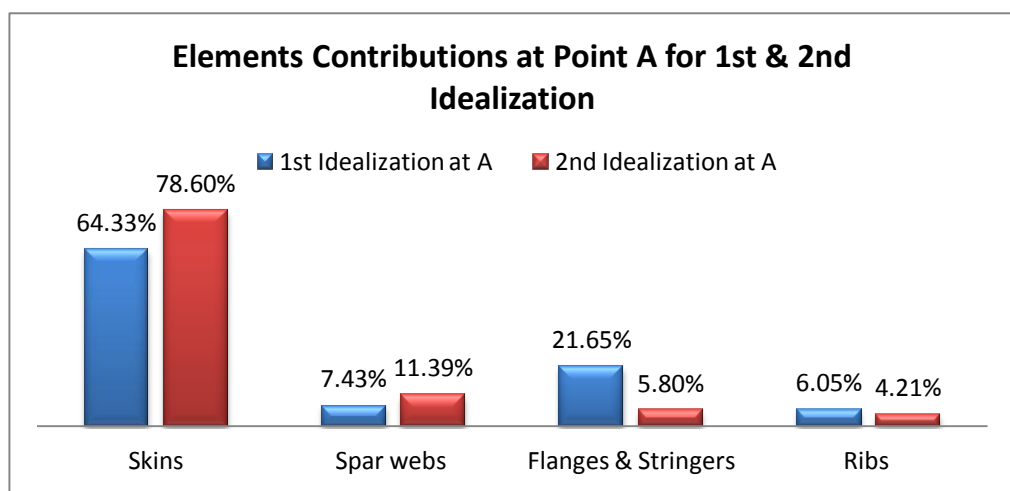


Figure 2.26: Mass Breakdown of the Wing Configurations Designed Using Structural Idealizations 1 and 2 – External Loading Calculated at Point A

2.6.4 Results of Flange Areas for the First and the Second Idealization

Tables 2.16 and 2.17 show standard flange areas of the first idealization determined based on the external loading calculated at points A and D. Spar and stringer areas tabulated in Tables 2.16 and 2.17 are the ones which satisfy the axial stress safety requirements. Figure 2.27 defines the spars and stringers of the wing torque box.

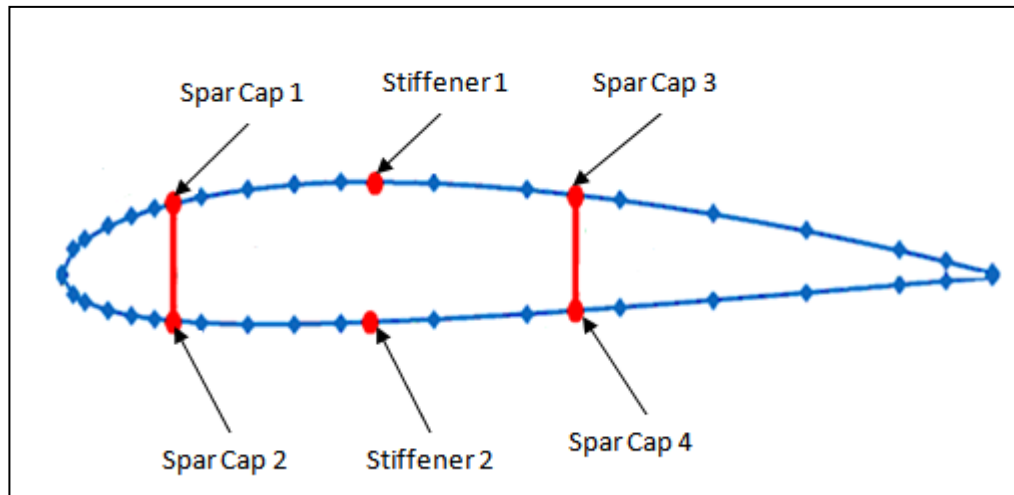


Figure 2.27: Wing Spars and Stiffeners Definitions

Table 2.16: Standard Flange Areas Determined Using the 1st Idealization - Point A

FLANGE AREAS (in mm ²) Point A							
Root	Station	Spar Cap 1	Spar Cap 2	Spar Cap 3	Spar Cap 4	Stiffener 1	Stiffener 2
	1	613	444	246	375	525	430
	2	573	312	184	232	375	312
	3	375	184	98	137	213	184
	4	184	88	58	73	104	88
	5	58	44	44	44	44	44
Tip	6	44	44	44	44	44	44

Table 2.17: Standard Flange Areas Determined Using the 1st Idealization - Point D

FLANGE AREAS (in mm ²) Point D							
Root	Station	Spar Cap 1	Spar Cap 2	Spar Cap 3	Spar Cap 4	Stiffener 1	Stiffener 2
	1	613	444	246	375	525	430
	2	573	312	184	232	375	312
	3	375	184	98	137	213	184
	4	184	94	58	73	104	88
	5	58	44	44	44	44	44
Tip	6	44	44	44	44	44	44

Tables 2.16 and 2.17 show that spar cap 1 (front spar upper flange) has the largest area. Spar cap and stringer areas are largest at the root of the wing, and they decrease towards the tip of the wing where the wing loads are smaller.

Tables 2.18 and 2.19 show standard flange areas of second idealization determined based on the external loading calculated at points A and D. Spar and stiffener areas tabulated in Tables 2.18 and 2.19 are the ones which satisfy the axial stress safety requirements.

Table 2.18: Standard Flange Areas Determined Using the 2nd Idealization - Point A

FLANGE AREAS (in mm²) Point A							
Root	Station	Spar Cap 1	Spar Cap 2	Spar Cap 3	Spar Cap 4	Stiffener 1	Stiffener 2
	1	44	44	44	44	44	44
	2	44	44	44	44	44	44
	3	44	44	44	44	44	44
	4	44	44	44	44	44	44
	5	44	44	44	44	44	44
Tip	6	44	44	44	44	44	44

Table 2.19: Standard Flange Areas Determined Using the 2nd Idealization - Point D

FLANGE AREAS (in mm²) Point D							
Root	Station	Spar Cap 1	Spar Cap 2	Spar Cap 3	Spar Cap 4	Stiffener 1	Stiffener 2
	1	44	44	44	44	44	44
	2	44	44	44	44	44	44
	3	44	44	44	44	44	44
	4	44	44	44	44	44	44
	5	44	44	44	44	44	44
Tip	6	44	44	44	44	44	44

Second idealization results in constant spar caps and stiffeners areas. This area is the minimum standard area that satisfies axial stress safety requirements. It should be noted that in the second idealization, skin and spar web thicknesses obtained after satisfying the stress and local buckling constraints provide sufficient overall inertia such that small spar flange and stringer areas turn out to satisfy the axial stress constraints for these one dimensional members. Therefore, total mass of the spar flanges and the stringers are considerably small compared to the total flange and

stringer mass obtained by the first idealization. However, it should be noted that spar flanges and stringers also serve as boundaries for the skin and web panels in each bay. In the local buckling calculations, the boundaries of the skin and web panels are assumed to be simply supported. To provide real simple support boundary conditions, spar flange and stringer dimensions must be of certain size and shape. Therefore, in practice the actual spar flange and stringer areas may have to be increased to provide simple support boundary conditions for the skin and web panels. However, since this study specifically deals with the preliminary design stage, the details of the spar flange and stringer areas to provide are not considered in design process.

Figures 2.28 - 2.33 show the variation of the spar cap and stiffener areas along the wing span for both structural idealizations. Figures 2.28 - 2.33 give the results of the design performed based on the external loading calculated at point A on the V-N diagram. As shown in Figures 2.28 - 2.33, in the first idealization spar and stiffener areas decrease towards the wing tip because in the first idealization bending loads are carried by the spars and stringers.

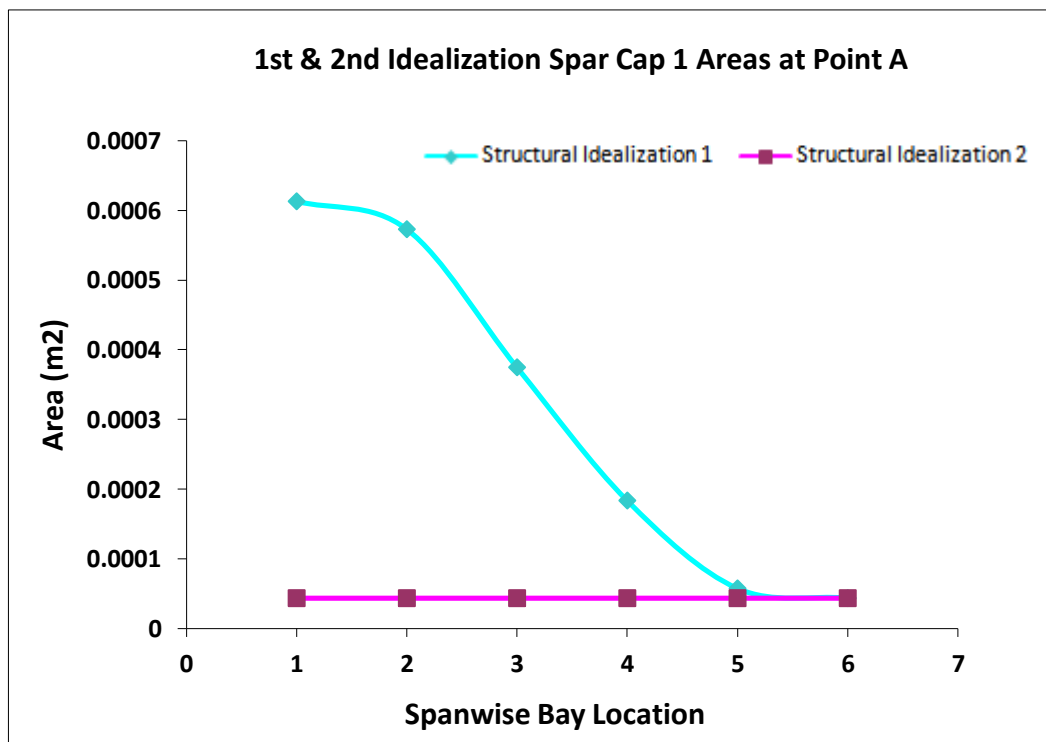


Figure 2.28: Spanwise Variation of the Area of Spar Cap 1 Determined by Using the 1st and the 2nd Structural Idealization

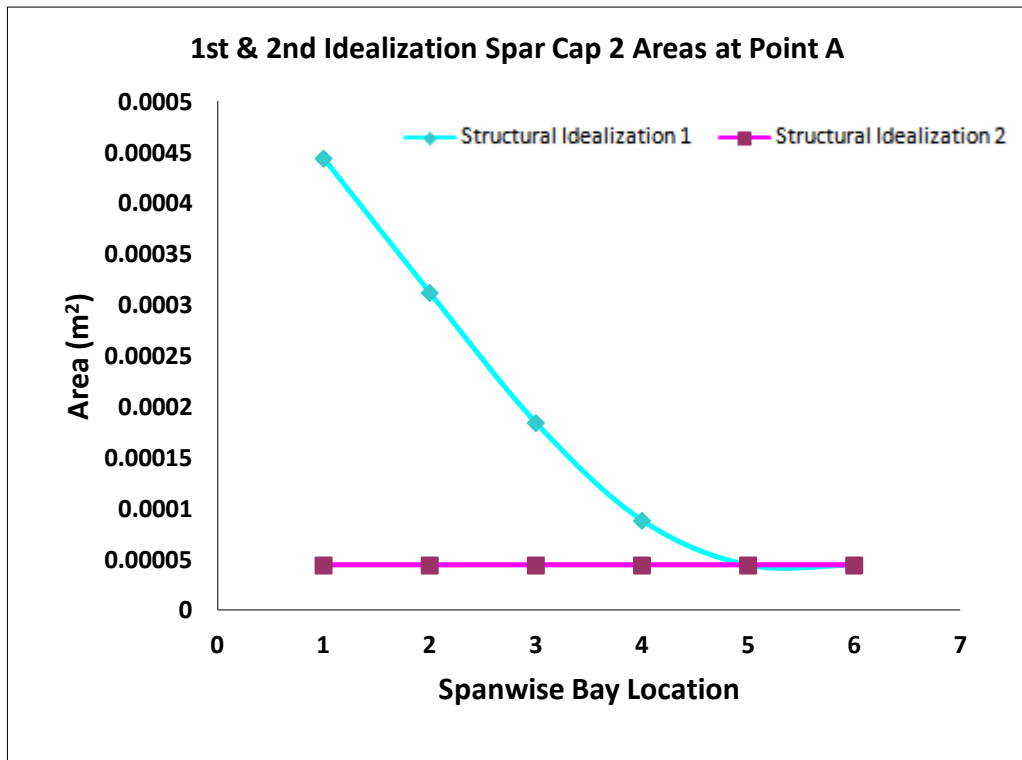


Figure 2.29: Spanwise Variation of the Area of Spar Cap 2 Determined by Using the 1st and the 2nd Structural Idealization

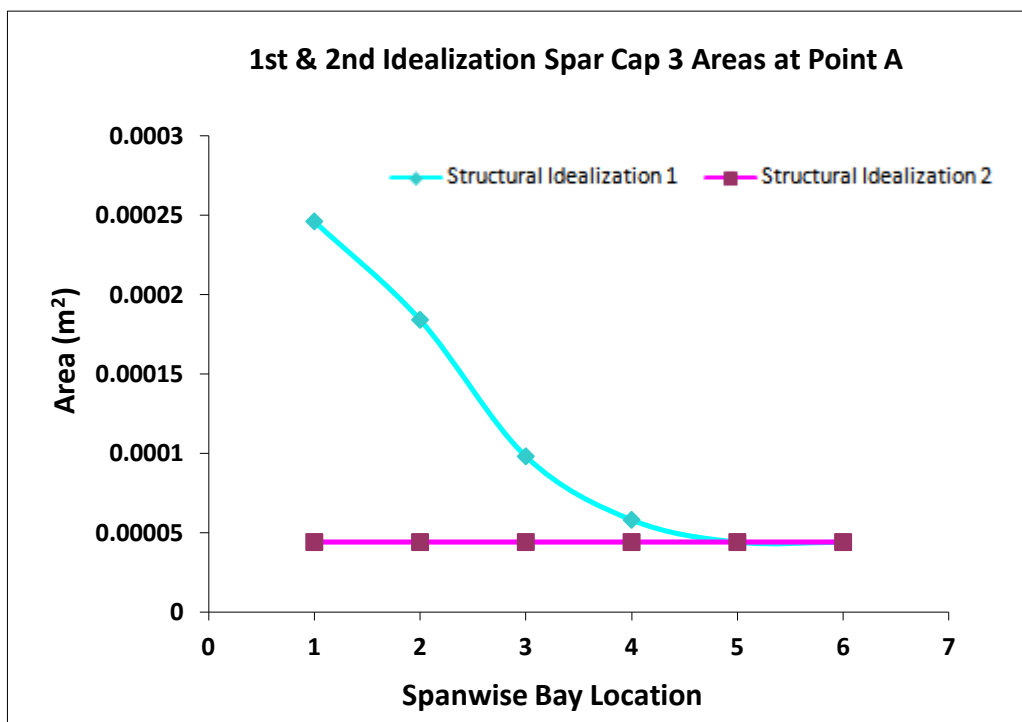


Figure 2.30: Spanwise Variation of the Area of Spar Cap 3 Determined by Using the 1st and the 2nd Structural Idealization

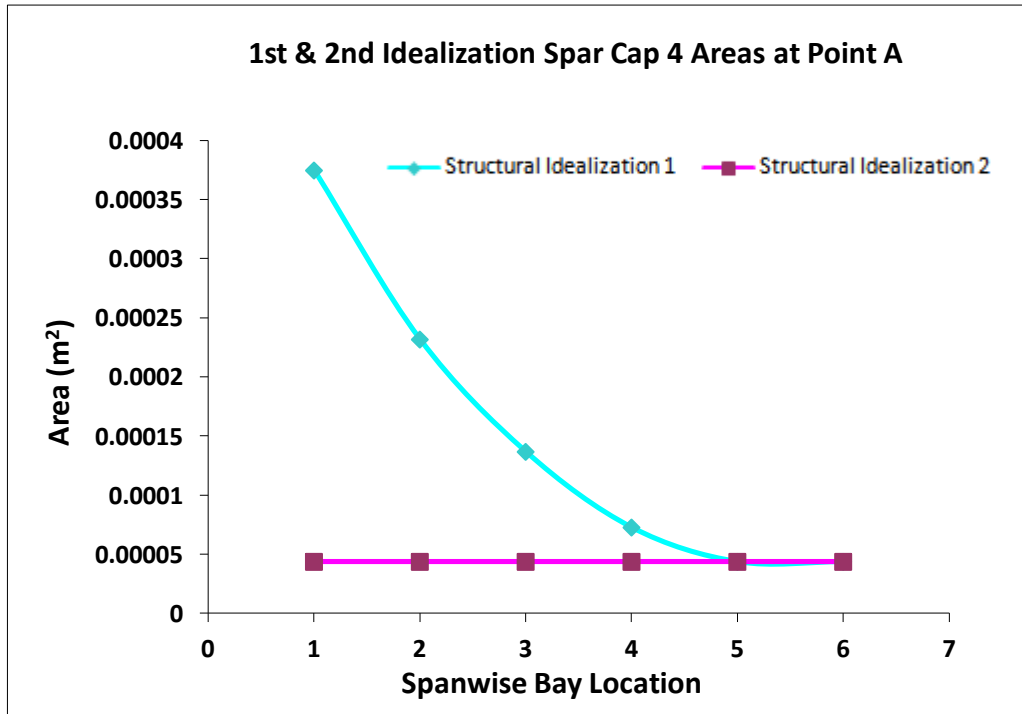


Figure 2.31: Spanwise Variation of the Area of Spar Cap 4 Determined by Using the 1st and the 2nd Structural Idealization

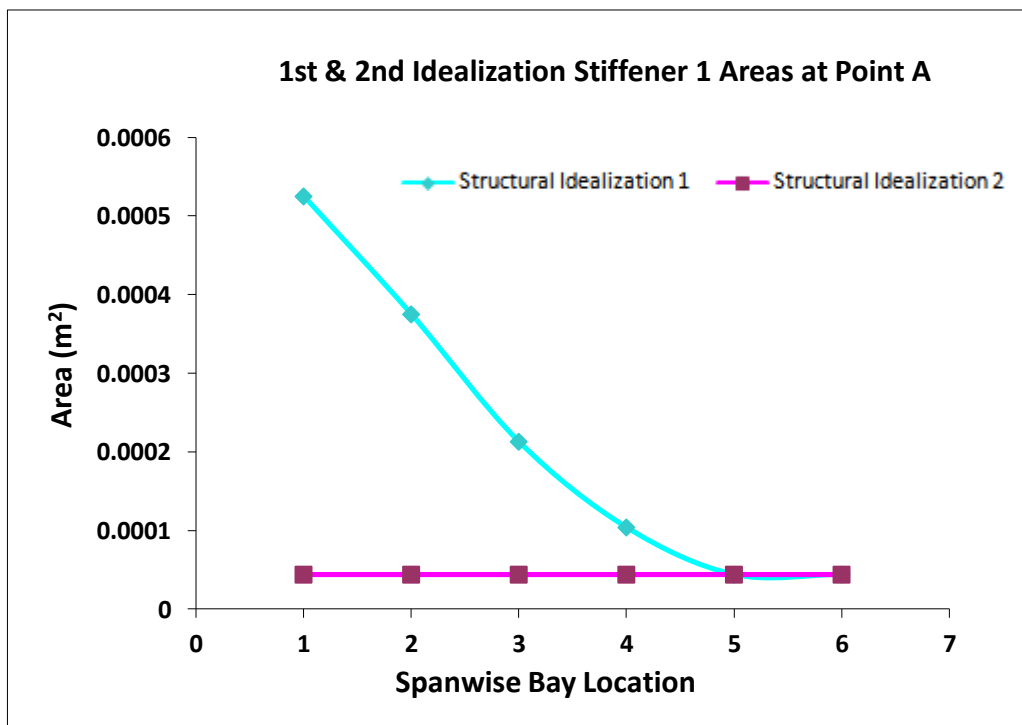


Figure 2.32: Spanwise Variation of the Area of Stringer 1 Determined by Using the 1st and the 2nd Structural Idealization

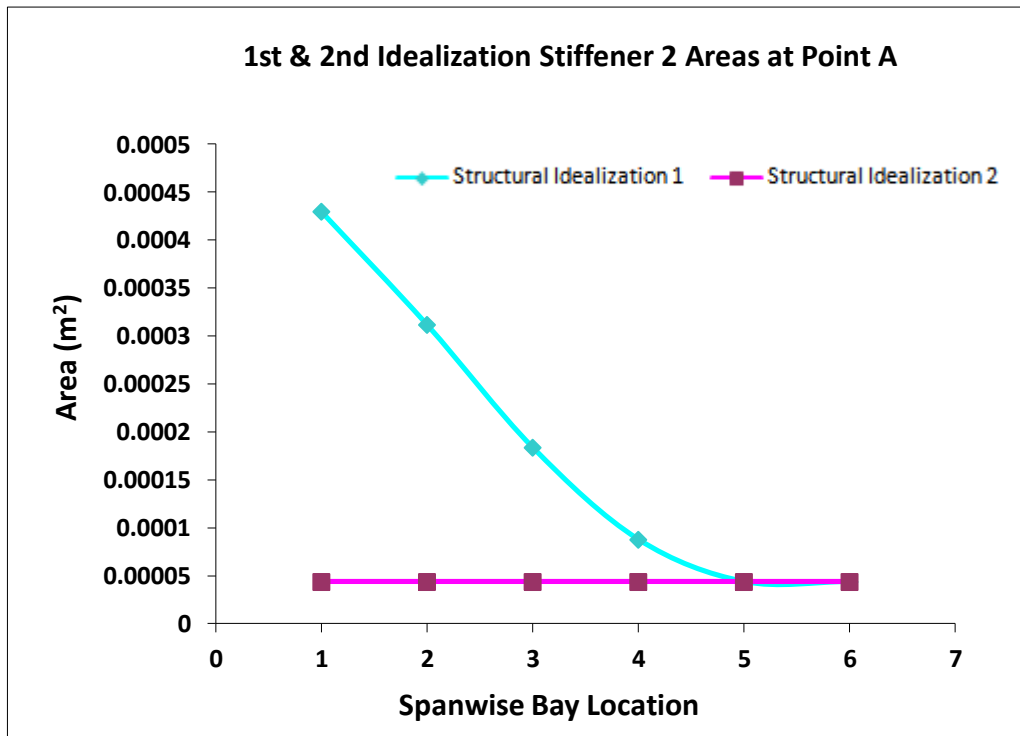


Figure 2.33: Spanwise Variation of the Area of Stringer 2 Determined by Using the 1st and the 2nd Structural Idealization

2.6.5 Results of Skin and Spar Web Thicknesses for the First and the Second Structural Idealizations

In the first structural idealization, the skin and spar web thicknesses are first determined such that they can carry the maximum shear stresses acting on them safely and then the buckling constraints are checked. Finally, the thicknesses are selected to safely satisfy both shear strength and buckling constraints.

In the second idealization, since skins and spar webs also carry axial load, maximum Von Mises stresses are calculated in each bay and strength check is first made based on the maximum Von Mises stress. Then, buckling check of each panel between the ribs stations are carried out. Thus, sizing is based on two level check of strength and satisfaction of the buckling constraints. Thickness definitions of the wing are shown in Figure 2.34.

It must be noted that while solving for the nose skin thickness, the upper nose skin thickness and lower nose skin thickness are taken into account separately in the

design iterations, but the final nose skin thickness is taken as the larger of the two thicknesses that satisfy the buckling constraints.

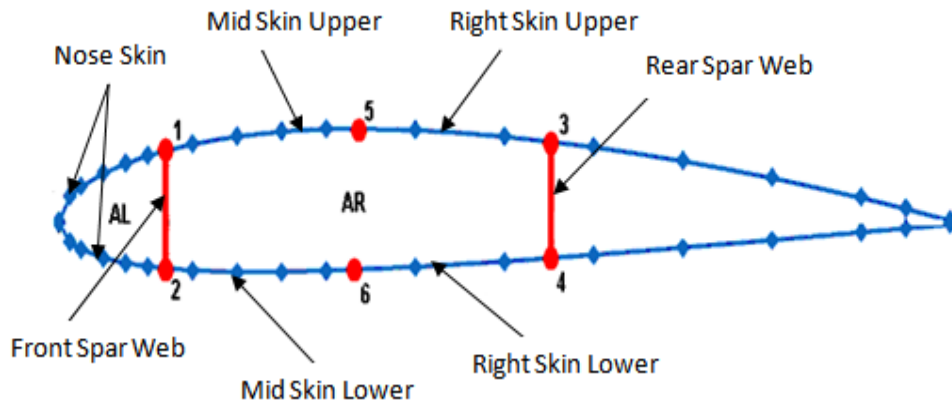


Figure 2.34: Thickness Definitions of the Wing

The selected standard sizes for the skin and the web thicknesses for first idealization at point A and D are shown in Tables 2.20 and 2.21.

Table 2.20: Standard Thicknesses Determined Using the 1st Idealization - Point A

SKIN and SPAR WEB THICKNESSES (in m) Point A								
Root	Station	Nose Skin	Mid- Up Skin	R-Spar Web	Mid-L Skin	F-Spar Web	Right-Up Skin	Right-L Skin
	1	0.0025	0.0020	0.0013	0.0032	0.0023	0.0020	0.0020
	2	0.0023	0.0018	0.0010	0.0032	0.002	0.0018	0.0018
	3	0.0023	0.0016	0.0010	0.0032	0.0018	0.0018	0.0016
	4	0.0020	0.0016	0.0010	0.0023	0.0016	0.0016	0.0013
	5	0.0016	0.0013	0.0008	0.0018	0.0013	0.0013	0.0010
Tip	6	0.0010	0.0008	0.0005	0.0013	0.0008	0.0008	0.0004

Table 2.21: Standard Thicknesses Determined Using 1st Idealization - Point D

SKIN and SPAR WEB THICKNESSES (in m) Point D								
Root	Station	Nose Skin	Mid- Up Skin	R-Spar Web	Mid-L Skin	F-Spar Web	Right-Up Skin	Right-L Skin
	1	0.0032	0.0020	0.0013	0.0041	0.0023	0.0018	0.0020
	2	0.0025	0.0020	0.0010	0.0032	0.0020	0.0016	0.0020
	3	0.0023	0.0018	0.0010	0.0032	0.0018	0.0016	0.0018
	4	0.0020	0.0016	0.0008	0.0023	0.0016	0.0013	0.0016
	5	0.0016	0.0013	0.0008	0.0018	0.0013	0.0010	0.0010
Tip	6	0.0010	0.0010	0.0005	0.0013	0.0008	0.0006	0.0006

Tables 2.22 and 2.23 show the standard sizes for skin and web thicknesses for the second idealization at point A and D.

Table 2.22: Standard Thicknesses Determined Using 2nd Idealization - Point A

SKIN and SPAR WEB THICKNESSES (in m) Point A								
Root	Station	Nose Skin	Mid- Up Skin	R-Spar Web	Mid-L Skin	F-Spar Web	Right-Up Skin	Right-L Skin
	1	0.0048	0.0032	0.0013	0.0010	0.0032	0.0018	0.0010
	2	0.0048	0.0018	0.0013	0.0006	0.0032	0.0013	0.0008
	3	0.0048	0.0010	0.0013	0.0004	0.0025	0.0006	0.0008
	4	0.0048	0.0010	0.0013	0.0004	0.0023	0.0004	0.0008
	5	0.0025	0.0008	0.0008	0.0004	0.0013	0.0004	0.0008
Tip	6	0.0010	0.0006	0.0005	0.0003	0.0008	0.0004	0.0006

Table 2.23: Standard Thicknesses Determined Using 2nd Idealization - Point D

SKIN and SPAR WEB THICKNESSES (in m) Point D								
Root	Station	Nose Skin	Mid- Up Skin	R-Spar Web	Mid-L Skin	F-Spar Web	Right-Up Skin	Right-L Skin
	1	0.0048	0.0032	0.0013	0.0010	0.0032	0.0018	0.0008
	2	0.0048	0.0018	0.0013	0.0006	0.0032	0.0013	0.0008
	3	0.0048	0.0010	0.0013	0.0006	0.0032	0.0006	0.0006
	4	0.0048	0.0010	0.0013	0.0005	0.0023	0.0003	0.0006
	5	0.0025	0.0010	0.0008	0.0005	0.0013	0.0003	0.0006
Tip	6	0.0013	0.0008	0.0005	0.0004	0.0008	0.0003	0.0005

Figures 2.35 - 2.41 show the skin and spar web thickness variations along the span of the wing for the first and second idealization based on the loading calculated at point A.

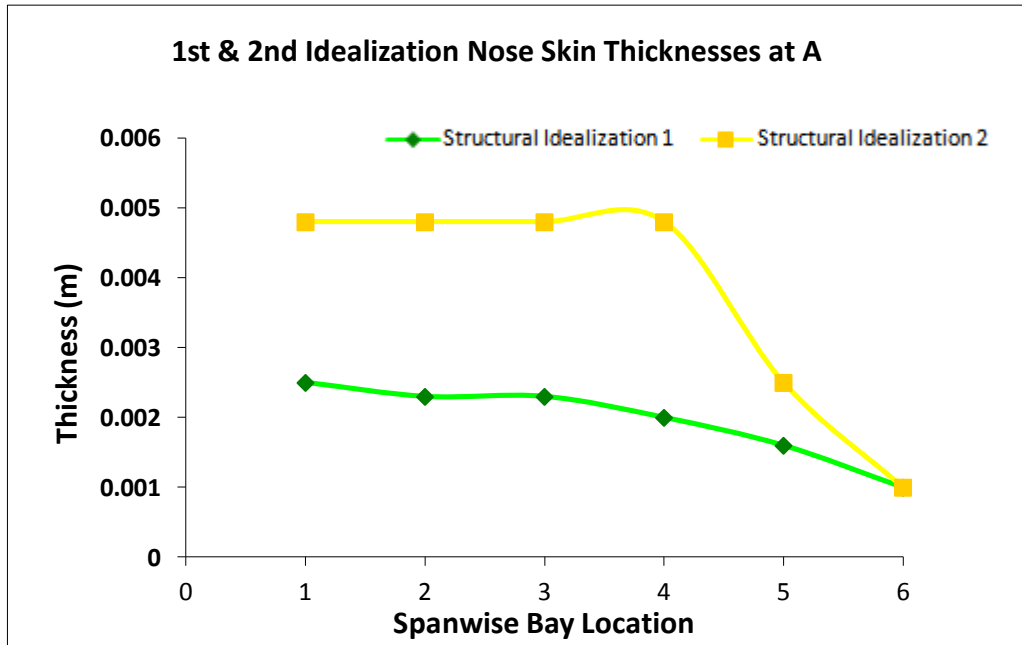


Figure 2.35: Spanwise Variation of the Nose Skin Thickness for the 1st and 2nd Structural Idealization

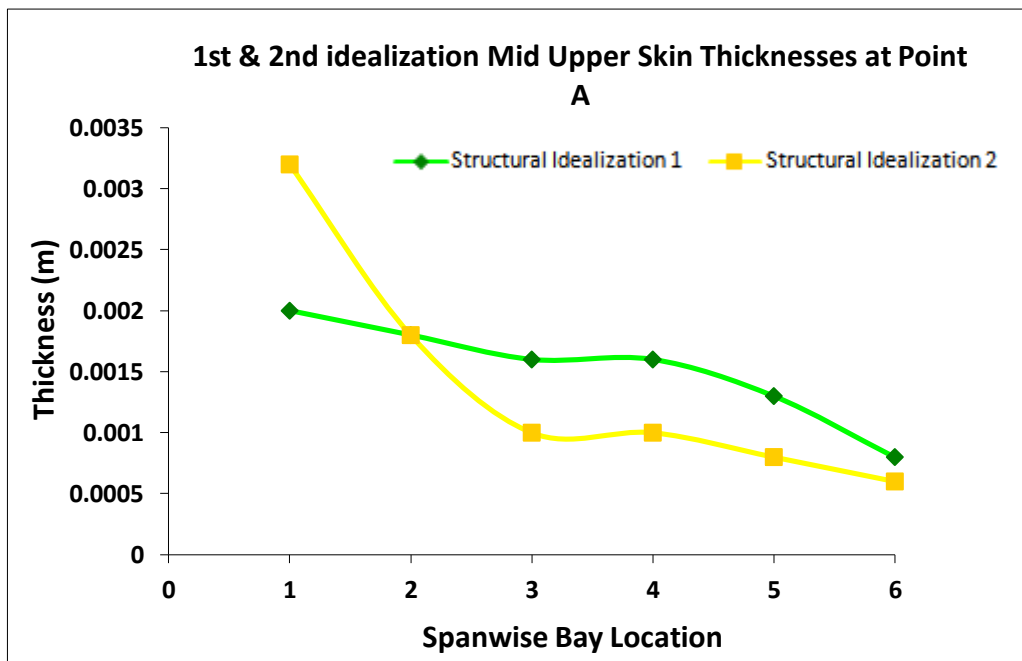


Figure 2.36: Spanwise Variation of the Mid-Upper Skin Thickness for the 1st and 2nd Structural Idealization

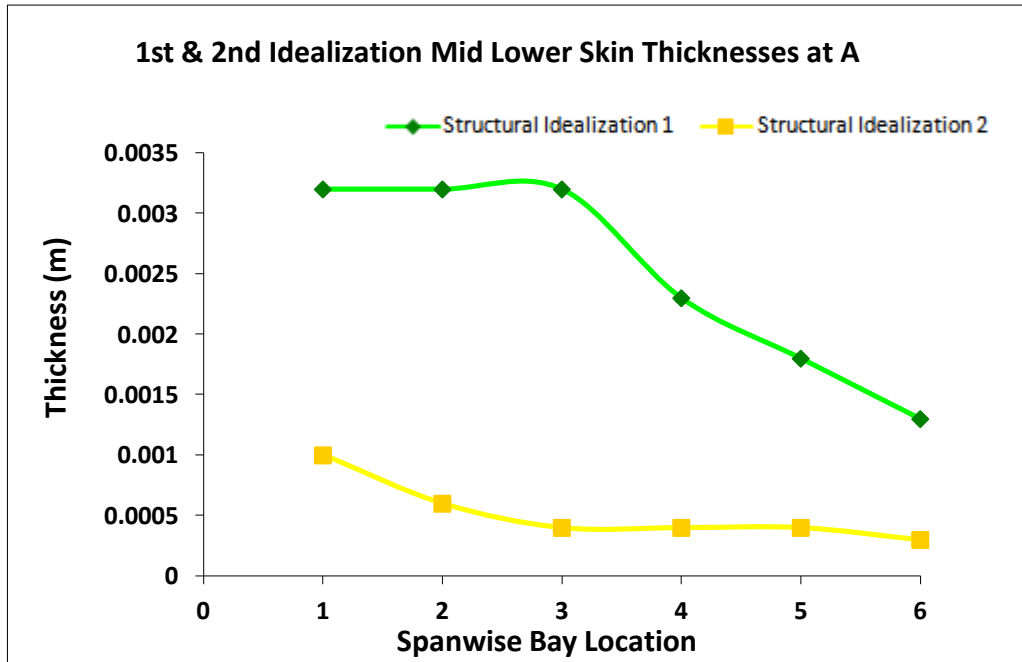


Figure 2.37: Spanwise Variation of the Mid-Lower Skin Thickness for the 1st and 2nd Structural Idealization

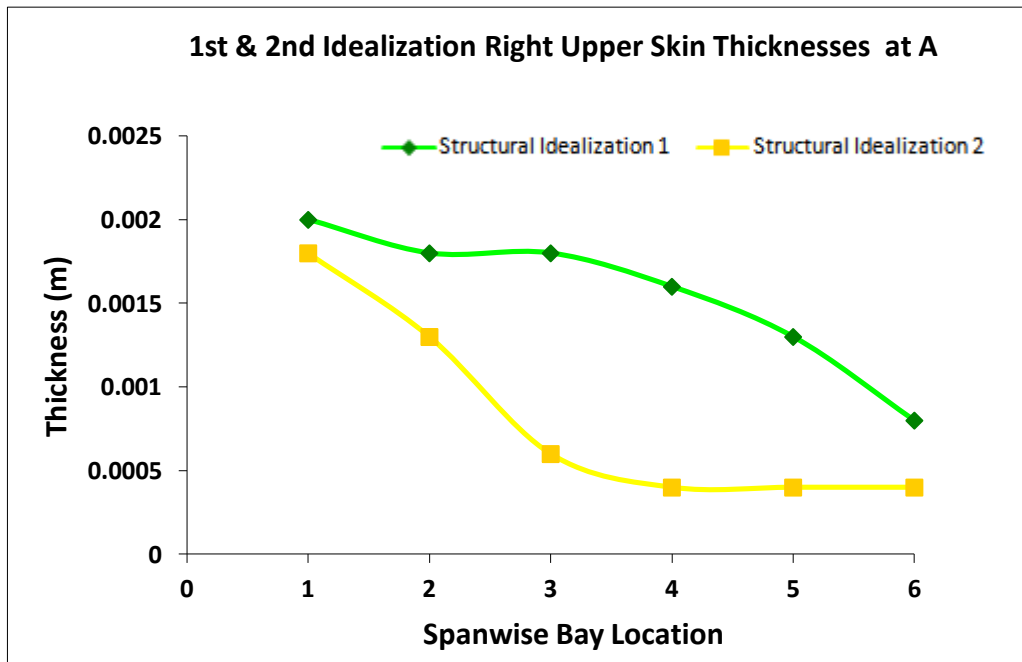


Figure 2.38: Spanwise Variation of the Right-Upper Skin Thickness for the 1st and 2nd Structural Idealization

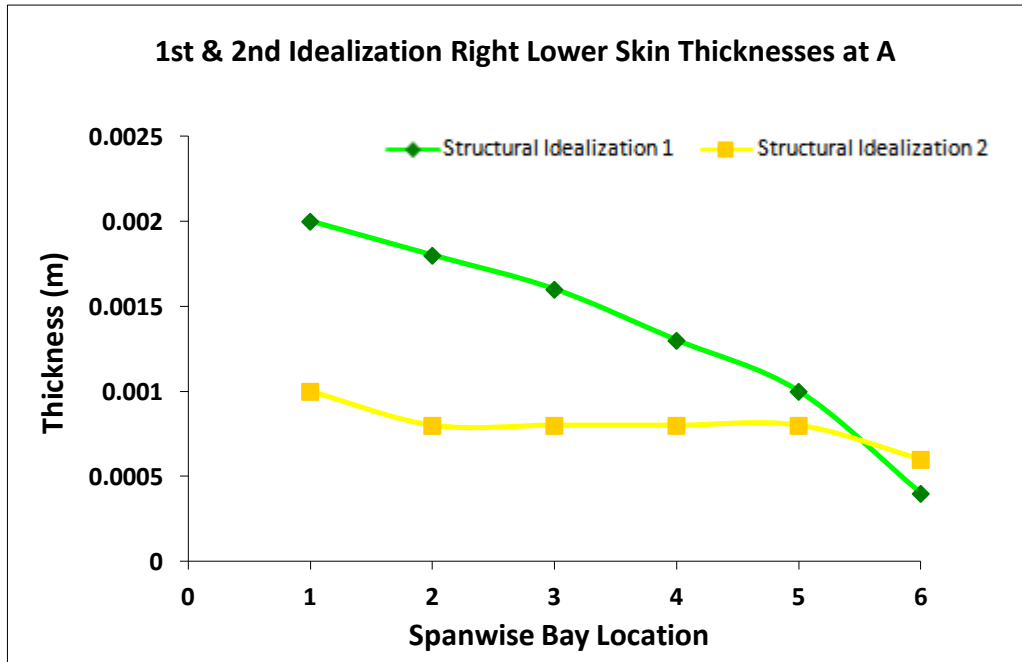


Figure 2.39: Spanwise Variation of the Right-Lower Skin Thickness for the 1st and 2nd Structural Idealization

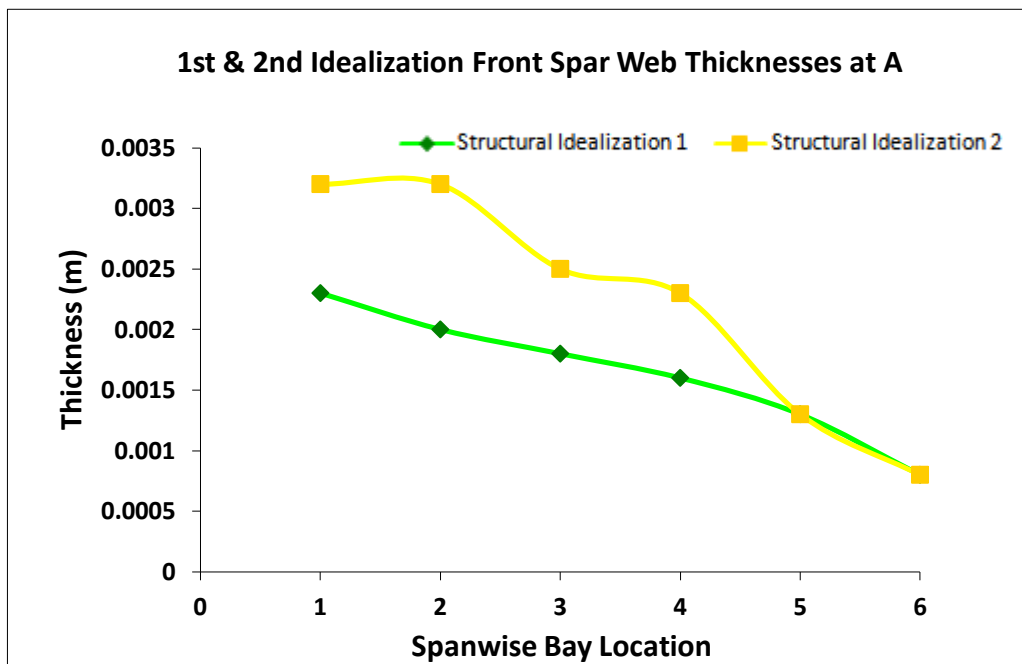


Figure 2.40: Spanwise Variation of the Front Spar Web Skin Thickness for the 1st and 2nd Structural Idealization

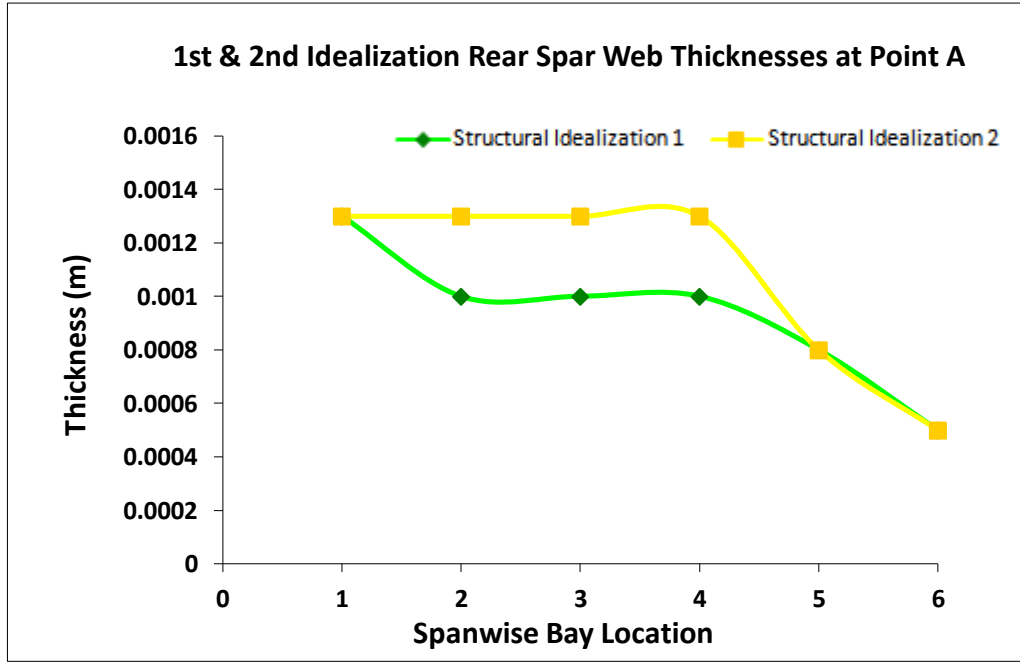


Figure 2.41: Spanwise Variation of the Rear Spar Web Skin Thickness for the 1st and 2nd Structural Idealization

As shown in Figures 2.35 and 2.40, in the second idealization nose skin and front spar web thicknesses are generally higher compared to the corresponding thicknesses determined based on the first structural idealization. The trend in the thickness variation is in accordance with the mass breakdown bar chart given in Figure 2.26. However, not all the skin panels follow the same trend. For instance, as Figure 2.36 shows, in bays away from the wing root structural idealization 1 predicts higher skin thickness. It should be noted that skins thicknesses are determined as a result of two level checks of strength and local buckling. In general, it is experienced that local buckling condition is the main driver of the design. In the first structural idealization shear stress ratio given by Eqn. (2.26) is used for the local buckling check. For the second structural idealization, the interaction equation given by Eqn. (2.27) is used for the local buckling check for the upper skin panels which are under combined shear and compression.

$$R_S = \frac{\tau}{K_S E \left(\frac{t}{b}\right)^2} \leq 1 \quad (2.26)$$

$$R_S^2 + R_C \leq 1 \quad (2.27)$$

If local buckling drives the design, then shear stress ratio (R_S) the compression stress ratio (R_C) are the critical factors which determine the final thicknesses of the upper skin panels. It should be noted in the interaction equation given by Eqn. (2.27) shear stress ratio is squared, whereas in the first structural idealization, shear stress ratio is used in the local buckling check. Therefore, to decide on which structural idealization gives higher thickness for the upper skin panels, relative magnitudes of the shear stresses predicted by the first and second structural idealizations and the compression stress ratio have to be checked. Based on the thickness plot given in Figure 2.36, it can be said that after bay 2, the left hand side of Eqn. (2.27) becomes smaller than the shear stress ratio Eqn. (2.26) which is determined for the first structural idealization.

2.6.6 Results of Rib Thicknesses for the First and the Second Idealization

The rib thicknesses are calculated to satisfy shear strength and shear buckling criteria for both structural idealizations. In the minimum weight design, the selected standard sizes for rib thicknesses for the first and second idealization are tabulated in Table 2.24 and 2.25. As can be seen from both tables, the thicknesses at point A and D turned out to be almost the same with very small differences.

Table 2.24: Standard Rib Thicknesses of 1st Idealization - Points A and D

RIB THICKNESSES (in m)					
	Rib Number	Point A		Point D	
		Nose Rib	Mid Rib	Nose Rib	Mid Rib
Root	1	0.0010	0.0025	0.0010	0.0023
	2	0.0010	0.0023	0.0010	0.0023
	3	0.0010	0.0020	0.0010	0.0020
	4	0.0010	0.0016	0.0010	0.0016
	5	0.0008	0.0013	0.0008	0.0013
	6	0.0006	0.0008	0.0008	0.0010
Tip	7	0.0003	0.0003	0.0003	0.0003

Table 2.25: Standard Rib Thicknesses of 2nd Idealization - Point A and D

RIB THICKNESSES (in m)					
	Rib Number	Point A		Point D	
		Nose Rib	Mid Rib	Nose Rib	Mid Rib
Root	1	0.0008	0.0010	0.0008	0.0010
	2	0.0008	0.0010	0.0008	0.0010
	3	0.0008	0.0010	0.0008	0.0010
	4	0.0008	0.0008	0.0008	0.0008
	5	0.0008	0.0008	0.0008	0.0008
	6	0.0006	0.0006	0.0006	0.0008
Tip	7	0.0003	0.0003	0.0003	0.0003

Figures 2.42 and 2.43 show the nose rib and mid rib thicknesses variations along the span of the wing of the first and second idealization at point A.

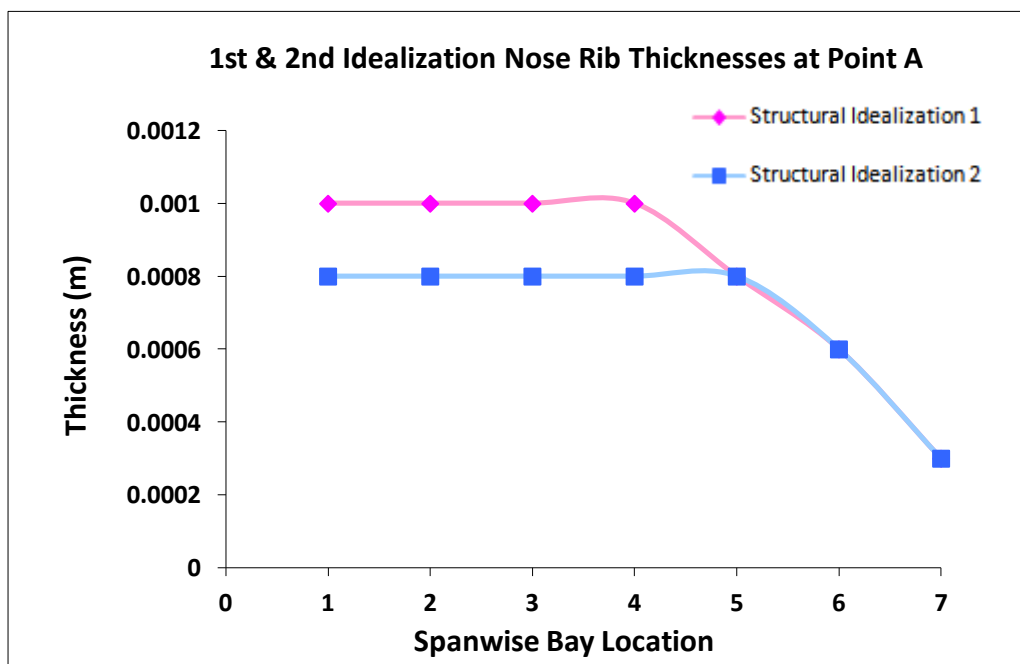


Figure 2.42: Nose Rib Thickness Variation of the 1st and 2nd Structural Idealization – Point A

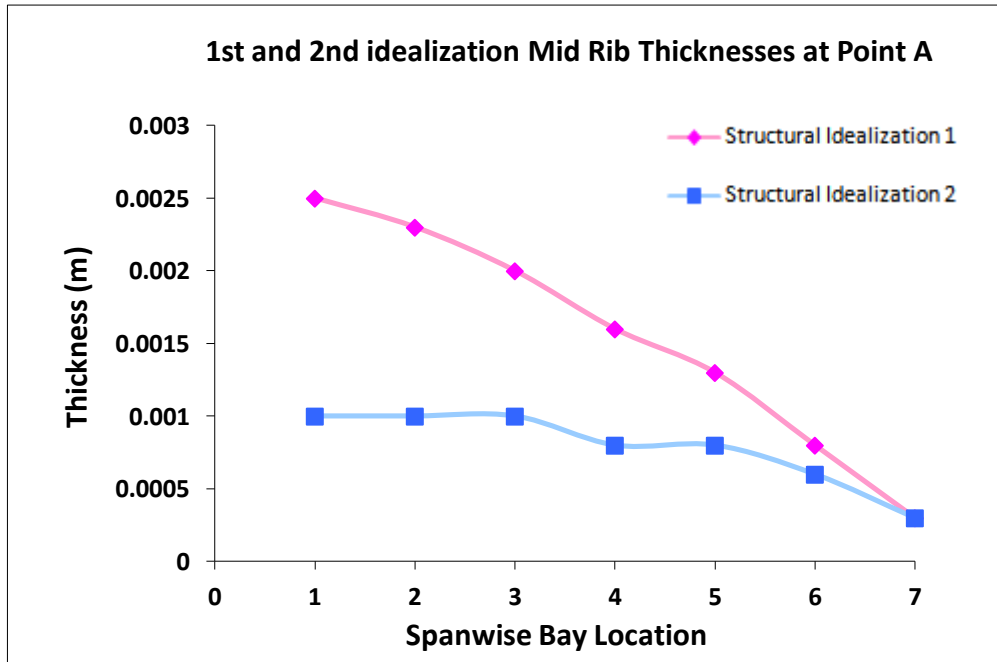


Figure 2.43: Mid Rib Thickness Variation for the 1st and 2nd Structural Idealization
- Point A

2.6.7 Divergence Speed Results of the Design Determined by the First and the Second Idealization

As described in section 2.5.7 divergence speeds are calculated for both idealizations using the external loading calculated at points A and D, respectively. Tables 2.26 and 2.27 give the results of divergence speeds calculated based on the slender beam model.

Table 2.26: Divergence Speed Calculated Using the 1st Idealization

	1st Idealization	
	Point A	Point D
e (m)	0.3375	0.3108
J at 75 % Span (m²)	7.2037×10^{-5}	6.9512×10^{-5}
CLα	4.2798	4.3989
Divergence Speed (m/s)	423.67	427.83

Table 2.27: Divergence Speed Calculated Using the 2nd Idealization

	2nd Idealization	
	Point A	Point D
e (m)	0.1235	0.1171
J at 75 % Span (m²)	5.3538 x 10 ⁻⁵	5.2765 x 10 ⁻⁵
CLα	4.2798	4.3989
Divergence Speed (m/s)	603.88	607.32

The second idealization results in higher divergence speed than the divergence speed obtained for the first idealization. The smaller shear center - aerodynamic center distance is considered to be the main reason for the higher divergence speed that is calculated for the second idealization.

CHAPTER 3

FINITE ELEMENT ANALYSIS OF WING TORQUE BOXES

3.1 Introduction

This chapter is devoted to the finite element analysis of one of the wing configurations designed in chapter two using different structural idealizations that are typically used in practice. MSC[®]/PATRAN package program is used to model the wing torque boxes and structural analysis of the designed wing structure is performed by the finite element analysis software MSC.NASTRAN[®]. The main objective of this study is to investigate the effect of using different finite element types on the analysis results of a wing torque box, which is designed by hand calculation method using two different structural idealizations, and also to make comparisons between the analysis results of finite element solution and hand calculation. One further objective of this section is to decide on appropriate mesh sizes which are used in Chapter 4 for the structural optimization study.

3.2 Wing Configuration Selection

One of the wing configuration presented in chapter two is selected to model the wing torque boxes using MSC[®]/PATRAN program and to carry out finite element analysis of the wing using MSC.NASTRAN[®] software.

For the finite element analysis study, wing structure which is designed using the second structural idealization is taken as the configuration to be studied. Since the second structural idealization assumes that skin panels and spar webs also carry axial stress on top of shear stress, wing configuration designed using the second structural idealization is more close to reality. For this purpose wing, which is designed using

the external load calculated at point A, is selected. Tables 3.1, 3.2 and 3.3 summarize the sizing of the wing configuration which is designed based on the external load calculated at point A in the V-N diagram.

Table 3.1: Standard Flange Areas of 2nd Idealization - Point A

FLANGE AREAS (in mm²) at Point A							
Root	Station	Spar Cap 1	Spar Cap 2	Spar Cap 3	Spar Cap 4	Stiffener 1	Stiffener 2
	1	44	44	44	44	44	44
	2	44	44	44	44	44	44
	3	44	44	44	44	44	44
	4	44	44	44	44	44	44
	5	44	44	44	44	44	44
Tip	6	44	44	44	44	44	44

Table 3.2: Standard Thicknesses of 2nd Idealization - Point A

SKIN and SPAR WEB THICKNESSES (in m) at Point A								
Root	Station	Nose Skin	Mid- Up Skin	R-Spar Web	Mid-L Skin	F-Spar Web	Right-Up Skin	Right-L Skin
	1	0.0048	0.0032	0.0013	0.0010	0.0032	0.0018	0.0010
	2	0.0048	0.0018	0.0013	0.0006	0.0032	0.0013	0.0008
	3	0.0048	0.0010	0.0013	0.0004	0.0025	0.0006	0.0008
	4	0.0048	0.0010	0.0013	0.0004	0.0023	0.0004	0.0008
	5	0.0025	0.0008	0.0008	0.0004	0.0013	0.0004	0.0008
Tip	6	0.0010	0.0006	0.0005	0.0003	0.0008	0.0004	0.0006

Table 3.3: Standard Rib Thicknesses of 2nd Idealization - Point A

RIB THICKNESSES (in m)			
Rib Number		Point A	
		Nose Rib	Mid Rib
Root	1	0.0008	0.0010
	2	0.0008	0.0010
	3	0.0008	0.0010
	4	0.0008	0.0008
	5	0.0008	0.0008
	6	0.0006	0.0006
Tip	7	0.0003	0.0003

3.2.1 Wing Structural Lay-Out

The wing studied is a straight and unswept wing, and it has a NACA 2412 airfoil profile with a rectangular planform. Chord length is 1.524 m and semi-span length is 4.572 m. As it is stated in Chapter 2, the designed wing is composed of two spars, two stiffeners and seven ribs dividing the wing into 6 equal sections of length 0.762 m. The root extensions of the front and rear spars are of 0.5 m in length. The front spar is located at 25 % of the chord length; the rear spar is located at 70% of the chord length, and the upper and lower stiffeners are located respectively at 50 % and 46% of the chord length, Figure 3.1 shows the structural lay-out of the wing.

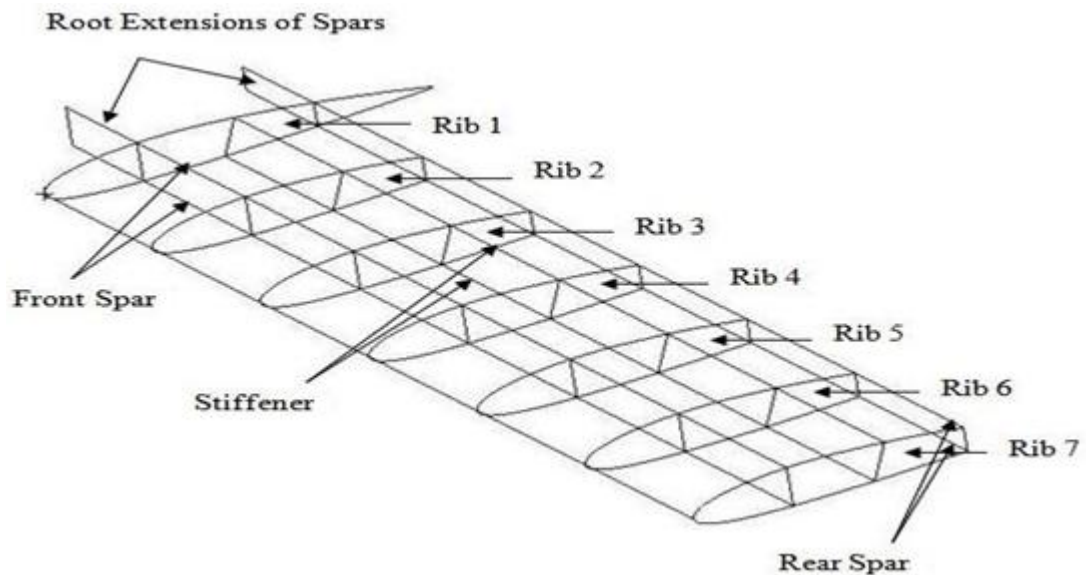


Figure 3.1: Structural Lay-Out of the Wing

3.2.2 Material Properties

The material used in modeling the wing is Aluminum Al 2024 T3 which has a Density value of 2768 kg/m^3 , Modulus of elasticity value is 73.1 MPa and Poisson's Ratio of 0.3.

3.2.3 Aerodynamic Loading and Boundary Conditions Acting On the Wing Torque Box

The aerodynamic loading is distributed to the wing structure in a discrete fashion by calculating equivalent force components section by section at the 25 % of the chord length. As mentioned in Chapter 2 section 2.3.6, the calculation of the external aerodynamic load is performed using the code provided by ESDU, ESDUpac A9510 attached in ESDU 95010 [9]. In ESDU 95010, lift force and pitching moment are considered as line loading, and they are distributed along the lower flange of the front spar, as shown in Figure 3.2. Since the wing loading is given as a line loading, it could have been distributed along the upper flange which could also make sense because in cambered airfoil upper skin has higher contribution to the generation of the lift force through. However, for the purpose of the current study, applying the external load along the lower flange or upper flange is not the main issue. Because the main aim of the analysis section is to investigate the effect of using different element pairs on the analysis results. During the course of the finite element analysis study conclusions are also inferred with regard to the deficiency of certain element types in handling the true external load acting on the wing structure. Finite element analysis of the wing structure is performed by assuming that the wing is fully fixed at wing root extensions, as indicated by the numbers 123456 which imply that three displacements (123) and three rotations (456) of the nodes, whose analysis coordinate system is the global coordinate system, are fixed.

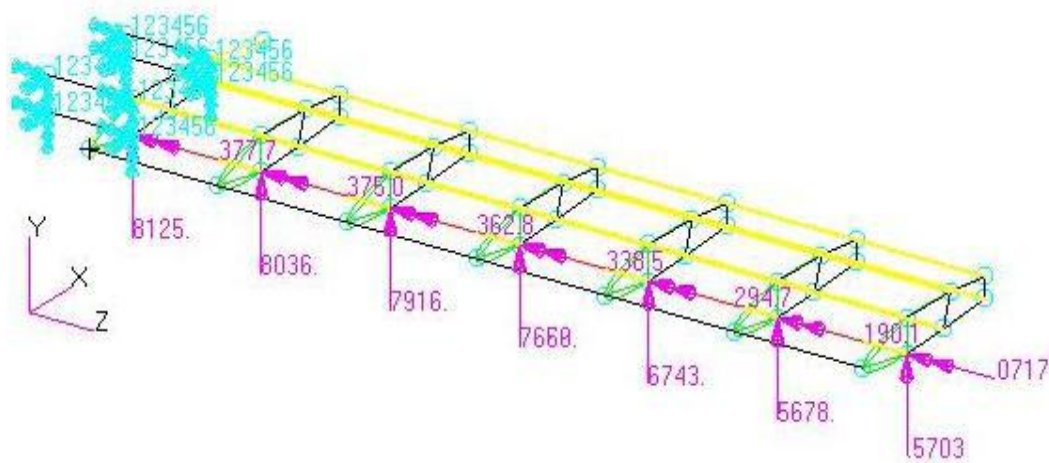


Figure 3.2: External Aerodynamic Load Distribution and Boundary Conditions

3.3 Selection of Element Types

Traditional modeling approach of aerospace structures, which are characterized by very thin elastic sheets and stiffeners, is to use shear panels to model thin sheets and to use rod elements to account for the extensional behavior of the stringers. In general, to model thin walled shell structures three main element types may be used. These elements are shear panel, and shell elements having only membrane or only bending or both membrane and bending behavior [20]. Revised formulation of shell elements, which takes the drilling degrees of freedom into account, are also used depending on the external loading condition. On the other hand, stringers or spar caps may be modeled with beam or rod elements. The correct use of the element types is linked very closely to the loading conditions.

Figure 3.3 shows the typical 1D and 2D finite element types that are used in practice to model spar flanges/stringers and skin and web panels.

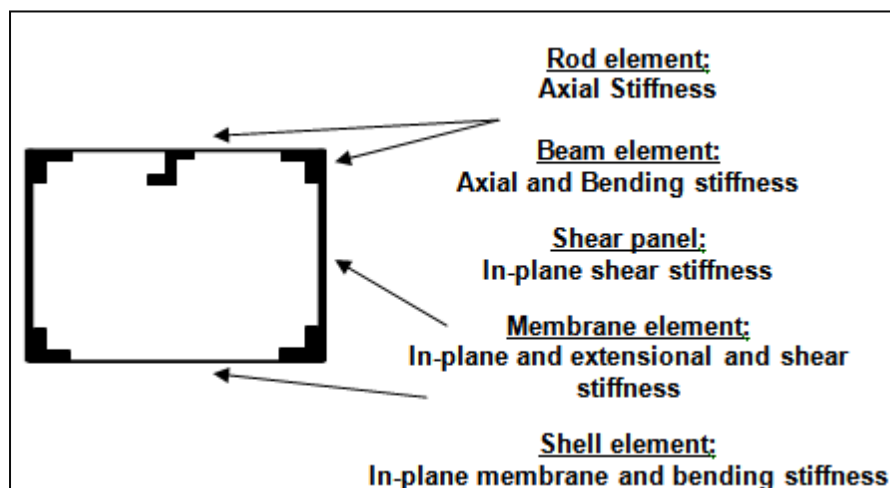


Figure 3.3: Element Types and Definitions

3.4 Case Study on the Use of Shell and Membrane Elements

In order to understand the correct use of elements types in modeling wing structures which are under different loading conditions, a slender box beam model is created with membrane and shell elements and different load cases are applied. Table 3.4 shows box beam dimensions and material properties. In order to make comparisons with the results of simple hand calculation, the box beam is taken as a slender beam

on purpose so that boundary effects can be eliminated and more reliable comparisons can be made with the finite element results.

Table 3.4: Box Beam Dimensions and Properties

Box Beam Dimensions and Properties	
Length	2 m
Height	0.05 m
Width	0.2 m
Shell Thickness	0.003 m
Moment of inertia based on shell thicknesses	$8.134 \times 10^{-07} m^4$
Elastic Modulus (E)	$7 \times 10^{10} \text{ Pa}$
Poisson Ratio	0.3

3.4.1 Tip Moments Producing Pure Torsion

Initially, the box beam is modeled using shell and membrane elements and a tip moment of a magnitude of 0.5 Nm is applied as shown in Figure 3.4.

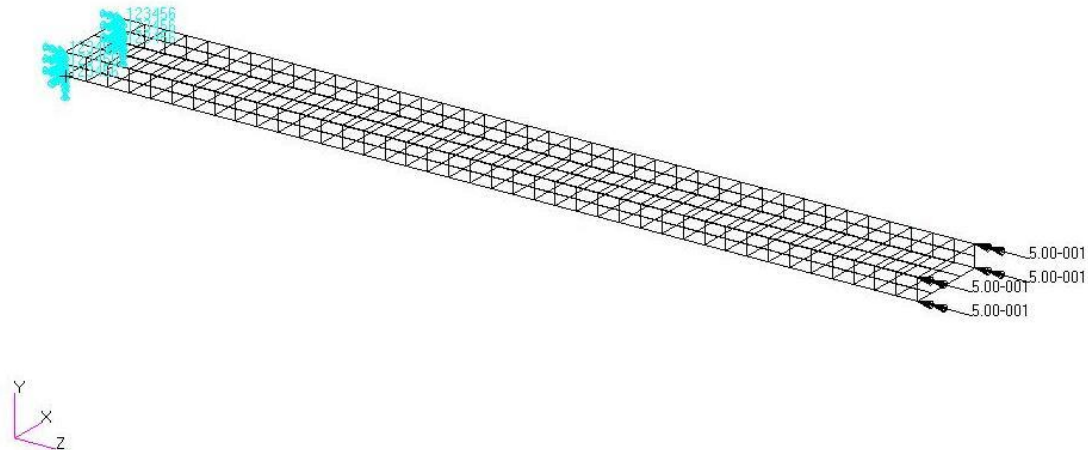


Figure 3.4: Tip Moment Loading on Box Beam Model

Theoretical shear stress away from the restrained end is given by the approximate result based on membrane analogy, which is not a 3D elasticity solution. However, for thin walled box beams shear stress given by the membrane analogy is very accurate.

$$\tau = \frac{T}{2 A t} = \frac{0.5 \times 4}{2 \times 0.2 \times 0.05 \times 0.003} = 33333.33 \text{ Pa} \quad (3.1)$$

Shell Finite Element Results: In order to compare with the simplified analytical solution given above, results of shell finite element are taken at the mid section sufficiently far away from the restraint end and away from the tip where the tip loads are applied. In-plane shear stresses which are determined on the top skin (same as the lower skin) are shown in the Figure 3.5 below. The axial coordinate is varied over a range away from the restraint end and the tip of the box beam, and the variation of the in-plane shear stress is monitored. As it can be seen in Figure 3.5, away from the restraint end shear stress is almost constant and shear stress is also seen to be close to the theoretical result.

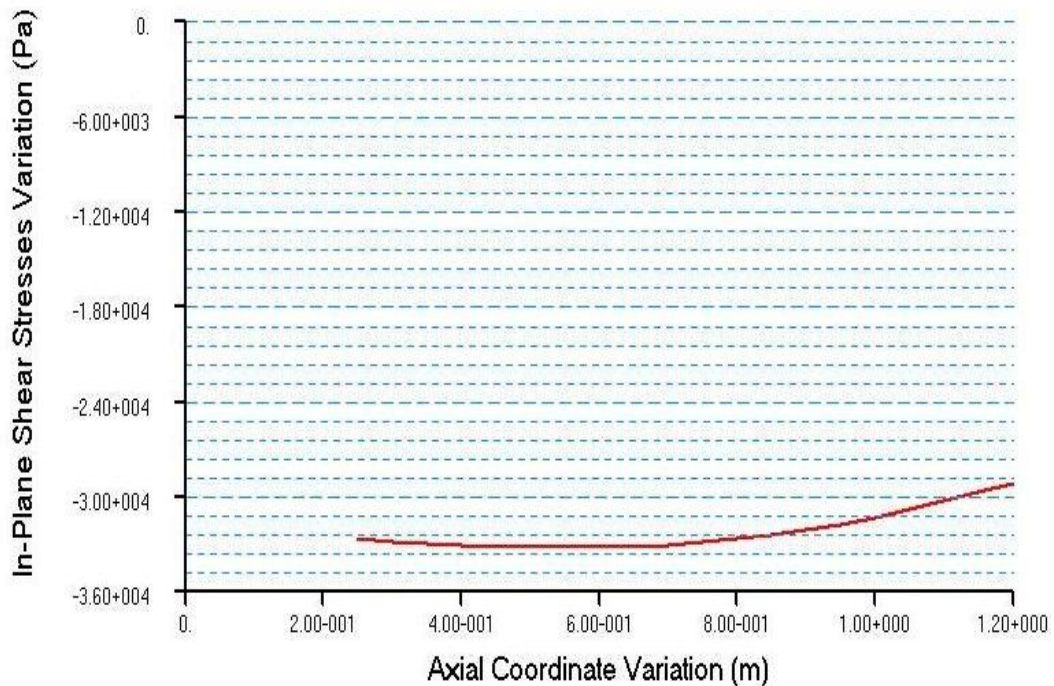


Figure 3.5: Shell Shear Stress Results

Membrane Finite Element Results: For the tip torques shown above box beam modeled with membrane elements does not deform, as expected. This is because membrane elements do not have out-of-plane translational and rotational stiffness. Therefore, loads which generate out-of-plane deformation can not be resisted by the membrane elements

Membrane-R Finite Element Results: The box beam is modeled using membrane elements with revised formulation denoted by membrane - r which possesses drilling degrees of freedom. A tip moment of a magnitude of 0.5 Nm is applied in the same way as shown previously in Figure 3.4. For the tip torque loading, the box beam modeled with membrane - r elements also does not deform because revised membrane element also do not have out-of-plane translational and rotational degrees of freedom. However, if the box beam had a rib at the tip of the box beam where the tip torque loads are applied, then the box beam would have deformed as long as tip rib is meshed with the membrane element with drilling degrees of freedom.

Shear Panel Finite Element Results: The box beam which is modeled using shear panels elements also does not deform under the tip torque loading. More details about the use of shear panels will be discussed in last sections of this chapter.

3.4.2 Uniform Pressure on the Lower and Upper Skin

In this load case a uniform pressure is applied to the upper and lower skin of the box beam all along the span the beam. Directions of the top and bottom surface pressures are adjusted such that they act in the same direction as shown in Figure. 3.6.

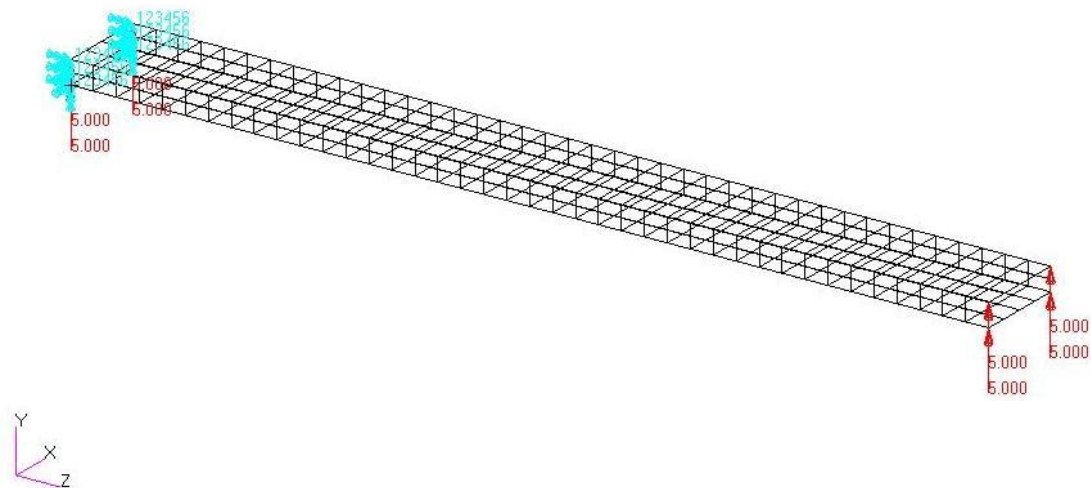


Figure 3.6: Uniform Pressure Loading on the Box Beam Model

Theoretical axial stresses are calculated using the classical beam theory. A uniform pressure of 5 Pa is applied on the lower and upper skin. Bending stress, which is determined by the beam bending theory on the top skin at 1 m away from the wing tip, is given by:

$$\sigma_1 = \frac{Mc}{I} = \frac{(5+5) \times 0.2 \times 1 \times 0.5 \times \left(\frac{0.05}{2}\right)}{8.134 \times 10^{-7}} = -30735 \text{ Pa} \quad (3.2)$$

where σ_1 is axial stress at the mid plane of the top skin

$$\sigma_2 = \frac{Mc}{I} = \frac{(5+5) \times 0.2 \times 1 \times 0.5 \times \left(\frac{0.05}{2} + \frac{0.003}{2}\right)}{8.134 \times 10^{-7}} = -32579 \text{ Pa} \quad (3.3)$$

where σ_2 is axial stress at the top surface of the top skin

$$\sigma_3 = \frac{Mc}{I} = \frac{(5+5) \times 0.2 \times 1 \times 0.5 \times \left(\frac{0.05}{2} - \frac{0.003}{2}\right)}{8.134 \times 10^{-7}} = -28891 \text{ Pa} \quad (3.4)$$

where σ_3 is axial stress at the bottom surface of the top skin

Case 1: Four Elements in the Width Direction

Initial finite element results are obtained with 4 elements in the width direction. This is the case which corresponds to somewhat finer mesh of the box beam.

Shell Finite Element Results: Axial stress results are obtained for the shell elements shown in Figure 3.7 below. Node 308 is at the mid span at (0.1, 0.05, 1.0) coordinates, and it is at the intersection of top skin elements 238, 239, 242 and 243.

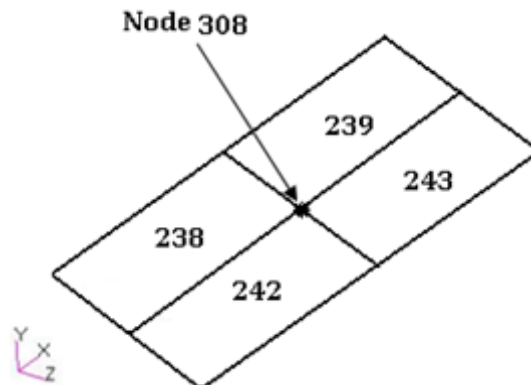


Figure 3.7: Shell Elements 238, 239, 242 and 243

The grid point stresses are defined as the stresses calculated at the grid points from the adjoining plate elements in the global coordinate system.

The grid point stresses at node 308 are as follow:

The stress at the top surface of the upper skin is $\sigma_{z_2} = -31350 Pa$. On the other hand, the stress at the bottom surface of the upper skin is $\sigma_{z_1} = -30740 Pa$ and the stress at the mid plane of the upper surface is $\sigma_{mid} = -31050 Pa$.

Stresses at node 308 of elements 238, 239, 242 and 243 are shown in Table 3.5.

Table 3.5: Shell Element Stresses at Node 308

Element ID	Node Id	Fiber Distance (m)	Stresses (Pa)
238	308	- 0.0015	-32187
		0.0015	-32983
239	308	- 0.0015	-32187
		0.0015	-32983
242	308	- 0.0015	-29297
		0.0015	-29727
243	308	- 0.0015	-29297
		0.0015	-29727

The average stress at the bottom surface of the upper skin equals - 30742 Pa, and the average stress at the top surface of the upper skin equals - 31355 Pa.

Comparison with Beam Theory Results:

Theoretical axial stresses which are calculated using the classical beam theory are compared to the shell finite element stresses results determined at the mid span which is sufficiently far away from the restraint end and the free edge.

At the mid plane, $\sigma_{mid,theory} = -30735 Pa$ and $\sigma_{mid,FE} = -31050 Pa$.

At the top surface of the upper skin, $\sigma_{2,theory} = -32579 Pa$ and $\sigma_{z_2,FE} = -31350 Pa$

At the bottom surface of the upper skin, $\sigma_{3,theory} = -28891 Pa$ and $\sigma_{z_1,FE} = -30740 Pa$.

As it can be seen, away from the restraint end, axial stresses determined by the finite element solution are close to the theoretical results.

Membrane Finite Element Results:

Axial stress is obtained at the same grid location, node 308 in Figure 3.8, for the box beam modeled with membrane elements.

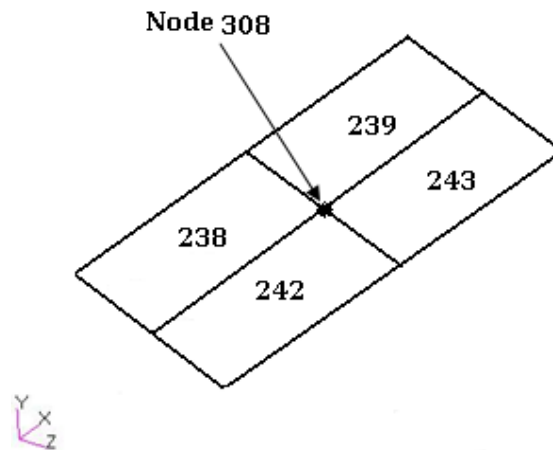


Figure 3.8: Membrane Elements 238, 239, 242 and 243

The grid point stress at node 308 is determined as -7771 Pa. Since membrane elements do not have bending stiffness, there is no distinction between the top, bottom and mid surface stresses.

Membrane stresses at node 308 of elements 238, 239, 242 and 243 are shown in Table 3.6:

Table 3.6: Membrane Element Stresses at Node 308

Element ID	Node Id	Fiber Distance (m)	Stresses (Pa)
238	308	- 0.0015	-8155
		0.0015	-8155
239	308	- 0.0015	-8155
		0.0015	-8155
242	308	- 0.0015	-7386
		0.0015	-7386
243	308	- 0.0015	-7386
		0.0015	-7386

The average stress at a fiber distance of - 0.0015 equals - 7771 Pa and the average stress at a fiber distance of 0.0015 equals - 7771 Pa.

As it can be seen from the results, the membrane element stress result is approximately 4 times smaller than the shell element result which is very close to the beam bending theory result.

Comparison of the Displacement Plots

Figure 3.9 shows the deformation plots determined by shell elements. The max displacement determined as is 7.11×10^{-5} m.

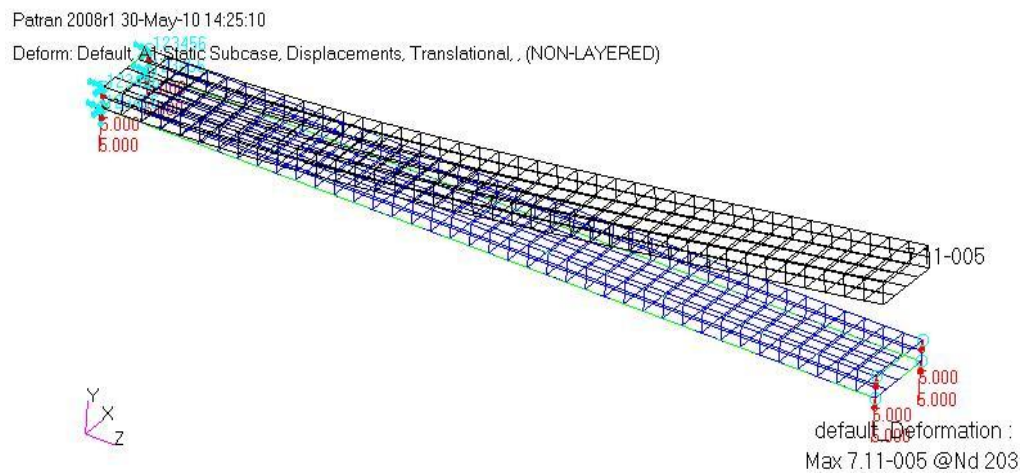


Figure 3.9: Deformation Plot of the Shell Model - Four Shell Elements in the Width Direction

Figure 3.10 shows the deformation plot determined by the membrane elements. The maximum displacement is determined as 1.77×10^{-5} m. Again, the box beam, modeled with membrane elements, has a maximum deformation which is approximately 4 times smaller than the maximum deformation determined by the box beam modeled with shell elements. This result is in accordance with the stress results. When membrane elements are used, stresses are four times less and displacements are also four times less.

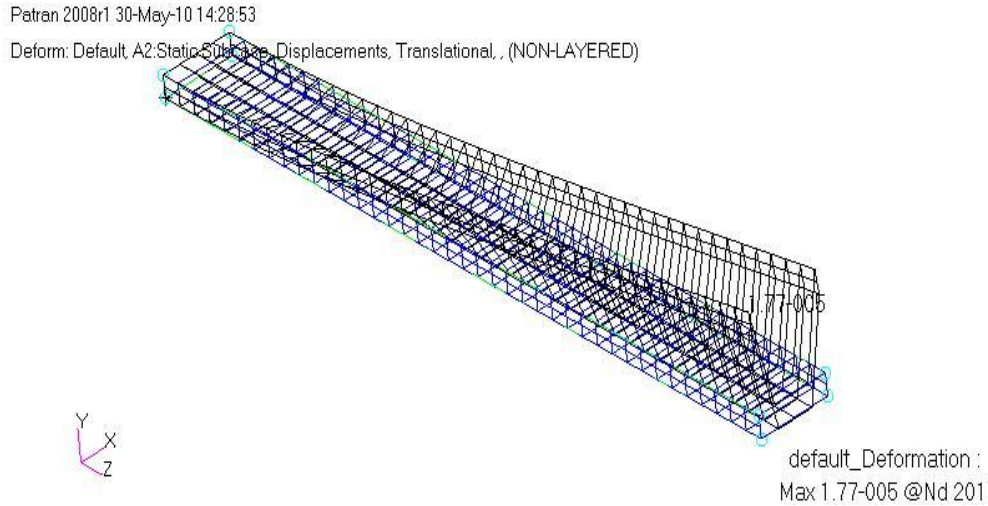


Figure 3.10: Deformation Plot of the Membrane Model - Four Membrane Elements in the Width Direction

As it can be seen from Figure 3.10, when four membrane elements are used in the width direction, membrane elements in the upper and lower skin do not deform because membrane elements do not permit out-of-plane deformation. However, membrane elements on the side webs deform because their deformation is in-plane. Therefore, the deformation plot obtained by the use of membrane elements has a strange appearance.

Case 2: One Element in the Width Direction

Shell Finite Element Results:

To make comparisons with the beam theory results, axial stress results, obtained by the use of shell elements in the model, are given for the element which is at the center of the beam. In this case box beam has 11 elements in the span-wise direction. Figure 3.11 shows the shell elements taken from the mid-section of the box beam.

Patran 2008r1 24-Jul-11 13:14:04
Tensor: Default, A2:Static Subcase, Stress Tensor, , , At Z2

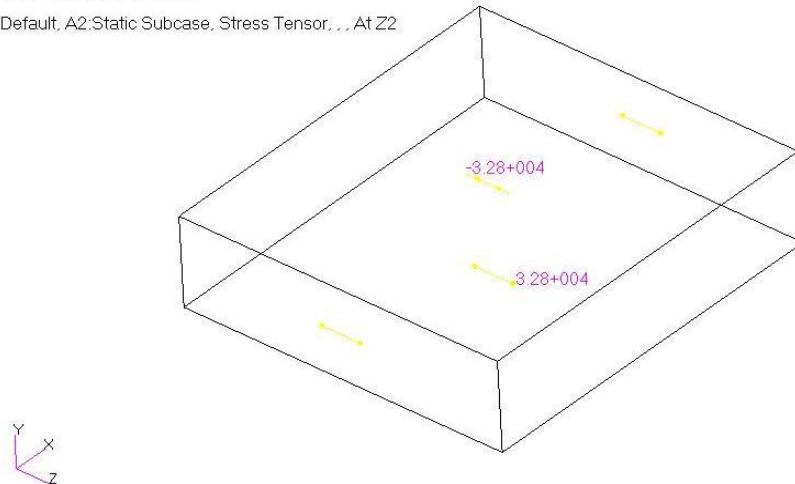


Figure 3.11: Axial Stresses Obtained by the Shell Elements at the Center of the Box Beam

The axial stresses on the middle surface of the upper and lower skin are -3.28×10^4 Pa and 3.28×10^4 Pa. These values are comparable to the results obtained by the beam bending theory.

Membrane Finite Element Results:

Axial stresses are determined by using membrane elements for the same element as the shell model. Figure 3.12 shows the axial stress on the upper and lower surfaces of the box beam. As one can see, the top and bottom surface stresses are the same. The stress 3.10×10^4 Pa is almost same as the grid point stress at node 308 of the fine mesh. This result is quite accurate and comparable to the axial stress determined by the beam theory.

Patran 2008r1 24-Jul-11 13:24:25
Tensor: Default, A1:Static Subcase, Stress Tensor, . . . At Z2

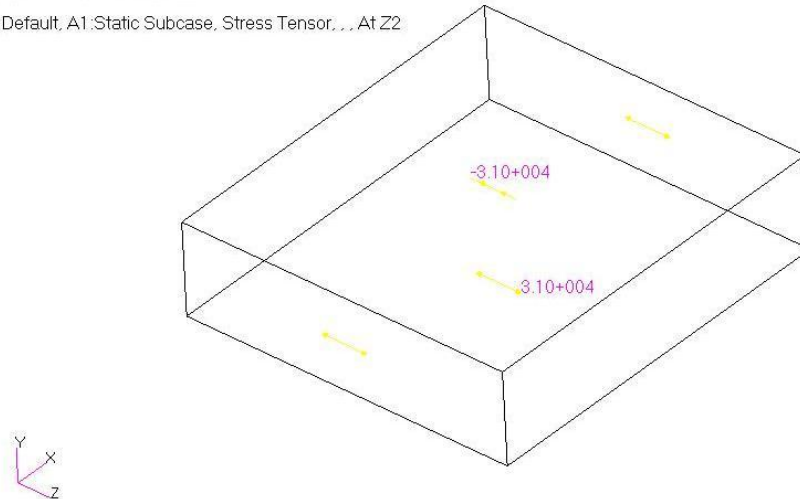


Figure 3.12: Axial Stresses Obtained by the Membrane Elements at the Center of the Box Beam

Comparison of the Displacement Plots

Figure 3.13 shows the deformation plot determined by shell elements. The maximum displacement is determined as 7.17×10^{-5} m.

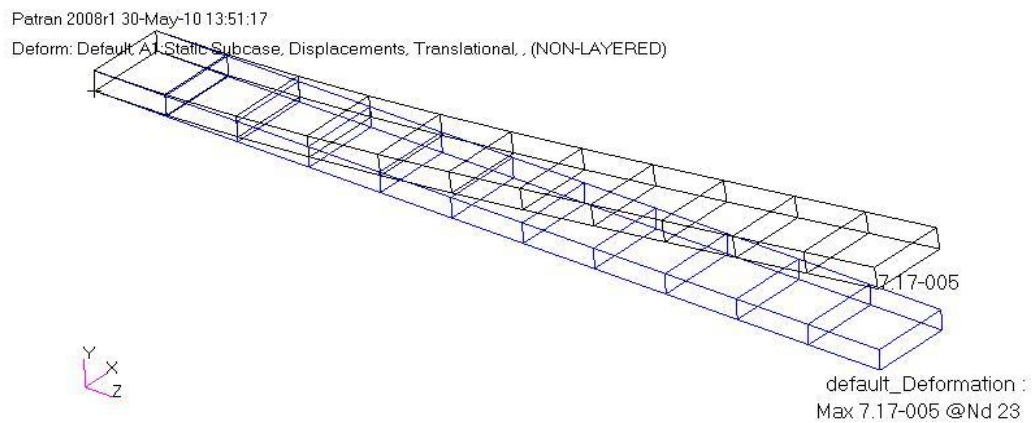


Figure 3.13: Deformation Plot of the Shell Model - One Shell Element in the Width Direction

Figure 3.14 shows the deformation plot determined by membrane elements. The maximum displacement is determined as 7.03×10^{-5} m.

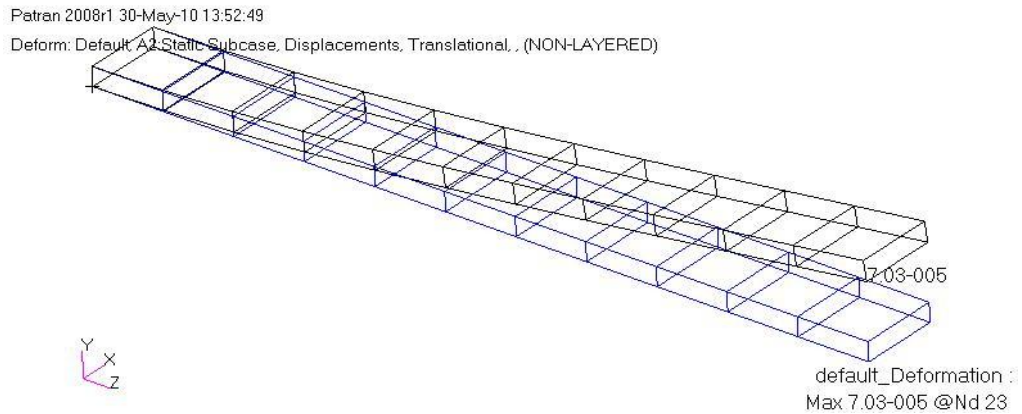


Figure 3.14: Deformation Plot of the Membrane Model - One Membrane Element in the Width Direction

Comments on the Results of Fine and Coarse Mesh:

As it can be seen, for the coarse mesh case deformation plots are almost same for the shell and membrane model. Maximum deformations determined by the coarse mesh shell and membrane models are also very close to the maximum deformation obtained by the fine mesh shell model. However, for the fine mesh case, the middle elements of the membrane model do not deform because pressure is an out-of-plane load and the out-of-plane displacements of the inner nodes are zero. For the membrane model, in the fine mesh case the actual load is only partially applied on the box beam. For the membrane model and the coarse mesh with 11 span-wise elements, maximum displacement is given by 7.03×10^{-5} m. For the fine mesh case, which has 40 span-wise elements, maximum displacement is given by 1.77×10^{-5} m (element size 0.05 x 0.05) by the membrane model. Ratio of the displacements is 3.97 which mean that the model which has fine mesh has 4 times lower external load, because in linear analysis load is proportional to displacement. To check if this is indeed the case, consider Figure 3.15 which shows membrane elements taken from the top skin of the box beam. In Figure 3.15, for the fine mesh case, the span-wise dimension is taken as the span-wise length of the membrane element of the coarse mesh.

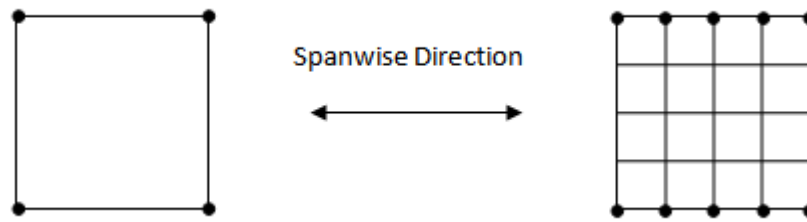


Figure 3.15: Membrane Elements Taken from the Top Skin of the Box Beam - Coarse and Fine Mesh

For the coarse mesh, for a pressure of P , the total load picked up by the four corner loads is $P * (0.2 * 0.2) = 0.04P$ where 0.2 m is the width of the box beam. However, for the fine mesh case only the nodes which are at the intersection with the webs, which are indicated by the dots in Figure 3.15, pick up the consistent loads, and the total load picked up by the nodes shown is given by:

$$P * [(0.05 * 0.05) / 4] * 8 * 2 = 0.01P$$

where *2 comes from the contribution from two side edges and *8 comes from the contribution from one edge. It should be noted that $P * 0.05 * 0.05$ is the total load on a single element of the fine mesh case, and the total load divided by 4 is the load on a corner node along the intersection the membrane element of the top skin with the membrane element on the side web. The ratio of the loads is exactly 4 which is almost same as the ratio of maximum deflections and also the ratio of the axial stresses. So, this example shows that when membrane elements are used in problems with out-of-plane loads, one has to be careful to make sure that the finite element model picks up the external loading accurately. In the single element case, in the width direction, pressure load is picked up by the corner nodes which can displace in the vertical direction because they are also the nodes of the elements on the side webs. Pressure load on the top or bottom skins act as in-plane load for the side web elements, therefore when single element is used in the width direction, the total external load is distributed to the box beam through the corner nodes accurately. In this particular problem, if one wants to use membrane elements, single element in the width direction gives the correct result, but any finer mesh with the use of more than one element in the width direction does not improve the accuracy but rather accuracy

becomes worse because the middle nodes do not react to the loads acting on them. Thus, the structure becomes too stiff.

3.4.3 Tip Force Loading

In case of a tip loading, a tip force of 5 N is applied at the lower skin of the box beam model as shown in Figure 3.16.

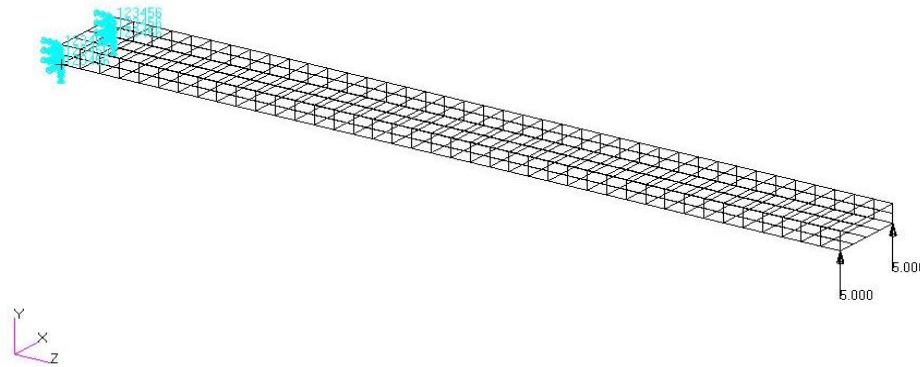


Figure 3.16: Tip Force Loading on Box Beam Model

Theoretical axial stresses are calculated using the classical beam theory. A tip force of 5 N is applied on the lower skin. Bending stress is determined on the top skin by the beam bending theory at a section 1 m away from the wing tip.

$$\sigma_1 = \frac{Mc}{I} = \frac{2 \times (5+5) \times 0.5 \times \left(\frac{0.05}{2}\right)}{8.134 \times 10^{-7}} = -307350 \text{ Pa} \quad (3.5)$$

where σ_1 is axial stress at the mid plane of the top skin

$$\sigma_2 = \frac{Mc}{I} = \frac{2 \times (5+5) \times 0.5 \times \left(\frac{0.05}{2} + \frac{0.003}{2}\right)}{8.134 \times 10^{-7}} = -325792 \text{ Pa} \quad (3.6)$$

where σ_2 is axial stress at the top surface of the top skin

$$\sigma_3 = \frac{Mc}{I} = \frac{2 \times (5+5) \times 0.5 \times \left(\frac{0.05}{2} - \frac{0.003}{2}\right)}{8.134 \times 10^{-7}} = -288910 \text{ Pa} \quad (3.7)$$

where σ_3 is axial stress at the bottom surface of the top skin

Case 1: Four Elements in the Width Direction

Shell Finite Element Results:

Axial stress results are obtained by the finite element model composed of shell elements. Stress monitor point is selected as node 308 which is at the mid span at (0.1, 0.05, 1.0) coordinates, and it is at the intersection of top skin elements 238, 239, 242 and 243 as shown in Figure 3.17.

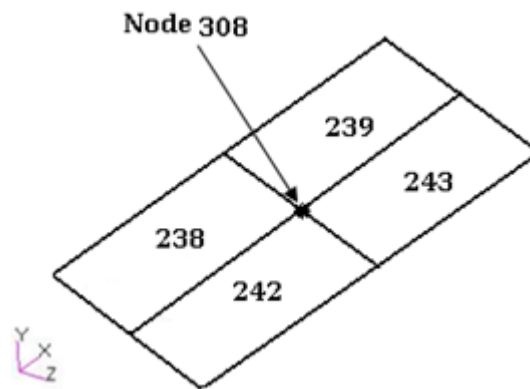


Figure 3.17: Shell Elements 238, 239, 242 and 243 and the Stress Monitor Point 308

The grid point stresses which are calculated at the node 308 from the adjoining plate elements are given as:

The stress at the top surface of the upper skin is $\sigma_{z_2} = -325800 \text{ Pa}$. On the other hand, the stress at the bottom surface of the upper skin is $\sigma_{z_1} = -288900 \text{ Pa}$ and the stress at the mid plane of the upper surface is $\sigma_{mid} = -307300 \text{ Pa}$.

The element stresses at the node 308 which is at the intersection of elements 238, 239, 242 and 243 are shown in Table 3.7 below.

Table 3.7: Shell Element Stresses at Node 308

Element ID	Node Id	Fiber Distance (m)	Stresses (Pa)
238	308	- 0.0015	- 296134
		0.0015	- 333931
239	308	- 0.0015	- 296134
		0.0015	- 333931
242	308	- 0.0015	- 218683
		0.0015	- 317647
243	308	- 0.0015	- 218683
		0.0015	- 317647

The average stress at a fiber distance of -0.0015m is -257408 Pa and the average stress at a fiber distance of 0.0015 m is -325789 Pa. These results are comparable to the beam theory results given above.

Membrane Finite Element Results:

Axial stress results, which are obtained by the finite element model composed of membrane elements, are shown below.

The grid point stresses which are calculated at the grid point 308 from the adjoining plate elements are as follow:

The stress at the top surface of the upper skin is $\sigma_{z_2} = -307700 Pa$. On the other hand, the stress at the bottom surface of the upper skin is $\sigma_{z_1} = -307700 Pa$ and the stress at the mid plane of the upper surface is $\sigma_{mid} = -307700 Pa$.

The element stresses at the node 308 of elements 238, 239, 242 and 243 are shown in Table 3.8.

Table 3.8: Membrane Element Stresses at Node 308

Element ID	Node Id	Fiber Distance (m)	Stresses (Pa)
238	308	- 0.0015	- 315385
		0.0015	- 315385
239	308	- 0.0015	- 315385
		0.0015	- 315385
242	308	- 0.0015	- 300000
		0.0015	- 300000
243	308	- 0.0015	- 300000
		0.0015	- 300000

The average stress at a fiber distance of -0.0015 m is -307693 Pa and the average stress at a fiber distance of 0.0015 m is -307693 Pa.

As shown in Figure 3.16, in case of tip loading from the skin-web intersection point's axial stress obtained by the membrane elements is close to the axial stress obtained by the shell elements.

Comparison of the Displacement Plots

Figure 3.18 shows the deformation plot determined by the finite element model of the box beam meshed with shell elements. The maximum displacement is determined as 5.82×10^{-4} m.

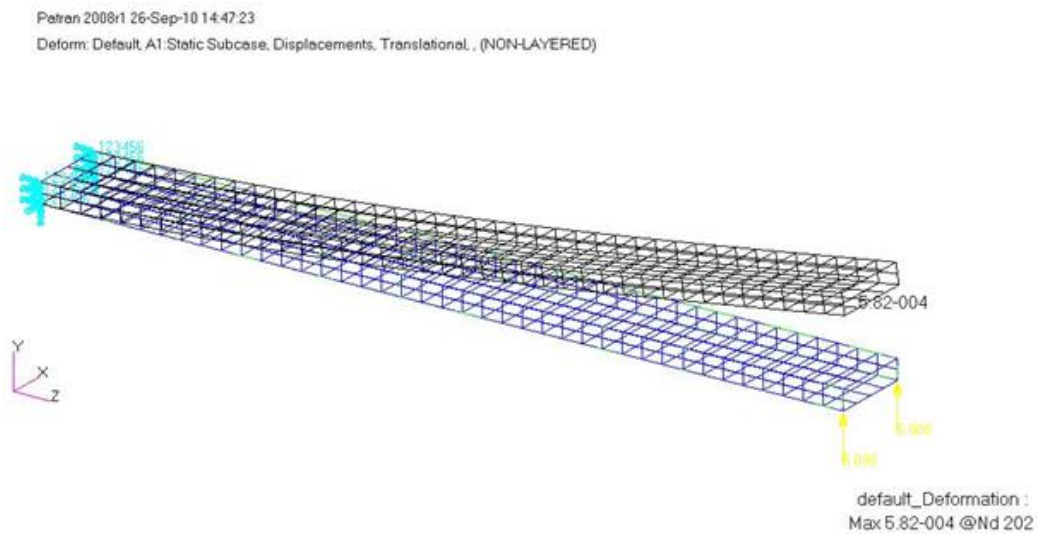


Figure 3.18: Deformation Plot of the Shell Model - Four Shell Elements in the Width Direction

Figure 3.19 shows the deformation plot determined by the finite element model of the box beam meshed with membrane elements. The maximum displacement is determined as 5.83×10^{-4} m.

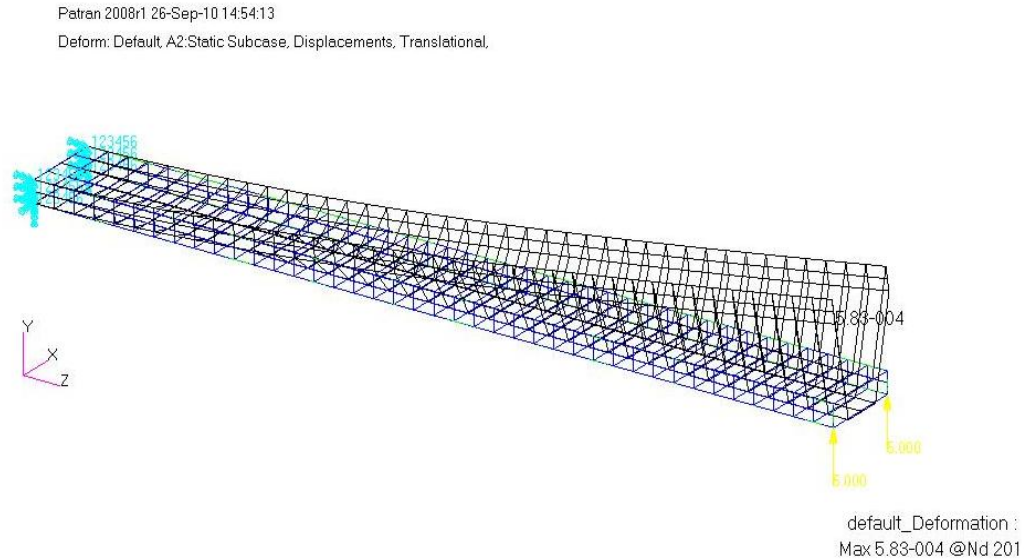


Figure 3.19: Deformation Plot of the Membrane Model - Four Shell Elements in the Width Direction

As one can see, in case of tip loading through the skin-web intersection nodes as shown in Figure 3.16, membrane elements gives very close results to the beam theory and shell finite element results. However, deformation plot of the model meshed with membrane elements show that although the maximum displacement is nearly same as the maximum displacement determined by the shell finite element model, those nodes which are not at the skin web intersection do not experience any deformation. Therefore, the deformed shape of the box beam is not predicted accurately by the membrane model. However, in this case since the tip loads act at the nodes which are at the skin-web intersections, these loads act like in-plane loads for membrane elements on the side webs. The in-plane degrees of freedom of the membrane elements on the side web take up the full external load and therefore external load is fully accounted for because of the existence of the web elements. Thus, axial stress and maximum displacement results are very close to the shell finite element model.

Case 2: One Element in the Width Direction

Shell Finite Element Results:

To make comparisons with the beam theory results, axial stress results, obtained by the use of shell elements in the model, are given for the element which is at the center of the beam. In this case box beam has 11 elements in the span-wise direction. Figure 3.20 shows the shell elements taken from the mid-section the box beam.

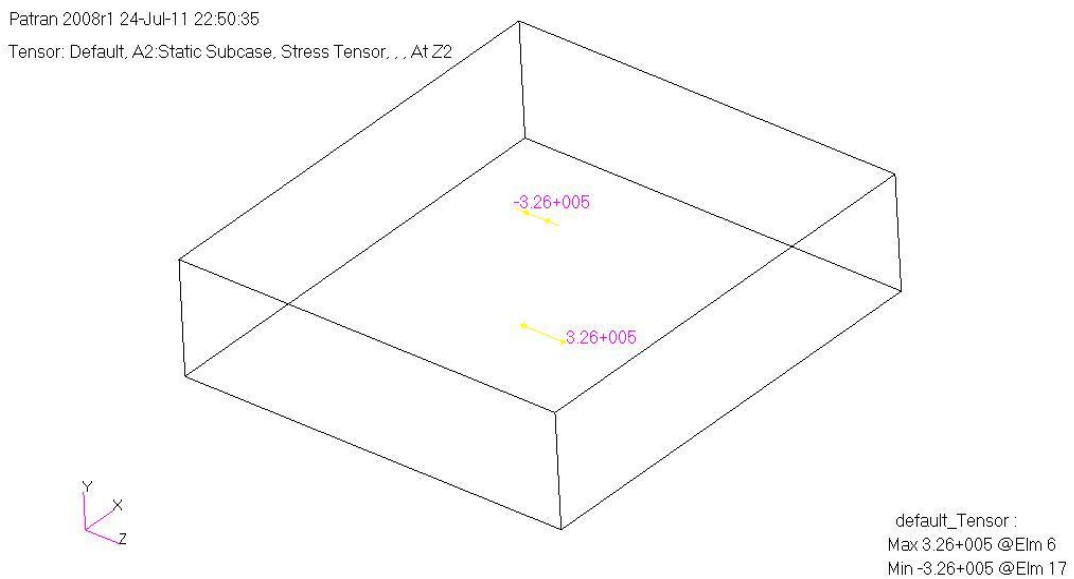


Figure 3.20: Axial Stresses Obtained by the Shell Elements at the Center of the Box Beam

The stresses -3.26×10^5 Pa and 3.26×10^5 Pa as can be seen in Figure 3.20 are comparable to the results found by the classical beam bending theory.

Membrane Finite Element Results:

Axial stresses are determined by using membrane elements for the same element as the shell model. Figure 3.21 shows the axial stress on the top and bottom surfaces. As one can see, the top and bottom surface stresses are the same. The stress 3.08×10^5 Pa is close to the grid point stress at node 308 of the fine mesh. This result is quite accurate and comparable to the axial stress determined by the beam bending theory.

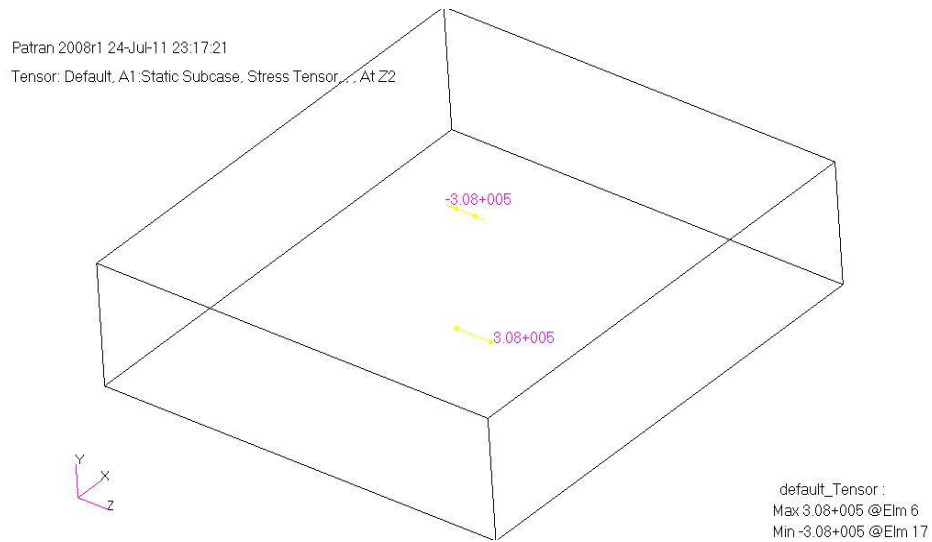


Figure 3.21: Axial Stresses Obtained by the Membrane Elements at the Center of the Box Beam

Comparison of the Displacement Plots

Figure 3.22 shows the deformation plot determined by shell elements. The maximum displacement is as 4.67×10^{-4} m.

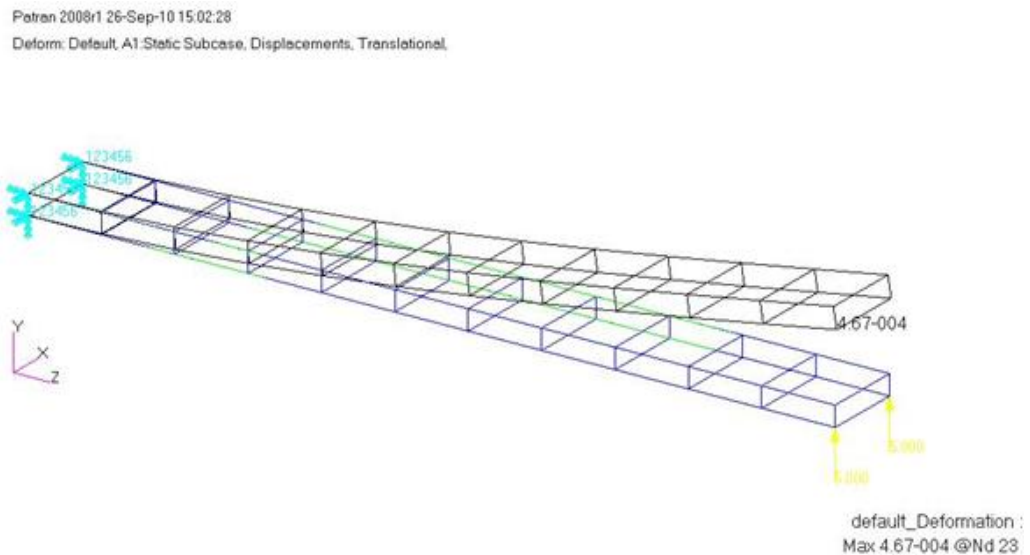


Figure 3.22: Deformation Plot of the Shell Model - One Shell Element in the Width Direction

Figure 3.23 shows the deformation plot determined by membrane elements. The max displacement is as 4.67×10^{-4} m.

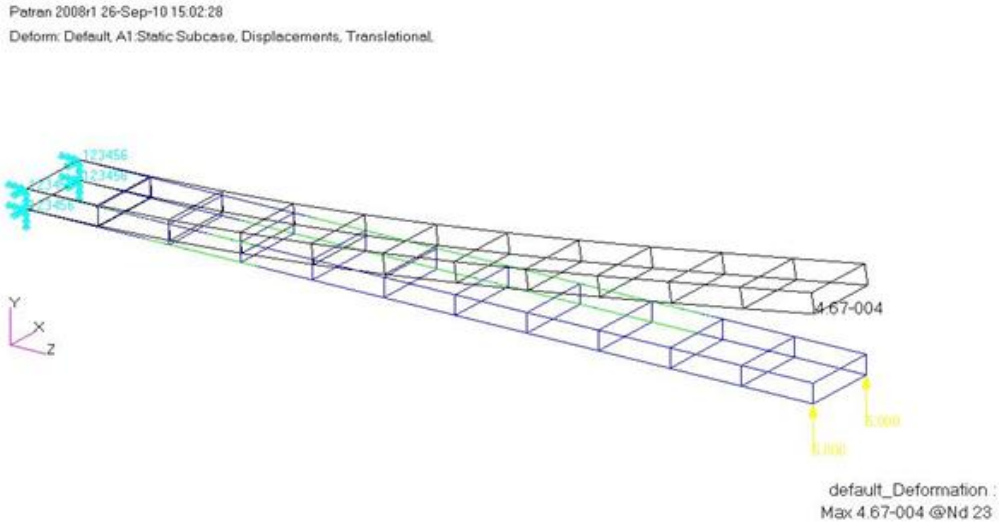


Figure 3.23: Deformation Plot of the Shell Model - One Membrane Element in the Width Direction

As one can see from the results of single element in the width direction, shell and membrane elements give similar stress and deflection results, as expected. The external tip loading is fully accounted for by the membrane elements for the box beam. However, coarse mesh box beam structure is stiffer; therefore the maximum displacements of the coarse mesh shell or membrane element models are slightly less than the maximum displacements of the fine mesh shell or membrane element models.

3.4.4 Tip Moments Producing Pure Torsion – Box Beam Model with Flanges

The box beam is modeled using membrane elements, and rod and beam elements are also used to model the flanges and a tip moment of a magnitude of 0.5 Nm is applied as shown in Figure 3.24. One element in width direction is used and no ribs are used in the box beam.

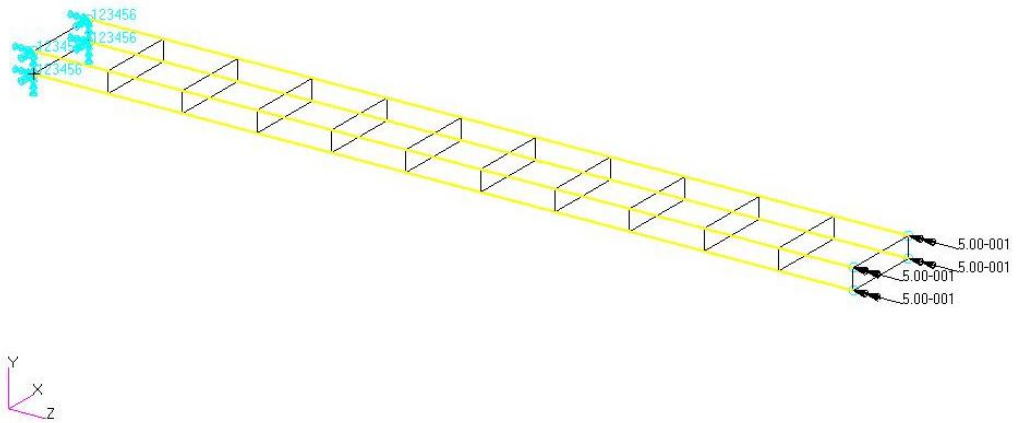


Figure 3.24: Tip Moment Loading on Box Beam Model with Flanges and No Ribs

The box beam model is analyzed using the membrane – rod finite element model and membrane – beam finite element model under pure pitching moment loading acting at the tip. By studying these two models, it is found that, although the rod and beam elements have torsional stiffness, both models could not handle the pure pitching moment loading resulting in zero deformation. As an example, Figure 3.25 shows the deformation plot for membrane – beam finite element model which does not experience any deformation. This example shows that having flanges elements with rotational degrees of freedom does not assure the load transfer to the membrane elements, because membrane elements do not have out-of-plane rotational degrees of freedom. Even though the beam elements have beam-axis rotational degrees of freedom, since the membrane elements joining the beam elements do not have the associated degrees of freedom the box beam does not deform.

Patran 2008r1 25-Jul-11 14:58:58

Fringe: Default, A2:Static Subcase, Displacements, Translational, Magnitude, (NON-LAYERED)

Deform: Default, A2:Static Subcase, Displacements, Translational.

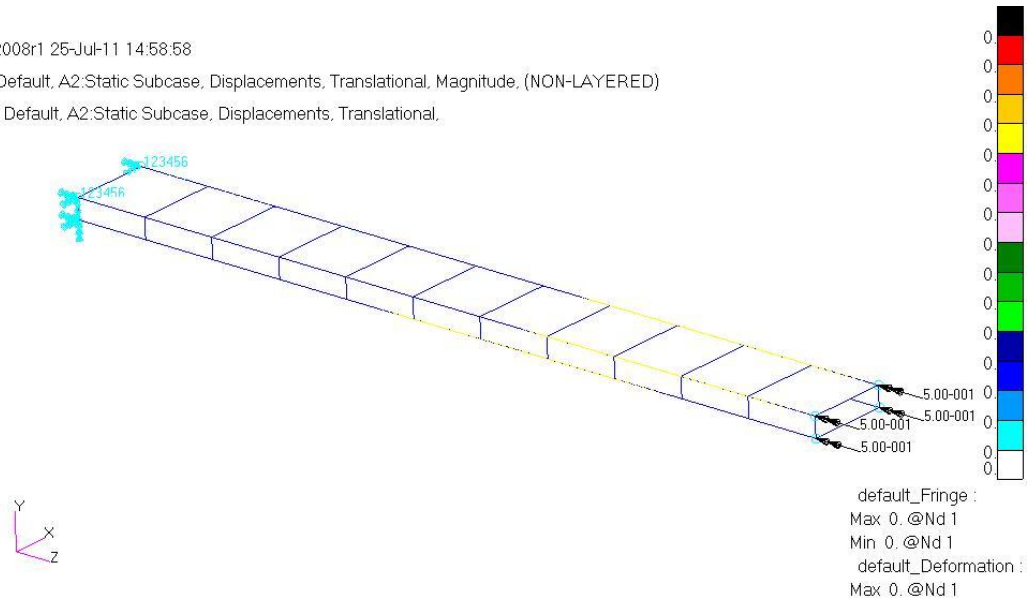


Figure 3.25: Deformation Plot of the Membrane - Beam Model - One Membrane Element in the Width Direction

3.4.5 Distributed Line Force Loading – Box Beam Model with Flanges and Ribs

The thin walled skin and webs of the box beam is modeled using membrane, membrane – r and shell elements, and rod and beam elements are used to model the flanges and six ribs are used dividing the beam box into five equal sections. A distributed line force (N/m) acting along the front spar is applied as shown in Figure 3.26.

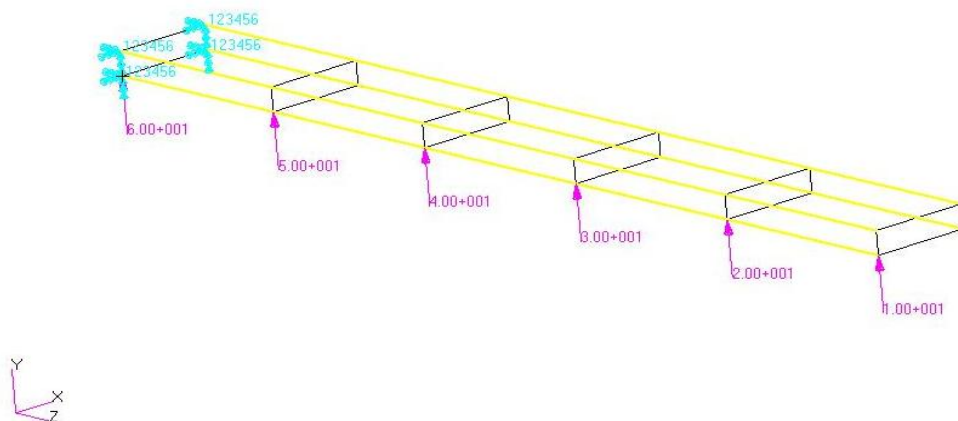


Figure 3.26: Distributed Line Force on the Box Beam Model

Case 1: One Element in the Width Direction

Shell and Membrane Finite Element Results:

The box beam model is studied for coarse mesh with a single element in the width direction and five elements in span-wise direction. Box beam shell and membrane models with flanges and ribs and without flanges or ribs are investigated in this study to have a clear idea on the correct element type to use in the finite element model. The results of all models show that as long as there are side webs, the external line load is fully accounted for by the use of shell and/or membrane elements. All three models give very close axial stress and deflection results.

Figure 3.27 and 3.28 show the deformation plots of box beam shell and membrane models without flanges but ribs.

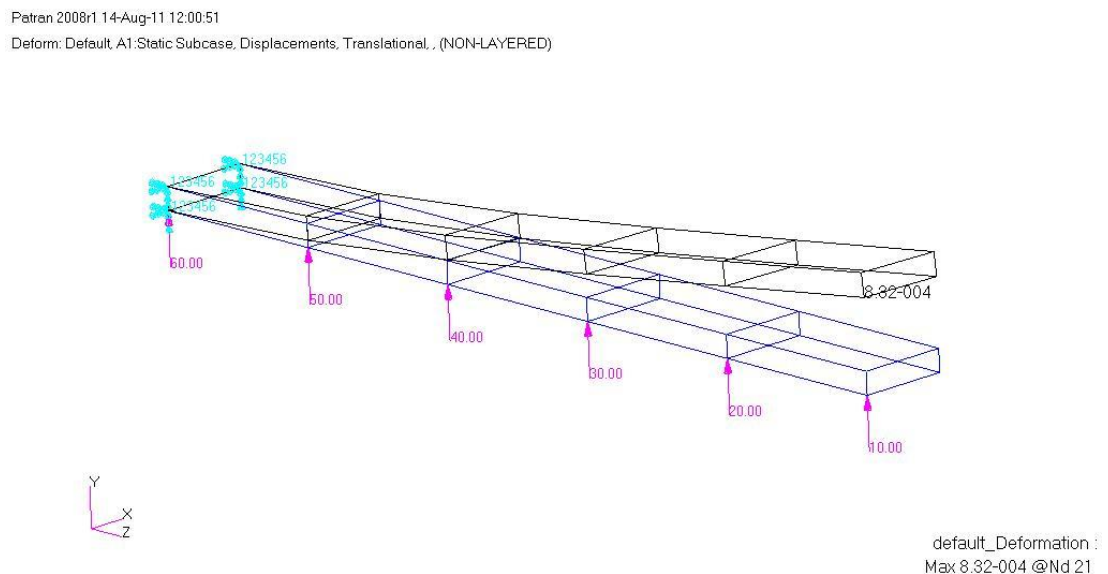


Figure 3.27: Deformation Plot of the Membrane Model Under Distributed Line Force – One Element in the Width Direction

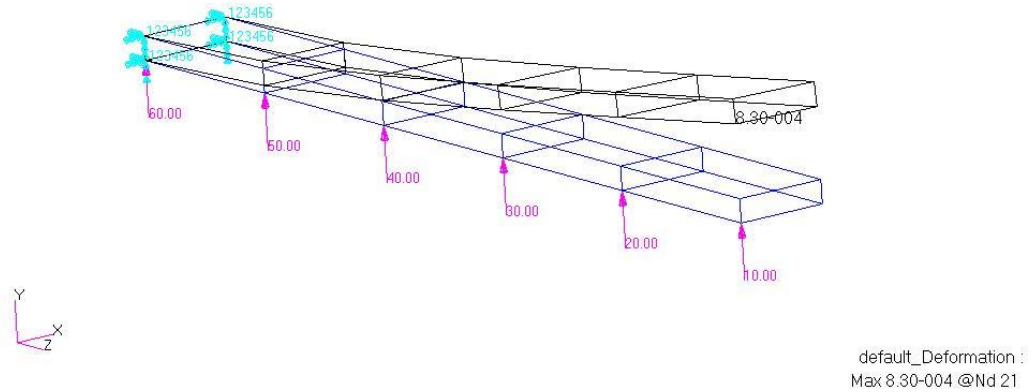


Figure 3.28: Deformation Plot of the Shell Model Under Distributed Line Force - One Element in the Width Direction

As it can be seen from Figures 3.27 and 3.28 the maximum displacements are 8.32×10^{-4} m and 8.30×10^{-4} m for box beam shell and membrane models respectively. In this particular example, consistent nodal loads calculated due to distributed line loading acting through the side web, are fully accounted for with the membrane elements on the side webs.

Case 2: Four Elements in the Width Direction and Between the Ribs

Shell and Membrane Finite Element Results:

The same box beam model is studied for the finer mesh case with four elements in the width direction and between the ribs. For the fine mesh case, deformation shape of the membrane and membrane - r model in the width direction does not reflect the true deformation as can be seen from Figures 3.29 and 3.30. Middle elements in the width direction does not deform in the out of plane direction. In addition, although there is line loading through the side web, there is little twisting of the box beam even with shell elements. Since in this case, the ribs provide additional torsional stiffness which reduces the twisting.

Patran 2008r1 14-Aug-11 12:11:57
Deform: Default, A1:Static Subcase, Displacements, Translational, (NON-LAYERED)

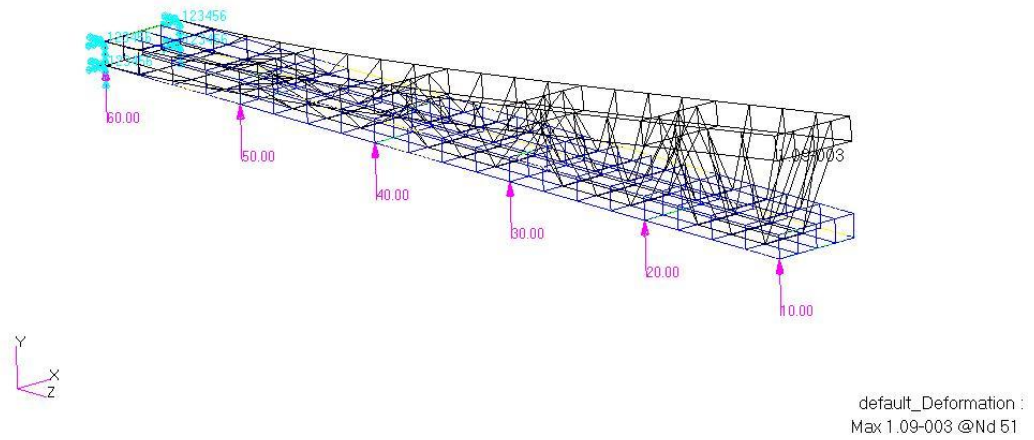


Figure 3.29: Deformation Plot of the Membrane Model Under Distributed Line Force - Four Elements in the Width Direction and Between the Ribs

Patran 2008r1 14-Aug-11 12:18:51
Deform: Default, A1:Static Subcase, Displacements, Translational, (NON-LAYERED)

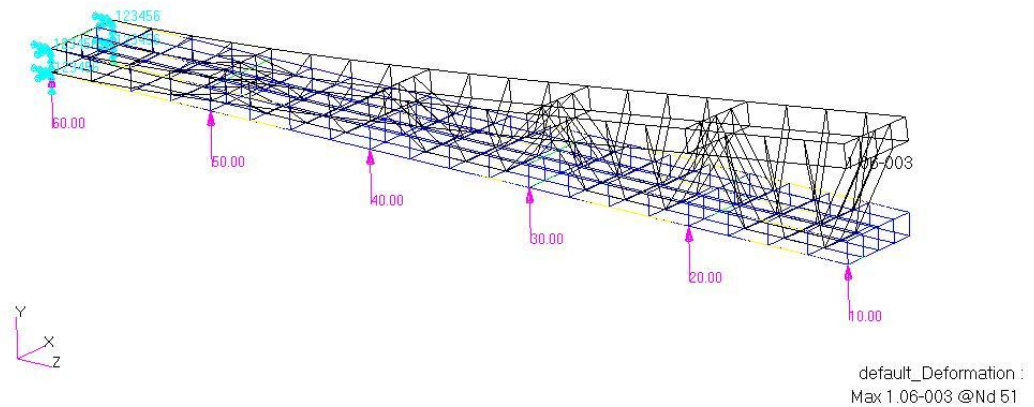


Figure 3.30: Deformation Plot of the Membrane - R Model Under Distributed Line Force - Four Elements in the Width Direction and Between the Ribs

This example shows that although the maximum displacement of the fine mesh case is similar to the coarse mesh case, the deformed shape is not the true deformed shape. Again, the use of fine mesh finite element model with membrane elements does not

improve the accuracy of the finite element solution, but makes it even worse. Also in this problem since the line load acting through the side web is an in-plane load for the membrane elements on the side web, the use of membrane elements with drilling degrees of freedom does not produce any appreciable effect on the deformed shape of the box beam.

3.4.6 Distributed Line Pitching Moment Loading

For this load case, the box beam is modeled using membrane elements and six ribs are used dividing the beam box into five equal sections. A distributed line pitching moment (Nm/m) acting along the front spar is applied, as shown in Figure 3.31.

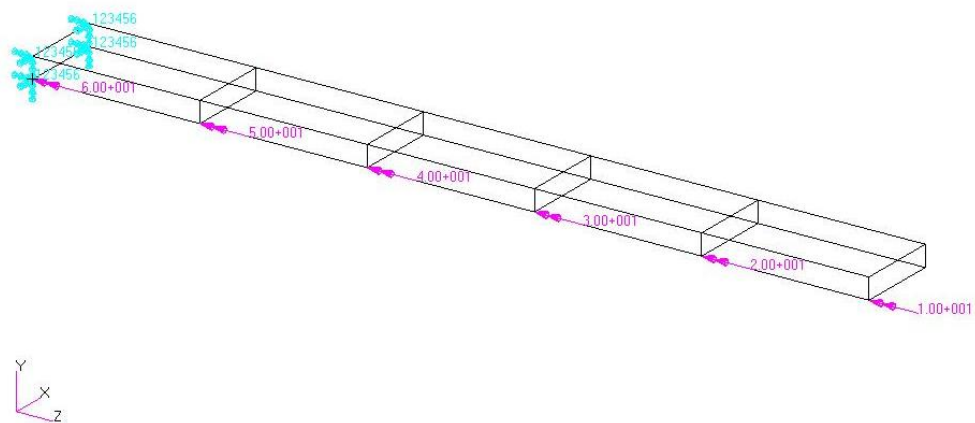


Figure 3.31: Distributed Line Pitching Moment Acting on the Box Beam Model

The box beam model is studied using membrane elements and revised formulation of membrane elements denoted by membrane - r which also has drilling degrees of freedom.

Case 1: One Element in the Width Direction and One Element Between the Ribs

Membrane and Membrane-R Finite Element Results:

The box beam finite element model is prepared using coarse mesh with a single element in the width direction and five elements in the span-wise direction. The membrane and membrane – r models are studied under line pitching moment loading

Case 2: Four Elements in the Width Direction and Four Elements Between the Ribs

Membrane and Membrane-R Finite Element Results:

The box beam model is studied for the fine mesh case with four elements in the width direction. The membrane and membrane – r models are loaded by the line pitching moment and deformation plots are obtained. As it can be seen from Figures 3.34 and 3.35, box beam model with membrane elements cannot handle the line pitching moment because the box beam does not deform. On the other hand, membrane – r model deforms and that gives us an indication that it can handle the line pitching moment also for the fine mesh case.

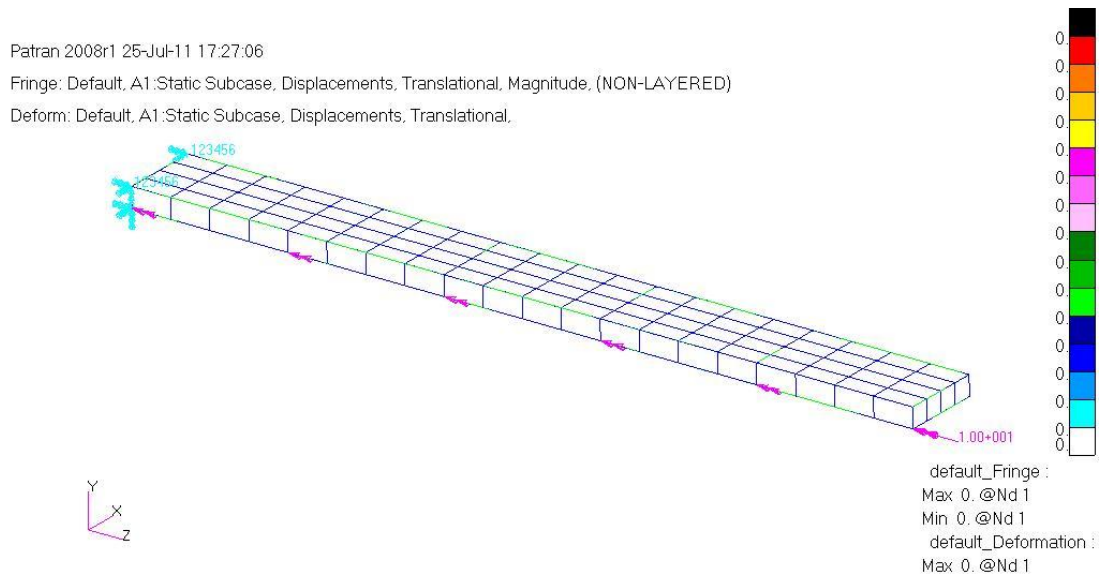


Figure 3.34: Deformation Plot of the Membrane Model Under Distributed Line Pitching Moment - Four Elements in the Width Direction

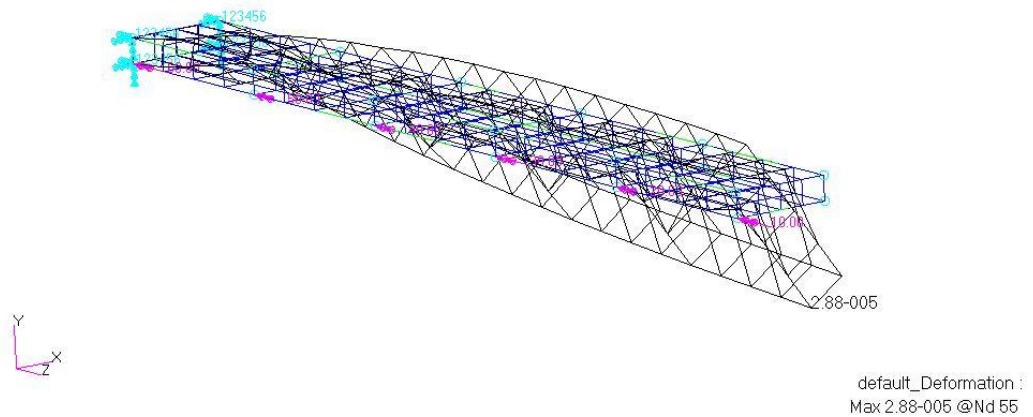


Figure 3.35: Deformation Plot of the Membrane - R Model Under Distributed Line Pitching Moment - Four Elements in the Width Direction

It should be noted that when four elements are used between the ribs, for the box beam model without flanges, the maximum deformation is approximately 4.6 times less compared to the maximum displacement of the single element case between the ribs. The reason for this is that when single element is used between the ribs, consistent nodal in-plane bending moments have their associated drilling degrees of freedom on the membrane elements on the ribs. Therefore, the external loading is handled accurately. However, when four elements are used between the ribs, consistent nodal in-plane bending moments for the nodes between the ribs do not have their associated degrees of freedom because nodal pitching moment acts like out-of-plane bending moment for the nodes of membrane elements on the front spar web and on the lower wing skin. Therefore, consistent nodal moments acting on the nodes which are between the rib stations are not carried by the box beam. For the four element case, the resulting deformation is due to the consistent moments acting on the nodes at the intersection of the front spar web and the ribs. Since the element length is small for the four element case, consistent nodal moments are also small and that is why the fine mesh model deforms less compared to the course mesh case.

By considering the results of the studies carried out by using different finite element types and while being under different loading condition, it is important to clarify the following points.

First, in the case of a distributed line force loading condition, shell elements handles this type of loading just right for both coarse and fine mesh. In the case of membrane and membrane – r elements, they are able to handle the distributed line force loading correctly for coarse mesh only with single element in width direction. Unfortunately, membrane and membrane – r elements do not reflect the true deformation of a model but still can reflect close results for axial stresses.

Second, in the case of a distributed line pitching moment loading condition, shell elements handle this type of loading just right for both coarse and fine mesh. In the case of membrane – r element, it is able to handle the distributed line pitching moment correctly for the coarse and the fine mesh models. On the other hand, finite element models with membrane elements without the use of revised formulation fail to handle this load for both coarse and fine mesh cases.

So in the case of a combined loading condition of distributed line force and distributed pitching moment, shell elements work well for both coarse and fine mesh models. Only membrane – r elements with coarse mesh (one element in width direction and between the ribs) can handle this loading. One last comment is that in revised formulation membrane elements are used in the finite element model, ribs are necessary to account for the distributed line pitching moment. Thus, the examples studied so far have shown that if membrane elements are to be used in the finite element model, the distributed line lift and pitching moment loading that is calculated by the ESDU 95010 can only be handled accurately if revised formulation is used and when ribs exist. It should be noted that in wing structures always have ribs, so the use of membrane elements in the finite element model can be justified as long as right kinematic description is used depending on the external loading acting on the structure.

3.5 Finite Element Modeling of Wing Torque Boxes

To get prepared for the optimization study which is given in Chapter 4, in this section finite element models are prepared using different element pairs to model the semi-monocoque wing torque box. The wing torque box is modeled using the MSC®/PATRAN software. Different finite elements types are used to create six different models. The correct use of element types depends on the type of loading that the structure carries. In the current study, lift and pitching moment loads are considered as line loading acting along the spar of the wing. Therefore, thin sheet panels of wing torque box are modeled using shell elements, revised formulation of shell element and revised formulation of membrane elements which take the drilling degrees of freedom into account.

Revised formulation is required to be used with the membrane elements in the wing ribs, because the external pitching moment, which is calculated by ESDU 95010, is a line load which can not be handled by the standard membrane elements accurately, as discussed in the previous sections for the box beam example.

On the other hand, stringers and spar caps are modeled with beam and rod elements. For the particular line loading used in this study, the use of shear panels also does not work because the shear panels can not handle the distributed pitching moment the same way as the membrane elements with no drilling degrees of freedom.

Table 3.9 shows the element pairs that are used to model two dimensional and one dimensional members of the wing structure.

Table 3.9: Combination of Element Types Used in Modeling the Wing Torque Box

Model	Thin Walled Panels	Spar Caps and Stiffeners
1	Shell Element (CQUAD4)	Rod Element (CROD)
2	Shell Element (CQUAD4)	Beam Element (CBAR)
3	Shell-R Element (CQUADR)	Rod Element (CROD)
4	Shell-R Element (CQUADR)	Beam Element (CBAR)
5	Membrane-R Element (CQUADR)	Rod Element (CROD)
6	Membrane-R Element (CQUADR)	Beam Element (CBAR)

3.5.1 Structural Model

The structural models of the wing torque boxes are created using MSC®/PATRAN software. The model consists of 71 surfaces including the upper skin surfaces and 36 curves are used to represent spars and stiffeners. Figure 3.36 shows the surface model of the wing torque box.

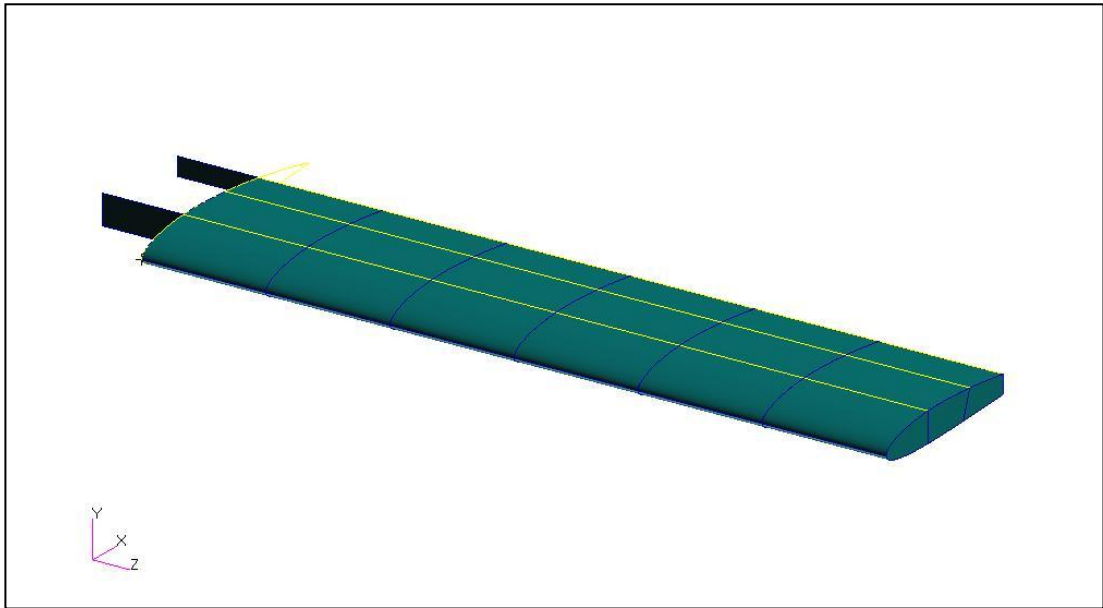


Figure 3.36: Surface Model of the Wing

Figure 3.37 gives the surface model of the internal structure of the wing which includes ribs, spar webs, spars and stiffeners arrangements.

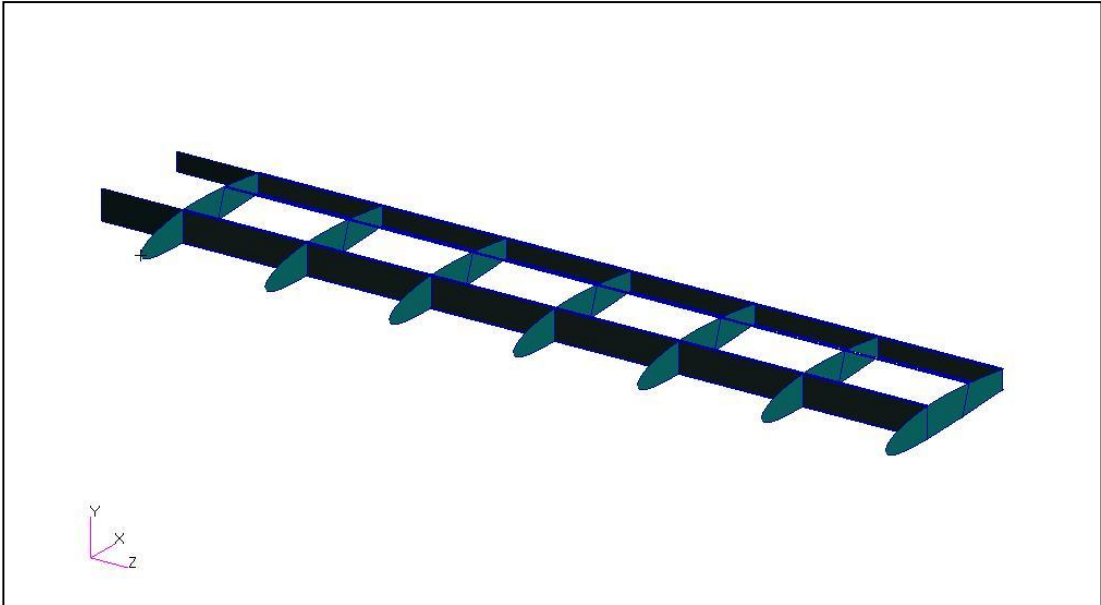


Figure 3.37: Surface Model of the Internal Structure of the Wing

Figure 3.38 shows the surface of upper and lower skins of the wing.

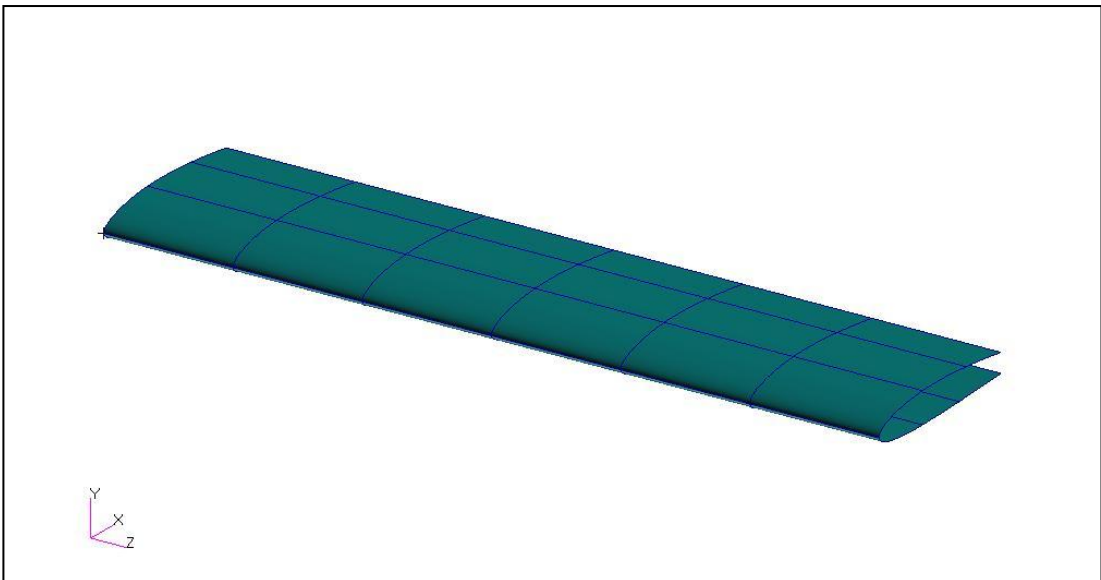


Figure 3.38: Upper and Lower Surfaces of the Wing Structure

Figure 3.39 shows the surface model of the ribs of the wing structure which also includes the nose ribs and mid ribs.

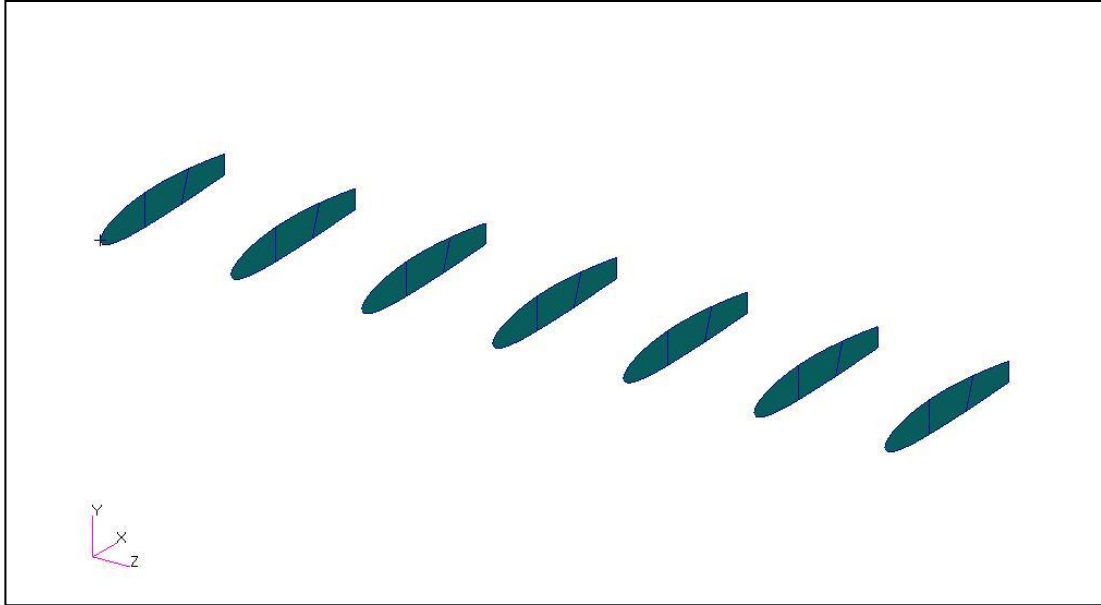


Figure 3.39: Surface Model of the Ribs

3.5.2 Mesh Convergence Study

Before performing the finite element analysis of the wing structure models, it is important to guarantee that the model contains a sufficient number of elements in order to arrive to the correct solution. So in order to the solution obtained to be as close as to reality, solutions should be obtained from several meshes starting from a low density mesh model referred to as the very coarse mesh and finishing with a high density mesh model referred to as the very fine mesh. While preparing the wing torque box models for the analysis solutions the mesh has been made coarser and finer to evaluate mesh convergence. Six different mesh size models are prepared. The first model is the coarsest mesh model that is generated by using a single element between the ribs. In the coarsest mesh, the total number of one dimensional and two dimensional elements is 107. The second model is a coarser mesh model with a total number of 531 one dimensional and two dimensional elements. The third model is the coarse mesh model and it contains a total number of 819 of one

dimensional and two dimensional elements. The fourth model is a fine mesh model with a total number of 1984 elements. The fifth model is a finer mesh model with a total number of 2416 elements and the last finest mesh model consists of 3097 elements intotal.

Mesh converging testing is performed for all pairs of elements as mentioned in Table 3.10 that is used in the analysis part. In the convergence study, tip displacement and Von Mises stress results of the wing are used as the parameter to monitor the effect of using different mesh sizes and ensure that a convergence solution is achieved.

Figures 3.40, 3.41 and 3.42 show the finite element mesh cases of the wing structure.

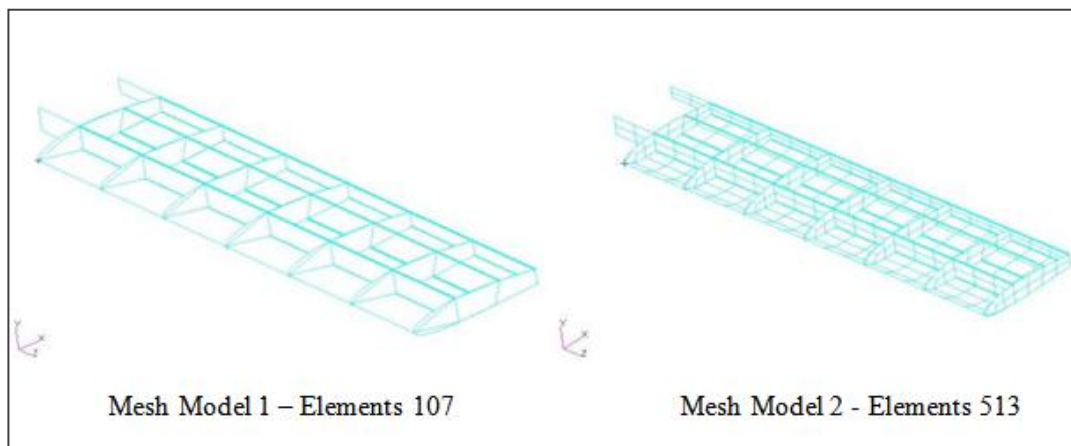


Figure 3.40: 1st and 2nd Mesh Models of the Wing Structure

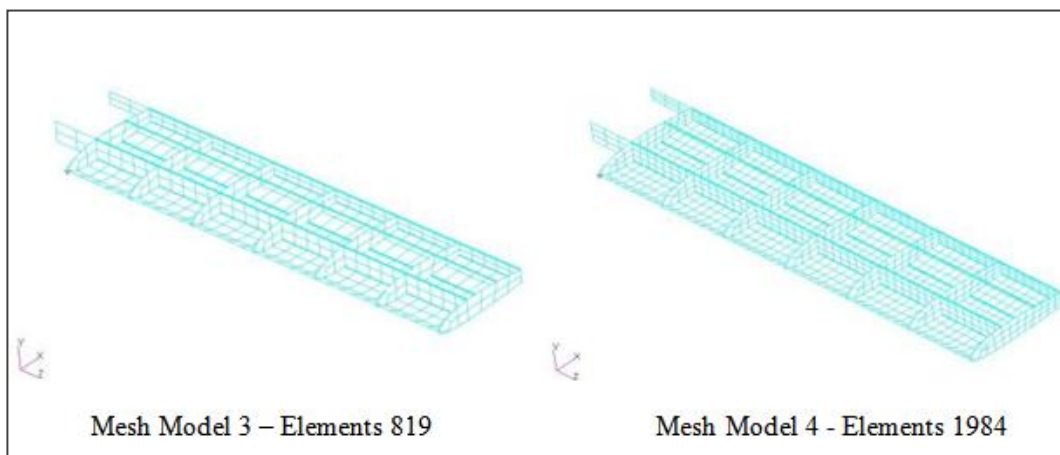


Figure 3.41: 3rd and 4th Mesh Models of the Wing Structure

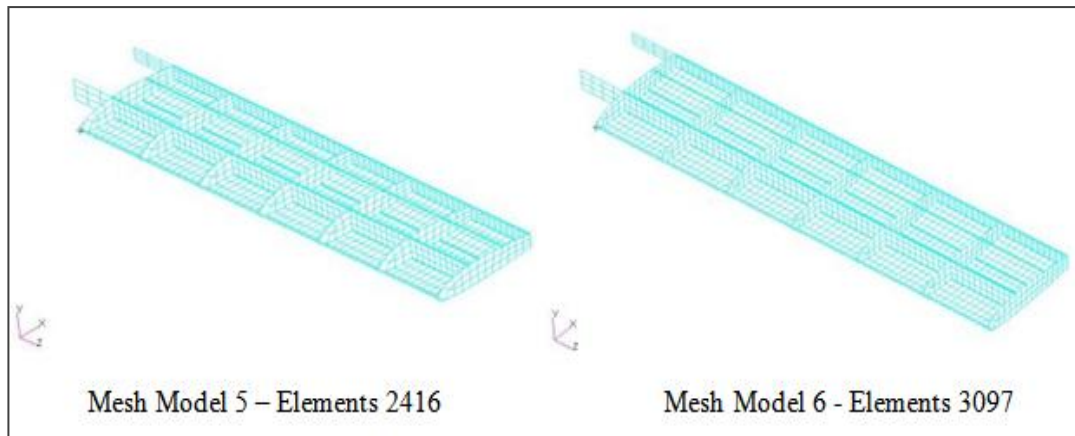


Figure 3.42: 5th and 6th Mesh Models of the Wing Structure

Table 3.10 summarizes the maximum tip displacement and Von Mises stress results obtained at the center of the middle upper skin, (Figure 2.34) of bay 4 (Figure 2.25) in chapter 2, for rod/shell model with six mesh density cases.

Table 3.10: Comparisons of Maximum Tip Displacement and Von Mises Stress – Six Mesh Cases

Mesh Density	Tip Displacement (cm)	Von Mises Stress (MPa)
Model 1 - Coarsest	18.5	40.35
Model 2 - Coarser	17.4	25.78
Model 3 - Coarse	17.5	24.37
Model 4 - Fine	18.1	27.21
Model 5 - Finer	18.2	26.54
Model 6 - Finest	18.4	25.83

Results in Table 3.10 shows converged solutions are achieved in terms of tip displacement and Von Mises stresses. As expected, even with the coarse mesh, converged solution is reached. In the current study, the results of the coarsest mesh and the finest mesh finite element models are used to make comparative study with the results of the simplified method of analysis using structural idealizations 1 and 2. It should be noted, a solution is considered to be converged one while it is nearly independent of meshing errors, and a very coarse mesh will always give a very approximate solution which is in a way or another can be far away from the real

solution. As the mesh is refined by reducing the size of elements in a model the solution will gradually approaches a solution that can be considered very close to the exact solution.

3.6 Analysis of Wing Torque Box Finite Element Models

Structural analysis of the designed wing structure is performed by the finite element analysis software MSC.NASTRAN®. The loading and boundary conditions are as described previously in (Figure 3.2). The analysis study is performed using the six different models previously defined in Table 3.9. The main objective of this study is to investigate the effect of using different finite element types on the analysis results which include deformation results, Von Mises stresses and axial stresses for both coarse and fine mesh models.

3.6.1 Analysis Results of Rod – Shell Finite Element Model

The semi-monocoque wing structure is modeled using 1D rod and 2D Shell element pairs, and coarse and fine mesh FE models are analyzed. Figures 3.43 and 3.44 show the deformation plots of fine and coarse mesh wing torque box models.

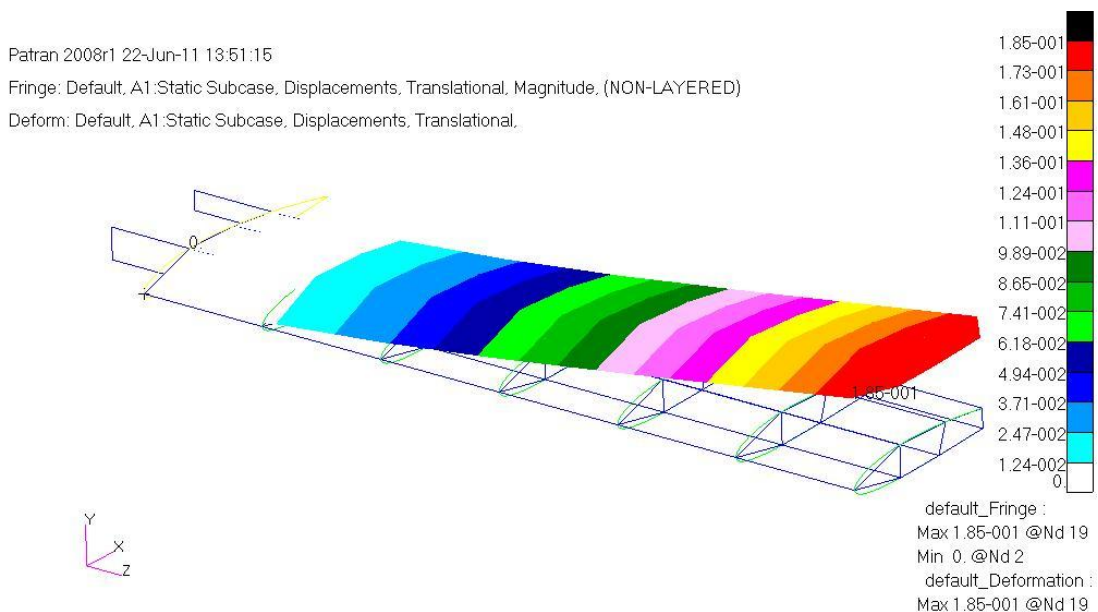


Figure 3.43: Deformation Plot of the Wing for the Coarse Mesh Case Rod/Shell Model

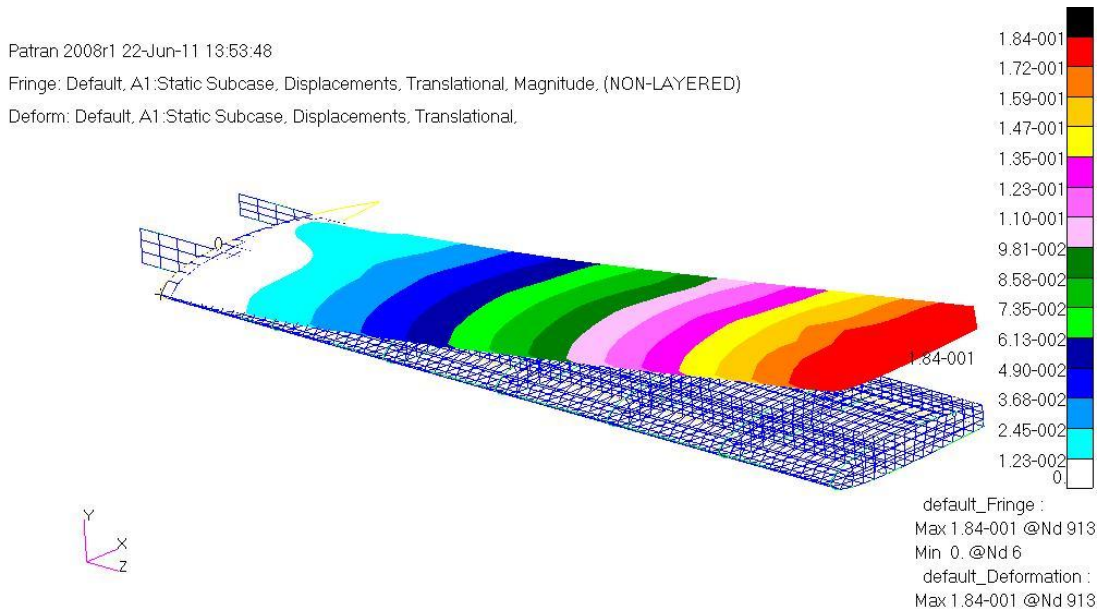


Figure 3.44: Deformation Plot of the Wing for the Fine Mesh Case Rod/Shell Model

The maximum tip displacement is determined as 18.5 cm and 18.4 cm for the coarse and the fine mesh cases, respectively. On the other hand, Figures 3.45 and 3.46 give the Von Mises stress plots as seen from Figures 3.45 and 3.46, Von Mises stress values are high at the root region of the wing and they decrease towards the tip of the wing. However, as one can see from the color scales of the Von Mises stresses in Figures 3.45 and 3.46, maximum Von Mises stress of the fine mesh case is 5 times higher than the Von Mises stress of the coarse mesh. However, maximum Von Mises stress is confined to the front spar – wing root intersection and away from the restraint end, if one looks at the color scales carefully, it can be seen that there is no big difference between the Von Mises stresses determined by the coarse and fine mesh models.

Patran 2008r1 18-May-11 01:04:31

Fringe: Default, A1:Static Subcase, Stress Tensor, , von Mises, At Z2

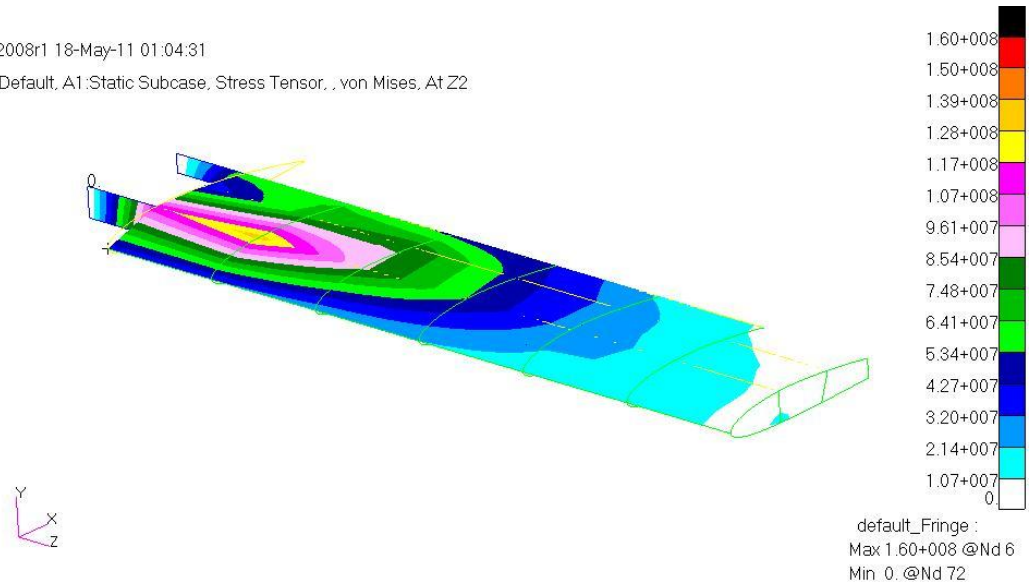


Figure 3.45: Von Mises Stress Distribution on the Shell Elements for the Fine Mesh
Case - Rod/Shell Model

Patran 2008r1 18-May-11 01:15:20

Fringe: Default, A1:Static Subcase, Stress Tensor, , von Mises, At Z2

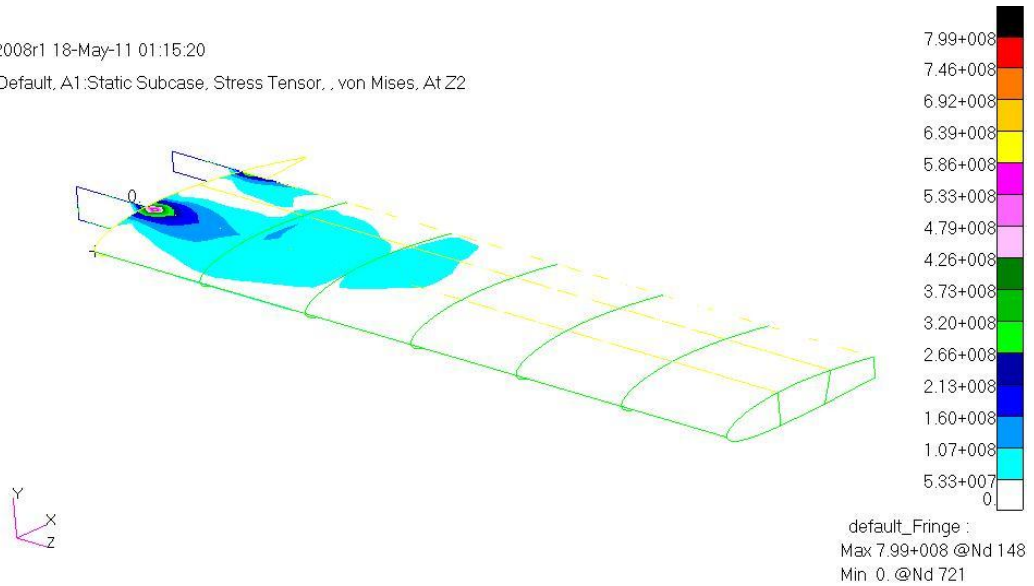


Figure 3.46: Von Mises Stress Distribution on the Shell Elements for the Fine Mesh
Case - Rod/Shell Model

Table 3.11 shows the Von Mises stresses results for rod/shell model away from the restraint end on the upper middle skin. Stresses are calculated at the center of bays 2-5 in both coarse and fine mesh solutions.

Table 3.11: Comparison of Von Mises Stress on the Top Middle Skin of the Rod/Shell Model

Von Mises Stresses (MPa)				
Mesh Type	Bay 2	Bay 3	Bay 4	Bay 5
Coarse	125.50	77.89	40.35	18.49
Fine	81.40	57.95	25.83	11.12

Table 3.11 shows that Von Mises stresses calculated by the fine mesh finite element models are actually lower than the Von Mises stresses calculated by the coarse mesh models at the identical locations on the wing structure. However, since fine mesh finite element models capture the stress gradients better, the maximum stresses predicted by the fine mesh models are usually higher than the maximum stresses predicted by the coarse mesh models. A more thorough interpretation of the results is given in Section 3.7.4.

Figures 3.47 and 3.48 give the axial stresses on the upper front spar and on the upper middle stiffener for both coarse and fine mesh models for bays 2 - 5. It should be noted that in the case of a coarse mesh each flange is modeled with a single CROD element in each bay, whereas in the fine mesh case, in each bay each flange consists of 11 elements, and the axial stresses plotted for the fine mesh case in Figures 3.47 and 3.48 are for the middle element in the bays.

Axial stresses acting on both flanges are compression stresses and as it can be seen from Figures 3.47 and 3.48, axial stresses are high at the region closer to the root of the wing (bay 2) and they decrease towards wing tip in both fine and coarse mesh models. It is also noted that similar to the results obtained for the Von Mises stresses, axial stresses predicted by the fine mesh model, on the upper flange of the front spar, are lower than the axial stresses predicted by the coarse mesh model at the identical locations on the flange.

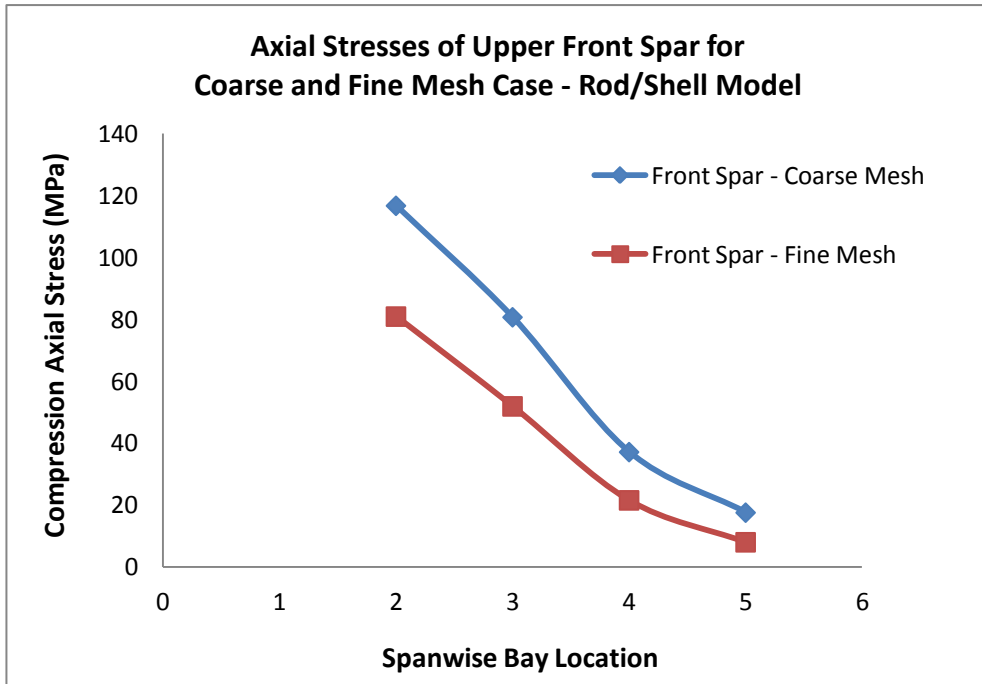


Figure 3.47: Axial Stress Distribution on the Front Spar Upper Flange for the Coarse and the Fine Mesh Cases – Rod/Shell Model

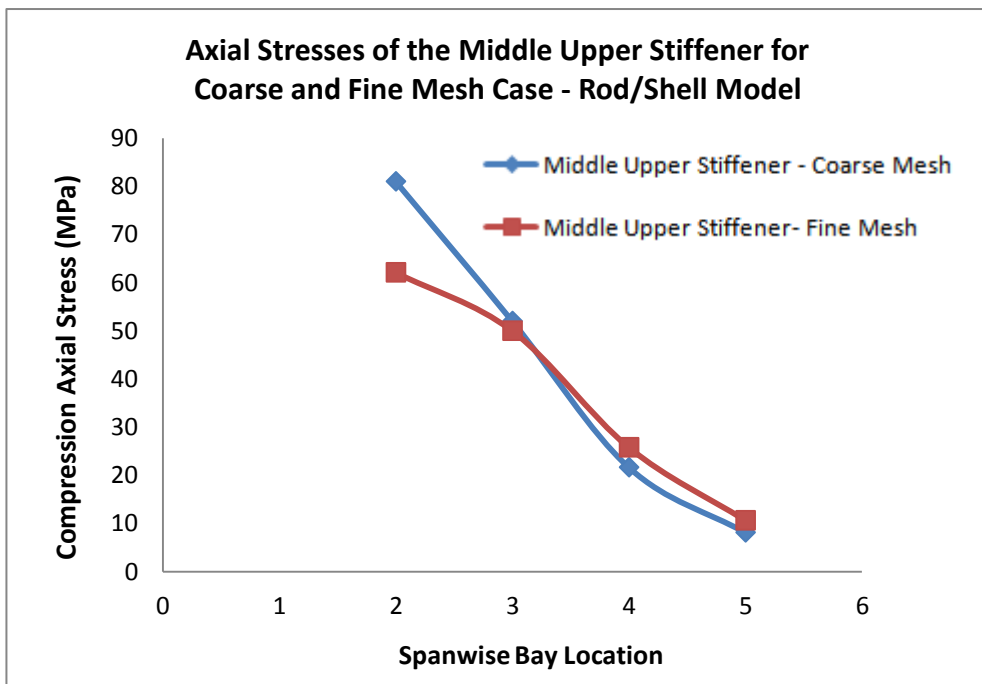


Figure 3.48: Axial Stress Distribution on the Upper Middle Stiffener for the Coarse and the Fine Mesh Cases – Rod/Shell Model

3.6.2 Analysis Results of Beam – Shell Finite Element Model

The semi-monocoque wing structure is modeled using 1D beam and 2D Shell element pairs, and coarse and fine mesh FE models are analyzed. Figures 3.49 and 3.50 show the deformation plots of fine and coarse mesh wing torque box models.

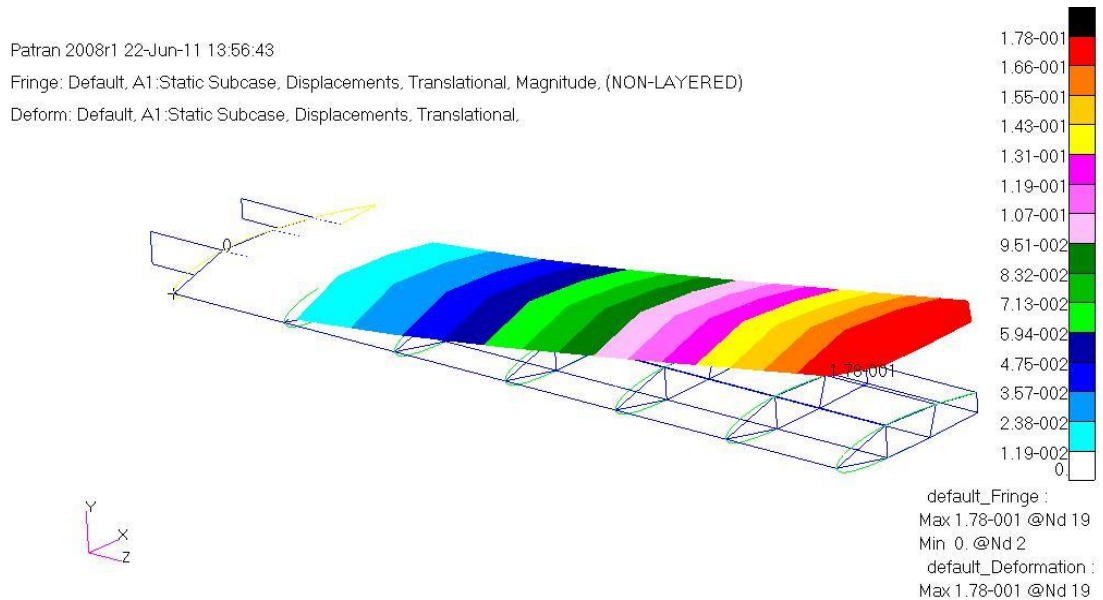


Figure 3.49: Deformation Plot of the Wing for the Coarse Mesh Case Beam/Shell Model

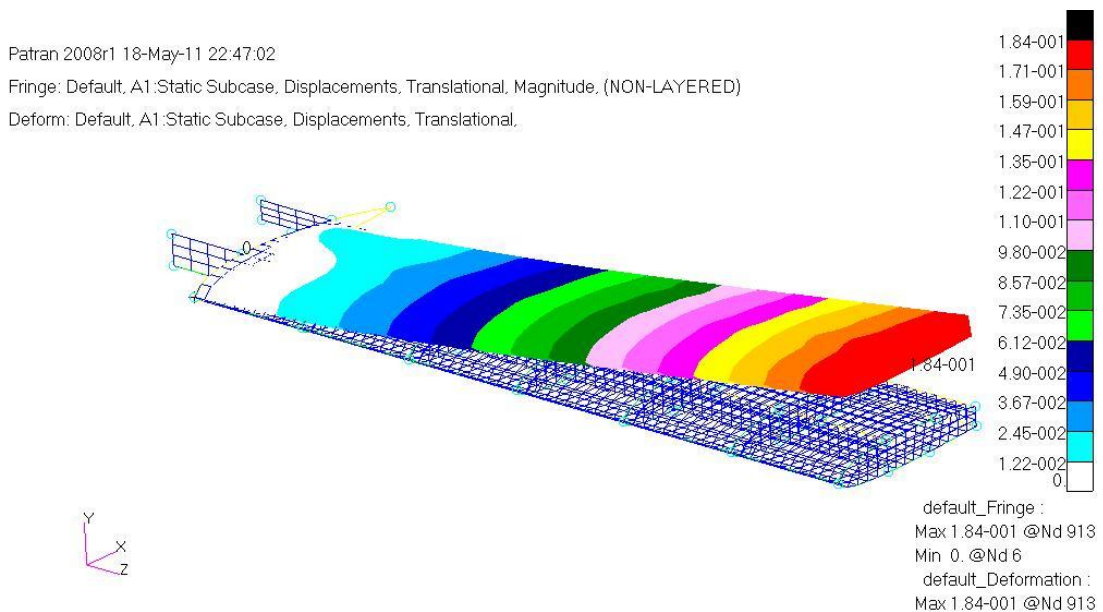


Figure 3.50: Deformation Plot of the Wing for the Fine Mesh Case Beam/Shell Model

The maximum tip displacements are determined as 17.8 cm and 18.4 cm for the coarse and the fine mesh cases, respectively. Figures 3.51 and 3.52 give the Von Mises stress plots for the coarse and the fine mesh cases, respectively.

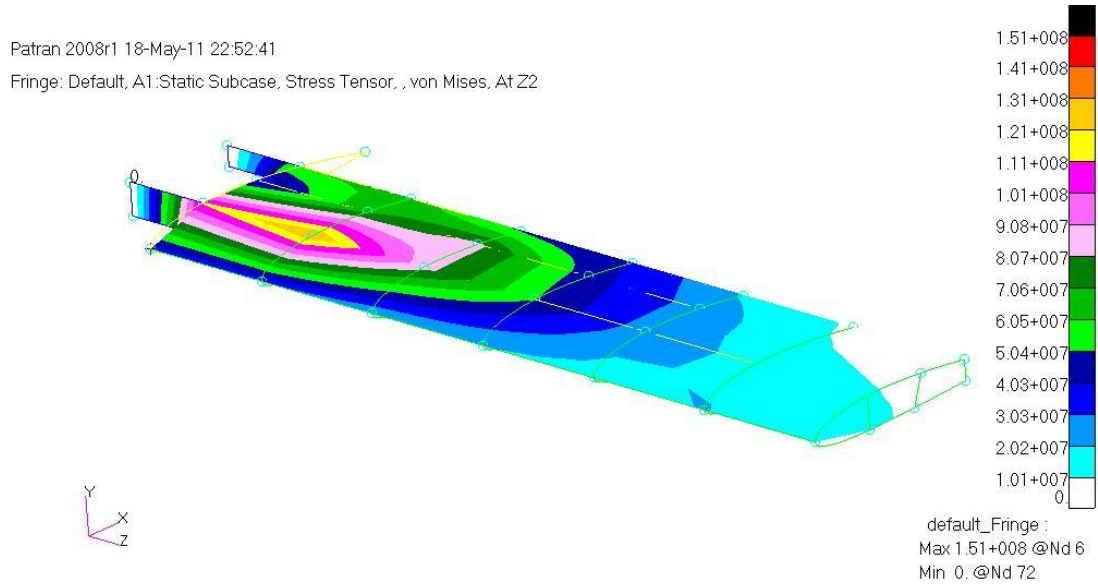


Figure 3.51: Von Mises Stress Distribution on the Shell Elements for the Coarse Mesh Case - Beam/Shell Model

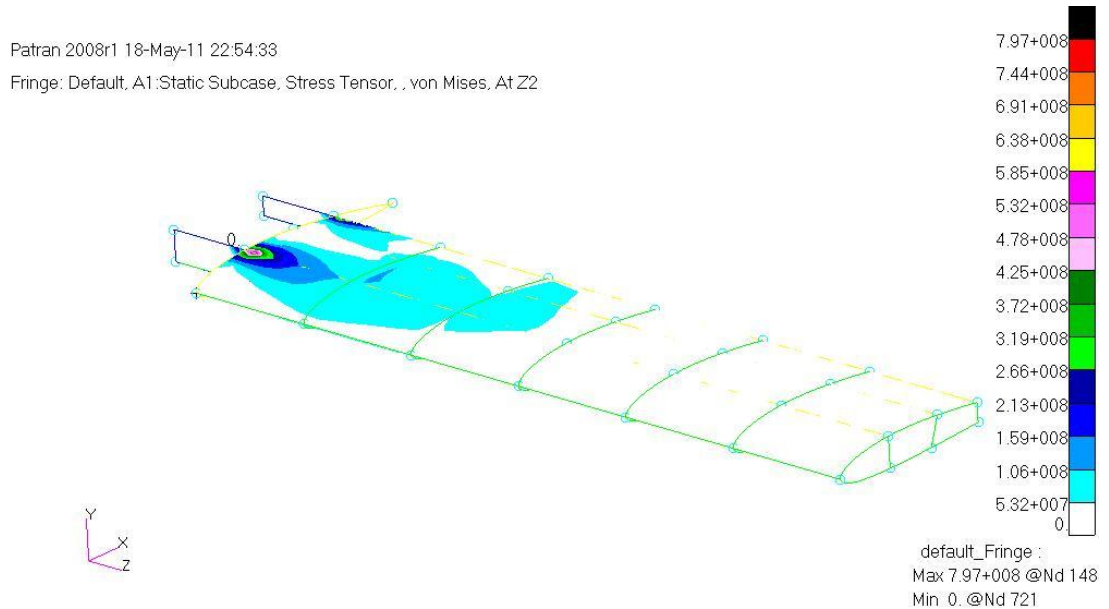


Figure 3.52: Von Mises Stress Distribution on the Shell Elements for the Fine Mesh Case - Beam/Shell Model

Table 3.12 shows the Von Mises stresses results for beam/shell model away from the restraint end on the upper middle skin. Stresses are calculated at the center of bays 2-5 in both coarse and fine mesh solutions. For the fine mesh case, an element at the center of each bay was selected as the stress monitor point.

Table 3.12: Comparison of Von Mises Stress on the Top Middle Skin of the Beam/Shell Model

Von Mises Stresses (MPa)				
Mesh Type	Bay 2	Bay 3	Bay 4	Bay 5
Coarse	124.06	75.28	37.78	16.42
Fine	81.74	57.62	25.53	10.72

Table 3.12 again shows similar Von Mises stress trend as the rod/shell model. Comments on the comparison of the Von Mises stresses predicted by the different finite element models is given in Section 3.7.4 after presenting results of all finite element models.

Figures 3.53 and 3.54 give the axial stresses on the upper front spar and on the upper middle stiffener for both coarse and fine mesh models for bays 2 - 5. It should be noted that in the case of a coarse mesh each flange is modeled with a single CBAR element in each bay, whereas in the fine mesh case, in each bay each flange consists of 11 elements.

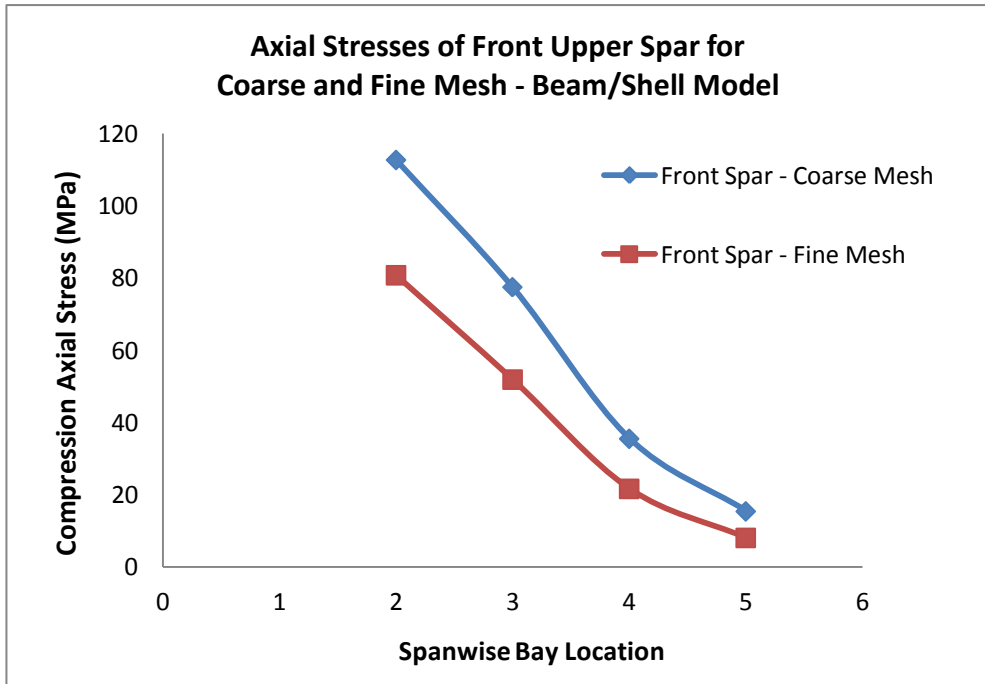


Figure 3.53: Axial Stress Distribution on the Front Spar Upper Flange for the Coarse and the Fine Mesh Cases – Beam/Shell Model

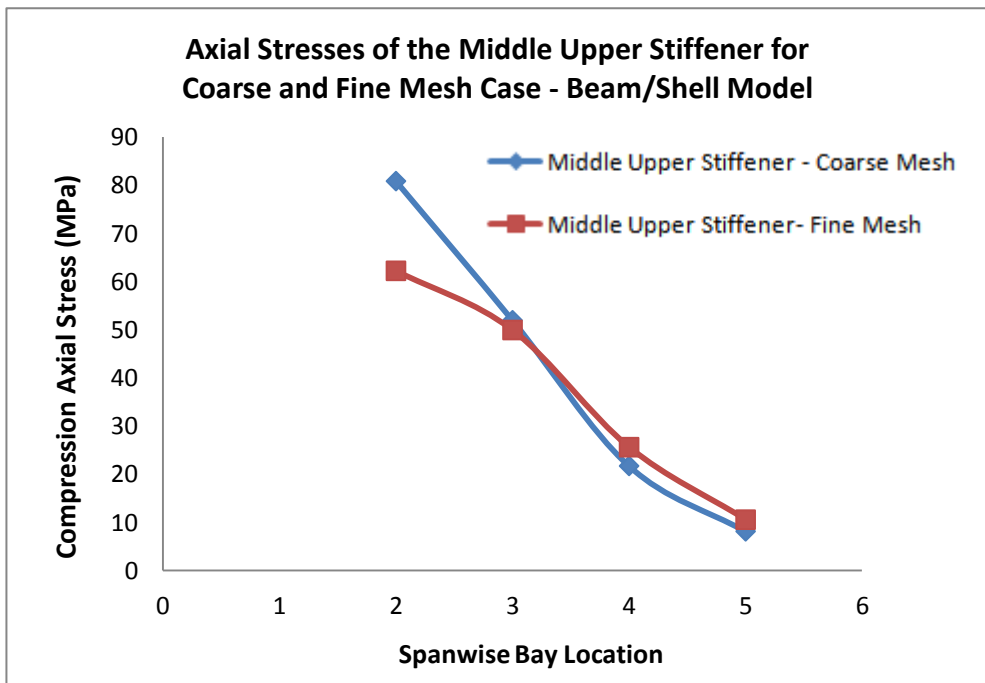


Figure 3.54: Axial Stress Distribution on the Upper Middle Stiffener for the Coarse and the Fine Mesh Cases – Beam/Shell Model

A quick comparison of the Von Mises stresses predicted by the rod/shell and the beam/shell models show reveal that that in general Von Mises stresses predicted by the beam/shell model are slightly lower than the Von Mises stresses predicted by the rod/shell finite element model. One reason for the slight decrease of the Von Mises stress on the shell elements in the beam/shell model may be attributed to the bending stress capability of the beam elements which are used to model the spar caps and the stiffeners. Spar caps and stiffeners are subject to minor bending since they are away from neutral axis of the wing torque box. However, slight bending of the beam elements takes up bending loads that are otherwise carried by the shell elements in the rod/shell model. It should also be noted that beam elements possess additional degrees of freedom that rod elements do not have. Thus, wing torque box, with spar caps and stiffeners modeled with beam elements, is more flexible compared to the wing torque box with spar caps and stiffeners modeled with rod elements. Another reason for the slight decrease of the Von Mises stresses could be due to slight stress relaxation caused by the slightly more flexible beam/shell model compared to the rod/shell model.

3.6.3 Analysis Results of Rod – Shell-R Finite Element Model

The semi- monocoque wing structure is modeled using 1D rod and 2D revised shell element pairs, and coarse and fine mesh FE models are analyzed. Revised shell elements possess drilling degree of freedom. Figures 3.55 and 3.56 show the deformation plots of coarse and fine mesh wing torque box models.

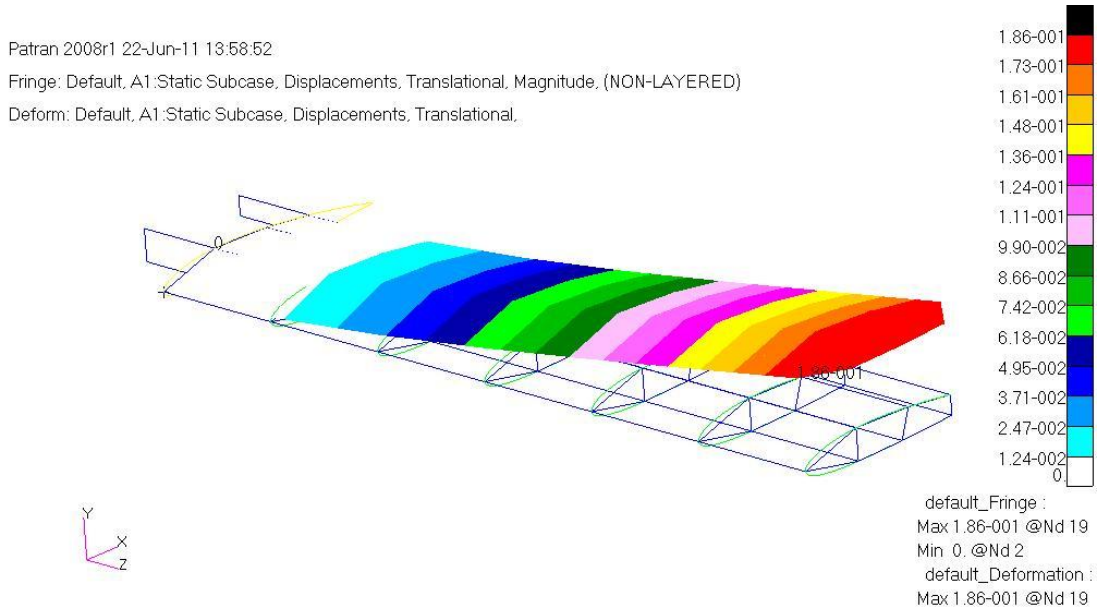


Figure 3.55: Deformation Plot of the Wing for the Coarse Mesh Case Rod Shell-R Model

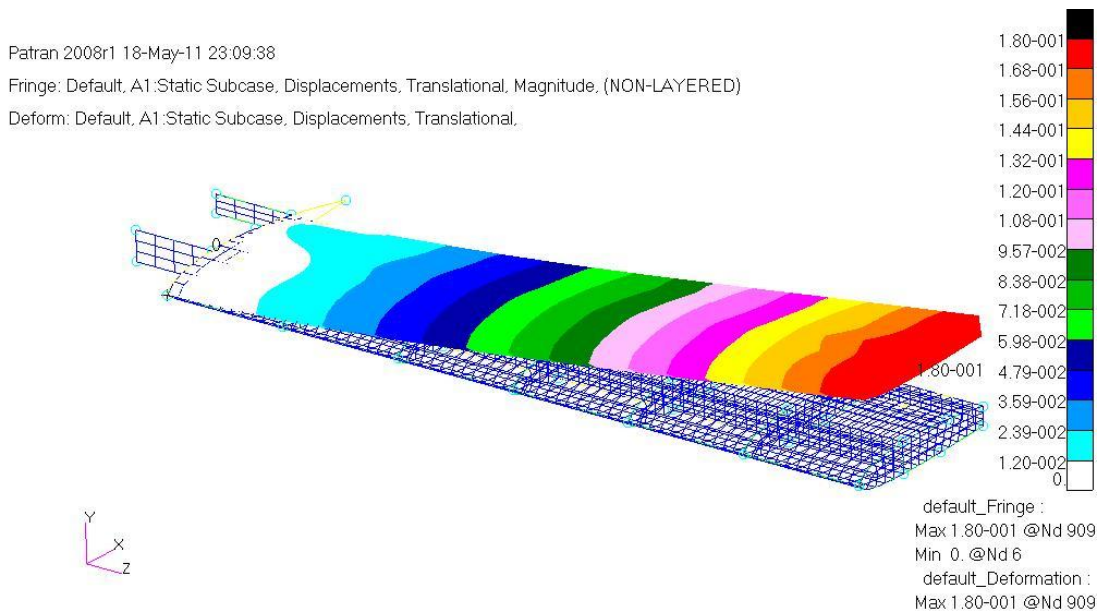


Figure 3.56: Deformation Plot of the Wing for the Fine Mesh Case Rod Shell-R Model

The maximum tip displacement is determined as 18.6 cm and 18.0 cm for the coarse and fine meshes, respectively. Figures 3.57 and 3.58 give the Von Mises stress plots.

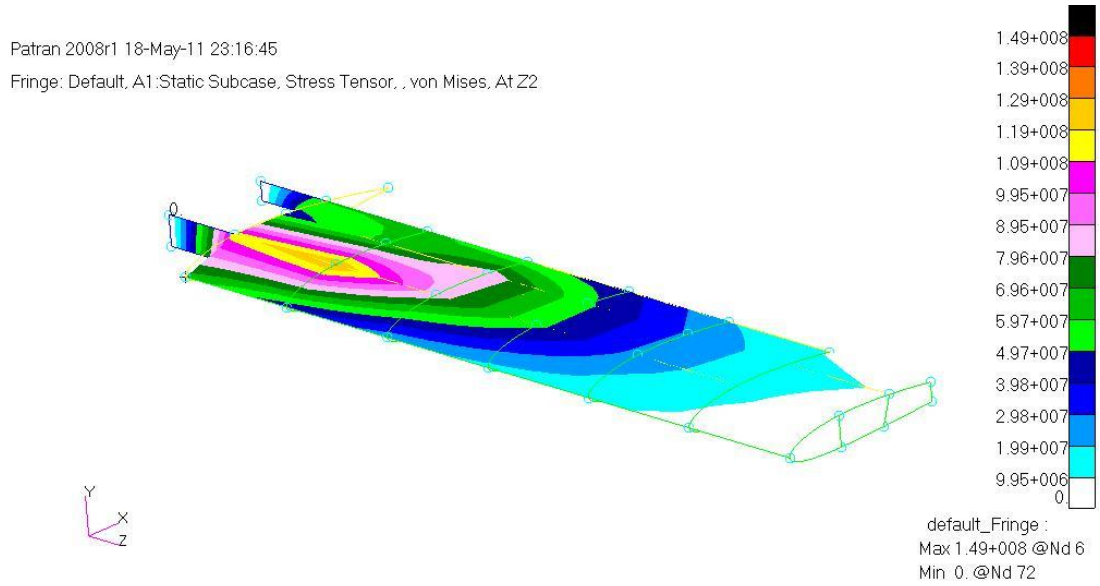


Figure 3.57: Von Mises Stress Distribution on the Shell-R Elements for the Coarse Mesh Case - Rod/Shell-R Model

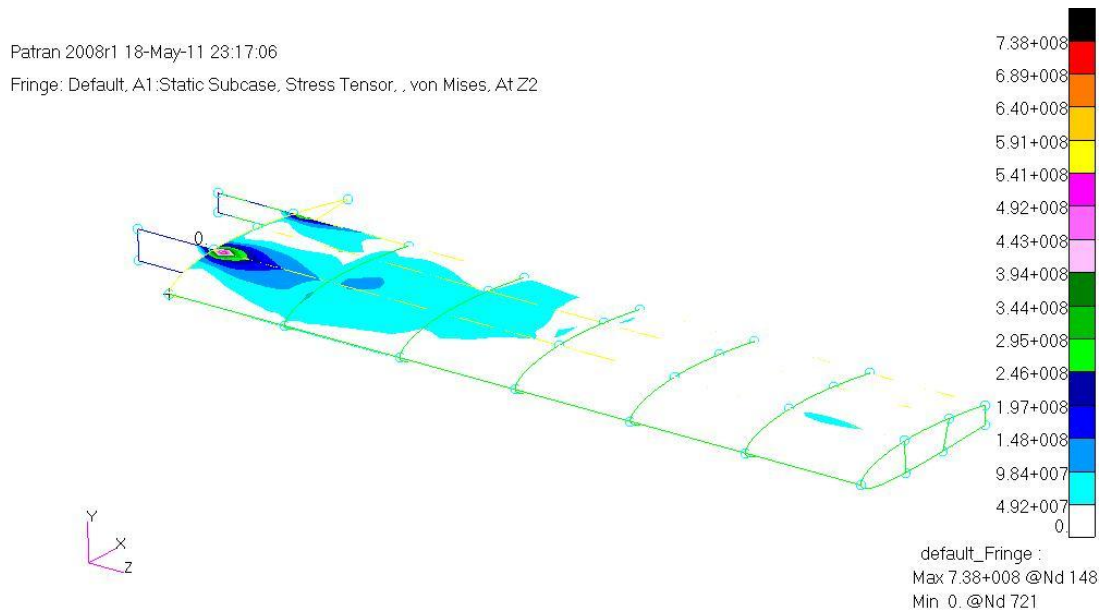


Figure 3.58: Von Mises Stress Distribution on the Shell-R Elements for the Fine Mesh Case - Rod/Shell-R Model

Table 3.13 shows the Von Mises stresses results of rod/shell - r model away from the restraint at the centers of the top middle skins of bays 2-5 for both coarse and fine mesh solutions.

Table 3.13: Comparison of Von Mises Stresses on the Top Middle Skin of the Rod/Shell-R Model

Von Mises Stresses (MPa)				
Mesh Type	Bay 2	Bay 3	Bay 4	Bay 5
Coarse	125.64	76.70	39.31	18.45
Fine	80.66	57.34	25.64	11.02

Comparison of Tables 3.11 and 3.13 shows that the use of revised shell elements with drilling degrees of freedom does not have an appreciable effect on the Von-Mises stresses predicted. Both rod/shell and rod/shell - r finite element models predict similar Von Mises stresses at the center of the top middle skin of each bay.

Figures 3.59 and 3.60 give the axial stresses on the upper flanges of the front spar and the upper middle stringers in bays 2-5, for both coarse and fine mesh models, respectively. It is seen that the rod/shell - r fine mesh finite element model predicts lower axial stress than the coarse mesh finite element model on both front spar flange and the upper stringer. It should be noted that away from any structural discontinuity one can expect to have lower stresses by the fine mesh finite element models compared to the coarse mesh finite element models. However, since fine mesh finite element models capture the stress gradients better, the maximum stresses predicted by the fine mesh models are usually higher than the maximum stresses predicted by the coarse mesh models.

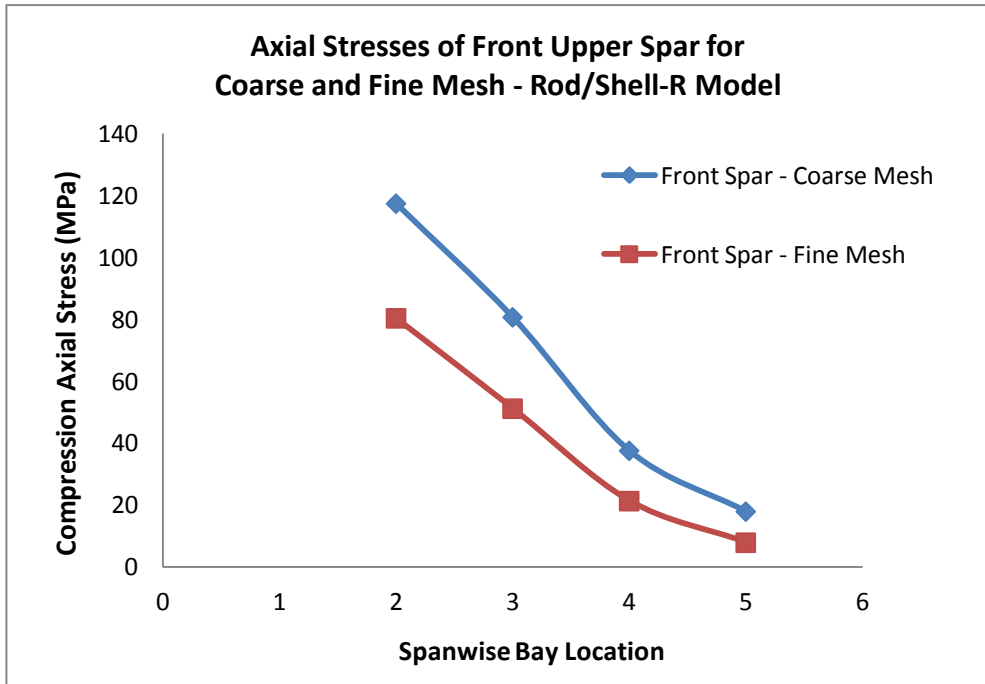


Figure 3.59: Axial Stress Distribution on the Upper Flange of the Front Spar for the Coarse and the Fine Mesh Case – Rod/Shell-R Model

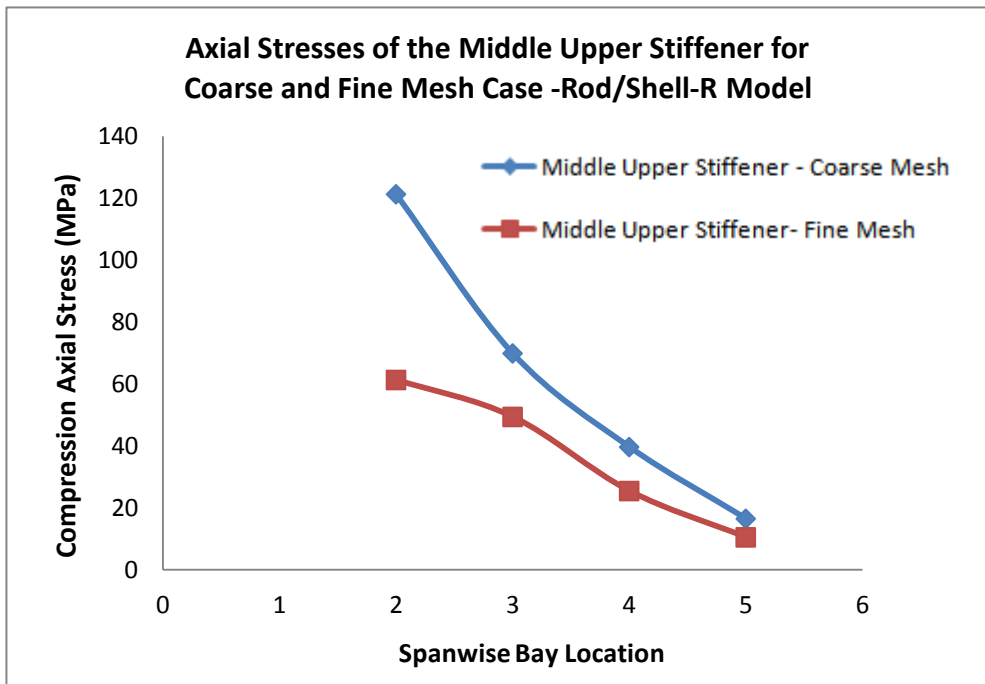


Figure 3.60: Axial Stress Distribution on the Upper Middle Stiffener for the Coarse and the Fine Mesh Case – Rod/Shell-R Model

3.6.4 Analysis Results of Beam – Shell-R Finite Element Model

The semi-monocoque wing structure is modeled using 1D beam and 2D revised shell element pairs, and coarse and fine mesh FE models are analyzed. Figures 3.61 and 3.62 show the deformation plots of the coarse and fine mesh wing torque box models.

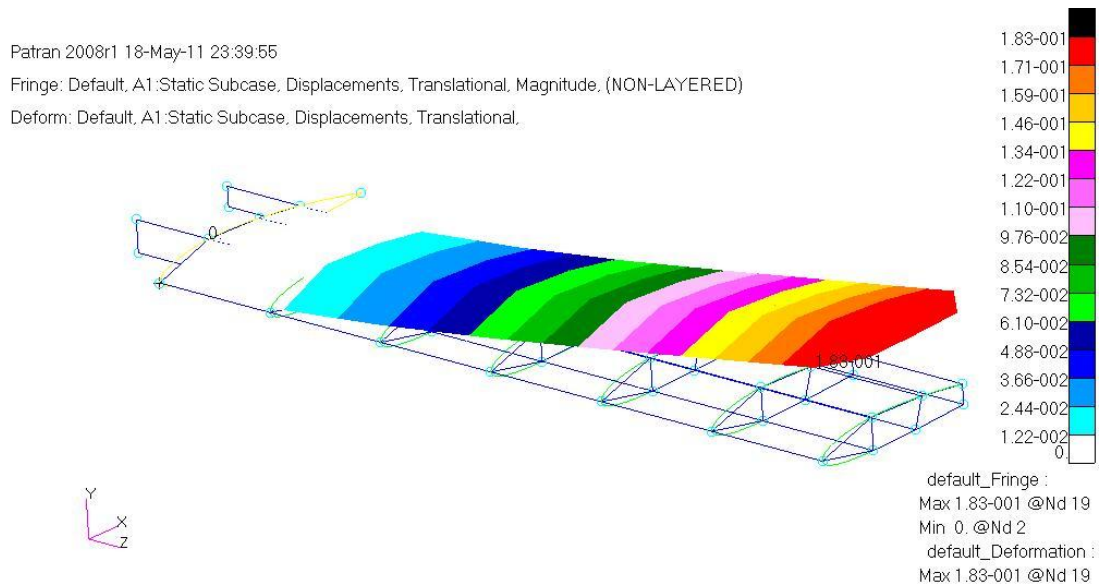


Figure 3.61: Deformation Plot of the Wing for the Coarse Mesh Case Beam/Shell-R Model

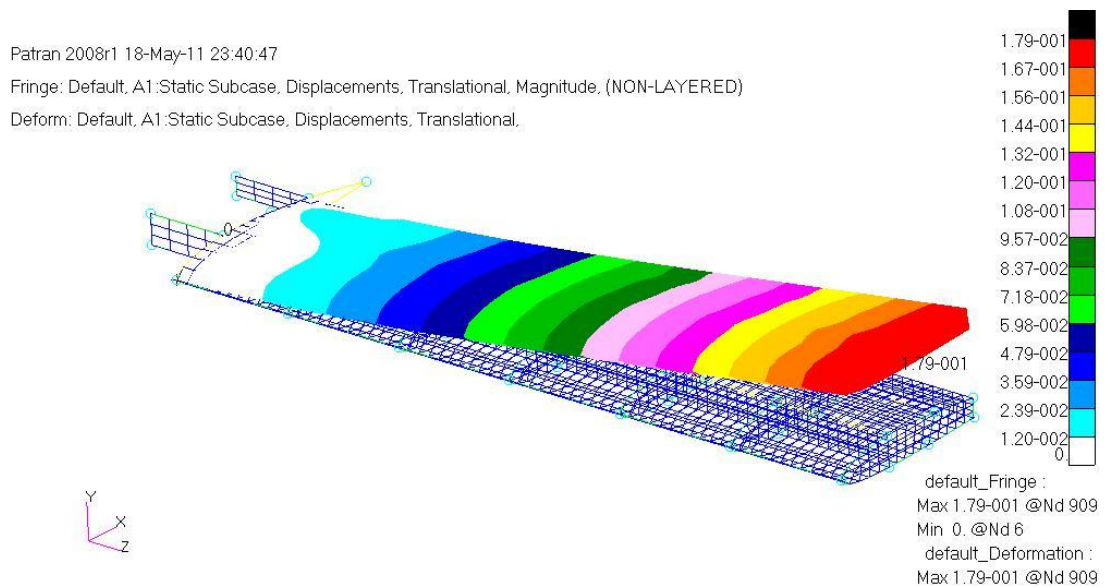


Figure 3.62: Deformation Plot of the Wing for the Fine Mesh Case Beam/Shell-R Model

The maximum tip displacement is determined as 18.3 cm and 17.9 cm for the coarse and the fine meshes, respectively. Figures 3.63 and 3.64 give the Von Mises stress plots for the coarse and fine mesh finite element models.

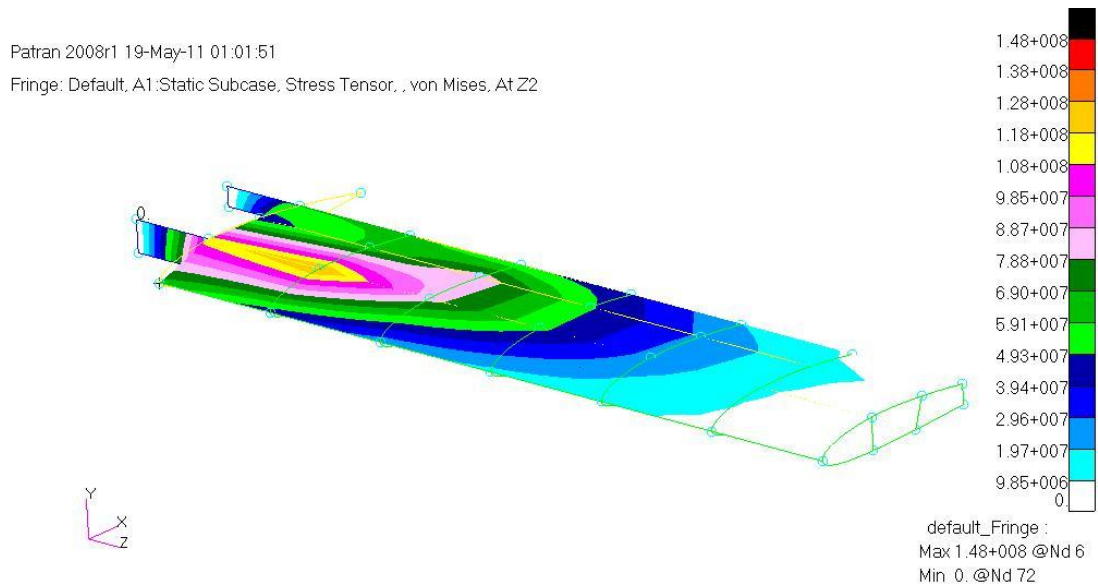


Figure 3.63: Von Mises Stress Distribution on the Shell-R Elements for the Coarse Mesh Case - Beam/Shell-R Model

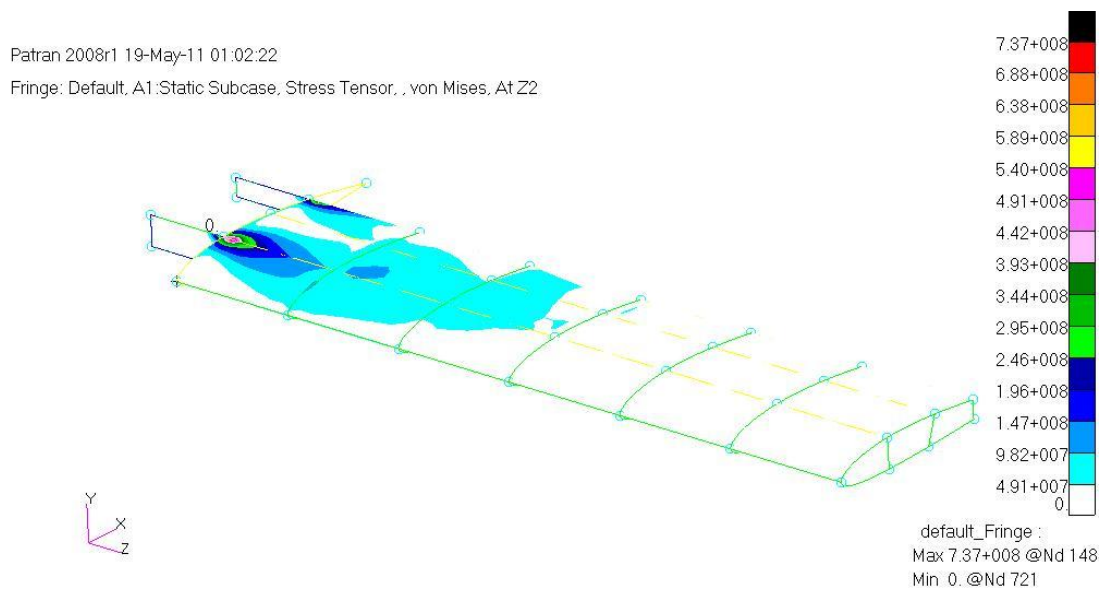


Figure 3.64: Von Mises Stress Distribution on the Shell-R Elements for the Fine Mesh Case - Beam/Shell-R Model

Table 3.14 gives the Von Mises stresses results of beam/shell - r model at the centers of the top middle skins in bays 2-5 for both coarse and fine mesh solutions.

Table 3.14: Comparison of Von Mises Stress on the Top Middle Skin of Beam/Shell-R Model

Von Mises Stresses (MPa)				
Mesh Type	Bay 2	Bay 3	Bay 4	Bay 5
Coarse	127.23	76.08	38.15	16.34
Fine	81.03	57.07	25.28	10.50

It is observed that in the beam/shell - r model, Von Mises stresses are nearly same as Von Mises stresses on the shell elements of the rod/shell - r model, but slightly less in bays 3-5. Slight reduction of the Von Mises stresses may be attributed to the use of beam elements in the spar caps and the stiffeners which share the bending load with the shell elements, resulting in slight reduction in Von Mises stresses in the shell elements.

Figures 3.65 and 3.66 give the axial stresses on the upper flange of the front spar and on the upper middle stiffener for both coarse and fine mesh models away in bays 2-5, respectively. So far, in all the models it is observed that fine and coarse mesh results deviate more from each other towards the root of the wing. Thus, it can be concluded that coarse mesh finite element models produce less accurate results in bays which are closer to the wing root. Such a result is expected, because towards the wing root, stress gradients are higher and coarse mesh finite element models are less capable of in capturing the true stresses in wing sections where the stress gradients are higher

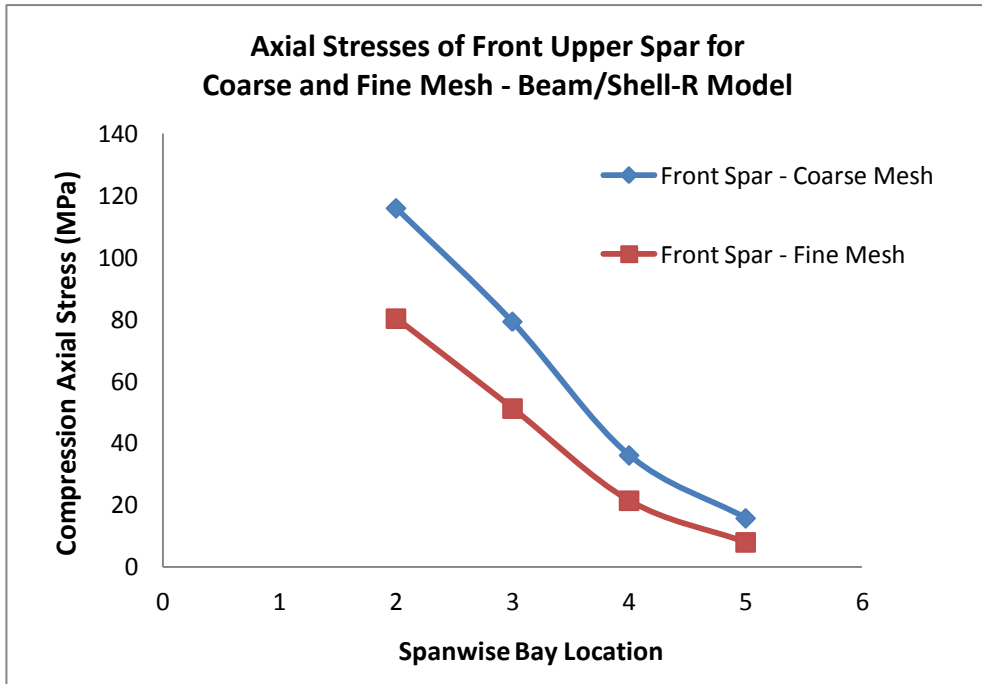


Figure 3.65: Axial Stress Distribution on the Upper Flange of the Front Spar for the Coarse and the Fine Mesh Case – Beam/Shell-R Model

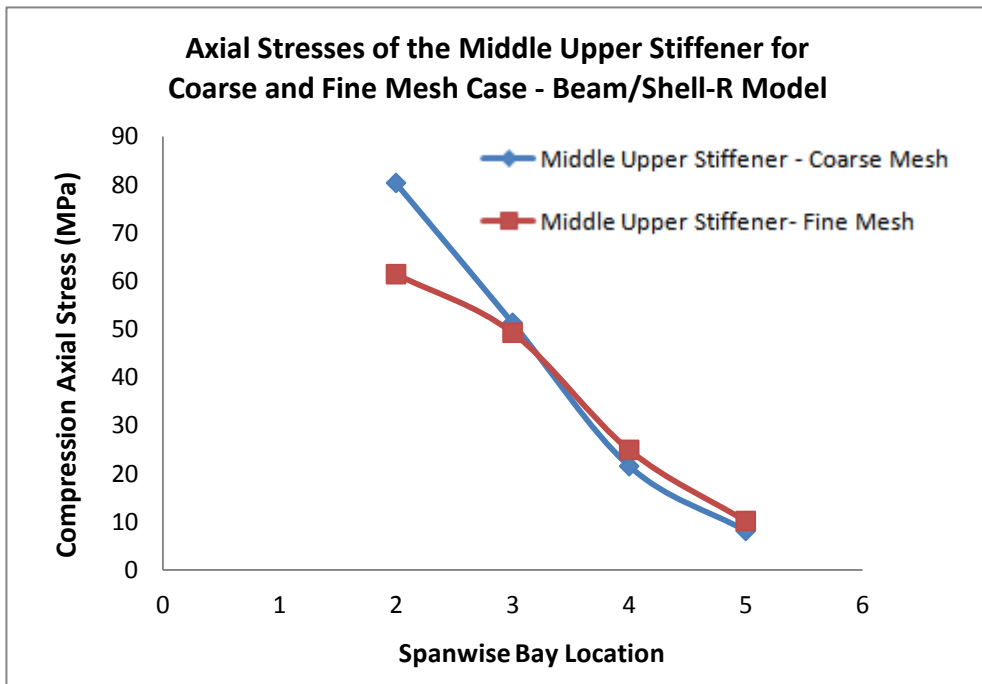


Figure 3.66: Axial Stress Distribution on the Upper Middle Stiffener for the Coarse and the Fine Mesh Case – Beam/Shell-R Model

When beam elements are used in combination with the shell - r elements no major change in Von Mises stresses and axial stresses are observed compared to the results of rod/shell - r finite element model. Again, there is slight reduction in the Von Mises stresses and axial stresses when compared to rod/shell - r model.

3.6.5 Analysis Results of Rod – Membrane-R Finite Element Model

The semi-monocoque wing structure is modeled using 1D rod and 2D revised membrane element pairs, and only coarse FE model is analyzed. Figure 3.67 shows the deformation plot of coarse mesh wing structure. The maximum tip displacement is determined as 20.2 cm.

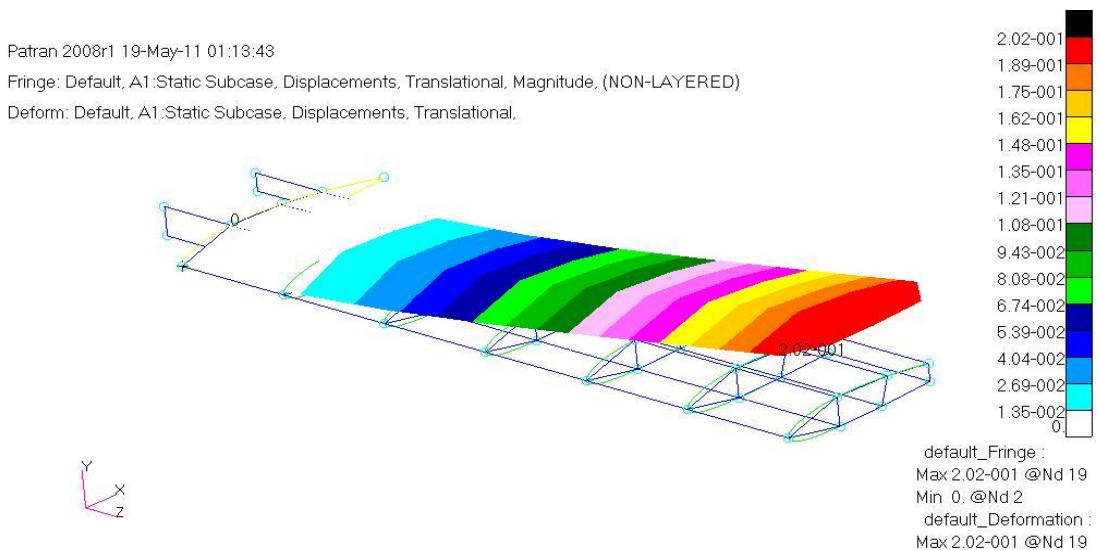


Figure 3.67: Deformation Plot of the Wing for the Coarse Mesh Case
 Rod/Membrane-R Model

Figure 3.68 gives the Von Mises stress plot for this case.

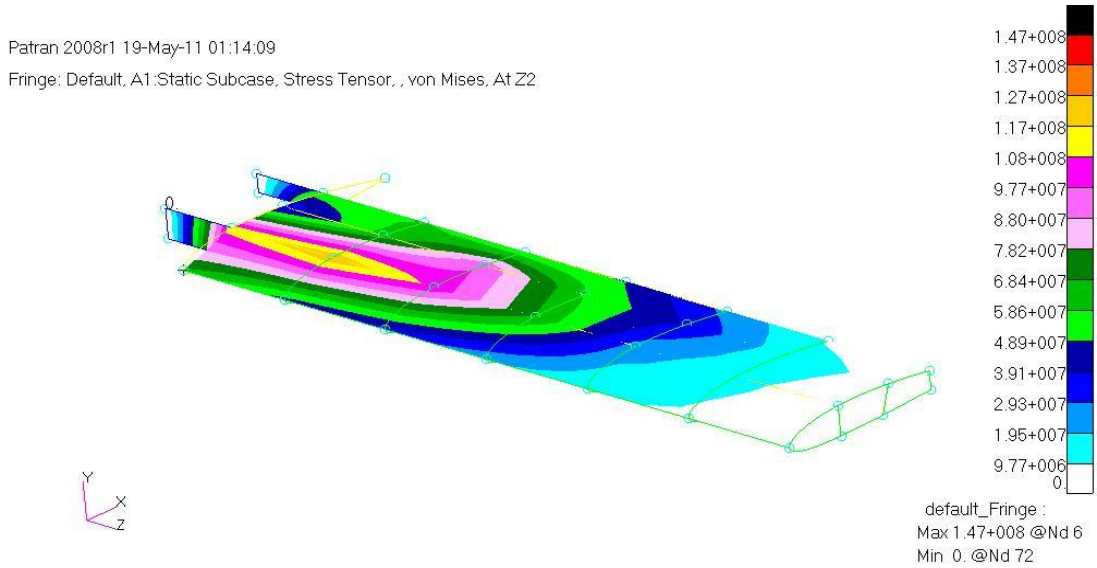


Figure 3.68: Von Mises Stress Distribution on the Membrane-R Elements for the Coarse Mesh Case - Rod/Membrane-R Model

Table 3.15 shows the Von Mises stress results of the rod/membrane - r model at the center of the upper middle skin of bays 2-5.

Table 3.15: Von Mises Stress on the Top Middle Skin of the Rod/Membrane-R Model

Von Mises Stress (MPa)				
Mesh Type	Bay 2	Bay 3	Bay 4	Bay 5
Coarse	133.05	77.11	38.66	17.26

It is noticed that Von Mises stresses determined by the rod/membrane - r model are comparable to the Von Mises stresses determined by the previous four models with shell elements except for bay 2. In bay 2 Von Mises stress predicted by the rod/membrane model is higher than the Von Mises stress predicted by the finite element models which have shell elements.

Figures 3.69 and 3.70 give the axial stresses on the upper flange of the front spar and on the upper middle stiffener for the coarse mesh model in bays 2-5.

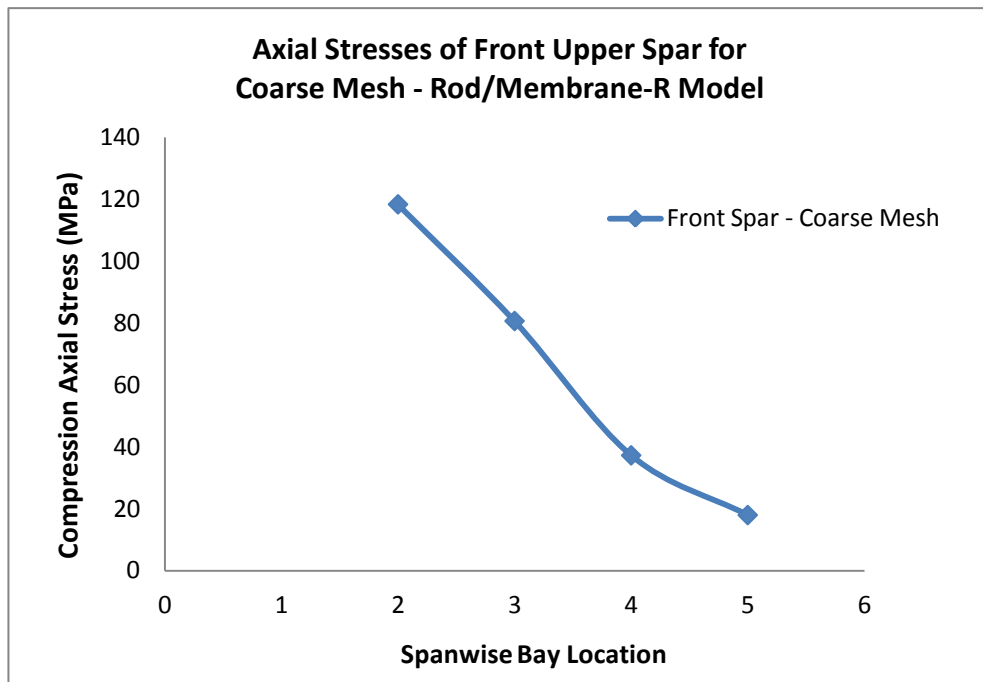


Figure 3.69: Axial Stress Distribution on the Upper Flange of the Front Spar for the Coarse Mesh Case – Rod/Membrane-R Model

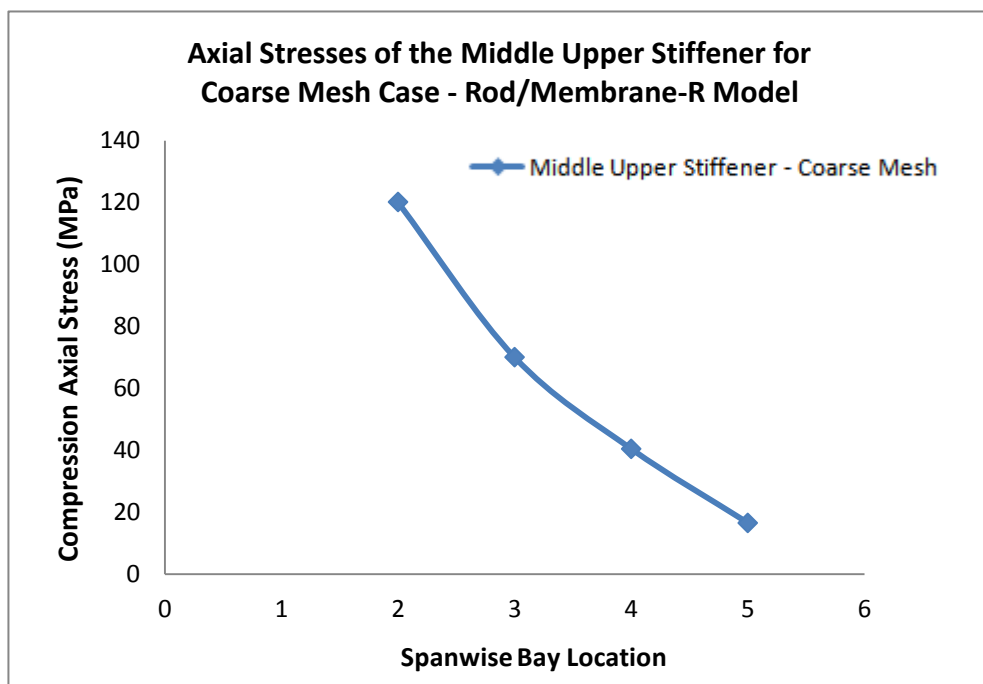


Figure 3.70: Axial Stress Distribution on the Upper Middle Stiffener for the Coarse Mesh Case – Rod/Membrane-R Model

3.6.6 Analysis Results of Beam – Membrane-R Finite Element Model

The semi-monocoque wing structure is modeled using 1D rod and 2D revised membrane element pairs, and only coarse FE model is analyzed. Figure 3.71 shows the deformation plot of coarse mesh wing structure model.

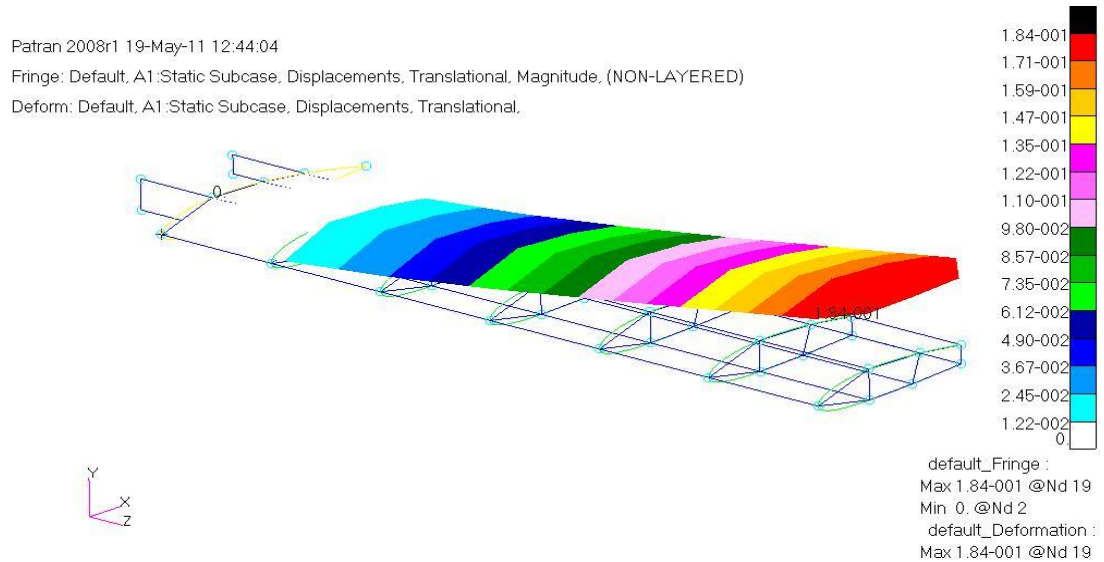


Figure 3.71: Deformation Plot of the Wing for the Coarse Mesh Case
Beam/Membrane-R Model

The maximum tip displacement is determined as 18.4 cm, slightly lower than the maximum displacement of the rod/membrane - r model. Figure 3.72 gives the Von-Mises stress plot for the beam/membrane - r finite element model.

Patran 2008r1 19-May-11 12:43:12

Fringe: Default, A1:Static Subcase, Stress Tensor, , von Mises, At Z2

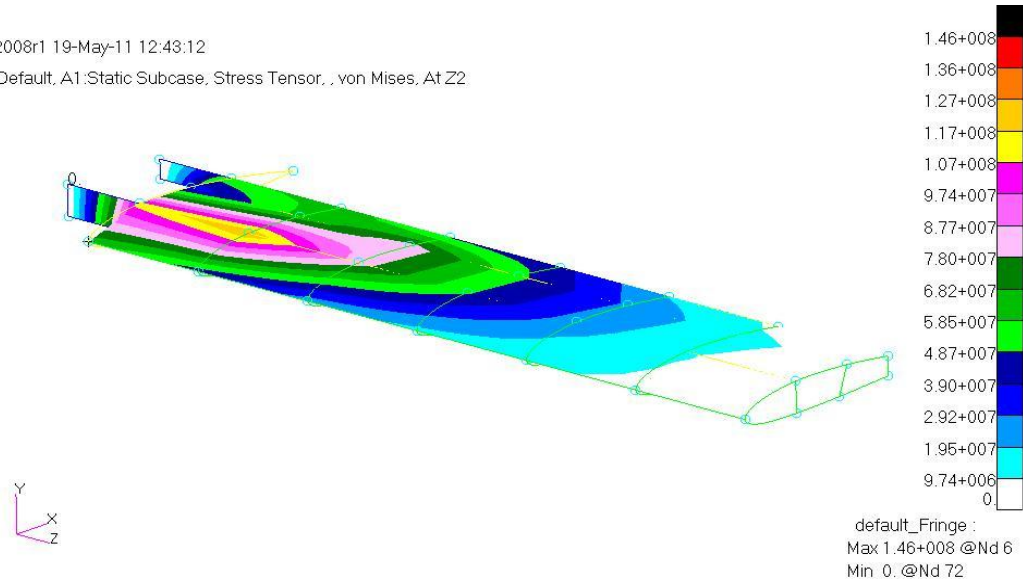


Figure 3.72: Von Mises Stress Distribution on the Membrane-R Elements for the Coarse Mesh Case - Rod/Membrane-R Model

Table 3.16 shows the Von Mises stress results of the beam/membrane - r model at the center on the upper middle skin of bays 2-5.

Table 3.16: Von Mises Stress on the Top Middle Skin of the Beam/Membrane-R Model

Von Mises Stress (MPa)				
Mesh Type	Bay 2	Bay 3	Bay 4	Bay 5
Coarse	131.42	75.33	36.88	15.08

Figures 3.73 and 3.74 give the axial stresses at the center of the upper flange of the front spar and the upper middle stiffener in bays 2-5.

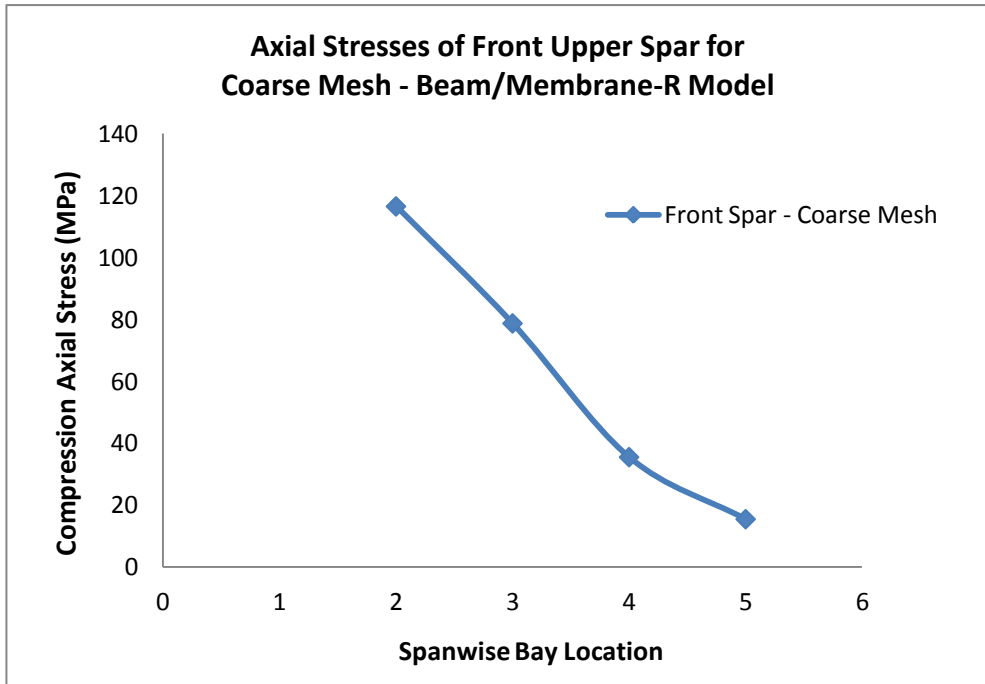


Figure 3.73: Axial Stresses Distribution of the Upper Front Spar for the Coarse Mesh Case – Beam/Membrane-R Model

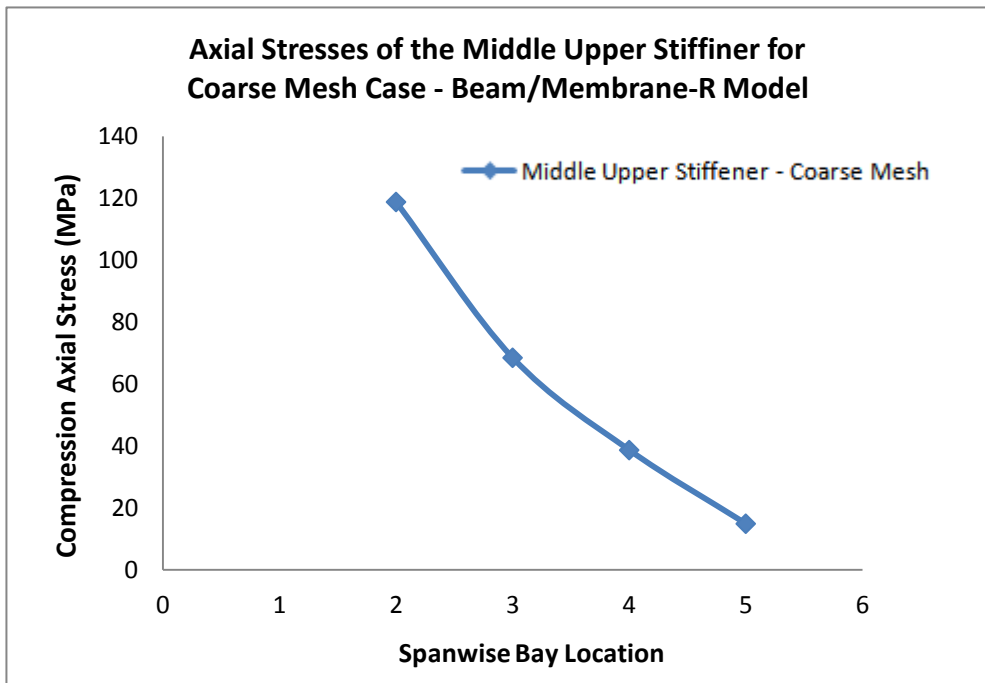


Figure 3.74: Axial Stresses Distribution of the Middle Upper Stiffener for the Coarse Mesh Case – Beam/Membrane-R Model

Similar to the finite element solution obtained by the shell elements, when beam elements are used in combination with the membrane - r elements, no major change in the Von Mises stresses and the axial stresses are observed. Beam/membrane - r finite element model predicts slightly lower Von Mises and axial stresses compared to the corresponding stresses determined by the rod/membrane - r model.

3.7 Finite Element Analysis Study with Shear and Membrane Elements

As it has been discussed in previous sections, the correct use of element types depends on the type of loading that the structure is carrying. In the current study, the lift and the pitching moment loads are considered as line loading acting along the span of the wing through the front spar. In order to understand the effect of using membrane elements without revised formulation, and shear panels on the wing structure analysis, three case studies are conducted.

3.7.1 Wing Torque Box Case Study Using Rod-Membrane Model

The wing torque box is modeled using rod-membrane elements. Membrane elements are used without revised formulation and a single element in the chordwise direction of the wing is used. The wing torque box model is analyzed under two different loading conditions. The first load case has lift force only and the second load case has pitching moment only. Figures 3.75 and 3.76 show the deformation plots for the pure pitching moment and pure lift force line loading cases, respectively.

Patran 2008r1 10-Jun-11 13:23:27

Fringe: Default, A1:Static Subcase, Displacements, Translational, Magnitude, (NON-LAYERED)

Deform: Default, A1:Static Subcase, Displacements, Translational.

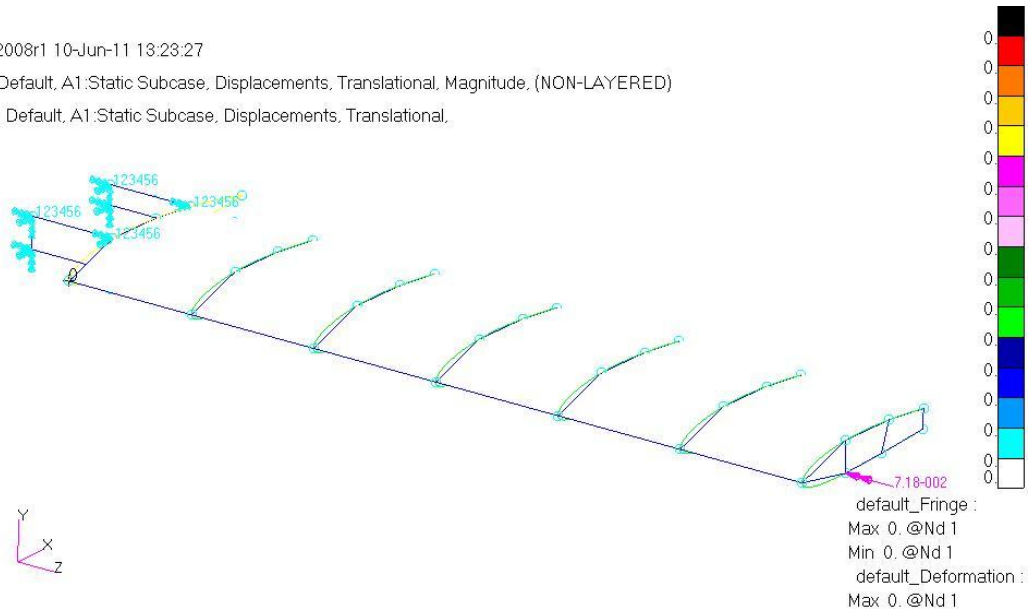


Figure 3.75: Deformation Plot of the Rod/Membrane Model of the Wing Structure under Pure Line Pitching Moment Loading

Patran 2008r1 10-Jun-11 13:52:21

Fringe: Default, A1:Static Subcase, Displacements, Translational, Magnitude, (NON-LAYERED)

Deform: Default, A1:Static Subcase, Displacements, Translational.

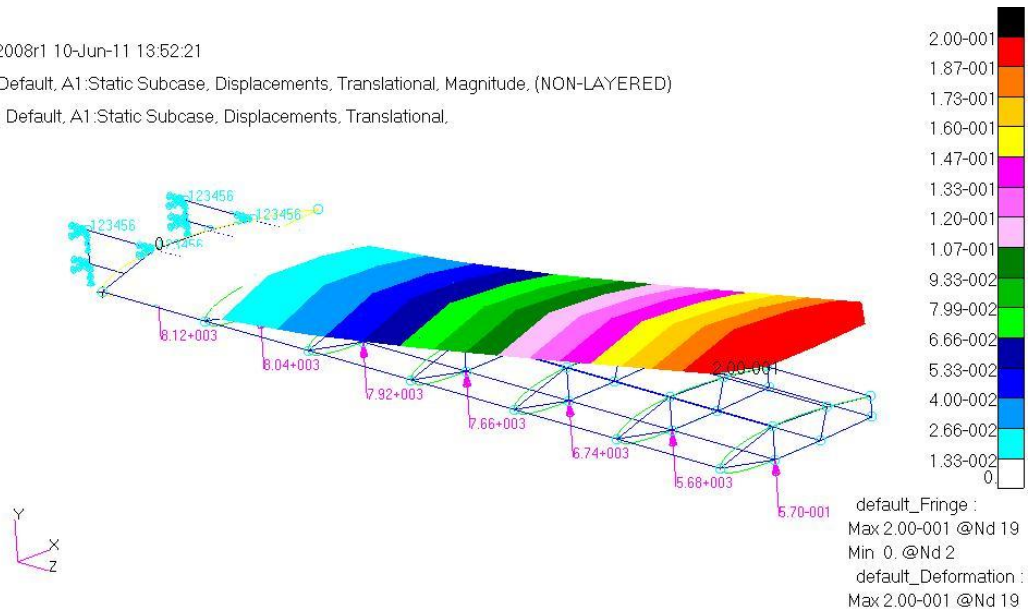


Figure 3.76: Deformation Plot of the Rod/Membrane Model of the Structure under Pure Line Lift Force Loading

As it can be seen from Figures 3.75 and 3.76, the rod-membrane model of the wing structure, under pure pitching moment loading, does not deform but the same model under pure lift force loading deforms, as expected. Thus, it can be concluded that membrane element with no drilling degrees of freedom in the wing ribs is not able to carry line pitching moment loading.

3.7.2 Wing Torque Box Case Study Using Rod-Membrane-R Model

The wing torque box is modeled using rod/membrane - r elements. Membrane elements are used with revised formulation and a single element in the chordwise direction of the wing is used. The wing torque box model is analyzed under two different loading conditions; the first case considered lift force only and the second case considered pitching moment only. Figures 3.77 and 3.78 show the deformation plots for the pure pitching moment and pure lift force line loading cases, respectively.

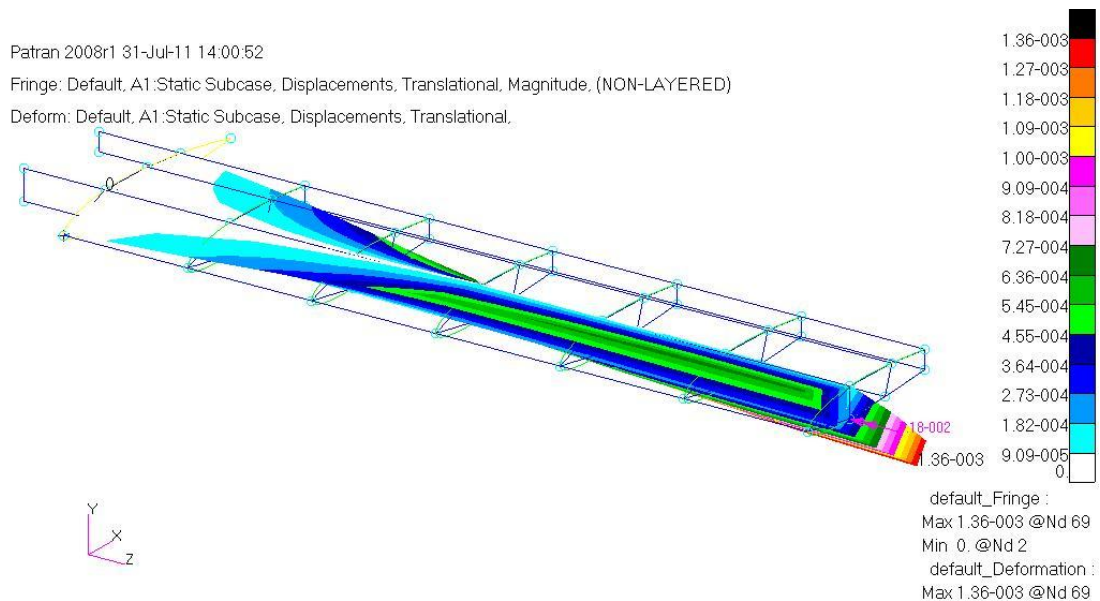


Figure 3.77: Deformation Plot of the Rod/Membrane-R Model of the Wing Torque Box under Pure Pitching Moment Loading

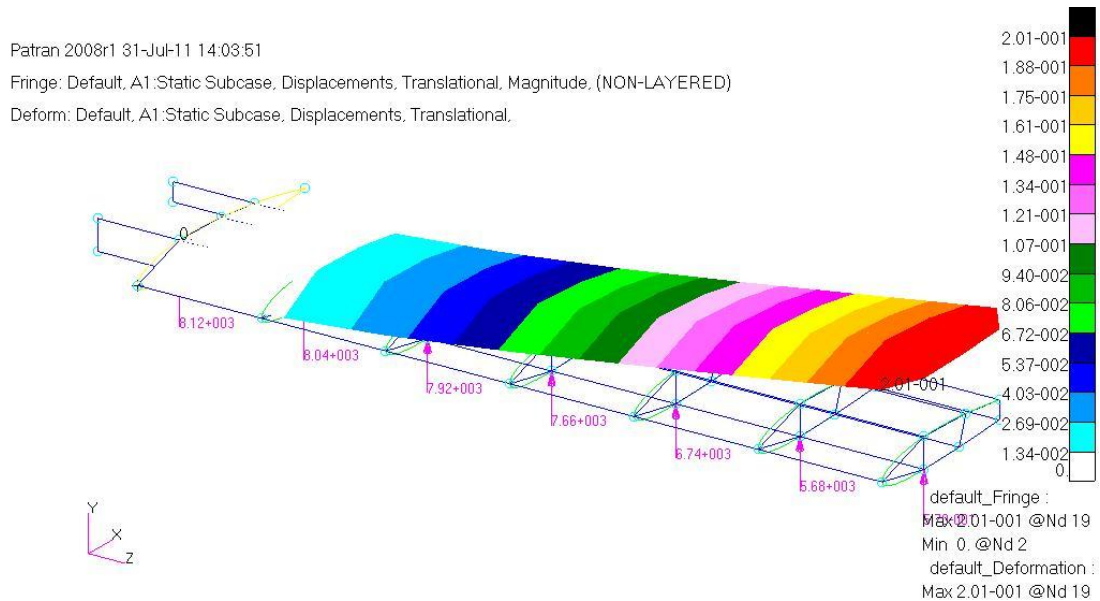


Figure 3.78: Deformation Plot of the Rod/Membrane-R Model of the Wing Torque Box under Pure Lift Force Loading

As it can be seen from Figures 3.77 and 3.78, the rod/membrane - r model of the wing torque box deforms under both pure pitching moment loading and pure lift force loading. The use of membrane - r elements in the wing ribs accounts for the accurate transfer of the external pitching moment through the consistent in-plane moments acting at the drilling degrees of freedom of the membrane elements on the wing rib.

3.7.3 Wing Torque Box Case Study Using Rod-Shear Panels Model

Shear panels are used extensively within aerospace structures, it was a common practice in aircraft companies to use shear panels to model wings, fuselages and empennage structures. Shear panels are essential elements for modeling aerospace structures as well as other structures characterized by very thin elastic sheets and stiffeners. Shear panels are modeled by using a combination of ROD and SHEAR elements, where the RODs account for the extensional behavior of the stiffeners and the SHEAR elements account for the load carried by the thin elastic sheet.

Since the CSHEAR element in Nastran normally carries shear loads only, every shear panel must be surrounded on all four sides by normal stress carrying elements such as rod elements to carry end loads in the equivalent areas. If the model does not

contain elements which provide extensional stiffness on either side of the shear panel, fictitious rod elements must be provided on the sides to prevent the singularity.

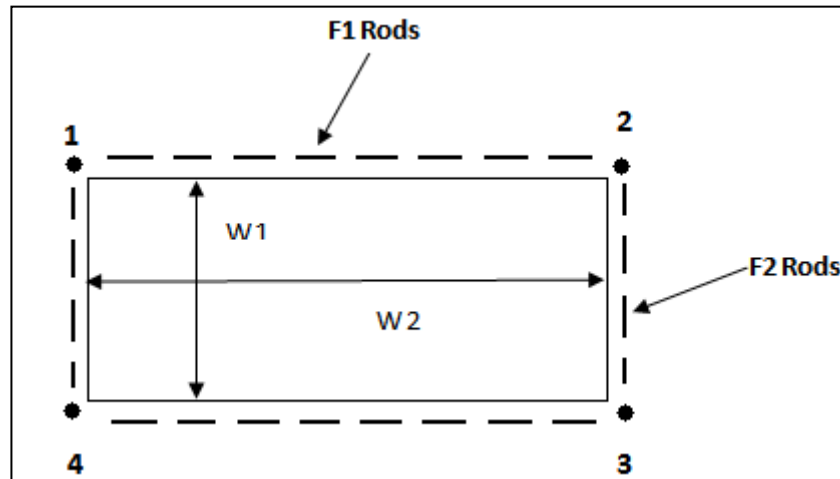


Figure 3.79: Extensional Areas for the Shear Panel

The effective extensional area is defined by means of equivalent rods on the perimeter of the element by using the F1 and F2 Factors. As it can be seen from Figure 3.79 the F1 is the effectiveness factor for extensional stiffness along edges 1-2 and 3-4, whereas F2 is the effectiveness factor for extensional stiffness along edges 2-3 and 1-4.

- If F1 or F2 is set to 1.0, the equivalent rods will be set to areas of $0.5 \times t \times w_1$ or $0.5 \times t \times w_2$ where t defines the shear panel thickness and in this case the shear panel is fully effective for extension in 1-2 and 3-4 directions.
- If $F < 1.01$, the equivalent rods will be set to areas of $0.5 \times F1 \times t \times w_1$ or $0.5 \times F2 \times t \times w_2$, in this case the shear panel is less than fully effective.
- If $F > 1.01$, the equivalent rods will be set to areas of $0.5 \times F1 \times t^2$ or $0.5 \times F2 \times t^2$, in this case the shear panel is less than fully effective.

In this section, wing torque box is modeled using rod/shear panel elements. Single shear panels are in the chordwise direction of the wing. The use of shear panels

requires distributed reinforcements in two directions and this is done by creating stringers around each panel. It must be noted that since already the wing structure has spars and stringer in span-wise direction, it is only needed to create rods in the chordwise direction. The effectiveness factor value F for the extensional stiffness along edges is defined as 0.80 and this value is less than 1.01 which indicates that the shear panel is less than fully effective and by using this value the equivalent rods are set to areas of $0.5 \times F \times t \times w_1$ and $0.5 \times F \times t \times w_2$, where t defines the thickness of the shear panel and w defines the edge width in both directions as described previously in Figures 3.80. Figure 3.81 shows the wing torque box rod-shear panel model after creating and adding the equivalent rods on the edges of shear panels.

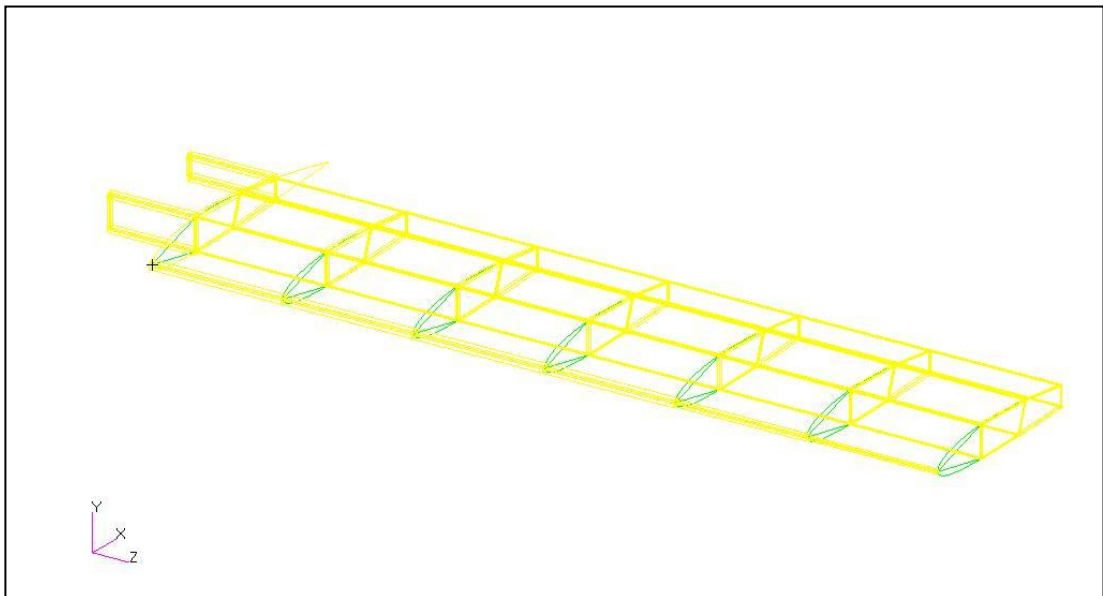


Figure 3.80: Extensional Rod Areas for Rod/Shear Panel of the Wing Torque Box

As it can be seen from Figure 3.80, in the coarse mesh model, nose ribs elements are single elements of type TRIA3, which are triangular shell elements. Since triangular elements can not be assigned shear panel properties, they are kept as shell elements. Figures 3.81 and 3.82 show the deformation plots for the pure pitching moment and pure lift force line loading cases, respectively.

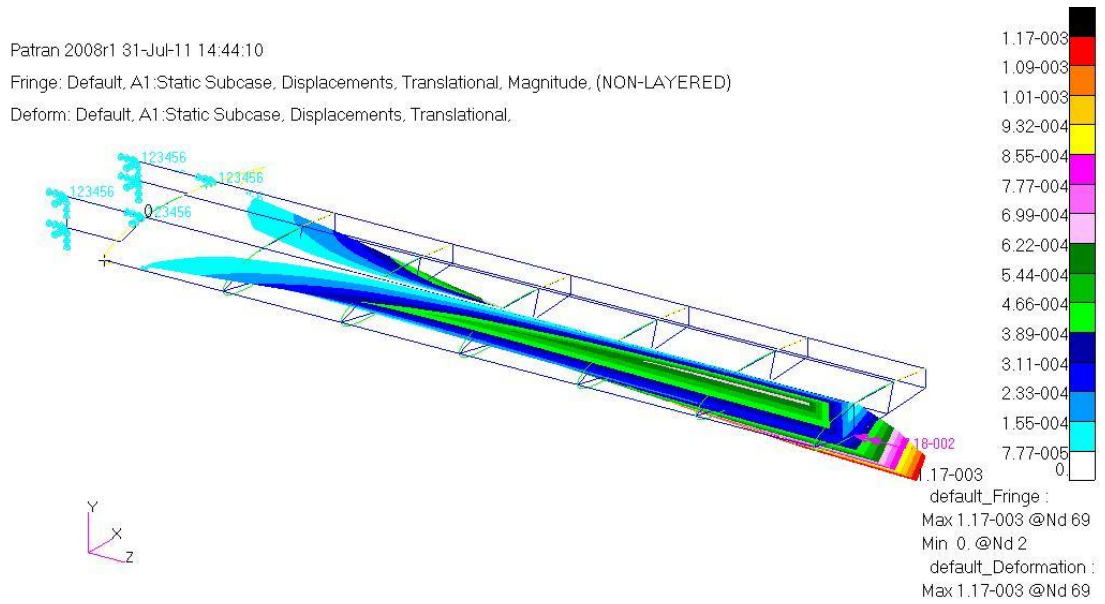


Figure 3.81: Deformation Plot of the Rod/Shear Model of the Wing Torque Box under Pure Pitching Moment Loading

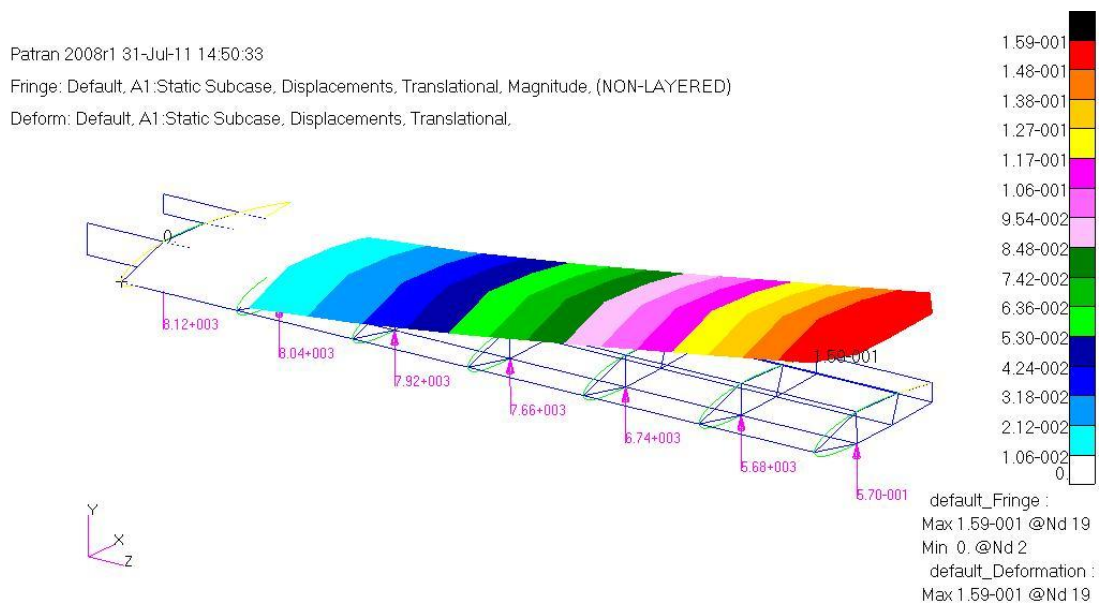


Figure 3.82: Deformation Plot of the Rod/Shear Model of the Wing Torque Box under Pure Lift Force Loading

From Figure 3.81, it can be easily mistaken to say that rod-shear panel model is able to carry pitching moment line loading. However, the deformation is due to the fact

that nose ribs elements are single elements of type TRIA3, which are triangular shell elements. Since triangular elements can not be assigned shear panel properties, they are kept as shell elements. Thus, the deformation seen in Figure 3.81 is due to the use of triangular shell elements in the nose part of the wing. On the other hand, as it can be seen from Figure 3.82, rod-shear panel model of the wing torque box deforms under distributed lift force which acts through the lower flange of the front spar with a value of 15.9 cm.

3.7.4 Overview of Maximum Displacement, Von Mises Stress and Axial Stress Determined by Different Element Pairs

Tables 3.17 and 3.18 give the comparison of maximum tip displacement, maximum Von Mises stresses and Von Mises stresses calculated at the middle of bay 4 on the middle upper skin.

Membrane elements are used with revised formulation, denoted by membrane - r, which has drilling degrees of freedom. As discussed before, revised formulation is required because the external pitching moment, which is calculated by ESDU 95010, is a line load which cannot be handled by the standard membrane element accurately.

Table 3.17: Comparison of Maximum Tip Displacement, Maximum Von Mises Stress and Von Mises Stress at the Mid Span for the Coarse Mesh Wing Torque Box Models

Model (Coarse Mesh)	Displacement (cm)	Max Von Mises (MPa)	Von Mises at the Mid Span (MPa)
Rod-Shell	18.5	160	40.35
Beam-Shell	17.8	151	37.78
Rod-Shell R	18.6	149	39.31
Beam-Shell R	18.3	148	38.15
Rod-Membrane R	20.2	147	38.66
Beam-Membrane R	18.4	146	36.88

Moreover, as it can be seen from Table 3.17, the rod/membrane model with revised formulation gives the highest displacement result among the rest of the models and the beam-shell model gives the lowest one. Comparison of the maximum displacements and Von Mises stresses, given in Table 3.17 for the coarse mesh case,

reveals that coarse mesh results for the maximum displacement and Von Mises stresses obtained with different rod/beam/shell/shell-r/membrane/membrane-r finite elements are close to each other and they are comparable. Thus, in the preliminary design stage, for the coarse mesh finite element models with the use of single elements between the rib stations, any element pair given Table 3.17 can be used.

Table 3.18: Comparison of Maximum Tip Displacement, Maximum Von Mises Stress and Von Mises Stress at the Mid Span for the Fine Mesh Wing Torque Box Models

Model (Coarse Mesh)	Displacement (cm)	Max Von Mises (MPa)	Von Mises at the Mid Span (MPa)
Rod-Shell	18.5	799	25.83
Beam-Shell	17.8	797	25.53
Rod-Shell R	18.6	738	25.64
Beam-Shell R	18.3	737	25.28

Table 3.18 gives the maximum displacements, maximum Von Mises stresses and Von Mises stresses calculated at the mid span of the wing for the upper middle skin in bay 4 of the fine mesh wing structure models. For the fine mesh case, membrane elements are excluded from the comparison because of the deficiency of the fine mesh membrane model in handling the distributed line force and pitching moment loading accurately. As it can be seen, the maximum Von Mises stresses of fine mesh models are higher than coarse mesh models. On the other hand, displacements results are almost the same when compared to the maximum displacements obtained by the coarse mesh models.

It should be noted that calculated maximum Von Mises stresses in the linear finite element analysis continue to increase beyond the yield stress as the mesh size decreases. Von Mises stress plots of the fine mesh cases clearly show that the peak stresses occur at the front spar wing root intersection in a very confined area. Spar root acts like a singular point because in the finite element analysis, all the rotations and displacements of the nodes on the wing root extensions are fixed, and this is a very stringent condition. In reality, a perfect fixed end condition is hard to achieve,

and therefore maximum Von Mises stresses near the front spar-wing root will be relaxed. Therefore, it would not be logical to continue commenting on the reasons of the peak Von Mises stress near the front spar-wing root intersection without generating a local model of the wing root and carrying out a finite element analysis on the local model. Such a local analysis would give more realistic stresses and would give more insight into the actual behavior of the wing structure near the intersection of the front spar and the wing root. However, at this point, it should also be noted that stresses that exceed the yield point are direct results of linear finite element analysis based on a linear stress-strain relationship. In reality, the stress in Al 2024 T3 material can only go slightly beyond the yield stress and a stress of “1.5 or 2” times the yield stress does not exist physically. As an example, the maximum Von Mises stress of the wing Rod-Shell model determined using a coarse and fine mesh FE models is 160 MPa and 799 MPa respectively and the fine mesh model results in 5 times larger stress than coarse mesh. Moreover, the maximum Von Mises stress of the rod/shell fine mesh wing model is 2.32 times higher than the yield stress of Al 2024 T3 material which has a yield stress of 345 MPa.

Comparison of the coarse and fine mesh results shows that there is a large discrepancy between the maximum Mises stresses of the coarse and fine mesh models. Since fine mesh finite element models capture the stress gradients better, the maximum stresses predicted by the fine mesh models are usually higher than the maximum stresses predicted by the coarse mesh models. On the other hand, the Von Mises stresses at the mid span for coarse and fine mesh models show more comparable results with the fine mesh models predicting lower stresses compared to the coarse mesh models. This observation makes sense because stress comparisons are made at the center of bay 4 away from the structural discontinuities. Since the fine mesh model is more flexible compared to the coarse mesh model, coarse mesh finite element models usually predict higher stress compared to fine mesh finite element models at regions which are away from the structural discontinuities.

It should be noted that the use of coarse mesh model is not justified in the detail design and analysis phase. Local models should be used to analyze regions which have high local stresses.

Tables 3.19 and 3.20 give the comparison of maximum axial stresses and mid span axial stresses calculated on the upper flange of the front spar at bay 4.

Table 3.19: Comparison of Maximum Axial Stress and Mid Span Axial Stress for the Coarse Mesh Wing Torque Box Models

Model (Coarse Mesh)	Max Axial Stress (MPa)	Axial Stress at the Mid Span (MPa)
Rod-Shell	237.36	37.19
Beam-Shell	229.95	35.56
Rod-Shell R	229.81	37.60
Beam-Shell R	228.02	36.12
Rod-Membrane R	231.36	37.13
Beam-Membrane R	229.50	35.56

Table 3.20: Comparison of Maximum Axial Stress and Mid Span Axial Stress for the Fine Mesh Wing Torque Box Models

Model (Fine Mesh)	Max Axial Stress (MPa)	Axial Stress at the Mid Span (MPa)
Rod-Shell	831.61	21.60
Beam-Shell	830.70	21.17
Rod-Shell R	797.46	21.53
Beam-Shell R	796.72	21.48

As it can be seen from Tables 3.19 and 3.20, the maximum axial stresses of fine mesh models are higher than coarse mesh models similar to the Von Mises stresses. On the other hand, the mid-span axial stresses determined by the fine mesh finite element models are less than the mid-span axial stresses determined by the coarse mesh finite element models.

The maximum axial stress of the wing Rod-Shell model determined using a coarse and fine mesh FE models is 237.36 MPa and 831.61 MPa respectively and the fine mesh model results in 3.5 times larger stress than coarse mesh. Moreover, the maximum axial stress of the Rod-shell fine mesh wing model is 1.72 times higher than the ultimate tensile stress of Al 2024 T3 material which has an ultimate stress of 483 MPa.

Therefore, in order to understand the accurate behavior of wing torque box structural model beyond the yield stress, non-linear stress analysis must be conducted, preferably by using local models for the areas where the stresses are high, such as

front spar wing root intersection. In addition, the type of external load and application point also has an effect on the stress distribution. In the present study, the loads acting on the wing torque box model are line loads acting through the front spar, and the effect of the line loading on the generation of the maximum Von Mises stress near the front spar – wing root intersection should not be overlooked. In the reality, the external aerodynamic load is applied through the differential pressure difference between the lower and upper skin of the wing. Distributed loads tend to relax the local stress jumps.

In the present study, the main aim in the finite element analysis part is not to use finite element method to verify the design but to study the effect of using different element pairs on the analysis results, prepare models to be used in the optimization part, and to make comparisons of the stress analysis results with the hand calculations. Therefore, no effort is spent to eliminate the maximum stresses which show up near the front spar – wing root intersection, simply because the main aim of the study is not to carry out a detailed design of a wing torque box, but rather to perform hand calculation and finite element based structural analysis in the preliminary design stage, to demonstrate the use of structural optimization early in the design phase which is given in Chapter 4. While performing structural analysis and optimization study, the effect of using different finite element pairs, which are typically used to model one dimensional and two dimensional structural elements, on the analysis and optimization results is also investigated.

3.8 Comparison of the Results of Finite Element Analysis and Hand Calculations

In this section, comparisons of the stresses that are determined with the finite element analysis are compared with the stresses obtained by using hand calculation. Stress results determined by the hand calculation are compared with the beam/shell model which is considered to be the most accurate finite element model representing the real structure. On the other hand, hand calculation is based on two structural idealizations both of which utilize the unsymmetrical bending beam theory. In the first idealization it is assumed that spar flanges and stiffeners carry axial load and skin panels and spar webs take up shear load only. Therefore, it is considered that the first structural idealization can best be approximated by the rod/shear panel finite

element model. On the other hand, in the second structural idealization, it is assumed that spar flanges and stiffeners take up axial load and skin panels and spar webs take up both axial and shear loads. Therefore, it is considered that the second structural idealization can best be approximated by the rod/membrane - r or rod/shell models.

3.8.1 Comparison of Axial Stresses in Spar Caps and Stiffeners

In order to compare the axial stresses of analytical solution with the finite element analysis results, it would make more sense to compare the stresses at the middle of the wing torque box away from the root and the tip. Since the analytical solution is based on beam analysis, stress results are not affected by the boundaries. However, in the finite element analysis stresses are affected from the boundaries, therefore the comparison of the stresses determined by the hand calculation and the finite element analysis is made away from the boundaries.

Since the second structural idealization used in the analytical model is considered to represent the true structural behavior more accurately, compared to the first structural idealization, first comparisons with the finite element analysis results are performed using the analytical model which employs the second structural idealization. Table 3.21 shows the axial stresses in the spar flanges and the stiffeners at bays number 3, 4 and 5 which are at the middle of the wing torque box, sufficiently away from the wing root and wing tip.

Table 3.21: Analytical Solution of Axial Stress in the Spars and Stiffeners

Analytical Solution – Axial Stress (MPa)						
Bay Number	Spar Cap 1	Spar Cap 2	Spar Cap 3	Spar Cap 4	Stiffener 1	Stiffener 2
Bay-3	- 80.00	57.00	- 36.20	48.20	- 66.60	56.20
Bay-4	- 41.70	30.10	- 18.30	25.90	- 34.40	29.90
Bay-5	- 19.30	13.60	- 9.00	11.20	-16.20	13.30

As it can be seen from Table 3.21, spar cap 1 which represents the upper flange of the front spar has the largest axial stress, and as expected axial stresses decrease from the root to the tip of the wing torque box.

Tables 3.22 - 3.24 give the axial stress results in the flanges of the spars and in the stiffeners, determined by the finite element analysis of wing using the rod/shell, rod/membrane R and beam/shell coarse mesh models at bays 3- 5, respectively.

Table 3.22: Finite Element Analysis Solution of Axial Stresses in the Spars and Stiffeners for the Rod/Shell Coarse Mesh Model of the Wing

FE Analysis Solution - Axial Stress (MPa)						
Bay Number	Spar Cap 1	Spar Cap 2	Spar Cap 3	Spar Cap 4	Stiffener 1	Stiffener 2
Bay-3	- 80.74	70.39	- 57.10	78.96	- 68.09	76.00
Bay-4	- 37.19	31.57	- 12.44	22.59	- 39.54	42.44
Bay-5	- 17.64	13.48	- 5.58	11.33	- 16.83	13.76

Table 3.23: Finite Element Analysis Solution of Axial Stresses in the Spars and Stiffeners for the Rod/Membrane-R Coarse Mesh Model of the Wing

FE Analysis Solution - Axial Stress (MPa)						
Bay Number	Spar Cap 1	Spar Cap 2	Spar Cap 3	Spar Cap 4	Stiffener 1	Stiffener 2
Bay-3	- 80.52	70.36	- 55.09	77.26	- 69.93	79.15
Bay-4	- 37.14	30.58	-14.10	24.08	- 40.32	42.82
Bay-5	- 17.85	13.25	- 5.44	10.17	- 16.38	13.32

Table 3.24: Finite Element Analysis Solution of Axial Stresses in the Spars and Stiffeners for the Beam/Shell Coarse Mesh Model of the Wing

FE Analysis Solution - Axial Stress (MPa)						
Bay Number	Spar Cap 1	Spar Cap 2	Spar Cap 3	Spar Cap 4	Stiffener 1	Stiffener 2
Bay-3	- 77.43	72.71	- 54.67	69.67	- 65.60	74.79
Bay-4	- 35.56	30.91	- 12.34	26.52	- 36.78	44.33
Bay-5	- 15.64	12.00	- 31.25	9.07	- 15.37	12.32

Figure 3.83 shows the axial bar stresses determined by the finite element analysis, at the center bays 3, 4 and 5 of the wing torque box which is modeled by the beam/shell finite element model.

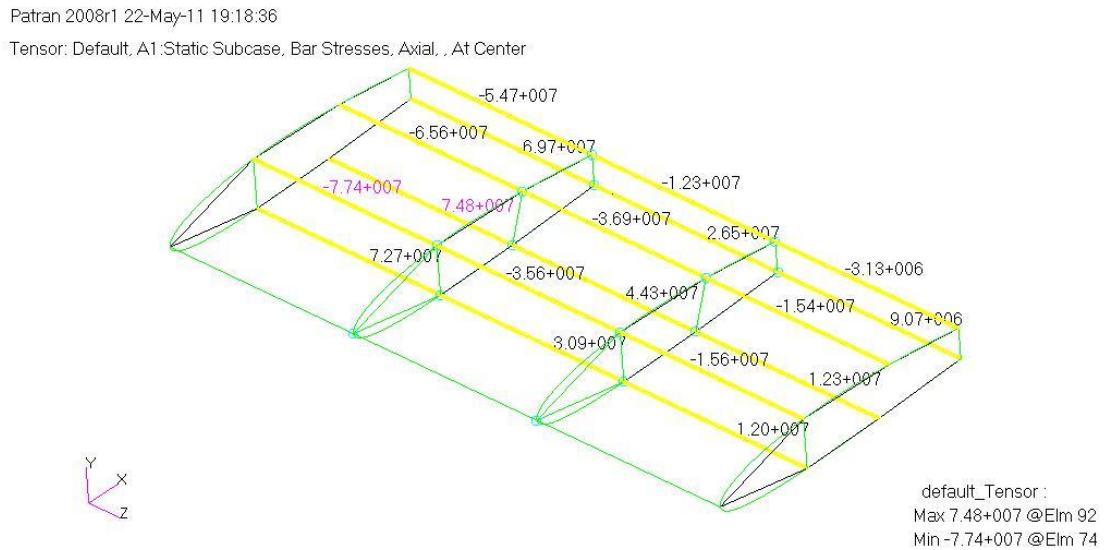


Figure 3.83: FE Axial Stress results in the Spar Flanges and Stiffeners at the Center Bays of the Wing Determined by the Finite Element Analysis- Beam/Shell Coarse Mesh Model

Tables 3.25 and 3.26 show the axial stress results in the flanges of the spars and in the stiffeners, determined by the finite element analysis of wing, using beam/shell and rod/shell fine mesh model at bays number 3-5, respectively. As it is seen in Figure 3.83, the middle elements of each bay are chosen for comparison purposes with the coarse mesh and analytical solutions. Figure 3.84 shows the locations where the axial stresses are calculated, and the finite element mesh size.

Table 3.25: Finite Element Analysis Solution of Axial Stresses in the Spars and Stiffeners for the Beam/Shell Fine Mesh Model of the Wing

FE Analysis Solution - Axial Stress (MPa)						
Bay Number	Spar Cap 1	Spar Cap 2	Spar Cap 3	Spar Cap 4	Stiffener 1	Stiffener 2
Bay-3	- 51.94	50.71	- 26.89	45.97	- 49.93	54.27
Bay-4	- 21.70	22.20	- 12.55	18.86	- 25.58	25.85
Bay-5	- 8.12	11.76	- 2.24	5.97	- 10.54	10.27

Table 3.26: Finite Element Analysis Solution of Axial Stresses in the Spars and Stiffeners for the Rod/Shell Fine Mesh Model of the Wing

FE Analysis Solution - Axial Stress (MPa)						
Bay Number	Spar Cap 1	Spar Cap 2	Spar Cap 3	Spar Cap 4	Stiffener 1	Stiffener 2
Bay-3	- 51.95	50.77	- 26.67	45.86	- 49.95	54.40
Bay-4	- 21.60	21.18	- 12.57	18.37	- 25.74	26.33
Bay-5	- 8.07	12.02	- 2.19	5.60	- 10.57	10.52

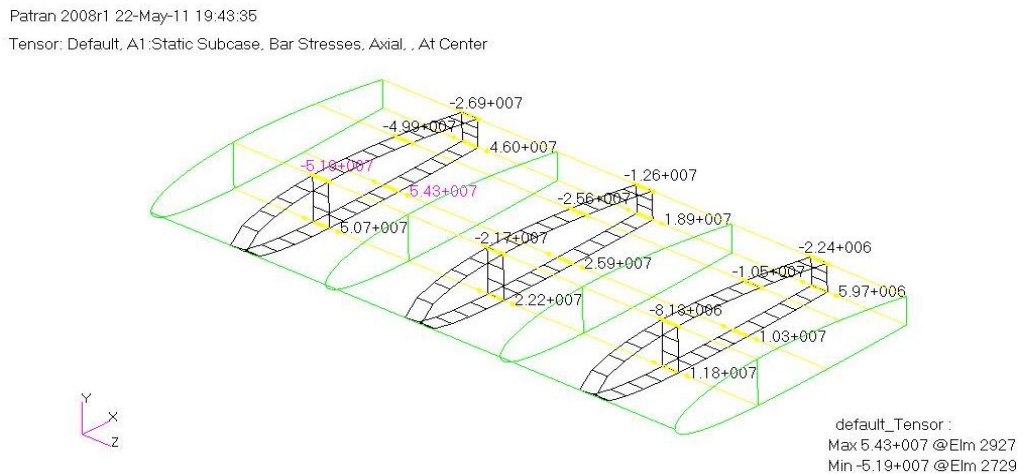


Figure 3.84: FE Axial Stress results in the Spar Flanges and Stiffeners at the Center Bays of the Wing Determined by the Finite Element Analysis- Beam/Shell Fine Mesh Model

From Tables 3.25 - 3.26 it can be seen that spar cap 1 (front spar upper flange) carries the largest axial stress which is a compressive stress as expected. On the other hand, it can be seen that coarse mesh model results in a higher axial stress values when compared to fine mesh results. Thus, it can be concluded that coarse mesh overestimates the axial stress in the beam elements which are used to model the spar caps and stiffeners. The differences in the axial stresses show the significance of the mesh refinement study that has to be conducted to reach to an acceptable mesh size which will give the accurate stress results.

Table 3.21 shows that axial stresses in the spar flanges and the stiffeners determined by the hand calculation based on unsymmetrical beam bending theory are higher than the fine mesh finite element results. It should be noted that it is reasonable for the

beam bending theory to predict higher stresses compared to the fine mesh finite element solution. Because in the unsymmetrical beam bending theory, two dimensional effects are ignored whereas, finite element solution is two dimensional. Thus, fine mesh model is more flexible compared to the one dimensional beam model, and this could one of the reasons for the differences in the results of the hand calculation and the finite element analysis. Again, it should be reminded that the comparison of the axial stresses is made at the centers of each bay away from structural discontinuity. Therefore, beam theory results are higher than the fine mesh finite element results. However, since fine mesh finite element models capture the stress gradients better, the maximum stresses predicted by the fine mesh models near structural discontinuities are usually higher than the maximum stresses predicted by the coarse mesh or the beam theory results.

3.8.2 Comparison of Axial Stress in Skins and Spar Webs

In order to compare the axial stresses in skins of the analytical solution with the finite element analysis results, it would make more sense to compare the stresses on the wing skins at the middle of the wing torque box away from the root and the tip. Since the analytical solution is based on beam analysis, stress results are not affected by the boundaries. However, in the finite element analysis stresses are affected from the boundaries, therefore the comparison of the stresses determined by the hand calculation and the finite element analysis is made away from the boundaries.

Table 3.27 shows the axial stresses (along the wing span) in the wing skins determined using the analytical solution. Axial stresses in the wing skin are given in bays 3 and 4 sufficiently away from the wing root and wing tip.

Table 3.27: Analytical Solution of Axial Stress in the Wing Skins

Analytical Solution – Axial Stress (MPa)						
Bay Number	Nose Skin Up	Nose Skin-L	Mid- Up Skin	Mid-L Skin	Right-Up Skin	Right-L Skin
Bay - 3	- 39.99	28.51	- 77.50	40.45	- 63.16	44.48
Bay - 4	- 20.85	15.05	- 40.00	21.40	- 32.80	23.60

Tables 3.28 and 3.29 show the finite element analysis stress results in the wing skins of the coarse mesh rod/shell and rod/membrane - r model at bays number 3, and 4 respectively.

Table 3.28: Finite Element Analysis Solution of Axial Stress in the Wing Skins for the Rod/Shell Coarse Mesh Model of the Wing

FE Analysis Solution - Axial Stress (MPa)						
Bay Number	Nose Skin Up	Nose Skin-L	Mid- Up Skin	Mid-L Skin	Right-Up Skin	Right-L Skin
Bay - 3	- 36.40	35.70	- 72.00	72.10	- 61.20	77.10
Bay - 4	- 15.70	11.30	- 37.50	34.90	- 24.90	31.80

Table 3.29: Finite Element Analysis Solution of Axial Stress in the Wing Skins for the Rod/Membrane-R Coarse Mesh Model of the Wing

FE Analysis Solution – Axial Stress (MPa)						
Bay Number	Nose Skin Up	Nose Skin-L	Mid- Up Skin	Mid-L Skin	Right-Up Skin	Right-L Skin
Bay - 3	- 35.30	40.40	- 74.10	73.70	- 59.80	75.60
Bay - 4	- 15.80	18.40	- 36.60	32.50	- 32.20	32.20

Figure 3.85 shows the finite element analysis results of the axial stresses, at bays number 3 and 4 in the wing upper skins and spar webs for the coarse mesh rod/shell Model.

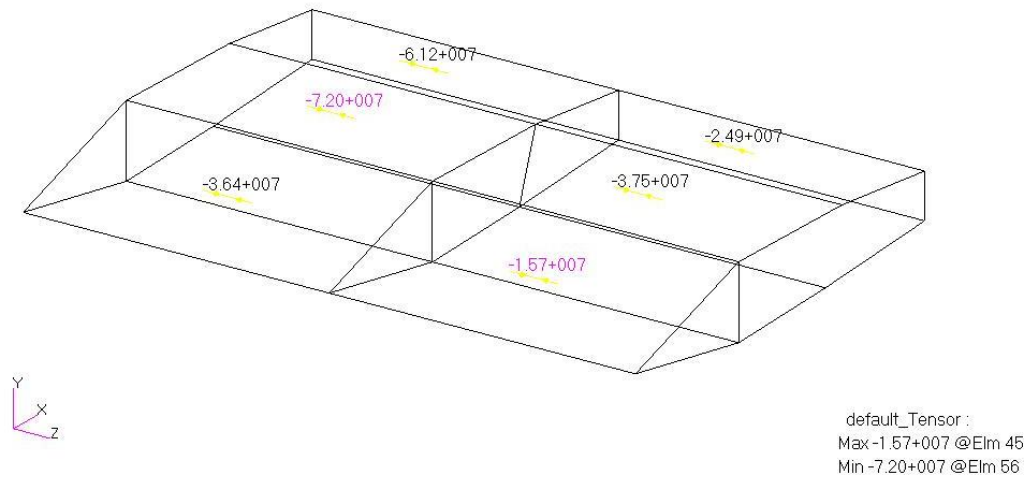


Figure 3.85: Axial Stress results in the Wing Upper Skins at the Center Bays of the Wing Determined by the Finite Element Analysis- Rod/Shell Coarse Mesh Model

Table 3.30 shows the finite element analysis stress results in the wing skins of the fine mesh rod-shell model at bays number 3 and 4 respectively.

Table 3.30: Finite Element Analysis Solution of Axial Stress in the Wing Skins for the Rod/Shell Fine Mesh Model of the Wing

FE Analysis Solution - Axial Stress (MPa)						
Bay Number	Nose Skin Up	Nose Skin-L	Mid- Up Skin	Mid-L Skin	Right-Up Skin	Right-L Skin
Bay - 3	- 41.30	38.70	- 58.00	58.30	- 38.80	50.20
Bay - 4	- 18.40	14.70	- 26.40	27.00	- 21.10	22.80

Figure 3.86 shows the finite element analysis results of the axial stresses, at bays number 3 and 4 in the wing upper skins for the fine mesh rod/shell.

Patran 2008r1 18-Aug-11 13:21:20

Tensor: Default, A1:Static Subcase, Stress Tensor, , , At Z2

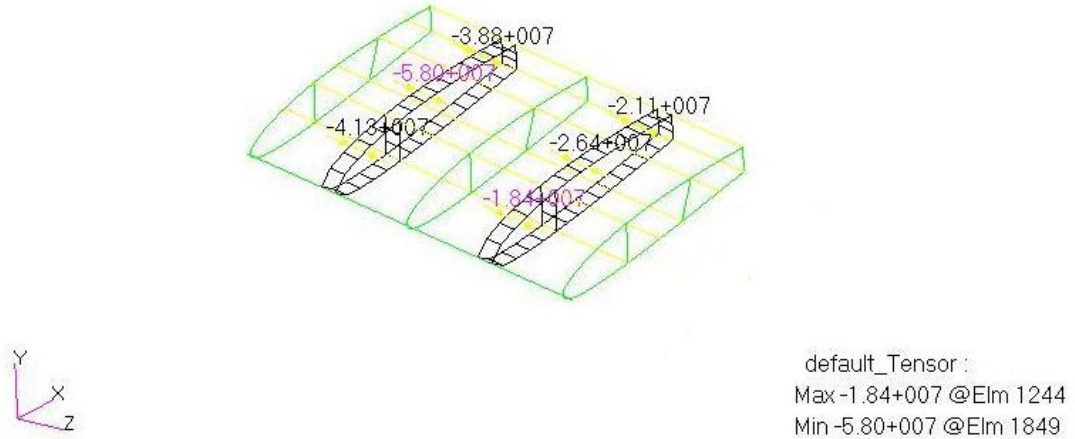


Figure 3.86: Axial Stress results in the Wing Upper Skins at the Center Bays of the Wing Determined by the Finite Element Analysis- Rod/Shell Fine Mesh Model

Comparison of the axial stresses given in Tables 3.27 - 3.30 show that in general analytically determined axial stresses at various points on the wing skin are comparable to the axial stresses determined by the coarse and fine mesh finite element models. The differences are again due to the fact that in the unsymmetrical beam bending theory two dimensional effects are ignored whereas finite element solution is two dimensional. However, it is considered that for the preliminary design purposes analytically determined axial stresses can be used in local buckling calculations.

3.8.3 Comparison of the Von Mises Stresses in the Wing Skins and Spar Webs

The Von Mises stresses obtained by analytical solution are given in Table 3.31. The stresses are calculated at the points indicated in Figure 3.87. Stress monitor points are selected on the wing skins and spar webs just before and just after the spar flanges and stiffeners, the average value of the stresses acting on each skin is used in calculating Von Mises stress. Figure 3.88 shows the wing skins and spar webs definitions on which Von Mises monitor points are selected.

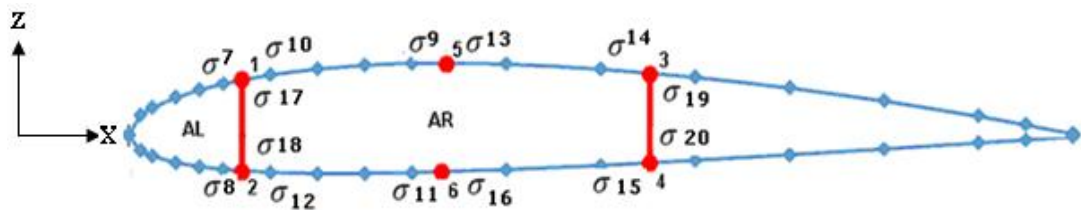


Figure 3.87: Von Mises Stress Monitor Points on the Wing Skins and Spar webs of the 2nd Idealization

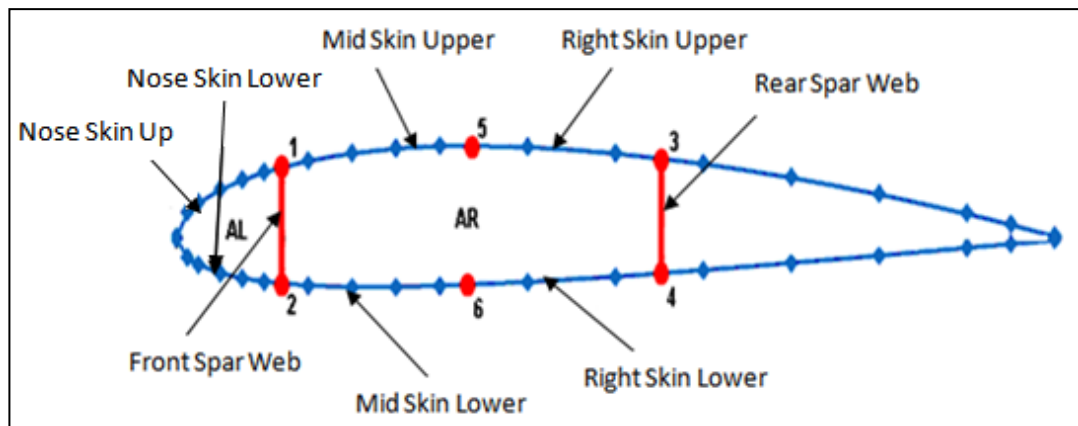


Figure 3.88: Wing Skins and Spar Webs Definition

From Figures 3.87 and 3.88, it can be seen that σ_7 refers to the Von Mises stress on the upper nose skin whereas σ_8 refers to the Von Mises stress on lower nose skin. In the same manner the rest of the Von Mises stresses are defined.

Table 3.31 gives the analytically determined the Von Mises stresses on the wing skins in bays 3 and 4.

Table 3.31: Von Mises Stress in the Wing Skins-Analytical results

Analytical Solution – Von Mises Stress (MPa)						
Bay Number	Nose Skin Up	Nose Skin-L	Mid- Up Skin	Mid-L Skin	Right-Up Skin	Right-L Skin
3	80.57	59.05	75.70	78.95	74.18	60.21
4	41.67	30.11	39.80	56.10	59.10	33.10

Tables 3.32 and 3.33 show the Von Mises stresses determined by the coarse mesh rod-shell and rod/membrane - r finite element models, respectively. Again the stresses determined at the center of the bays 3 and 4 are tabulated for comparison purposes.

Table 3.32: Finite Element Analysis Solution o of Von Mises Stress in the Wing Skins of the Rod/Shell Coarse Mesh Model of the Wing

FE Analysis Solution – Von Mises Stress (MPa)						
Bay Number	Nose Skin Up	Nose Skin-L	Mid- Up Skin	Mid-L Skin	Right-Up Skin	Right-L Skin
Bay - 3	39.98	50.52	77.89	90.34	69.54	78.79
Bay - 4	36.76	20.63	40.35	47.70	46.86	35.03

Table 3.33: Finite Element Analysis Solution of Von Mises Stress in the Wing Skins for the Rod/Membrane-R Coarse Mesh Model of the Wing

FE Analysis Solution – Von Mises Stress (MPa)						
Bay Number	Nose Skin Up	Nose Skin-L	Mid- Up Skin	Mid-L Skin	Right-Up Skin	Right-L Skin
Bay - 3	38.02	43.47	77.11	90.76	62.76	72.93
Bay - 4	18.55	20.07	38.66	42.77	45.73	36.06

Table 3.34 shows the finite element analysis stress results in the wing skins of the fine mesh rod/shell model at bays number 3 and 4 respectively.

Table 3.34: Finite Element Analysis Solution of Von Mises Stress in the Wing Skins for the Rod/Shell Fine Mesh Model of the Wing

FE Analysis Solution – Von Mises Stress (MPa)						
Bay Number	Nose Skin Up	Nose Skin-L	Mid- Up Skin	Mid-L Skin	Right-Up Skin	Right-L Skin
Bay - 3	41.87	40.59	57.95	63.57	50.84	51.64
Bay - 4	18.94	16.18	25.83	29.08	36.15	25.10

Comparison of Tables 3.31 - 3.33 with Table 3.34 shows that Von Mises stresses calculated by the fine mesh finite element models are actually lower than the Von Mises stresses calculated by the coarse mesh models at the identical locations on the wing structure. However, since fine mesh finite element models capture the stress gradients better, the maximum stresses predicted by the fine mesh models are usually higher than the maximum stresses predicted by the coarse mesh models. Table 3.33 also shows that coarse mesh rod/membrane – r model captures the Von Mises stresses nicely. There are no major differences between the Von Mises stresses predicted by the coarse mesh rod/shell and rod/membrane - r finite element models. Based on the comparison of the Von Mises stresses determined by the finite element solution and the simplified method of analysis using the second structural idealization several conclusions can be drawn. It should be noted that finite element models are two dimensional models, whereas in the simplified method one dimensional beam model is used. Therefore, finite element models are more flexible compared to the beam model of the simplified method, and the strain energy distribution is two dimensional. Therefore, in general one can expect to have lower stresses by the the finite element analysis away from any structural discontinuity. Fine mesh results given in Tables 3.31 and 3.34 confirm that Von Mises stresses predicted by the simplified method are consistently higher than the Von Mises stresses predicted the by the fine mesh finite element models. One main effect which is not considered in the simplified beam model is the axial stresses generated in the

flanges and skins due to torsion. However, since bays 3 and 4 are away from the restraint end the the effect of torsion on the results of the finite element model can be considered to be relatively small. On the other hand, except for the upper nose skin, Von Mises stresses determined by the coarse mesh finite element models and the simplified method are close to each other in bays 3 and 4. The closeness of the Von Mises stresses in the mid bays is due to the fact that coarse mesh finite element models behave more stiff compared to fine mesh finite element models, therefore beam model of the simplified method can be simulated best by the coarse mesh finite element models.

One final comment is that the Von Mises stresses determined by the analytical solution are consistently higher than the Von Mises stresses determined by the fine mesh rod/shell model. However, analytically determined axial stresses show better agreement to the axial stresses determined by the fine mesh rod/shell model. From these observation it can be concluded that in-plane shear stresses are the main reason for the discrepancy between the Von Mises stresses predicted by the simplified analytical method and the fine mesh rod/shell model. However, both axial stresses and Von Mises stresses predicted by the simplified analytical method show better agreement with the axial stresses and Von Mises stresses predicted by the coarse mesh rod/shell finite element model. This observation also confirms that simplified analytical method and the coarse mesh finite element models are more comparable to each other than the simplified analytical model and the fine mesh finite element model. It is seen that the highest discrepancy between the Von Mises stresses predicted by the simplified analytical method and the coarse mesh rod/shell model is in upper nose skin. However, for the upper nose skin axial stresses predicted by the simplified analytical method and the coarse mesh rod/shell model agree very closely. Therefore, it can again be concluded that shear stress predicted by the simplified analytical method is the main reason for the large discrepancy in the Von Mises stresses in the upper nose skin.

CHAPTER 4

STRUCTURAL OPTIMIZATION OF WING TORQUE BOXES USING DIFFERENT TYPES OF FINITE ELEMENTS

4.1 Introduction

Optimization techniques play a vital role in aerospace structural design. The main purpose in design optimization is to find the best ways a designer or a decision maker can obtain maximum benefit from the available resources. In this chapter, structural optimization of wing torque boxes is performed by the finite element software MSC.NASTRAN® using the gradient based option.

Different element combinations that are typically used in practice are used to model the wing torque boxes while carrying out the structural optimization. The main objective is to investigate the effect of using different one and two dimensional element pairs on the final optimized configuration of wing torque box. During the optimization, convergence is tried to be achieved with different mesh sizes, and the objective function is defined as minimizing the weight of the wing. The effects of different starting points and the effect of relaxing constraint on the optimized wing configurations are also investigated during the design optimization.

4.2 Optimization in Structural Design

The need for optimization arose in the challenging problems faced by engineers in different areas of engineering industry which include Aeronautics, Space

Automotive and Marine. Weight saving in aerospace structures is becoming ever more significant. Thin walled lifting surfaces are regions where substantial weight savings can be achieved if optimization techniques are used early in the design phase.

4.2.1 Requirements for Structural Design

The essential requirement for an efficient structural design is that the response of the structure must be acceptable while satisfying certain specifications. In other words, the design must be at least in the feasible design range. The desirable design is chosen among the designs in the feasible region depending on the objective function chosen which could be the minimum weight, minimum or maximum performance, minimum cost or a combination of them.

4.2.2 Structural Optimization Problem

The optimization problem can be defined as linear or non-linear depending on the the character of the objective function, constraints and the design variables. The optimization problem is defined as linear if the objective function and the constraints involving the design variables are linear. On the other hand, the optimization problem is defined as non-linear if just one of the objective function or constraints or design variables is non-linear [21].

The structural optimization problem can be deceptively simple to formulate. It can be written as:

$$\text{Find } \mathbf{x} \text{ to minimize } f(\mathbf{x}) \text{ subject to } \mathbf{g}(\mathbf{x}) \leq 0 \text{ and } \mathbf{h}(\mathbf{x}) = 0 \quad (4.1)$$

Minimize $f(\mathbf{x})$ subject to $\mathbf{g}(\mathbf{x}) \leq 0$ and $\mathbf{h}(\mathbf{x}) = 0$ where

$$\mathbf{g}(\mathbf{x}) \leq \mathbf{0} \Rightarrow \begin{cases} \mathbf{g}_1 \leq \mathbf{0} \\ \mathbf{g}_2 \leq \mathbf{0} \\ \vdots \\ \mathbf{g}_m \leq \mathbf{0} \end{cases} \quad \text{And} \quad \mathbf{h}(\mathbf{x}) = \mathbf{0} \Rightarrow \begin{cases} \mathbf{h}_1 = \mathbf{0} \\ \mathbf{h}_2 = \mathbf{0} \\ \vdots \\ \mathbf{h}_k = \mathbf{0} \end{cases}$$

where f is the objective function and it is a scalar, \mathbf{x} is vector of n components, \mathbf{g} is the vector of m inequality constraints, and \mathbf{h} is the vector of k equality constraints.

4.3 MSC.NASTRAN Design Optimization

In recent years, structural optimization has been combined with finite element analysis to size structures that minimize weight of the structure subject to a number of constraints. MSC.NASTRAN® is one of several programs offering optimization capabilities. It is capable of achieving satisfactory results while saving much of the designer time while performing optimization.

4.3.1 Optimization Process in MSC.NASTRAN

Design optimization capability of MSC Nastran is composed of two parts. The first part is the analysis model, in which grid locations, element structure and properties, material information, loads, boundary conditions and load cases are described. The second part is the design model which defines the design variables, relates the design variables to element properties, defines the design responses, and describes constraints and objectives in the design model. The initial design is the input to the MSC.NASTRAN® optimization process.

In MSC.NASTRAN® optimization process, a finite element analysis is performed first and for design sensitivity and optimization, it is necessary to perform multiple analyses frequently. The constraint screening activity refers to the process that is used to identify those constraints that are likely to drive the redesign process. In another words, by the constraint screening activity those constraints that are violated or likely to be violated are identified. These are set to be as active constraints. Sensitivity analysis is always performed automatically in MSC.NASTRAN® whenever design optimization is requested. Design sensitivity analysis computes the rates of change of structural response quantities or changes in the constraint values with respect to changes in the design variables.

MSC.NASTRAN® uses the DOT optimization code in the background as the optimizer [22]. The approximate model is constructed by using the information from

finite element analysis and sensitivity analysis. This model involves the construction of high-quality approximations to the finite element results so that the number of full scale finite element analysis is kept to a minimum. Optimizer performs optimization process by using the approximate model. By default, gradient based methods are used to construct improved design. Other available methods are sequential linear programming and sequential quadratic programming.

The improved model is the point at which the finite element model is updated based on the results from the optimizer so that a new finite element analysis is started. The improved model is compared with the previous model and if the changes are below the desired value, this means that soft convergence is achieved. Then, after the finite element analysis, one more convergence test for hard convergence is performed. Detailed information about MSC.NASTRAN® sensitivity analysis and optimization process is given in Reference [23]. However, it would be worthwhile to overview the approximation concepts used in the structural optimization in more detail. The optimizer programs need frequent function evaluations to calculate design responses and response derivatives to calculate design sensitivities. Therefore, the cost of optimization becomes very high if traditional optimization approach is followed which is depicted in Figure 4.1.

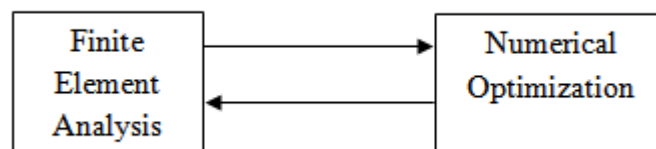


Figure 4.1: Traditional Optimization Approach

As it is shown in Figure 4.1, traditional approach of optimization involves request for a finite element analysis whenever the optimizer needs function evaluations. Therefore, in most design problems unless the problem is small in scale, the traditional approach tends to be useless. To overcome this major drawback, MSC Nastran employs concepts that limit the number of required finite element analysis. These concepts are named as approximation concepts used in structural optimization and they can be grouped into three major categories.

Design variable linking:

Design variable linking refers to narrowing the design task to that of determining the best combination of just few of design variables. It becomes much more efficient to link design variables if possible. That is, it would be advantageous if all the design variables could be varied in a suitably proportional manner according to the changes made to a much smaller set of independent variables. In Nastran this task is established by the user.

Constraint Screening:

Another concept which is employed by MSC Nastran that simplifies the numerical optimization process is to delete constraints which are not critical. In order to achieve constraint deletion, constraints that are violated or nearly violated must be identified. These constraints which are likely to be violated are the ones which derive the design. Constraint deletion allows the optimizer to consider a reduced set of constraints, and also reduces the computational effort associated with determining the required structural response derivatives.

Approximate Design Model:

Once the constraint set that seems to be deriving the design is identified, the next step that MSC Nastran follows is to perform parametric analysis in order to determine how these constraints vary as the design is modified. A parametric study is carried out with formal approximations, or series expansions of response quantities in terms of design variables. Formal approximations make use of the results of sensitivity analysis to construct an approximation to the true design space. Although formal approximations are locally valid, they are explicit in the design variables. The resultant explicit representation can then be used by the optimizer whenever function or gradient evaluations are required, instead of the costly implicit finite element analysis. The use of the approximate model is illustrated in Figure 4.2. Finite element model forms the basis for creation of the approximate models which is subsequently used by the optimizer. The approximate model includes the effect of design variable linking, constraint deletion, and formal approximations. Constraint deletion and formal approximations are performed automatically in MSC Nastran [23].

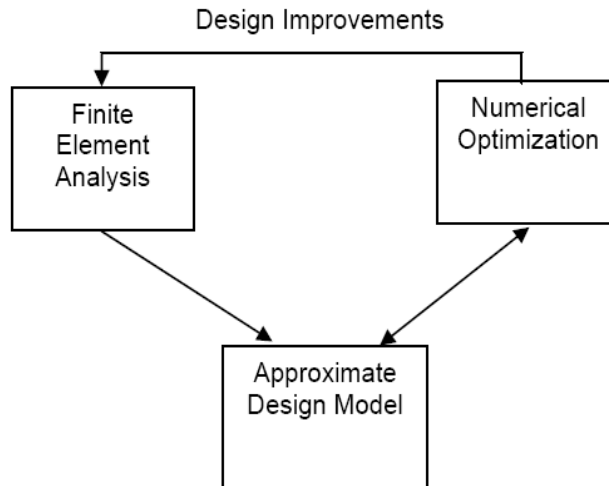


Figure 4.2: Coupling finite element analysis and optimization using approximate design model [23]

Once a new design has been proposed by the optimizer, based on the information supplied by the approximate model, in the next step a detailed analysis is performed of the new configuration to see if it has actually managed to satisfy the various design constraints and make improvement in the objective function. The upper segment denoted by ‘Design Improvements’ in Figure 4.2 represents the re-analysis update of the proposed designs. If a subsequent approximate optimization is needed, the finite element analysis serves as the new baseline from which to construct another approximate sub-problem. This cycle may be repeated as necessary until convergence is achieved, and these loops are referred to as design cycles in MSC Nastran [23]. Expanded version of Figure 4.2 is given in Figure 4.3. MSC Nastran utilizes the DOT optimization algorithm from Vanderplaats R&D, Inc. [22]. As Figure 4.3 shows, the optimizer interacts with the approximate model rather than the finite element model and produces an improved design. Once the improved design is obtained, the finite element model is updated based on the results from the optimizer so that a new finite element analysis can be performed.

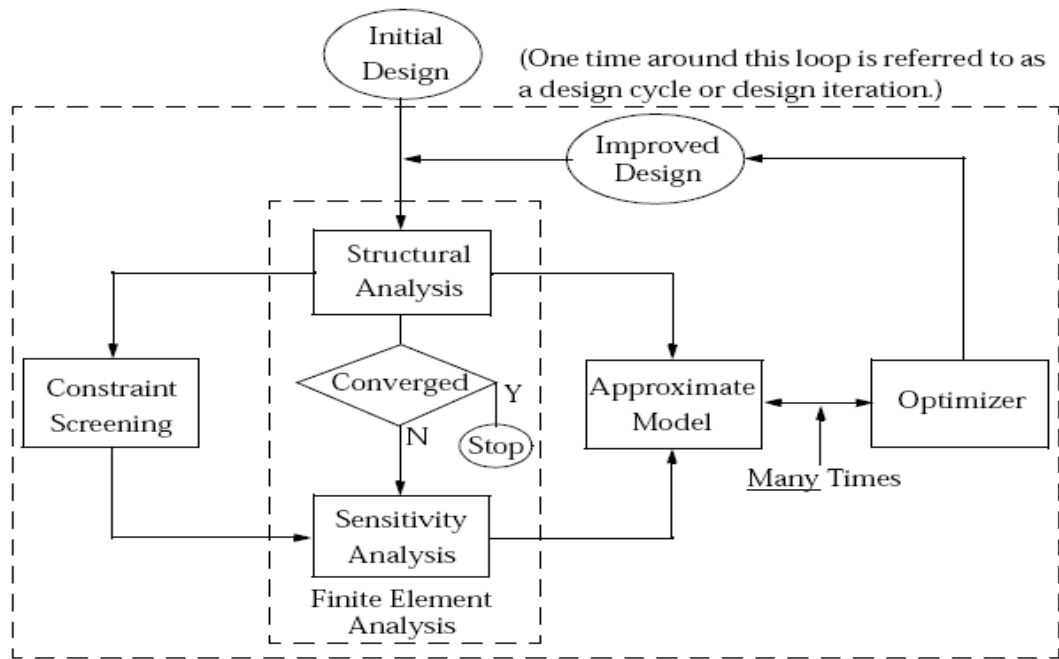


Figure 4.3: MSC.NASTRAN® Implementation of Structural Optimization

A key part of the implementation of the optimization process is to determine when to stop the iterations. There are two levels at which convergence is tested. The lower level is at the optimizer level, and it is at this level where the optimizer decides on the optimized solution based on the output of the approximate model. The second and higher level is with respect to the overall design cycles. Figure 4.3 shows the locations of higher level of convergence tests. As shown in Figure 4.3 hard convergence compares the most recent finite element analysis with those from the previous design cycle. Since this test compares exact results from two consecutive analyses, it is named as hard convergence. This test is used as the default test for determining whether or not to terminate the design-cycle process. On the other hand soft convergence compares the design variables and properties output from the approximate optimization with those of the input to the approximate optimization. If design variables and properties have not changed appreciably, another finite element analysis may not be asked for.

4.3.2 Steps of Performing Optimization Task

There are three steps to perform an optimization task using MSC.NASTRAN® optimization tools. The first step is creating an input .bdf-file which includes file management section, executive control section, case control section and bulk data section. The second step is executing a MSC.NASTRAN® run and the third step is post processing of the results.

4.3.2.1 Creating an Input BDF-File

The File Management Section (FMS) is primarily intended for the attachment and initialization of database sets (DBsets) and FORTRAN files. The initialization of DBsets includes specification of their maximum size, member names, and physical filenames. The initialization of FORTRAN files includes the specification of their filenames, FORTRAN unit numbers, and FORTRAN attributes.

In most classes of problems that use MD Nastran solution sequences (SOLs), no file management statements are required because a default file management section is executed at the beginning of every run.

The Executive Control Section describes the executive control statements. These statements select a solution sequence and various diagnostics. Most executive control statements are order independent. In executive control, the only required statement is “SOL 200” which implies design optimization.

The Case Control Section has several basic functions. These functions select loads and constraints, requests printing, plotting, and/or punching of input and output data, and finally define the sub-case structure for the analysis.

The Bulk Data Section contains entries that specify model geometry, element connectivity, element and material properties, boundary conditions, and loads. Some entries, such as loads and boundary conditions, are selected by an appropriate case control command. Entries are prepared in either fixed or free field format. More information is provided in Appendix [B] and Appendix [C].

4.3.2.2 MSC.NASTRAN Run

MSC.NASTRAN® job is submitted for optimization solution after completing bdf input file. The output file is written in .f06, .pch (punch) and .op2-files format. The xdb-file can also be used as an alternative of op2 file. A check for errors and warning must be done after each before post processing the results.

4.3.2.3 MSC.NASTRAN Post Processing

There are different ways of results post processing. One way is by importing the op2-files into MSC.NASTRAN® using post processor tool of MSC/PATRAN® history of each variables, objective function and constraints can be plotted on graphs. The results of structural analysis such as stress distribution, displacements, and grid point forces can be viewed on the final solution and also at each step of the optimization process. In addition, .pch-file provides information for the final design cycle and it is typically only these data that are of interest in subsequent analysis such as final grid locations final element properties, stress and displacement results at each design cycle. These outputs can be conveniently used as input into another computer analysis. Whereas xdb-file on the other hand is incapable of giving such results like history of each variables and objective function as op2-files do. The results that can be shown by importing the xdb-file into MSC.NASTRAN® are displacement and stress results and their plots at each optimization cycle.

The second results post-processing way is through the output .f06-files. F06-files contain similar information as op2-files but in formatted text form. Moreover .f06-files give the optimization results and convergence check for each design cycle based on the approximate model.

4.3.3 Continuous and Discrete Optimization in MSC.NASTRAN

Optimization problems can generally be described as either continuous or discrete, but may be a mix of both. MSC.NASTRAN® Sol 200 supports structural design optimization for continuous design variables but also has the capability to apply discrete variables in the optimization process. This is done in recognition of the fact

that practical engineering considerations frequently dictate that values of the designed properties be chosen from a discrete set. While the variables in continuous optimization problems are allowed to take on any values permitted by the constraints, discrete optimization is concerned with the case where the variables may only take on discrete and typically integer values.

MSC.NASTRAN® developed and implemented approaches to deal with discrete variables with limited computational cost. Design of Experiments (DOE) and Conservative Discrete Design (CDD) approaches together with engineering round-off and round-up methods, can be used to process discrete variables at any specified continuous design optimization cycle for structural design problems [11, 23]. The discrete optimization methods are now briefly reviewed.

4.3.3.1 Round-Up and Round-Off Discrete Variable Processing Methods

These two methods simply round up or round down the continuous solution obtained from solving a corresponding continuous optimization problem. These two methods have been implemented in MSC.Nastran® for quick discrete design solutions. These methods simply automate the simple rounding process a user might employ after a continuous optimization, and require no new analysis.

4.3.3.2 Conservative Discrete Design (CDD) Variable Processing Method

The CDD approach is employed to quickly obtain a conservative discrete solution based on the continuous optimal solution by using the sensitivity information. In the CDD method, each variable is independently set to the discrete values that bracket the continuous variable result. An approximate analysis is carried out for the discrete variable above the continuous value and also with the discrete variable below the continuous value. The constraint results of these two analyses are compared and the discrete variable is chosen that gives the minimum value for the maximum constraint. This is repeated for each design variable so that $2 \cdot n_{ddv}$ (where n_{ddv} is the number of design variables that can take on discrete sizes) approximate analysis are carried out for the CDD approach. In the CDD method the main aim is to search for a feasible discrete solution. The advantages of CDD methods is that it may be

used for a design with large number of discrete variables, and it is able to produce better discrete solution than round-off method.

4.3.3.3 Design of Experiments (DOE) Variable Processing Method

The DOE approach aims to obtain a good discrete design by evaluating the approximate objective and constraints with extra but limited computational cost.

The implementation of DOE employed in MSC.Nastran employs an exhaustive search when n_{ddv} (the number of design variables that can take on discrete sizes) is 2^{16} or less. Above this value, an Orthogonal Array concept is employed to select candidate arrays that provide a representative sampling of the overall design space.

The continuous optimal design obtained from the current SOL 200 solution is used instead of the initial design model as a baseline for discrete variable processing. DOE assumes that the discrete optimum is close to the continuous optimum, and it is expected that a discrete solution by the DOE be close to the discrete optimum due to the selected design baseline. Therefore, searching a feasible discrete design is emphasized in the DOE processing. A major advantage of the DOE is its simplicity in applications, non-gradient methodology, and ability to handle discrete variables. More detail information and discussion about the DOE can be found in References [11, 24].

4.4 Wing Torque Box Used in Structural Optimization

The wing structure that is used in optimization is the wing that is used in the analysis part given in Chapter 3. The technical specifications of the wing are repeated here for completeness. The wing structure used in structural optimization is for a single utility aircraft having a maximum takeoff weight of 1460 kg and minimum operating weight of 861 kg. The wing is straight and unswept and has a NACA 2412 airfoil profile with a rectangular planform, and a chord length of 1.524 m, semi-span of 4.572 m. The wing is composed of two spars, two stiffeners and seven ribs dividing the wing into 6 equal sections of length 0.762 m. The root extensions of the front and rear spars are of 0.5 m in length. The front spar is located at 25 % of the chord length, and the rear spar is located at 70% of the chord length, and the upper and

lower stiffeners are located respectively at 50 % and 46% of the chord length. Figure 4.4 shows the wing model that is used in the optimization study.

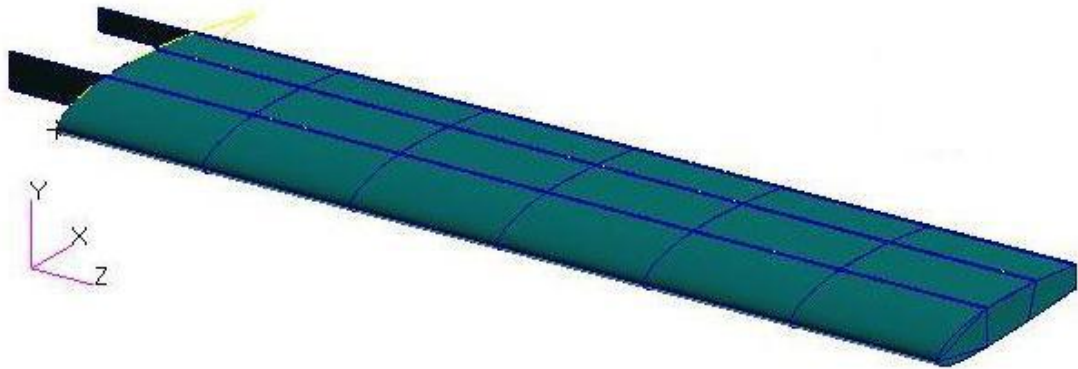


Figure 4.4: Wing Model Used in the Optimization Study

It should be noted that the wing structure used in the optimization study is selected from the one of the many wing designs performed in Chapter 2 using the hand calculation method. The particular wing configuration is the one that is analyzed in detail in Chapter 3 by the finite element method using different element pairs for the 1D and 2D finite elements.

4.5 Aerodynamic Loading Acting On the Wing Structure

The aerodynamic loading is distributed to the wing structure in a discrete fashion by calculating equivalent force components at the 25 % of the chord length. The calculation of the external aerodynamic load is performed using the code provided by ESDU, ESDUpac A9510 attached in ESDU 95010 [13].

Span-wise lift and pitching moment distributions at 25 % of the chord measured from the leading edge are given in Figures 4.5 and 4.6. The structural optimization is carried out by using the external aerodynamic load calculated at the minimum maneuvering speed, point A on the V-N diagram.

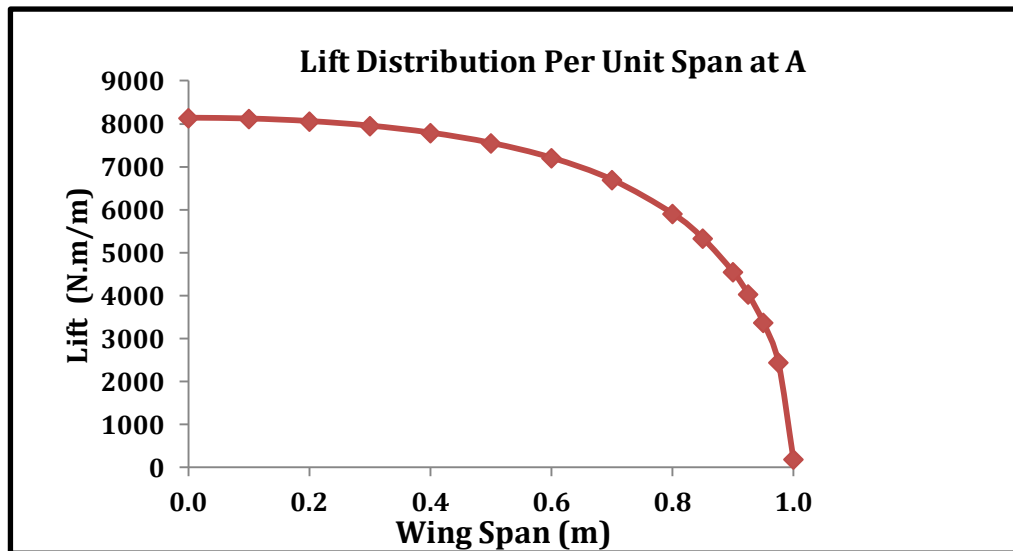


Figure 4.5: Span-wise Variation of the Aerodynamic Lift Distribution –Point A

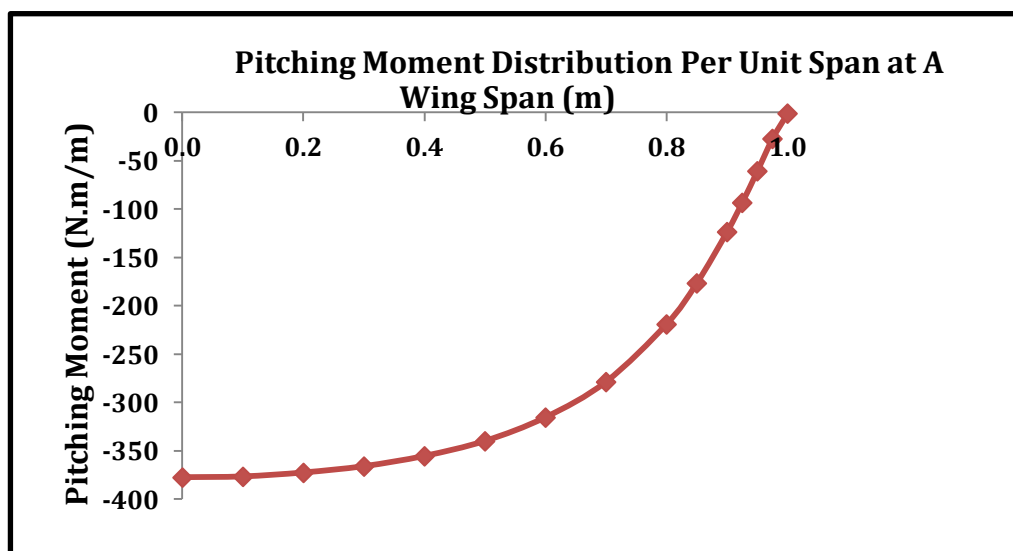


Figure 4.6: Span-wise Variation of the Aerodynamic Pitching Moment Distribution - Point A

Lift force and pitching moment are considered as line loading, and they are distributed along the lower front spar as shown in Figure 4.7. It is also assumed that the wing is fixed at wing root extensions.

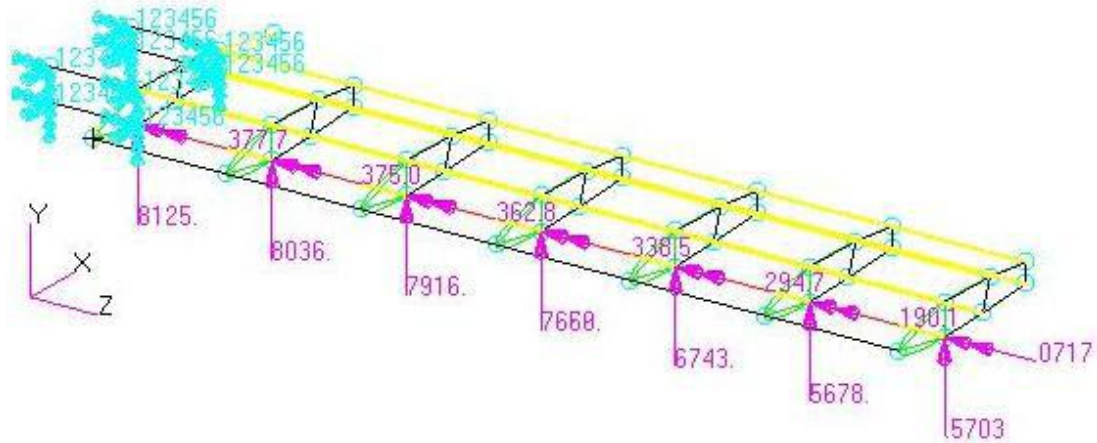


Figure 4.7: Distribution of the External Aerodynamic Loading

4.6 Finite Element Types Used in the Wing Torque Box Structural Optimization

The wing configuration is modeled by using MSC®/PATRAN software. Different finite elements types are used to create six different models. Table 4.1 shows the element pairs that are used to model the two dimensional and the one-dimensional members of the wing structure.

Table 4.1: Combination of FE Types Used in Different Models

Model	Thin Walled Panels	Spar Caps and Stiffeners
1	Shell Element (CQUAD4)	Rod Element (CROD)
2	Shell Element (CQUAD4)	Beam Element (CBAR)
3	Shell-R Element (CQUADR)	Rod Element (CROD)
4	Shell-R Element (CQUADR)	Beam Element (CBAR)
5	Membrane-R Element (CQUADR)	Rod Element (CROD)
6	Membrane-R Element (CQUADR)	Beam Element (CBAR)

The models defined above are used in the optimization of the wing torque box. In the definition of the structural optimization problem, objective function is taken as the weight of the wing with a goal to minimize the weight. The design constraints are defined on the Von Mises stress, axial stress, and the maximum tip displacement. Moreover, prevention of local buckling of the thin walled panels of the wing between

the rib stations is also defined as additional design constraint. Local buckling equations are defined by design equations and entered externally into the MSC. Nastran input file.

The design variables are defined as thicknesses of thin panels (skins, ribs and spar webs) and cross sectional areas of spar caps and stiffeners. By using MSC.NASTRAN®, continuous and discrete optimization solutions are carried out for all models. Finite element models are prepared for coarse mesh and fine meshes, and the effect of mesh size on the optimized results is also investigated.

4.7 Definition of the Wing Torque Box Optimization Problem

Definition

The wing torque box structural optimization that is performed in the thesis specifically deals with property optimization. Therefore, location of spars, stringers and ribs are taken as constant and shape optimization is not considered in this study. The wing torque box optimization problem is defined as:

Objective Function:

- Minimize the weight of the wing torque box.

Constraints:

Stress Constraints:

- Von Mises stresses in skins, spar webs and ribs: The lower limit is unconstrained; the upper limit is constrained with a maximum value of 322 MPa which is used as the allowable stress in the current study.
- Axial stresses of spars and stiffeners: The lower limit is constrained with a compression stress value of 322 MPa (-322 Mpa), and the upper limit is constrained with a tensile stress value of 322 MPa.

Deflection Constraints:

- The maximum tip displacement of the wing torque box is limited to 20 cm.

Local Buckling Constraints:

Local buckling equations are defined by design equations and entered externally to the MSC. Nastran input file.

- Combined compression/tension and shear local buckling of the upper wing skins should be prevented. In case of tension, the axial stress ratio R_C is taken as a negative number.

$$R_S^2 + R_C \leq 1 \Rightarrow \left(\frac{\tau}{K_S E \left(\frac{t}{b}\right)^2} \right)^2 + \left(\frac{\sigma_{Compression}}{K_C E \left(\frac{t}{b}\right)^2} \right) \leq 1 \quad (4.2)$$

- Combined bending and shear local buckling of the spar webs should be prevented

$$R_S^2 + R_b^2 \leq 1 \Rightarrow \left(\frac{\tau}{K_S E \left(\frac{t}{b}\right)^2} \right)^2 + \left(\frac{\sigma_{Compression}}{K_b E \left(\frac{t}{b}\right)^2} \right)^2 \leq 1 \quad (4.3)$$

- Buckling of ribs due to shear stress should be prevented

$$\frac{\tau}{K_S E \left(\frac{t}{b}\right)^2} \leq 1 \quad (4.4)$$

While writing the limits of the constraints, the lower limit is unconstrained, and the upper limit is constrained with a maximum value of 1.01.

Geometric or Side Constraints which includes the following:

Constraints on Thicknesses of Thin Walled Panels:

- Thicknesses of thin panels are forced to decrease from the root to the tip of the wing. Therefore, design equations relating the thicknesses are defined and entered externally to the MSC. Nastran input file. Such a constraint definition is necessary because in the gradient based optimization of wing torque box, it is very likely that the solution reached may be a local optimum solution. In the preliminary analysis carried out, it is experienced that in some of these local optimum solutions, thicknesses of some inboard thin panels turned out

to be smaller than the thicknesses of some outboard thin panels. Because in the gradient based solution, if the optimum solution is stuck around a local optimum, it may not get around it all the time, and in such cases such strange results may be obtained. Therefore, in the present study, design equations are written in the input file such that thicknesses of the thin walled panels are forced to decrease from wing root to wing tip. Thus, the optimizer is driven towards an optimum solution which makes sense from an engineering point of view. It should be noted that since the external load decreases from root to tip, and in the load case no local concentrated forces are considered along the span of the wing, side constraints drive the optimizer in the correct direction towards optimum solution.

Constraints on Spar Cap and Stiffener Areas:

- Spar cap and stiffener areas are also forced to decrease from the wing root to the tip of the wing. Equations relating areas are defined by design equations and entered externally to the MSC. Nastran input file. The same reasoning that is written for the thicknesses is also valid here.

Design Variables:

- For the finite element models which have flanges and stringers modeled with rod elements, 92 design variables are used which represent the thicknesses of wing skins, and spar webs, ribs, and spar flange and stringer areas.
- For the finite element models which have flanges and stringers modeled with beam elements, 128 design variables are used which represent the thicknesses of wing skins, and spar webs, ribs, and beam height and widths. In beam modeling of spar flanges and stringers, it is assumed that beams have rectangular cross-sections. In the discrete solution, beam heights are selected from the standard thickness lists assuming that spar caps and stringers are cut from standard size sheets, whereas continuous optimum solutions are used for the beam widths since beam widths, which are cut from thin sheets, can be adjusted to be any continuous value.

In the following the breakdown of the design variables is given. Figure 4.8 shows the wing model with spars, stiffeners, ribs and bays location.

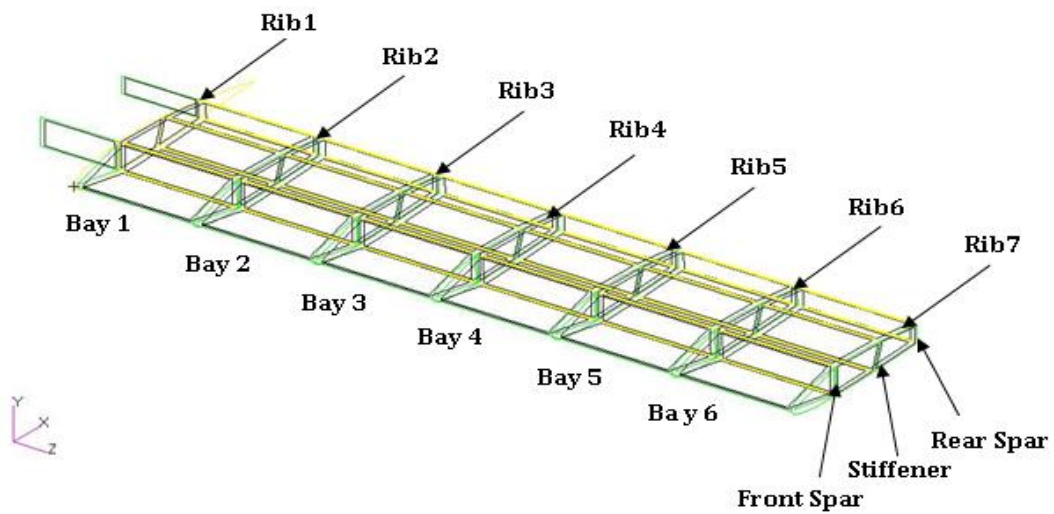


Figure 4.8: Wing Model Showing the Spar, Stiffener and Rib Locations

Design variables associated with the thicknesses of thin walled panels:

- Seven Nose Rib Thicknesses
- Seven Mid rib Thicknesses
- Six Front Spar Web Thicknesses
- Six Rear Spar Web Thicknesses
- Six Nose Skin Thicknesses
- Six Upper Mid-Skin Thicknesses
- Six Lower Mid-Skin Thicknesses
- Six Upper Rear (Right) -Skin Thicknesses
- Six Lower Rear (Right) -Skin Thicknesses

Figure 4.9 illustrates the rendered coarsest mesh finite element wing model and shows the two dimensional elements which are used to model the rib webs, skin panels, and spar webs.

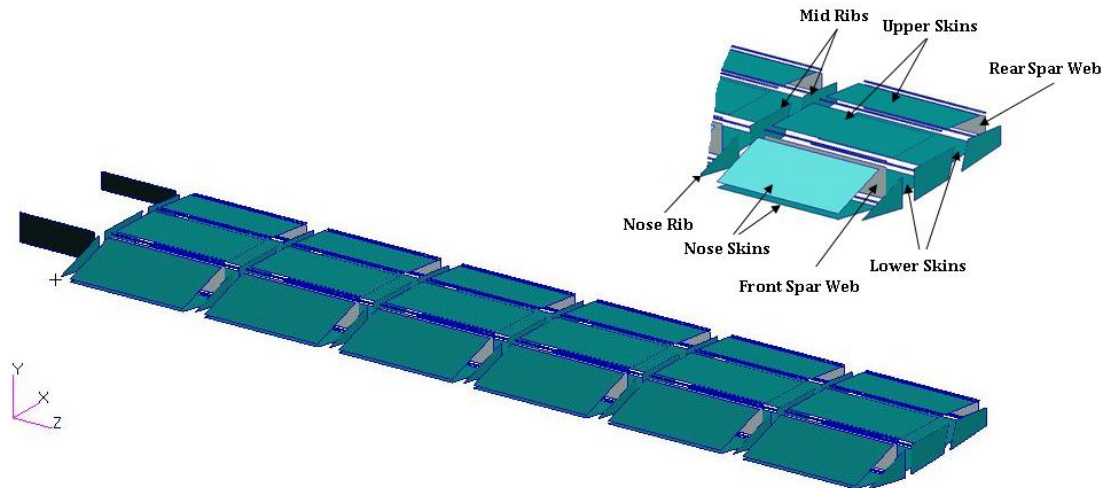


Figure 4.9: Rendered Finite Element Model of the Wing

Design variables associated with the areas of spar caps and stiffeners:

(When Rod Elements are used):

- Six Front Spar Upper Cap Areas
- Six Front Spar Lower Cap Areas
- Six Rear Spar Upper Cap Areas
- Six Rear Spar Lower Cap Areas
- Six Upper Skin Mid Stiffener Areas
- Six Lower Skin Mid Stiffener Areas

(When Beam Elements are used):

- Twelve Front Spar Upper Dimensions (Width and Height)
- Twelve Front Spar Lower Dimensions (Width and Height)
- Twelve Rear Spar Upper Dimensions (Width and Height)
- Twelve Rear Spar Lower Dimensions (Width and Height)
- Twelve Upper Skin Mid Stiffener Dimensions (Width and Height)
- Twelve Lower Skin Mid Stiffener Dimensions (Width and Height)

In the optimization process, all the thicknesses are assumed to have a lower limit of 0.0003 m and an upper limit of 0.00635 m. The cap areas of spars and stiffeners are

assumed to be rectangular areas in the case of using rod elements with a lower limit of 0.000038 m^2 and an upper limit of 0.000613 m^2 .

In the case of using beam elements, lower limit of the width is assigned as 0.02 m and the upper limit of the width is taken as 0.15 m and no discrete values are assigned for it since the width is assumed to be cut from a thin sheet. Since any value between 0.02 - 0.15 m can be assigned as the width of the beam, width of the beam is a continuous design variable. On the other hand, beam height is taken as a discrete design variable and it is assumed that beam height is the same as the thickness of the standard thickness thin sheets. In the optimization process, the lower limit of the beam height is taken as 0.0003 m and the upper limit is taken as 0.00635 m. The lower and upper limits of the thicknesses and flange/stiffener areas are taken as the lower and upper limits of the standard thicknesses and flange/stiffener areas.

For the discrete variable optimization the lists of standard thicknesses of thin sheets, standard cross-sectional areas of flanges and standard beam heights are given below. Appendix [E] also repeats the lists and gives the references used in the generating the lists.

Thin Panels Thicknesses Set {0.3, 0.4, 0.5, 0.63, 0.81, 1.016, 1.27, 1.20, 1.80, 2.03, 2.28, 2.54, 3.17, 4.06, 4.82, 6.35} $\times 10^{-3} \text{ m}$

Flange Cross Sectional Areas Set {38, 44, 48, 58, 63, 67, 73, 78, 88, 94, 98, 104, 108, 112, 116, 118, 131, 133, 137, 148, 151, 153, 161, 184, 195, 213, 232, 246, 280, 312, 375, 390, 415, 430, 444, 525, 573, 592, 613} $\times 10^{-6} \text{ m}^2$

Beam Heights Dimensions Set {0.3, 0.4, 0.5, 0.63, 0.81, 1.016, 1.27, 1.20, 1.80, 2.03, 2.28, 2.54, 3.17, 4.06} $\times 10^{-3} \text{ m}$

4.8 Optimization Studies Using Different Discrete Optimization Methods and Different Starting Points for Design Variables

The following two studies illustrate the effect of using different starting values for the design variables on the optimization results and demonstrate the correct use of discrete optimization methods in MSC.NASTRAN®.

4.8.1 Optimization Study Using Different Starting Values for Design Variables

In case of optimization of the wing structure with many design variables, it is very probable that local optimum design may be reached if different starting values are used for the design variables during the optimization. Therefore, the effect of different starting points on the optimized wing configuration is investigated in this section. The wing torque box is optimized by using rod/shell model with coarse mesh, using different starting points for the design variables. Again the objective function is to minimize the weight of the wing subjected to Von Mises stress, axial stress, tip deflection and local buckling constraints. Both continuous and discrete round-up solutions are conducted.

Model 1- Initial Values Taken as Lower Limit of the Design Variables:

The initial values of the design variables of wing torque box optimization problem are taken as the minimum values of skin/spar web/rib thicknesses and cross sectional areas of the flanges. The value of 0.3×10^{-3} m is assigned for thicknesses and 38×10^{-6} m² is assigned for flange cross sectional areas.

Model 2- Initial Values Taken as Mean of the Lower and Upper Limit of the Design Variables:

The initial values of the design variables of wing torque box optimization problem are taken as the mean value of the lower and upper limit of the design variables. The value of 1.60×10^{-3} m is assigned for thicknesses and 280×10^{-6} m² is assigned for flange cross sectional areas.

Model 3- Initial Values Taken as Upper Limit of the Design Variables:

The initial values of the design variables of wing torque box optimization problem are taken as the maximum values of skin/spar web/rib thicknesses and cross sectional areas of the flanges. The value of 6.35×10^{-3} m is assigned for thicknesses, and 613×10^{-6} m² is assigned for flange cross sectional areas.

Model 4- Initial Values Decrease by 10% for Each Bay Starting from the Maximum Values at the Root Bay:

The initial values of the design variables of wing torque box optimization problem are defined in a decreasing fashion from the root to the tip of the wing torque box. Thicknesses of skins, spar webs, ribs and cross sectional areas of flanges and stiffeners decrease by 10 % for each bay starting from the maximum values at the root bay. In each bay, values of $\{6.35, 4.82, 4.06, 3.17, 2.54, 2.88, 1.80\} \times 10^{-3}$ m are assigned for the thicknesses, and values of $\{613, 525, 430, 312, 213, 151\} \times 10^{-6}$ m² are assigned for the cross sectional areas of flanges and stiffeners.

Model 5- Initial Values Decrease by 20% for Each Bay Starting from the Maximum Values at the Root Bay:

The initial values of the design variables of wing torque box optimization problem are defined in a decreasing fashion from the root to the tip of the wing torque box. Thicknesses of skins/spar webs/ribs and cross sectional areas of flanges/stiffeners decrease by 20 % for each bay starting from the maximum values at the root bay. In each bay, values of $\{4.28, 2.54, 1.60, 1.27, 0.81, 0.50, 0.30\} \times 10^{-3}$ m are assigned for thicknesses and values of $\{444, 232, 137, 118, 98, 48\} \times 10^{-6}$ m² are assigned for cross sectional areas of flanges and stiffeners.

Model 6- Initial Values Taken as the Default Values of the Analytical Solution:

The initial values of the design variables of the wing torque box optimization problem are defined using the thicknesses and flange areas calculated from the analytical solution for the second idealization case based on the external load calculated at the minimum maneuvering speed V_A . Tables 4.2, 4.3 and 4.4 summarize the default values of the design variables.

Table 4.2: Summary of Standard Flange Areas of the 2nd Idealization - Point A

FLANGE AREAS (in mm ²) at Point A							
Root	Station	Spar Cap 1	Spar Cap 2	Spar Cap 3	Spar Cap 4	Stiffener 1	Stiffener 2
	1	44	44	44	44	44	44
	2	44	44	44	44	44	44
	3	44	44	44	44	44	44
	4	44	44	44	44	44	44
	5	44	44	44	44	44	44
Tip	6	44	44	44	44	44	44

Table 4.3: Summary of Standard Thicknesses of the 2nd Idealization - Point A

SKIN and SPAR WEB THICKNESSES (in m) at Point A								
Root	Station	Nose Skin	Mid- Up Skin	R-Spar Web	Mid-L Skin	F-Spar Web	Right-Up Skin	Right-L Skin
	1	0.0048	0.0032	0.0013	0.0010	0.0032	0.0018	0.0010
	2	0.0048	0.0018	0.0013	0.0006	0.0032	0.0013	0.0008
	3	0.0048	0.0010	0.0013	0.0004	0.0025	0.0006	0.0008
	4	0.0048	0.0010	0.0013	0.0004	0.0023	0.0004	0.0008
	5	0.0025	0.0008	0.0008	0.0004	0.0013	0.0004	0.0008
Tip	6	0.0010	0.0006	0.0005	0.0003	0.0008	0.0004	0.0006

Table 4.4: Summary of Standard Rib Thicknesses of the 2nd Idealization - Point A

RIB THICKNESSES (in m)			
	Rib Number	Point A	
		Nose Rib	Mid Rib
Root	1	0.0008	0.0010
	2	0.0008	0.0010
	3	0.0008	0.0010
	4	0.0008	0.0008
	5	0.0008	0.0008
	6	0.0006	0.0006
Tip	7	0.0003	0.0003

Table 4.5 shows the optimized masses of the wing torque box, using the same rod-shell model, but using different starting values for the design variables. In all solutions, hard convergence is achieved as well as hard feasible discrete design.

Table 4.5: Mass of the Optimized Wing Torque Box (kg) Using Different Starting Values for the Design Variables

Solutions Type	Optimized Mass of Wing Torque Box (kg)					
	Model 1 (Min)	Model 2 (Mean)	Model 3 (Max)	Model 4 (10 %)	Model 5 (20 %)	Model 6 (Default)
Continuous	41.30	40.09	41.29	39.85	39.80	41.09
Discrete – Round Up Method	45.93	45.10	45.94	44.32	44.00	46.77

As it can be seen from the results tabulated in Table 4.5 that, different local optimum designs can be reached in the gradient based optimization solution by using different starting values for the design variables, Because, the optimized wing configurations do not exactly have the same mass. However, the change in the masses among the models is small for both continuous and discrete optimization solutions. Moreover, using the results determined by hand calculation (default results) as starting values for the design variables during optimization; satisfactory solution is also obtained which is evident from the results given in Table 4.5.

4.8.2 Optimization Study Using Different Discrete Optimization Methods

In order to understand and examine the effect and correct use of discrete optimization methods available in MSC.NASTRAN®, Design of Experiments (DOE) and Conservative Discrete Design (CDD) engineering Round-Off and Round-Up methods, are used to perform discrete optimization and come up with optimized solutions for the wing torque box.

The discrete optimization methods are used to optimize the wing structure using the coarse mesh (single element in the between the ribs) rod-shell finite element model of the wing torque box. Again the objective function is defined as the minimization the weight of the wing subject to Von Mises stress, axial stress, tip deflection and local buckling constraints. Table 4.6 shows the optimized masses of the wing torque

box, using the same rod/shell model but by using discrete optimization options of MSC.NASTRAN.

Table 4.6: Mass of the Optimized Wing Torque Box (kg) Using Discrete Optimization Methods of MSC.NASTRAN®

Solutions Type	Optimized Mass of Wing Torque Box (kg)			
	DOE Method	CDD Method	Round-Up Method	Round-Off Method
Continuous	41.09	41.09	41.09	41.09
Discrete	44.81	42.62	46.77	40.03

A hard convergence solution at an optimum value is achieved using four different discrete optimization methods but feasible discrete designs are obtained only for the DOE and the Round-Up methods. On the other hand, CDD method could not obtain a feasible discrete solution. The reason might be due to fact that while the CDD method tries to produce a true conservative design; it neglects the interaction of discrete variables such that the approximations may not be accurate enough to find a feasible design. The Round-off method could also not obtain a feasible discrete solution, since it uses simple rounding down from the continuous solution obtained from solving a corresponding continuous optimization problem which requires no new analysis. Therefore, the chance of finding a feasible solution becomes smaller, since the round-off method also neglects the effect of the interaction of discrete variables.

4.9 Structural Optimization of Wing Torque Boxes Using Six Different Finite Elements Combinations

All finite element models defined previously in section 4.6 are used in the optimization of the wing torque box, subject to Von Mises stress, axial stress, tip deflection, local buckling constraints and side constraints defined before. By applying side constraints in the optimization problem, the flange areas of the spars/stiffeners, thicknesses of the webs, ribs and skins are allowed to change

discretely between the rib stations and no thickness or flange area variation is allowed in a bay.

In the analysis conducted, both continuous and discrete Round-Up optimized solutions are shot for. During the course of the optimization study, the effect of design constraints on optimum wing configurations is also evaluated by relaxing certain constraints such as tip deflection and local buckling.

4.9.1 Wing Torque Box Optimization Including All Design Constraints

In this section the wing torque box configurations are optimized for minimum weight with all the design constraints, defined in section 4.7, imposed. Design constraints include Von Mises stress, axial stress, deformation and local buckling constraints besides the side constraints. In this section, the effect of using different element types in the finite element model on the structurally optimized wing torque box configurations is investigated. The effect of mesh size on the final optimum configurations is also studied by employing finite element models, with different mesh sizes, in the optimization analysis.

In the case of fine mesh, MSC.PATRAN[®] offers different ways of assigning input bounds values to the design variables. One way is to assign input bounds to the property set. In this case, all elements, which belong to the same property set, are assigned to the same values. Thus, as long as property sets are defined accordingly, then design variables can be managed to change discretely between the domains. The following domains are defined in the finite element models:

- Spar flange and stringer lines between the ribs stations in each bay
- Nose skin, upper and lower middle skin, upper and lower right skin panels between the ribs stations in each bay
- Spar web panels between the ribs stations in each bay
- Ribs

In the second method, each element is picked separately in the property set and individual elements are assigned value corresponding to a design variable. In this case, properties of the individual elements, such as flange area or thickness, in the set are linked to different design variables. This is not the preferred in the current study,

because with such a definition of the property sets it is not possible to assign single design variable to a particular domain.

In the fine mesh case, the optimization problem is formulated by first assigning the same thicknesses and flange areas to the domains defined above. Since for each domain a distinct property set is defined, the properties associated with the domains are automatically linked to design variables. Thus, one to one correspondence is established between the design variables and the property sets. On the other hand, in the case of coarse mesh, since single elements are used in the domains it does not make any difference the way the input bounds are defined for the design variables.

Von Mises and axial stress constraints are assigned to the property sets defined. The Von Mises stress component is defined as maximum stress acting at the element center in the outer fiber where the stresses are expected to be highest. The maximum stress in the domain is selected as the active constraint.

For the axial stress acting on the flanges or the stringers, maximum axial stress component in the related property set is selected as the active constraint.

On the other hand, for local buckling constraints the average axial stress, along the wing axis, carried by the elements in the thin panels of each domain is assigned to distinct property sets to be used in the buckling constraints. In this case, average stress option is used while creating the property sets.

Same procedures are also used while defining stress constraints for the coarse mesh models. The tip displacement constraint is defined by selecting the tip nodes and then selecting the displacement component depending on the global coordinate of the model and then assigning the lower and upper bounds for the tip displacement. The side constraints and local buckling constraints are defined externally by writing design equations in the input .bdf file as described in Appendix [C].

4.9.1.1 Optimization Results of Model One (Rod/Shell Model)

Figures 4.10 and 4.11 show the history of the objective function for the coarse and the fine mesh models, with respect to design cycle. The objective function is defined as minimizing the total mass of the wing torque box subject to constraints defined before. Each design cycle represents an iterative process with a complete finite element analysis. During the optimization process hard convergence is achieved as well as hard and soft feasible discrete design. Appendix [D] gives some plots of the

design variables and the history of the maximum constraint. The maximum constraint value is defined as the percent violation of the constraint and its default value is 5 %. The details of soft and hard convergence criteria in Nastran optimization is explained in detail in Reference [9].

As it can be seen from Figures 4.10 and 4.11, both hard and soft convergences are achieved in 15 design iterations for the coarse mesh and in 18 design iterations for the fine mesh cases. Design iteration is the number of times the finite element analysis is performed. On Figure 4.3, each loop which starts with an entrance to finite element analysis and exit from the optimizer is regarded as one design iteration or design cycle.

Figures 4.10 and 4.11 show that for both coarse and fine mesh models, mass versus design iteration curves level out and converged solutions are achieved. Continuous optimization for the coarse mesh case is achieved in 14 design iterations and the 15th iteration corresponds to the round-up discrete solution. Similarly, continuous optimization for the fine mesh case is achieved in 17 design iterations, and the 18th iteration corresponds to the round-up discrete solution. In the round-up method, continuous solutions for the design variables are rounded-up to the first values in the standard size list for the design variables. Therefore, in Figures 4.10 and 4.11 the increase in the objective function value corresponds to the discrete solution obtained by using the round-up method.

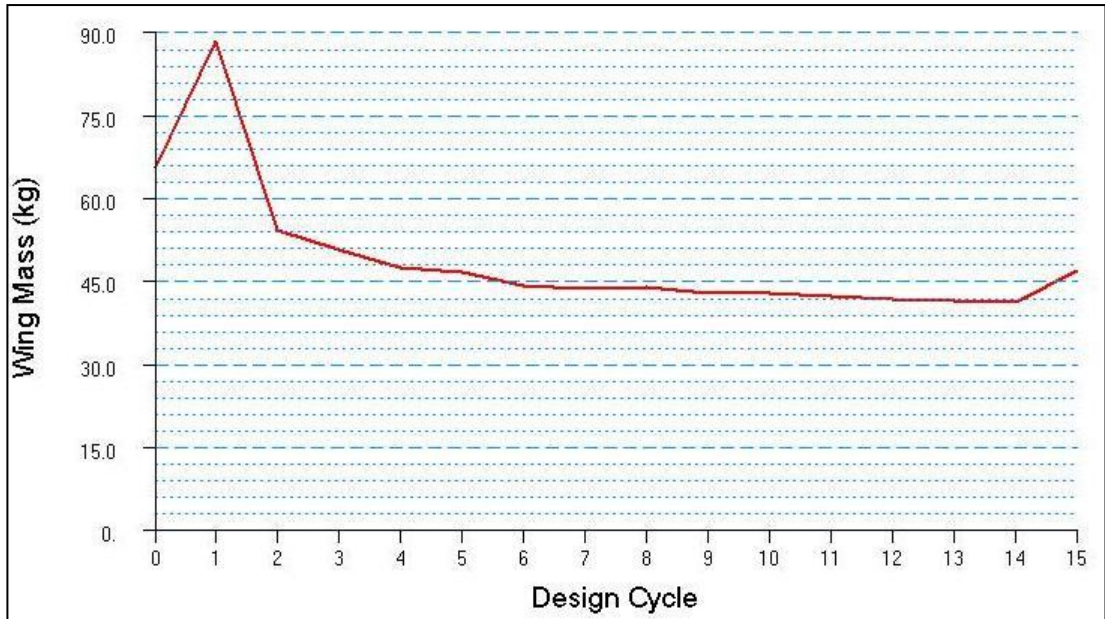


Figure 4.10: Variation of the Mass of Wing with Respect to Design Cycles - Coarse Mesh Rod/Shell Model

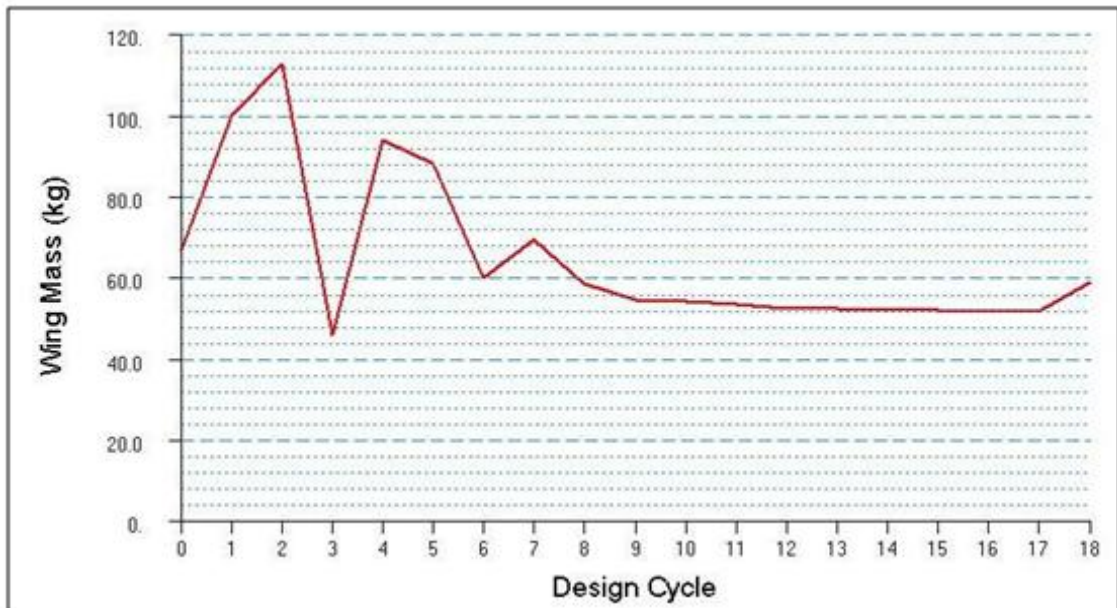


Figure 4.11: Variation of the Mass of Wing with Respect to Design Cycles - Fine Mesh Rod/Shell Model

Table 4.7 gives the initial and optimized weight of the wing torque box for continuous and discrete solutions for both mesh sizes. The initial mass of the wing is based on the initial values of the design variables.

Table 4.7: Initial and Final Optimized Mass of the Wing - Rod/Shell Model

Optimized Mass (kg) Of the Wing			
Mesh Size	Initial	Continuous	Discrete
Coarse	65.38	41.09	46.77
Fine	66.67	51.50	58.61

The initial mass of the fine mesh finite element models, which is calculated by the grid point weight generator, is slightly higher than the initial mass of the coarse mesh finite element models, because cambered surfaces of the wing is approximated better with the fine mesh.

Figures 4.12 - 4.15 show the thickness scalar plots for both coarse and fine mesh of the upper skin panels and interior panels, which include lower skin, spar webs and ribs panels, in the optimized wing torque box. It must be noted that these scalar plots refer to the discrete optimization solutions. From the scalar plots, it can be seen that thicknesses of the upper skin and interior panels decrease from the root to the tip of the wing, as expected. It should be reminded that the decrease of the thicknesses of skin/web/rib panels from the wing root to wing tip was specified as the side constraints. The solutions given in Figures 4.12 - 4.15 verify that the side constraints work fine, and thickness decreases from wing root to wing tip.

Patran 2008r1 03-Aug-11 18:35:02
Thickness Scalar Plot

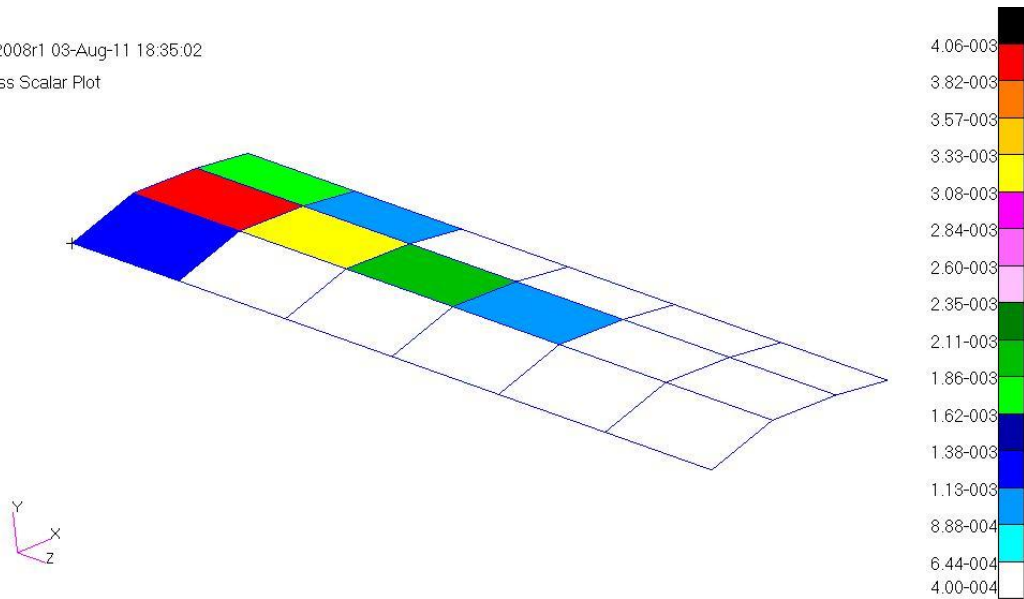


Figure 4.12: Thickness Scalar Plots of Upper Skin Panels in the Optimized Wing Torque Box- Coarse Mesh- Rod/Shell Model

Patran 2008r1 03-Aug-11 18:43:01
Thickness Scalar Plot

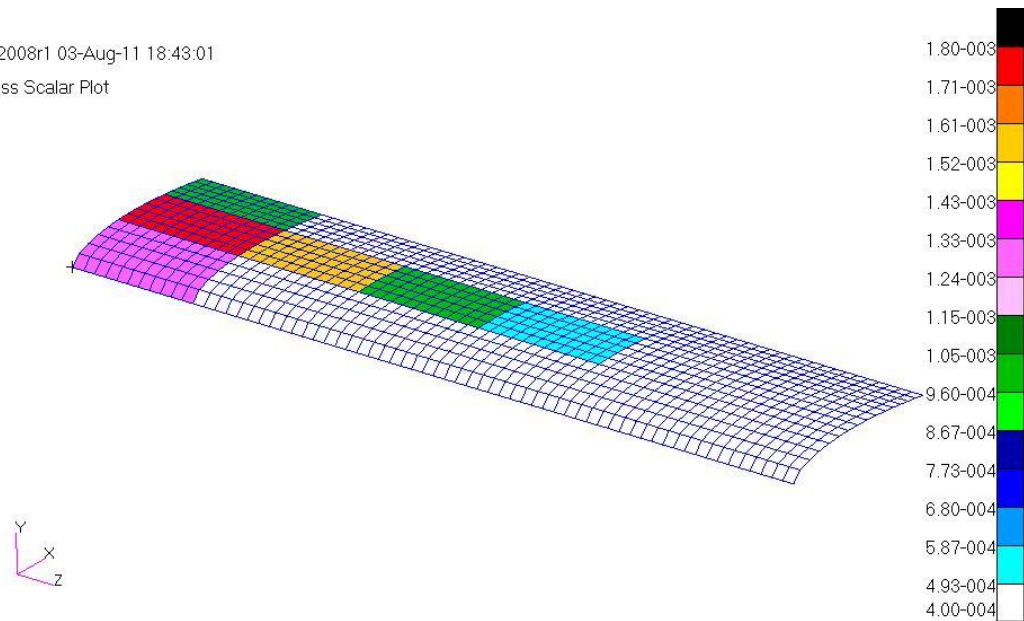


Figure 4.13: Thickness Scalar Plots of Upper Skin Panels in the Optimized Wing Torque Box - Fine Mesh – Rod/Shell Model

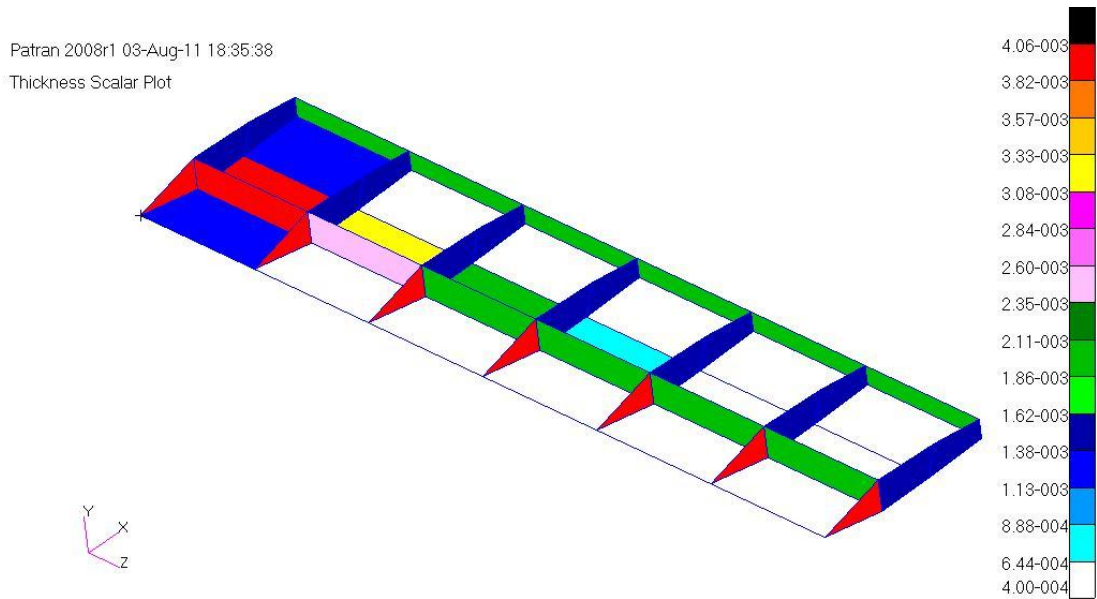


Figure 4.14: Thickness Scalar Plots of Lower Skin, Spar Web and Rib Panels in the Optimized Wing Torque Box- Coarse Mesh- Rod/Shell Model

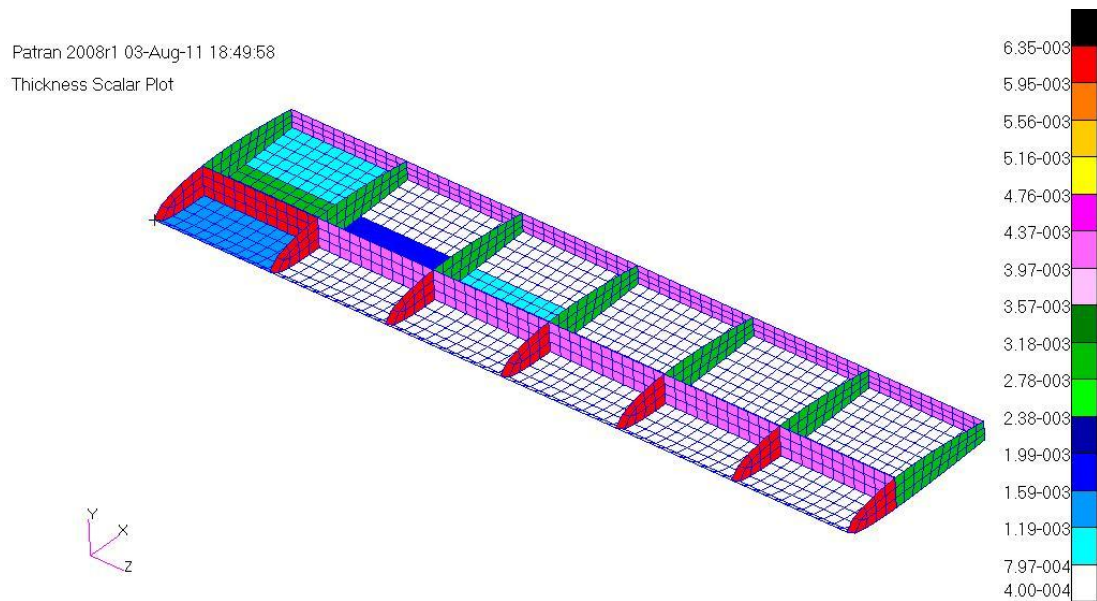


Figure 4.15: Thickness Scalar Plots of Lower Skin, Spar Web and Rib Panels in the Optimized Wing Torque Box - Fine Mesh- Rod/Shell Model

Tables 4.8 and 4.9 summarize the spar cap areas of the front and rear spar in the optimized wing torque box for both coarse and fine meshes models.

Table 4.8: Cross Sectional Areas of the Front Spar of the Wing – Rod/Shell Model

Front Spar Cross Sectional Area – Rod /Shell Model					
	Spar Cap (Root to Tip)	Coarse Mesh Model		Fine Mesh Model	
		Continuous Area (m²)	Discrete Area (m²)	Continuous Area (m²)	Discrete Area (m²)
Upper Flange	Bay 1	2.75E-04	2.80E-04	6.13E-04	6.13E-04
	Bay 2	4.15E-05	4.40E-05	5.20E-04	5.25E-04
	Bay 3	4.03E-05	4.40E-05	2.61E-04	2.80E-04
	Bay 4	4.03E-05	4.40E-05	6.81E-05	7.30E-05
	Bay 5	3.80E-05	4.40E-05	3.80E-05	4.40E-05
	Bay 6	3.80E-05	4.40E-05	3.80E-05	4.40E-05
Lower Flange	Bay 1	6.13E-04	6.13E-04	6.13E-04	6.13E-04
	Bay 2	4.16E-05	4.40E-05	4.65E-04	5.25E-04
	Bay 3	4.00E-05	4.40E-05	2.43E-04	2.46E-04
	Bay 4	3.96E-05	4.40E-05	6.80E-05	7.30E-05
	Bay 5	3.80E-05	4.40E-05	3.80E-05	4.40E-05
	Bay 6	3.80E-05	4.40E-05	3.80E-05	4.40E-05

Table 4.9: Cross Sectional Areas of the Rear Spar of the Wing - Rod/Shell Model

Rear Spar Cross Sectional Area – Rod/ Shell Model					
	Spar Cap (Root to Tip)	Coarse Mesh Model		Fine Mesh Model	
		Continuous Area (m²)	Discrete Area (m²)	Continuous Area (m²)	Discrete Area (m²)
Upper Flange	Bay 1	3.83E-05	4.40E-05	2.18E-04	2.32E-04
	Bay 2	3.81E-05	4.40E-05	4.99E-05	5.80E-05
	Bay 3	3.81E-05	4.40E-05	3.80E-05	4.40E-05
	Bay 4	3.80E-05	4.40E-05	3.80E-05	4.40E-05
	Bay 5	3.80E-05	4.40E-05	3.80E-05	4.40E-05
	Bay 6	3.80E-05	4.40E-05	3.80E-05	4.40E-05
Lower Flange	Bay 1	4.23E-05	4.40E-05	1.88E-04	1.95E-04
	Bay 2	4.12E-05	4.40E-05	4.87E-05	5.80E-05
	Bay 3	3.97E-05	4.40E-05	3.80E-05	4.40E-05
	Bay 4	3.80E-05	4.40E-05	3.80E-05	4.40E-05
	Bay 5	3.80E-05	4.40E-05	3.80E-05	4.40E-05
	Bay 6	3.80E-05	4.40E-05	3.80E-05	4.40E-05

From Tables 4.8 and 4.9, it can be seen that cross sectional areas of the spar caps decrease from the root to the tip of the wing, as expected. The fine mesh model results in larger spar caps areas since when the mesh is made finer, maximum axial stresses in the corresponding domains increase, and inevitably the spar caps areas also increase to satisfy the constraints defined. It should be noted that in the case of a fine mesh, maximum axial stresses occur at the inboard of the edges of the corresponding domains in each bay. Therefore, maximum stresses predicted by the fine mesh models are higher than the axial stresses predicted by the coarse mesh models, because in the coarse mesh models there is one element in each domain, and the axial stresses at the centers of the single elements are used in the stress constraints.

Table 4.10 summarizes the upper middle skin thicknesses in the optimized wing torque box for both coarse and fine meshes models. Table 4.10 clearly shows that in the round-up method, the first highest thickness, above the continuous solution, is selected from the list of standard sheet thicknesses.

Table 4.10: Thicknesses of the Upper Middle Skin of the Wing - Rod/Shell Model

Upper Middle Skin Thicknesses – Rod/ Shell Model					
	Thickness (Root to Tip)	Coarse Mesh Model		Fine Mesh Model	
		Continuous Thickness (m)	Discrete Thickness (m)	Continuous Thickness (m)	Discrete Thickness (m)
Upper Middle Skin	Bay 1	3.25E-03	4.06E-03	1.72E-03	1.80E-03
	Bay 2	2.82E-03	3.17E-03	1.37E-03	1.60E-03
	Bay 3	1.94E-03	2.03E-03	9.59E-04	1.02E-03
	Bay 4	8.25E-04	1.02E-03	4.53E-04	5.00E-04
	Bay 5	3.00E-04	4.00E-04	3.00E-04	4.00E-04
	Bay 6	3.00E-04	4.00E-04	3.00E-04	4.00E-04

4.9.1.2 Optimization Results of Model Two (Beam/Shell Model)

Figures 4.16 and 4.17 show the history of the objective function of the coarse and the fine mesh models, with respect to the design cycle. The objective function is defined as minimizing the total mass of the wing torque box subject to the constraints defined before. During the optimization process hard convergence is achieved as well as hard and soft feasible discrete designs.

Figures 4.16 and 4.17 show that for both coarse and fine mesh models, mass versus design iteration curves level out and converged solutions are achieved. Continuous optimization for the coarse mesh case is achieved in 32 design iterations but the last iteration corresponds to the round-up discrete solution. Similarly, continuous optimization for the fine mesh case is achieved in 26 design iterations. In the round-up method, continuous solutions for the design variables are rounded-up to the first values in the standard size list for the design variables. Therefore, in Figures 4.16 and 4.17 the increase in the objective function value corresponds to the discrete solution obtained by using the round-up method.

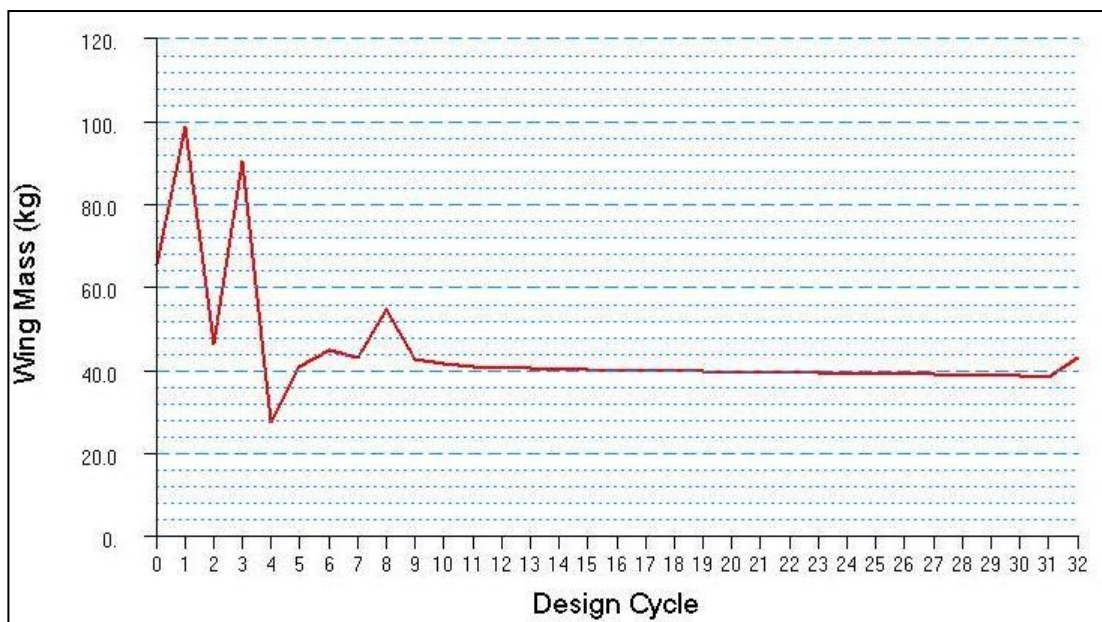


Figure 4.16: Variation of the Mass of Wing with Respect to Design Cycles - Coarse Mesh Beam/Shell Model

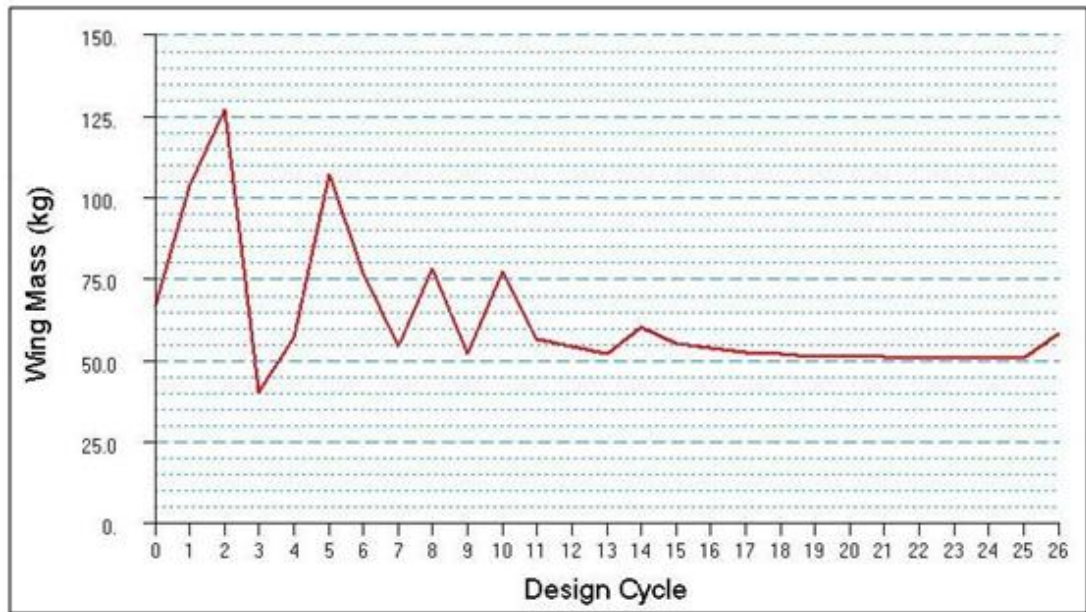


Figure 4.17: Variation of the Mass of Wing with Respect to Design Cycles – Fine Mesh Beam/Shell Model

Table 4.11 gives the initial and optimized masses of the wing torque box for both continuous and discrete optimization solutions and for both mesh sizes. The initial mass of the wing is based on the initial values of the design variables.

It is seen that similar to the rod/shell model case, the use of fine mesh finite element model in the optimization process results in higher optimized mass. As it is discussed before, maximum stresses predicted by the fine mesh models in the domains in each bay are higher than the stresses predicted by the coarse mesh models. Because, coarse mesh models have domains meshed with single elements.

Table 4.11: Initial and Final Optimized Mass of Wing Beam/Shell Model

Optimized Mass (kg) Of the Wing			
Mesh Size	Initial	Continuous	Discrete
Coarse	65.38	38.28	42.97
Fine	66.67	50.25	58.02

For both coarse and fine mesh models, Figures 4.18 - 4.21 show the thickness scalar plots, of the upper skin, lower skin, spar webs and ribs, in the optimized wing torque

box which is modeled with beam/shell element combination. It must be noted that these scalar plots refer to discrete optimization solution results.

From the scalar plots, it can be seen that thicknesses of the upper skin and interior panels decrease from the root to the tip of the wing, as expected. Again, the solutions given in Figures 4.18 - 4.21 verify that the side constraints work fine and thicknesses decrease from wing root to wing tip.

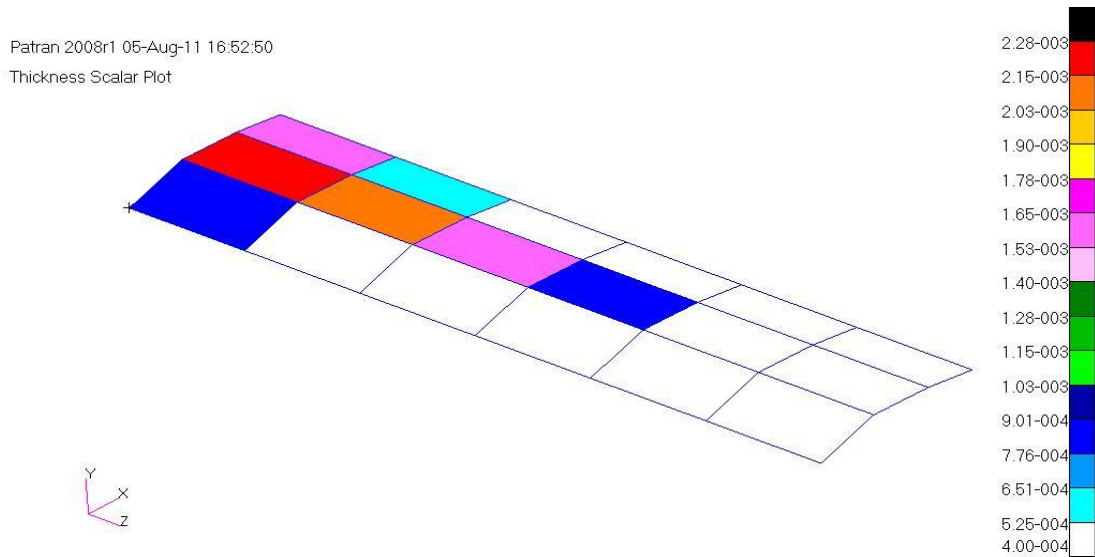


Figure 4.18: Thickness Scalar Plots of Upper Skin Panels in the Optimized Wing Torque Box - Coarse Mesh Beam/Shell Model

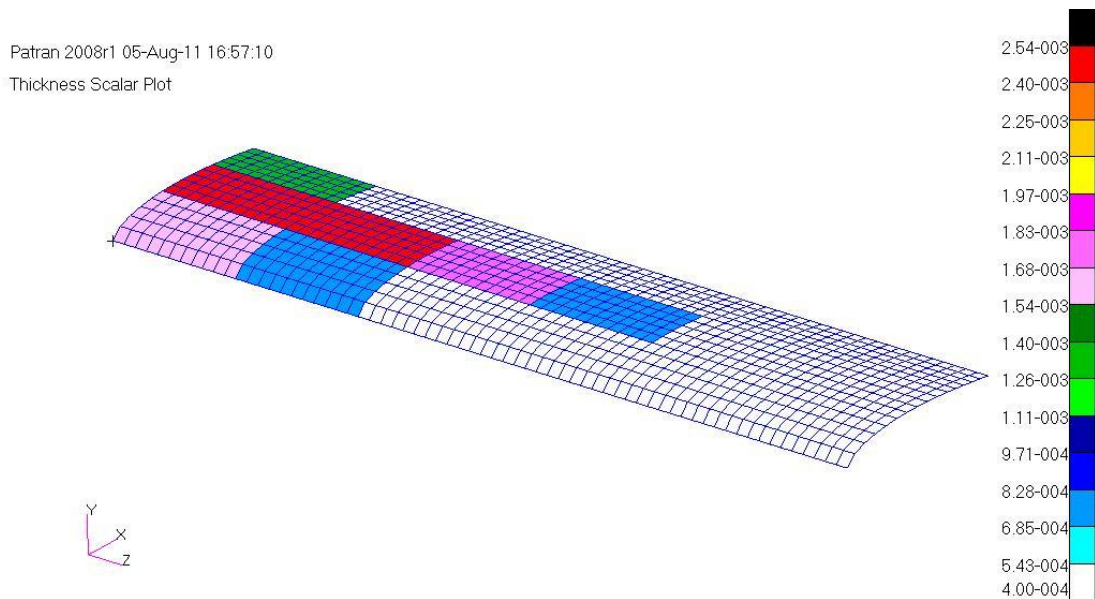


Figure 4.19: Thickness Scalar Plots of Upper Skin Panels in the Optimized Wing Torque Box - Fine Mesh Beam/Shell Model

Patran 2008r1 05-Aug-11 16:53:18
 Thickness Scalar Plot

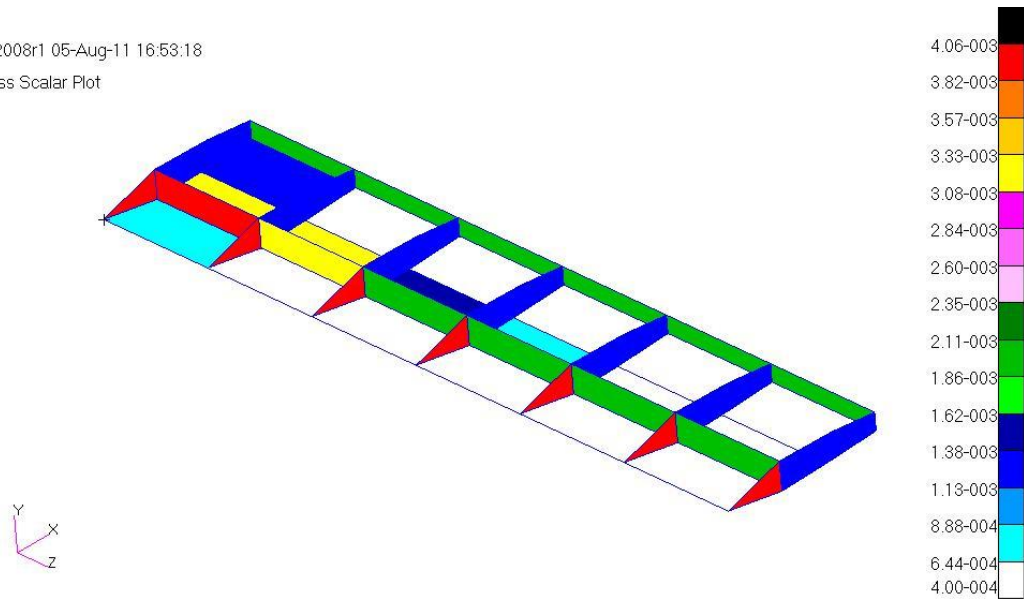


Figure 4.20: Thickness Scalar Plots of Lower Skin, Spar Web and Rib Panels in the Optimized Wing Torque Box - Coarse Mesh Beam/Shell Model

Patran 2008r1 05-Aug-11 16:57:57
 Thickness Scalar Plot

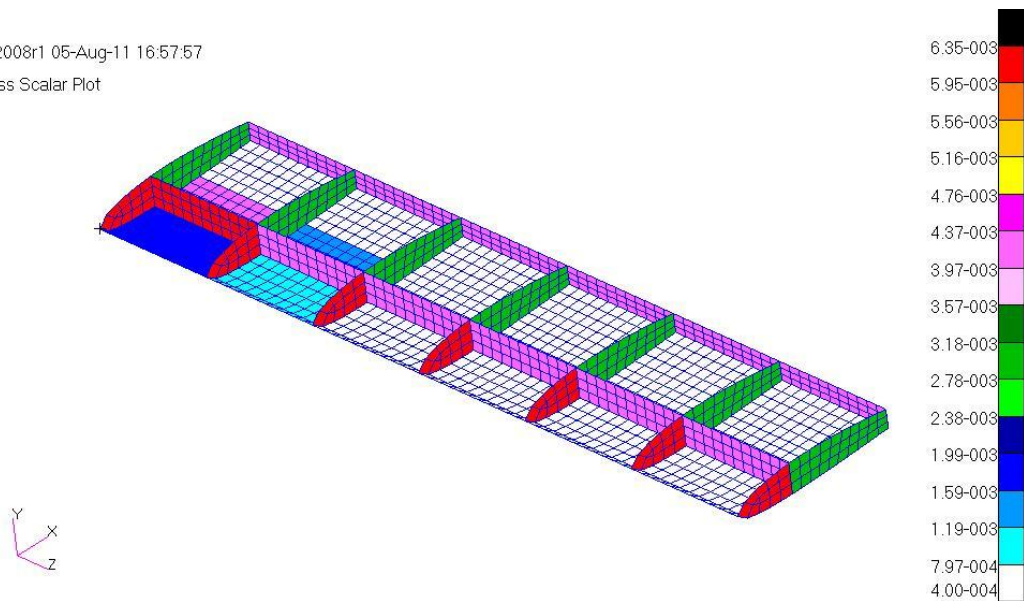


Figure 4.21: Thickness Scalar Plots of Lower Skin, Spar Web and Rib Panels in the Optimized Wing Torque Box - Fine Mesh Beam/Shell Model

Table 4.12 and 4.13 summarize the spar cap areas of the front and rear spar in the optimized wing torque box for both coarse and fine meshes models. In beam modeling, it is assumed that beam cross-sections which represent spar caps are rectangular.

Table 4.12: Cross Sectional Areas of the Front Spar of the Wing – Beam/Shell Model

Front Spar Cross Sectional Area – Beam/Shell Model					
	Spar Cap (Root to Tip)	Coarse Mesh Model		Fine Mesh Model	
		Continuous Area (m²)	Discrete Area (m²)	Continuous Area (m²)	Discrete Area (m²)
Upper Flange	Bay 1	6.07E-04	6.07E-04	6.09E-04	6.09E-04
	Bay 2	4.18E-04	4.19E-04	3.60E-05	4.25E-05
	Bay 3	2.03E-04	2.03E-04	1.99E-05	2.17E-05
	Bay 4	7.80E-05	8.02E-05	1.30E-05	1.43E-05
	Bay 5	1.77E-05	2.03E-05	8.66E-06	1.00E-05
	Bay 6	1.08E-05	1.26E-05	7.11E-06	8.00E-06
Lower Flange	Bay 1	6.08E-04	6.09E-04	6.09E-04	6.09E-04
	Bay 2	2.28E-04	2.40E-04	3.27E-04	3.27E-04
	Bay 3	1.74E-04	2.08E-04	2.73E-04	2.73E-04
	Bay 4	5.02E-05	5.49E-05	6.42E-05	7.15E-05
	Bay 5	1.71E-05	2.03E-05	1.40E-05	1.59E-05
	Bay 6	1.02E-05	1.26E-05	9.74E-06	1.00E-05

Table 4.13: Cross Sectional Areas of the Rear Spar of the Wing – Beam/Shell Model

Rear Spar Cross Sectional Area – Beam /Shell Model					
	Spar Cap (Root to Tip)	Coarse Mesh Model		Fine Mesh Model	
		Continuous Area (m²)	Discrete Area (m²)	Continuous Area (m²)	Discrete Area (m²)
Upper Flange	Bay 1	9.20E-05	9.35E-05	2.31E-04	2.36E-04
	Bay 2	2.86E-05	3.59E-05	9.76E-06	1.14E-05
	Bay 3	1.77E-05	2.07E-05	8.98E-06	1.05E-05
	Bay 4	1.67E-05	2.03E-05	8.81E-06	1.03E-05
	Bay 5	1.50E-05	1.62E-05	8.53E-06	1.00E-05
	Bay 6	1.09E-05	1.26E-05	8.48E-06	1.00E-05
Lower Flange	Bay 1	8.97E-05	9.34E-05	2.59E-04	2.87E-04
	Bay 2	4.38E-05	4.67E-05	8.97E-05	1.00E-04
	Bay 3	2.13E-05	2.61E-05	2.20E-05	2.44E-05
	Bay 4	1.99E-05	2.04E-05	1.58E-05	1.62E-05
	Bay 5	1.52E-05	1.62E-05	1.45E-05	1.62E-05
	Bay 6	1.10E-05	1.26E-05	1.14E-05	1.26E-05

From Tables 4.12 and 4.13, it can be seen that spar caps cross sectional areas decrease from the root to the tip of the wing, as expected. The fine mesh model results in larger spar caps areas since when the mesh is made finer, axial stresses increase, and inevitably the spar caps areas also increase to satisfy the constraints defined for optimized model.

As an example, Table 4.14 summarizes the upper middle skin thicknesses in the optimized wing torque box for both coarse and fine meshes models.

Table 4.14: Thicknesses of the Upper Middle Skin of the Wing - Beam/Shell Model

Upper Middle Skin Thicknesses – Beam/ Shell Model					
	Thickness (Root to Tip)	Coarse Mesh Model		Fine Mesh Model	
		Continuous Thickness (m)	Discrete Thickness (m)	Continuous Thickness (m)	Discrete Thickness (m)
Upper Middle Skin	Bay 1	2.23E-03	2.28E-03	2.39E-03	2.54E-03
	Bay 2	1.81E-03	2.03E-03	2.35E-03	2.54E-03
	Bay 3	1.42E-03	1.60E-03	1.62E-03	1.80E-03
	Bay 4	6.99E-04	8.10E-04	7.59E-04	8.10E-04
	Bay 5	3.00E-04	4.00E-04	3.00E-04	4.00E-04
	Bay 6	3.00E-04	4.00E-04	3.00E-04	4.00E-04

4.9.1.3 Optimization Results of Model Three (Rod/Shell-R Model)

Figures 4.22 and 4.23 show the history of the objective function of the coarse and the fine mesh models, with respect to the design cycle. The objective function is defined as minimizing total weight of the wing torque box subject to constraints defined. During the optimization process hard convergence is achieved as well as hard and soft feasible discrete designs.

Figures 4.22 and 4.23 show that for both coarse and fine mesh models, mass versus design iteration curves level out and converged solutions are achieved. Continuous optimization for the coarse mesh case is achieved in 17 design iterations but the last iteration corresponds to the round-up discrete solution. Similarly, continuous optimization for the fine mesh case is achieved in 19 design iterations.

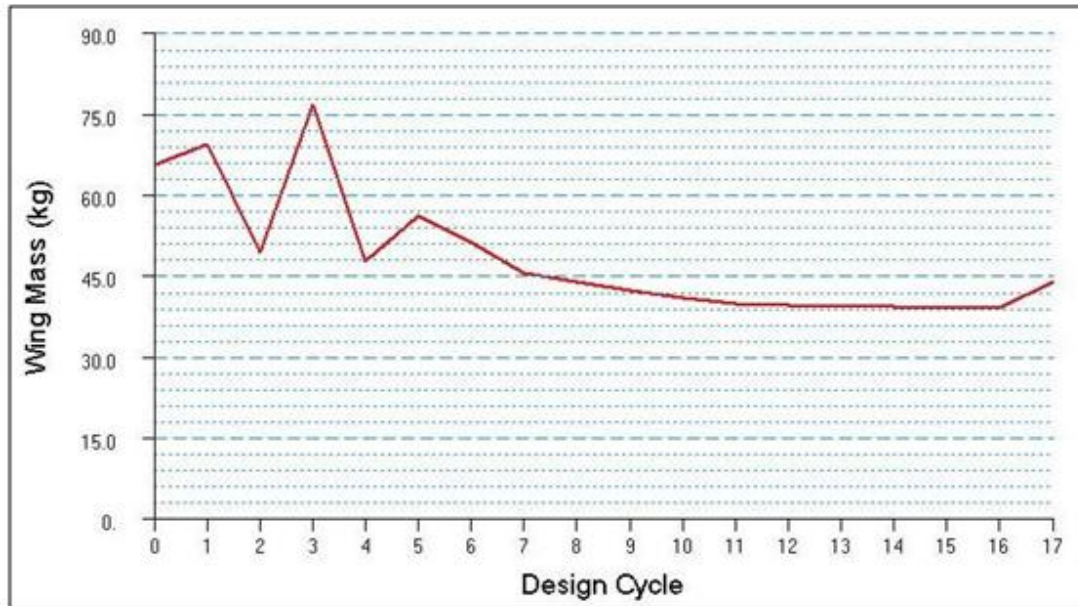


Figure 4.22: Variation of the Mass of Wing with Respect to Design Cycles - Coarse Mesh Rod/Shell-R Model

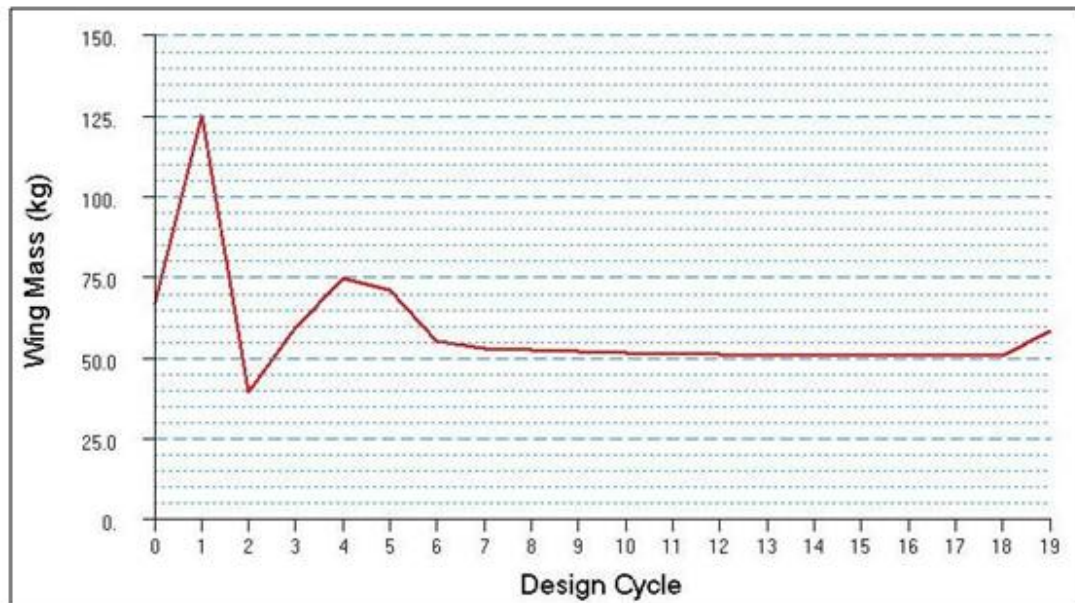


Figure 4.23: Variation of the Mass of Wing with Respect to Design Cycles - Fine Mesh Rod/Shell-R Model

Table 4.15 gives the initial and optimized masses of the wing torque box for both continuous and discrete optimization solutions and for both mesh sizes. The initial mass of the wing is based on the initial values of the design variables.

Comparison of Table 4.15 with Table 4.7 reveals the standard shell elements and revised shell elements results in slightly different minimum mass wing configurations. However, the difference between the optimized masses is small. It is noticed that in the continuous optimization solution, the use of shell elements with drilling degrees of freedom results in slightly lower minimum masses compared to the use of shell elements without drilling degrees of freedom. In Chapter 3, it is noted that in general finite element analysis of the wing torque box with revised shell elements results in slightly lower stresses compared to the use of standard shell elements in the finite element model. Therefore, it can be concluded that results of the continuous optimization solution is in accordance with the stress analysis results. It is considered that the final mass of the wing torque box configuration determined with the continuous optimization formulation utilizing the finite element model using revised shell elements is slightly lower due to slightly lower stresses obtained in the finite element analysis.

Table 4.15 gives the initial and optimized weight of the wing torque box for continuous and discrete solutions for both mesh sizes. The initial mass of the wing is based on the initial values of the design variables.

Table 4.15: Initial and Final Optimized Mass of the Wing – Rod/Shell-R Model

Optimized Mass (kg) Of the Wing			
Mesh Size	Initial	Continuous	Discrete
Coarse	65.38	38.88	43.57
Fine	66.67	50.12	58.23

For both coarse and fine mesh models, Figures 4.24 - 4.27 show the thickness scalar plots, of the upper skin, lower skin, spar webs and ribs, in the optimized wing torque box which is modeled with rod/shell - r element combination. It must be noted that these scalar plots refers to discrete optimization solution results. From the scalar plots, it can be seen that thicknesses of the upper skin and interior panels are decrease from the root to the tip of the wing, as expected.

Patran 2008r1 03-Aug-11 19:26:47
Thickness Scalar Plot

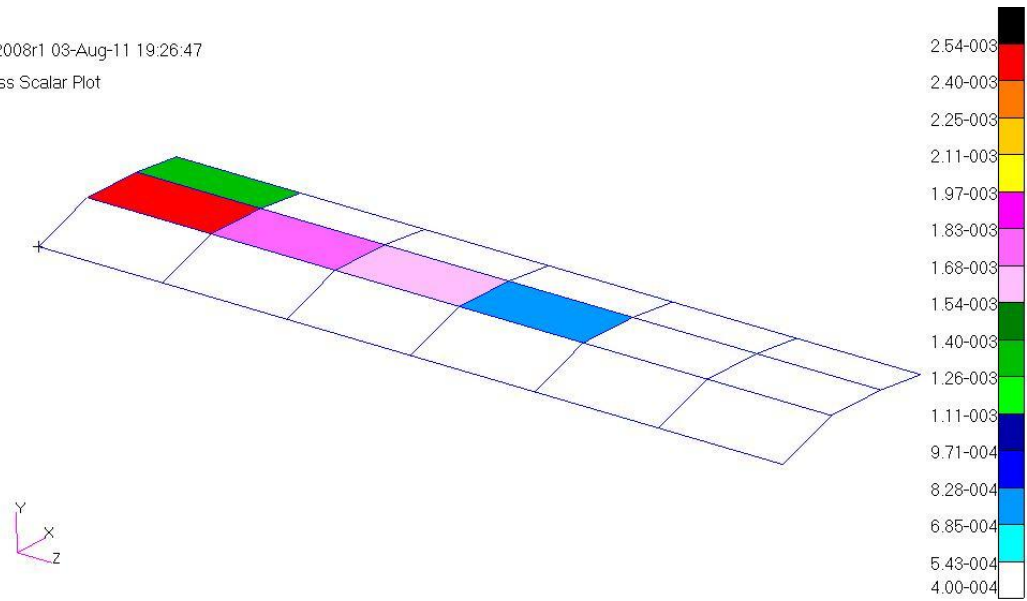


Figure 4.24: Thickness Scalar Plots of Upper Skin Panels in the Optimized Wing Torque Box - Coarse Mesh Rod/Shell-R Model

Patran 2008r1 03-Aug-11 19:30:07
Thickness Scalar Plot

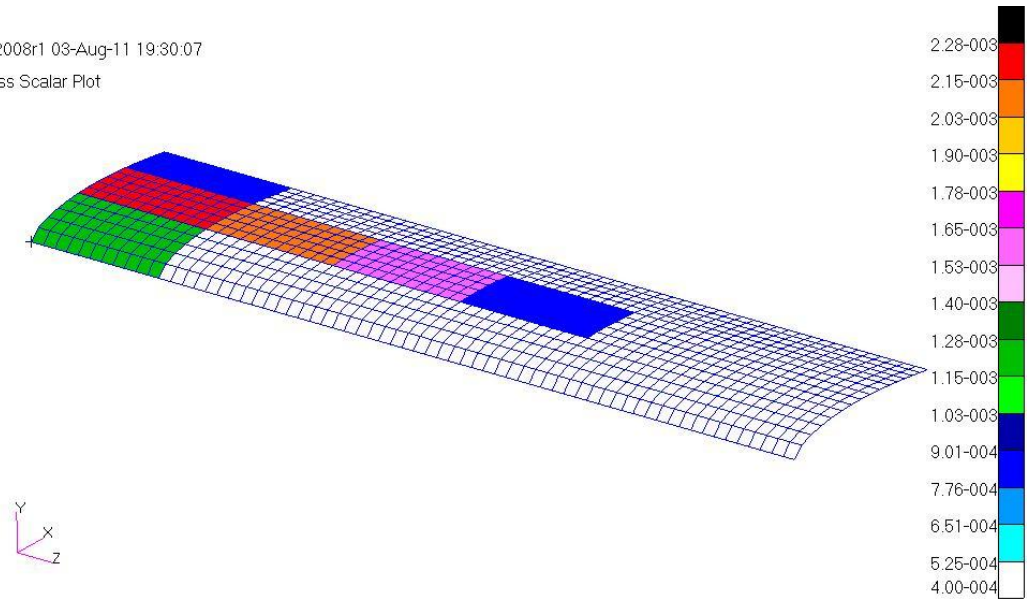


Figure 4.25: Thickness Scalar Plots of Upper Skin Panels in the Optimized Wing Torque Box - Fine Mesh Rod/Shell-R Model

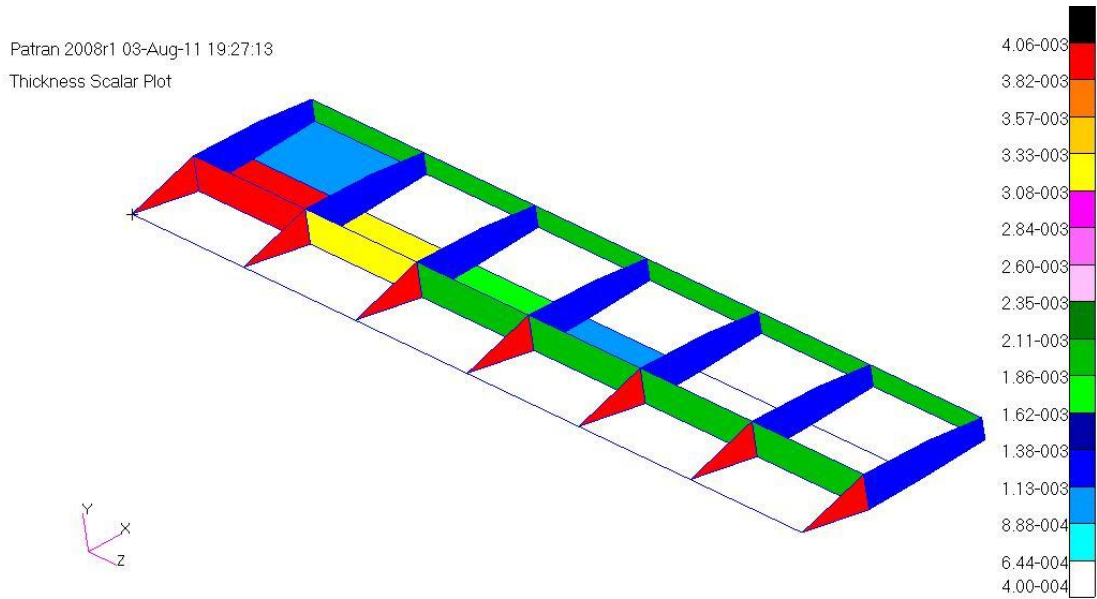


Figure 4.26: Thickness Scalar Plots of Lower Skin, Spar Web and Rib Panels in the Optimized Wing Torque Box - Coarse Mesh Rod/Shell-R Model

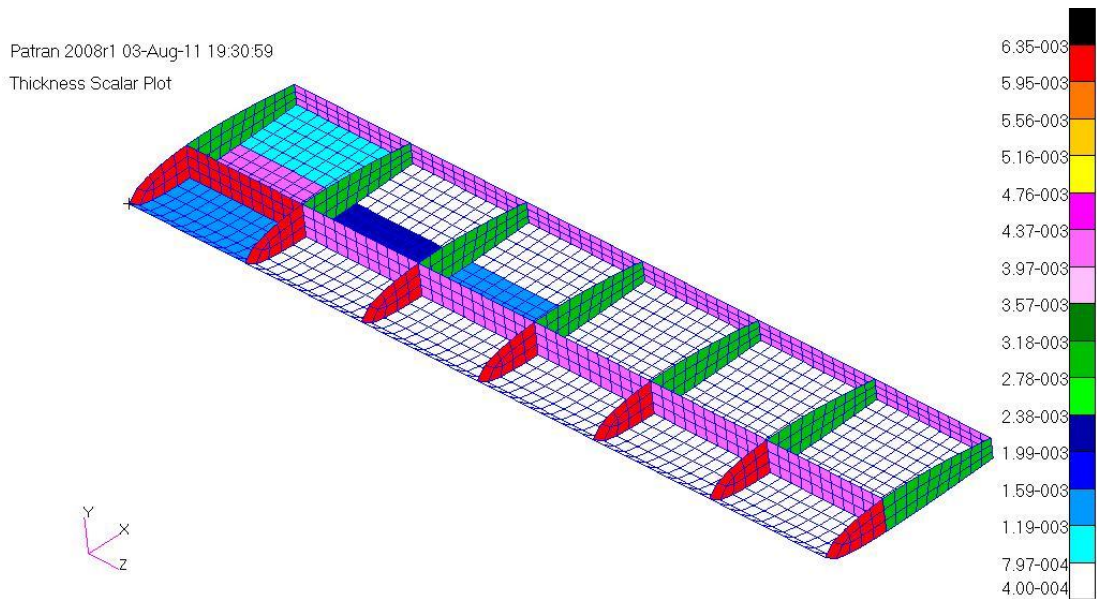


Figure 4.27: Thickness Scalar Plots of Lower Skin, Spar Web and Rib Panels in the Optimized Wing Torque Box - Fine Mesh Rod/Shell-R Model

Tables 4.16 and 4.17 summarize the spar cap areas of the front and the rear spar in the optimized wing torque box for both coarse and fine meshes models.

Table 4.16: Cross Sectional Areas of the Front Spar of the Wing- Rod/Shell-R Model

Front Spar Cross Sectional Area – Rod /Shell-R Model					
	Spar Cap (Root to Tip)	Coarse Mesh Model		Fine Mesh Model	
		Continuous Area (m²)	Discrete Area (m²)	Continuous Area (m²)	Discrete Area (m²)
Upper Flange	Bay 1	6.13E-04	6.13E-04	6.13E-04	6.13E-04
	Bay 2	4.52E-04	5.25E-04	2.60E-04	2.80E-04
	Bay 3	1.82E-04	1.84E-04	6.85E-05	7.30E-05
	Bay 4	7.78E-05	7.80E-05	3.84E-05	4.40E-05
	Bay 5	3.80E-05	4.40E-05	3.80E-05	4.40E-05
	Bay 6	3.80E-05	4.40E-05	3.80E-05	4.40E-05
Lower Flange	Bay 1	6.13E-04	6.13E-04	6.13E-04	6.13E-04
	Bay 2	2.01E-04	2.13E-04	3.32E-04	3.75E-04
	Bay 3	9.63E-05	9.80E-05	1.36E-04	1.37E-04
	Bay 4	3.99E-05	4.40E-05	3.82E-05	4.40E-05
	Bay 5	3.80E-05	4.40E-05	3.81E-05	4.40E-05
	Bay 6	3.80E-05	4.40E-05	3.81E-05	4.40E-05

Table 4.17: Cross Sectional Areas of the Rear Spar of the Wing – Rod/Shell-R Model

Rear Spar Cross Sectional Area – Rod /Shell-R Model					
	Spar Cap (Root to Tip)	Coarse Mesh Model		Fine Mesh Model	
		Continuous Area (m²)	Discrete Area (m²)	Continuous Area (m²)	Discrete Area (m²)
Upper Flange	Bay 1	6.14E-05	6.30E-05	1.72E-04	1.84E-04
	Bay 2	3.80E-05	4.40E-05	3.80E-05	4.40E-05
	Bay 3	3.80E-05	4.40E-05	3.80E-05	4.40E-05
	Bay 4	3.80E-05	4.40E-05	3.80E-05	4.40E-05
	Bay 5	3.80E-05	4.40E-05	3.80E-05	4.40E-05
	Bay 6	3.80E-05	4.40E-05	3.80E-05	4.40E-05
Lower Flange	Bay 1	6.53E-05	6.70E-05	1.41E-04	1.48E-04
	Bay 2	3.87E-05	4.40E-05	3.80E-05	4.40E-05
	Bay 3	3.85E-05	4.40E-05	3.80E-05	4.40E-05
	Bay 4	3.83E-05	4.40E-05	3.80E-05	4.40E-05
	Bay 5	3.82E-05	4.40E-05	3.80E-05	4.40E-05
	Bay 6	3.81E-05	4.40E-05	3.80E-05	4.40E-05

From Table 4.16 and 4.17 it can be seen that spar caps cross sectional areas are decreasing from the root to the tip of the wing, as expected.

Table 4.18 summarizes the upper middle skin thicknesses in the optimized wing torque box for both coarse and fine meshes models.

Table 4.18: Thicknesses of the Upper Middle Skin of the Wing - Rod/Shell-R Mode

Upper Middle Skin Thicknesses – Rod/ Shell-R Model					
	Thickness (Root to Tip)	Coarse Mesh Model		Fine Mesh Model	
		Continuous Thickness (m)	Discrete Thickness (m)	Continuous Thickness (m)	Discrete Thickness (m)
Upper Middle Skin	Bay 1	2.50E-03	2.54E-03	2.11E-03	2.28E-03
	Bay 2	1.75E-03	1.80E-03	1.95E-03	2.03E-03
	Bay 3	1.53E-03	1.60E-03	1.38E-03	1.60E-03
	Bay 4	7.86E-04	8.10E-04	6.31E-04	8.10E-04
	Bay 5	3.00E-04	4.00E-04	3.00E-04	4.00E-04
	Bay 6	3.00E-04	4.00E-04	3.00E-04	4.00E-04

4.9.1.4 Optimization Results of Model Four (Beam/Shell-R Model)

Figures 4.28 and 4.29 show the history of the objective function of coarse and fine mesh models, with respect to the design cycle. The objective function is defined as minimizing total weight of the wing torque box subject to constraints defined. During the optimization process hard convergence is achieved as well as hard and soft feasible discrete designs.

Figures 4.28 and 4.29 show that for both coarse and fine mesh models, mass versus design iteration curves level out and converged solutions are achieved. Continuous optimization for the coarse mesh case is achieved in 10 design iterations but the last iteration corresponds to the round-up discrete solution. Similarly, continuous optimization for the fine mesh case is achieved in 9 design iterations.

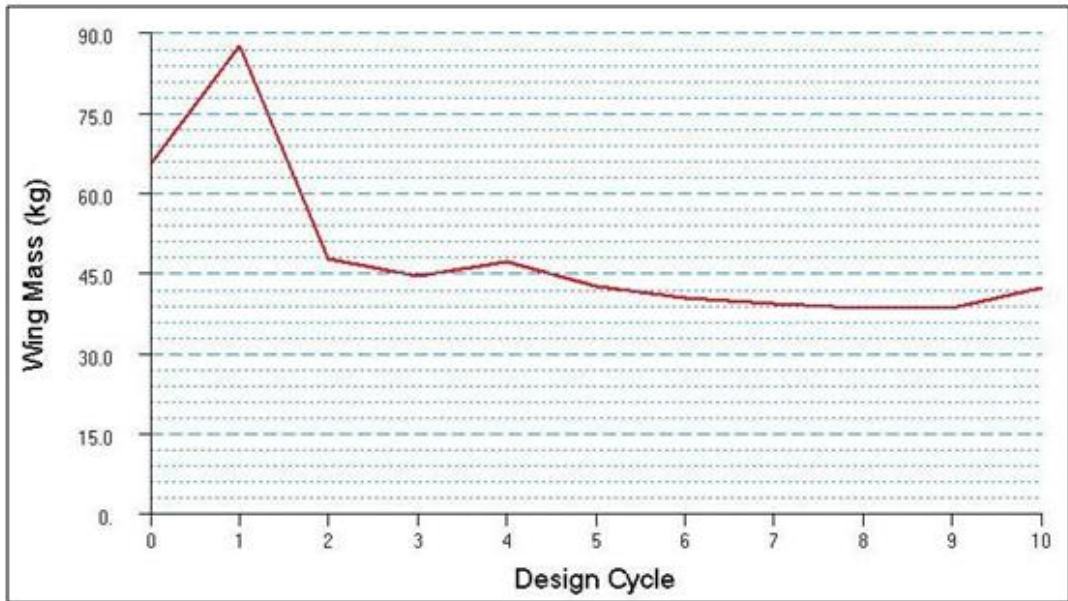


Figure 4.28: Variation of the Mass of the Wing with Respect to Design Cycles - Coarse Mesh Beam/Shell-R Model

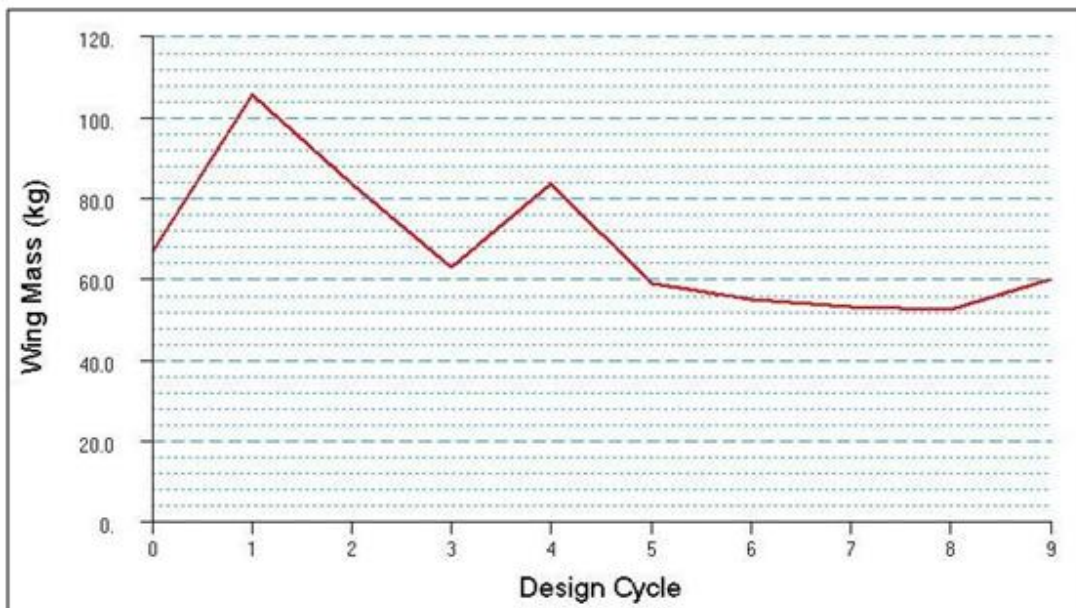


Figure 4.29: Variation of the Mass of the Wing with Respect to Design Cycles - Fine Mesh Beam/Shell-R Model

Table 4.19 gives the initial and optimized masses of the wing torque box for both continuous and discrete optimization solutions and for both mesh sizes. The initial mass of the wing is based on the initial values of the design variables.

Table 4.19: Initial and Final Optimized Mass of the Wing – Beam/Shell-R Model

Optimized Mass (kg) Of the Wing			
Mesh Size	Initial	Continuous	Discrete
Coarse	65.38	38.29	42.11
Fine	66.67	52.13	59.70

For both coarse and fine mesh models, Figures 4.30 - 4.34 show the thickness scalar plots, of the upper skin, lower skin, spar webs and ribs, in the optimized wing torque box which is modeled with beam/shell-r element combination. It must be noted that these scalar plots refer to discrete optimization solution results. From the scalar plots, it can be seen that thicknesses of the upper skin and interior panels are decrease from the root to the tip of the wing, as expected.

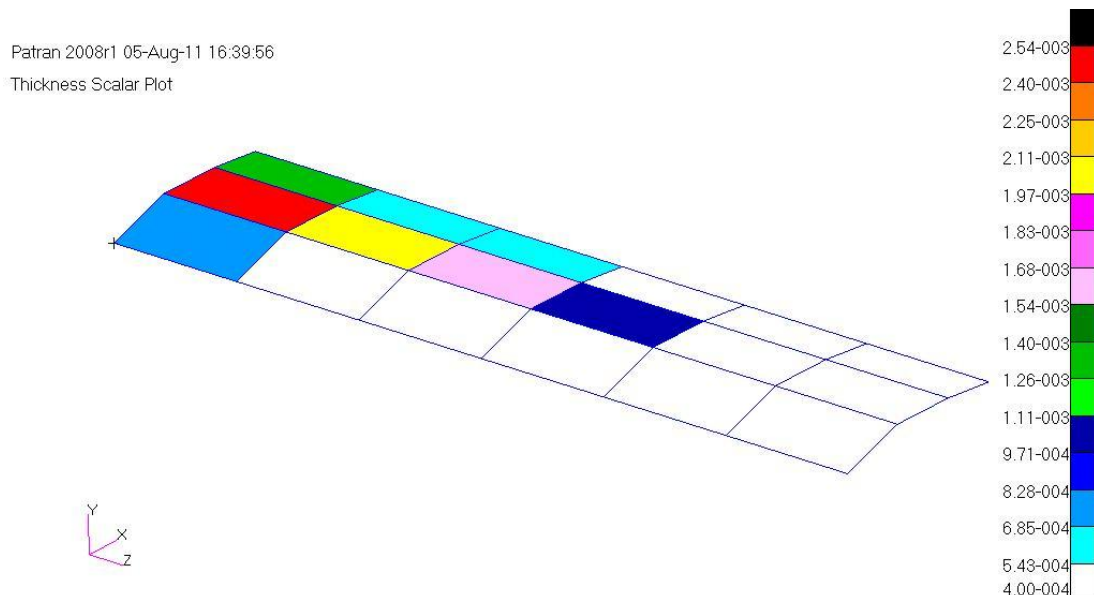


Figure 4.30: Thickness Scalar Plots of Upper Skin Panels in the Optimized Wing Torque Box - Coarse Mesh Beam/Shell-R Model

Patran 2008r1 05-Aug-11 16:48:08
Thickness Scalar Plot

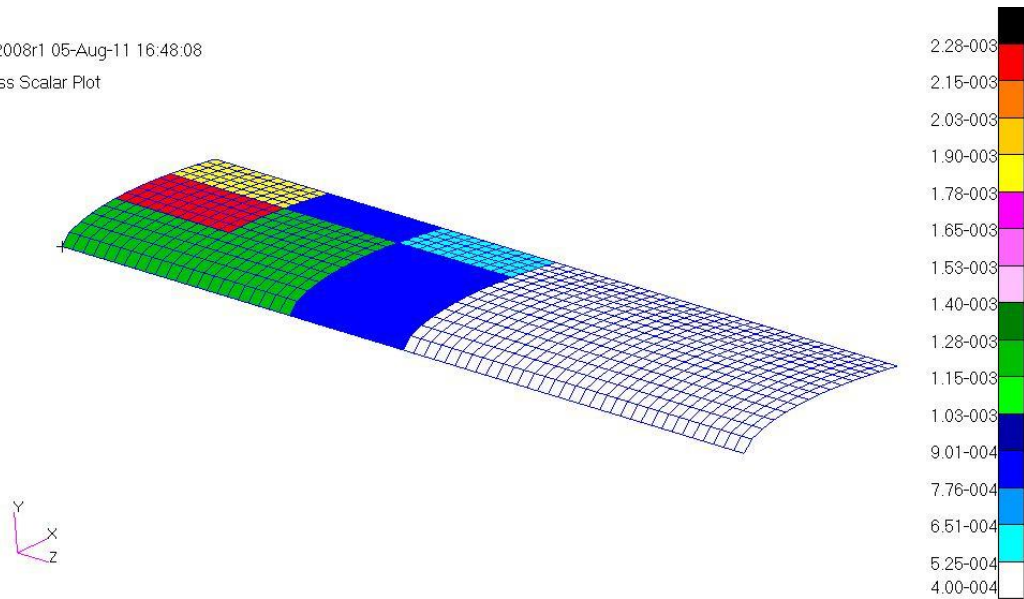


Figure 4.31: Thickness Scalar Plots of Upper Skin Panels in the Optimized Wing Torque Box - Fine Mesh Beam/Shell-R Model

Patran 2008r1 05-Aug-11 16:40:32
Thickness Scalar Plot

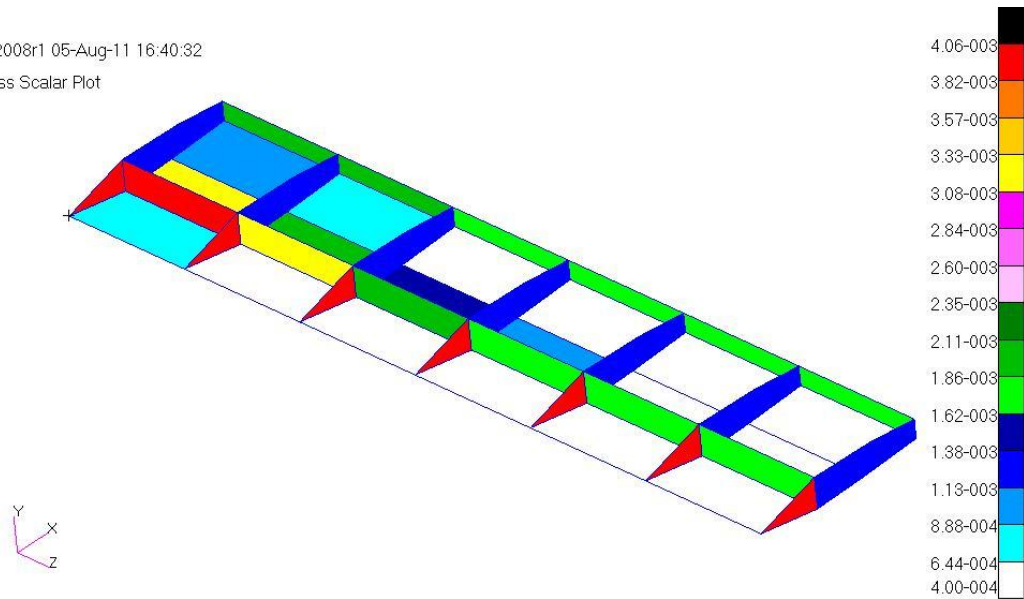


Figure 4.32 Thickness Scalar Plots of Lower Skin, Spar Web and Rib Panels in the Optimized Wing Torque Box - Coarse Mesh Beam/Shell-R Model

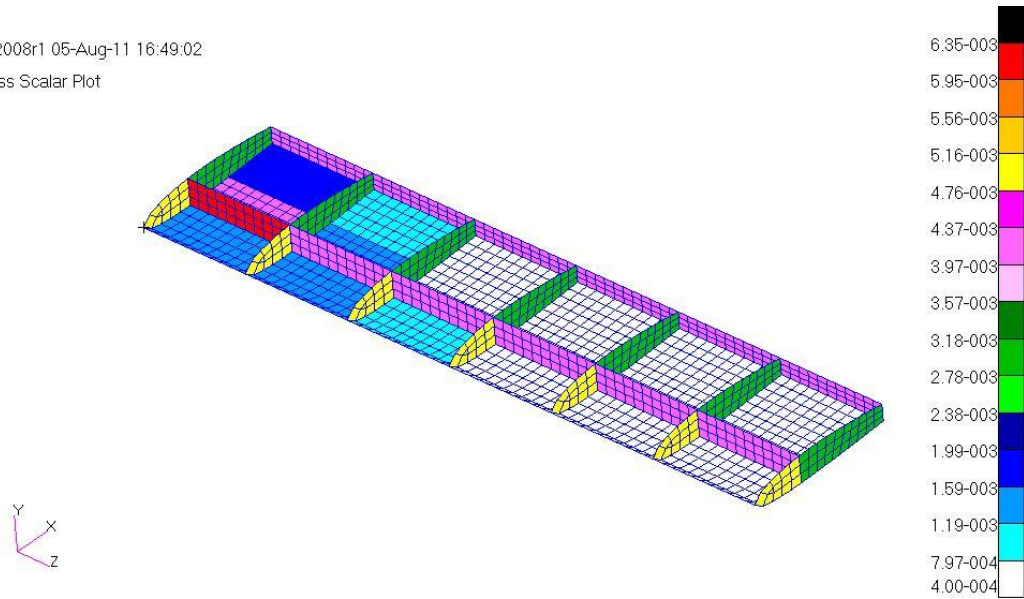


Figure 4.33: Thickness Scalar Plots of Lower Skin, Spar Web and Rib Panels in the Optimized Wing Torque Box - Fine Mesh Beam/Shell-R Model

Tables 4.20 and 4.21 summarize the spar cap areas of the front and rear spar in the optimized wing torque box for both coarse and fine meshes models. In the beam/shell - r model, it is assumed that spar caps are rectangular.

Table 4.20: Cross Sectional Areas of the Front Spar of the Wing – Beam/Shell-R Model

Front Spar Cross Sectional Areas (m ²) – Beam/Shell-R Model					
	Spar Cap (Root to Tip)	Coarse Mesh Model		Fine Mesh Model	
		Continuous Area (m ²)	Discrete Area (m ²)	Continuous Area (m ²)	Discrete Area (m ²)
Upper Flange	Bay 1	6.09E-04	6.09E-04	6.04E-04	6.06E-04
	Bay 2	3.07E-04	3.19E-04	1.10E-04	1.34E-04
	Bay 3	1.68E-04	1.94E-04	5.70E-05	5.73E-05
	Bay 4	3.19E-05	3.65E-05	3.87E-05	4.19E-05
	Bay 5	7.38E-06	8.05E-06	3.39E-05	3.48E-05
	Bay 6	6.02E-06	8.00E-06	2.72E-05	3.20E-05
Lower Flange	Bay 1	6.06E-04	6.08E-04	6.09E-04	6.09E-04
	Bay 2	2.68E-04	2.82E-04	2.74E-04	2.78E-04
	Bay 3	1.27E-04	1.31E-04	1.43E-04	1.53E-04
	Bay 4	2.75E-05	3.45E-05	9.49E-05	9.67E-05
	Bay 5	6.82E-06	8.05E-06	8.09E-05	8.10E-05
	Bay 6	6.00E-06	8.00E-06	1.95E-05	2.03E-05

Table 4.21: Cross Sectional Areas of the Rear Spar of the Wing – Beam/Shell-R Model

Rear Spar Cross Sectional Area (m²) – Beam/Shell-R Model					
	Spar Cap (Root to Tip)	Coarse Mesh Model		Fine Mesh Model	
		Continuous Area (m²)	Discrete Area (m²)	Continuous Area (m²)	Discrete Area (m²)
Upper Flange	Bay 1	8.18E-05	8.69E-05	4.03E-04	4.91E-04
	Bay 2	3.09E-05	3.27E-05	6.71E-05	7.27E-05
	Bay 3	1.94E-05	2.04E-05	4.89E-05	5.28E-05
	Bay 4	1.83E-05	2.04E-05	3.53E-05	3.72E-05
	Bay 5	6.49E-06	8.01E-06	2.83E-05	3.22E-05
	Bay 6	6.00E-06	8.00E-06	2.70E-05	3.20E-05
Lower Flange	Bay 1	1.40E-04	1.61E-04	4.15E-04	4.92E-04
	Bay 2	4.22E-05	4.37E-05	7.59E-05	7.78E-05
	Bay 3	3.87E-05	4.13E-05	5.01E-05	5.29E-05
	Bay 4	2.21E-05	2.30E-05	4.08E-05	4.13E-05
	Bay 5	6.49E-06	8.01E-06	3.44E-05	3.45E-05
	Bay 6	6.00E-06	8.00E-06	3.13E-05	3.41E-05

From Tables 4.20 and 4.21 it can be seen that spar caps cross sectional areas decrease from the root to the tip of the wing, as expected.

Table 4.22 summarizes the upper middle skin thicknesses in the optimized wing torque box for both coarse and fine meshes models.

Table 4.22: Thicknesses of the Upper Middle Skin of the Wing - Beam/Shell-R Model

Upper Middle Skin Thicknesses – Beam/Shell-R Model					
	Thickness (Root to Tip)	Coarse Mesh Model		Fine Mesh Model	
		Continuous Thickness (m)	Discrete Thickness (m)	Continuous Thickness (m)	Discrete Thickness (m)
Upper Middle Skin	Bay 1	2.43E-03	2.54E-03	2.09E-03	2.28E-03
	Bay 2	1.97E-03	2.03E-03	1.17E-03	1.27E-03
	Bay 3	1.38E-03	1.60E-03	6.71E-04	8.10E-04
	Bay 4	8.70E-04	1.02E-03	4.68E-04	5.00E-04
	Bay 5	3.03E-04	4.00E-04	3.93E-04	4.00E-04
	Bay 6	3.00E-04	4.00E-04	3.36E-04	4.00E-04

4.9.1.5 Optimization Results of Model Five (Rod/Membrane-R Model)

Figure 4.34 shows the history of the objective function of the coarse mesh model with respect to the design cycle. The objective function is defined as minimizing total weight of the wing torque box subject to constraints defined. During the optimization process, hard convergence is achieved as well as hard and soft feasible discrete designs. Since membrane elements with drilling degrees of freedom are used, in order to handle the external load accurately, only single elements are used between the rib stations in the finite element model.

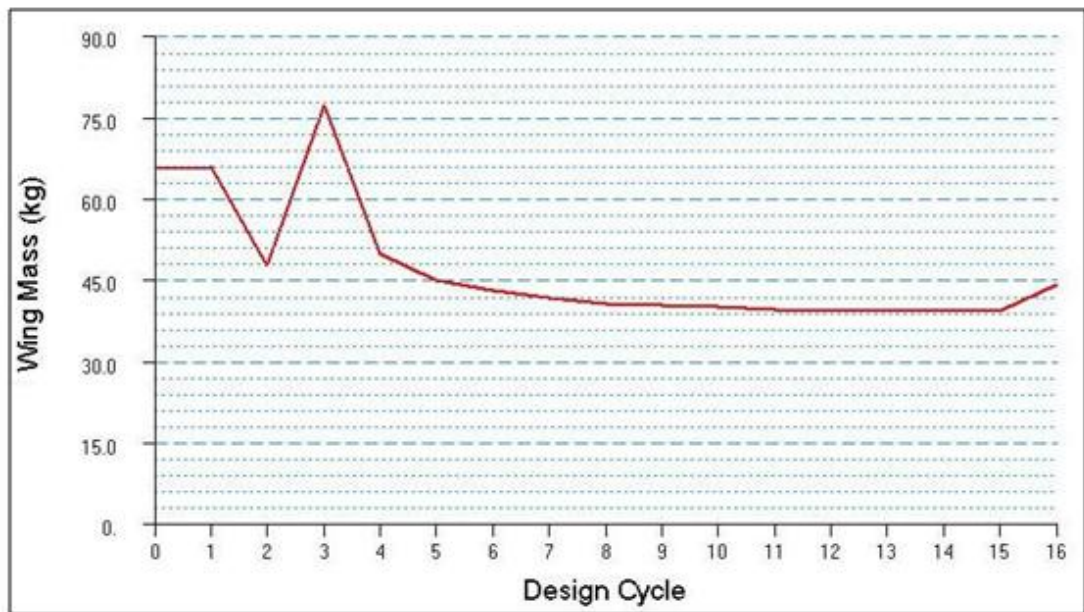


Figure 4.34: Variation of the Mass of the Wing with Respect to the Design Cycle - Coarse Mesh Rod/Membrane-R Model

Table 4.23 gives the initial and optimized masses of the wing torque box for the continuous and the discrete solutions for the coarse mesh model. The initial mass of the wing is based on the initial values of the design variables.

Table 4.23: Initial and Final Optimized Masses of the Wing - Rod/Membrane-R Model

Mass (kg) Of the Wing			
Mesh Size	Initial	Continuous	Discrete
Coarse	65.38	39.01	44.07

Figures 4.35 - 4.36 show the thickness scalar plots of the upper skin, lower skin, spar webs and ribs, in the optimized wing torque box which is modeled with rod/membrane - r element combination. It must be noted that these scalar plots refers to discrete optimization solution results.

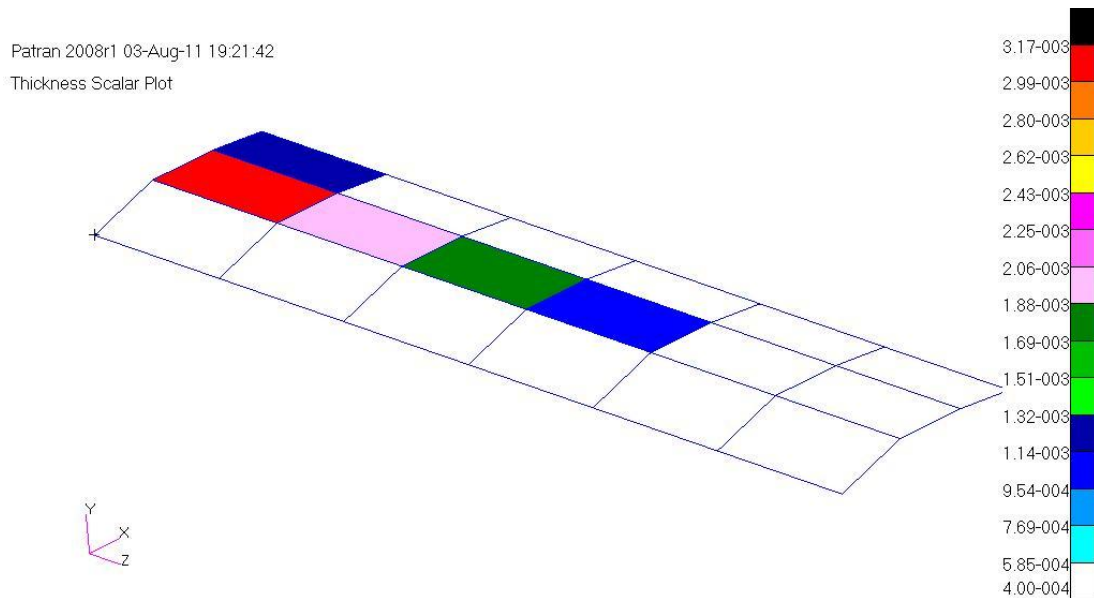


Figure 4.35: Thickness Scalar Plot of Upper Skin Panels in the Optimized Wing Torque Box - Coarse Mesh Rod/Membrane-R Model

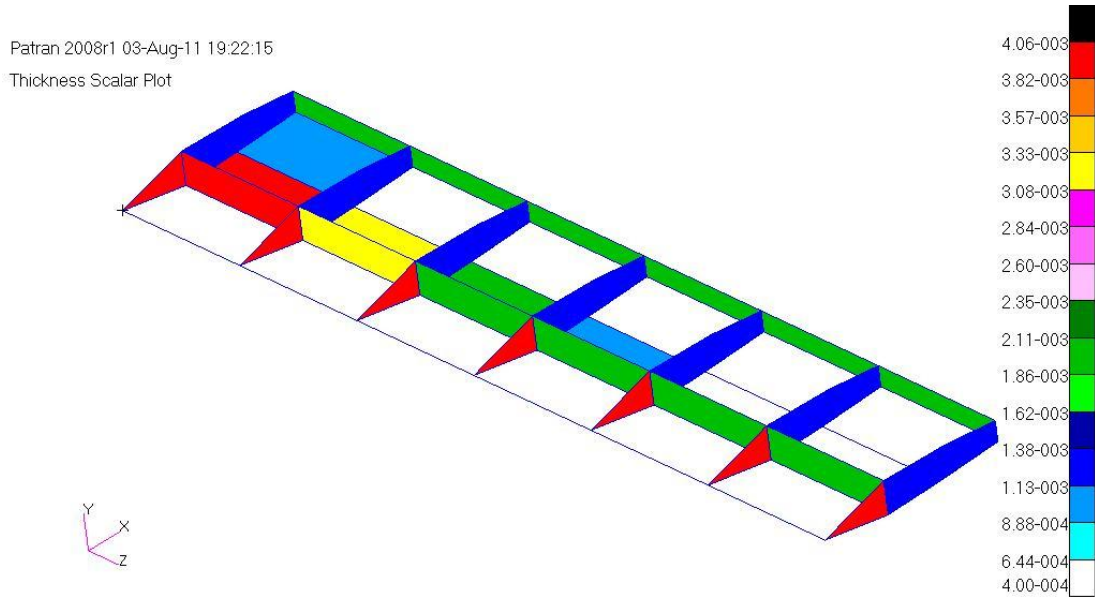


Figure 4.36: Thickness Scalar Plot of Lower Skin, Spar Web and Rib Panels in the Optimized Wing Torque Box - Coarse Mesh Rod/Membrane-R Model

Tables 4.24 and 4.25 summarize the spar cap areas of the front and the rear spar in the optimized wing torque box for the coarse mesh model.

Table 4.24: Cross Sectional Areas of the Front Spar of the Wing – Rod/Membrane-R Model

Front Spar Cross Sectional Area – Rod/Membrane-R Model			
	Spar Cap (Root to Tip)	Coarse Mesh Model	
		Continuous Area (m ²)	Discrete Area (m ²)
Upper Flange	Bay 1	6.13E-04	6.13E-04
	Bay 2	3.54E-04	3.75E-04
	Bay 3	5.37E-05	5.80E-05
	Bay 4	4.10E-05	4.40E-05
	Bay 5	3.80E-05	4.40E-05
	Bay 6	3.80E-05	4.40E-05
Lower Flange	Bay 1	6.13E-04	6.13E-04
	Bay 2	2.04E-04	2.13E-04
	Bay 3	4.43E-05	4.80E-05
	Bay 4	3.92E-05	4.40E-05
	Bay 5	3.80E-05	4.40E-05
	Bay 6	3.80E-05	4.40E-05

Table 4.25: Cross Sectional Areas of the Rear Spar of the Wing – Rod/Membrane-R Model

Rear Spar Cross Sectional Area – Rod/Membrane-R Model			
	Spar Cap (Root to Tip)	Coarse Mesh Model	
		Continuous Area (m²)	Discrete Area (m²)
Upper Flange	Bay 1	6.38E-05	6.70E-05
	Bay 2	3.80E-05	4.40E-05
	Bay 3	3.80E-05	4.40E-05
	Bay 4	3.80E-05	4.40E-05
	Bay 5	3.80E-05	4.40E-05
	Bay 6	3.80E-05	4.40E-05
Lower Flange	Bay 1	6.41E-05	6.70E-05
	Bay 2	3.80E-05	4.40E-05
	Bay 3	3.80E-05	4.40E-05
	Bay 4	3.80E-05	4.40E-05
	Bay 5	3.80E-05	4.40E-05
	Bay 6	3.80E-05	4.40E-05

Table 4.26 summarizes the upper middle skin thicknesses in the optimized wing torque box for coarse mesh model.

Table 4.26: Thicknesses of the Upper Middle Skin of the Wing - Rod/Membrane-R Model

Upper Middle Skin Thicknesses – Rod/Membrane-R Model			
	Thickness (Root to Tip)	Coarse Mesh Model	
		Continuous Thickness (m)	Discrete Thickness (m)
Upper Middle Skin	Bay 1	2.77E-03	3.17E-03
	Bay 2	2.02E-03	2.03E-03
	Bay 3	1.72E-03	1.80E-03
	Bay 4	8.23E-04	1.02E-03
	Bay 5	3.00E-04	4.00E-04
	Bay 6	3.00E-04	4.00E-04

The results presented in this section also show that skin thicknesses and spar flange areas also decrease from the root of the wing towards the tip of the wing in the rod/membrane - r model. This shows that side constraints work as expected.

Comparison of the upper skin thicknesses of the rod/shell and rod/membrane - r model shows that skin thicknesses of the rod/membrane - r model are slightly less than the skin thickness of the rod/shell model. On the contrary, spar flange areas of the rod/membrane - r model are higher than the spar flange areas of the rod/shell model. Based on this result it can be concluded that shell elements take higher share of the axial load than the membrane - r elements in the optimized configuration. On the contrary, spar flanges of the rod/membrane - r model take higher share of the axial load than the spar flanges of the rod/shell model. In a way, skins and flanges distribute the axial load in appropriate proportions.

4.9.1.6 Optimization Results of Model Six (Beam/Membrane-R Model)

Figure 4.37 shows the history of the objective function of the coarse mesh model with respect to the design cycle. The objective function is defined as minimizing total weight of the wing torque box subject to constraints defined. During the optimization process, hard convergence is achieved as well as hard and soft feasible discrete designs. Since membrane elements with drilling degrees of freedom are used, in order to handle the external load accurately, only single elements are used between the rib stations in the finite element model.



Figure 4.37: Variation of the Mass of Wing with Respect to the Design Cycle - Coarse Mesh Beam/Membrane-R Model

Table 4.27 gives the initial and the optimized masses of the wing torque box for the continuous and the discrete solutions for the coarse mesh model. The initial mass of the wing is based on the initial values of the design variables.

Table 4.27: Initial and Final Optimized Mass of the Wing – Beam/Membrane-R Model

Optimized Mass (kg) Of the Wing			
Mesh Size	Initial	Continuous	Discrete
Coarse	65.38	37.77	42.84

Comparison of the optimized masses of the beam/membrane - r and rod/membrane - r model show that the use of beam elements results in slightly lower mass in the final wing configuration. In the previous shell models, it was also observed that models which have spar flanges and stringers meshed with beam elements, had slight favorable overall mass.

Figures 4.38 - 4.39 show the thickness scalar plots of the upper skin, lower skin, spar webs and ribs, in the optimized wing torque box which is modeled with beam/membrane - r element combination.

Figures 4.38 - 4.39 show the thickness scalar plots for the coarse mesh of the upper skin panels and interior panels, which include lower skin, spar webs and ribs panels, in the optimized wing torque box which is modeled with beam/membrane - r element combination. It must be noted that these scalar plots refers to discrete optimization solution results

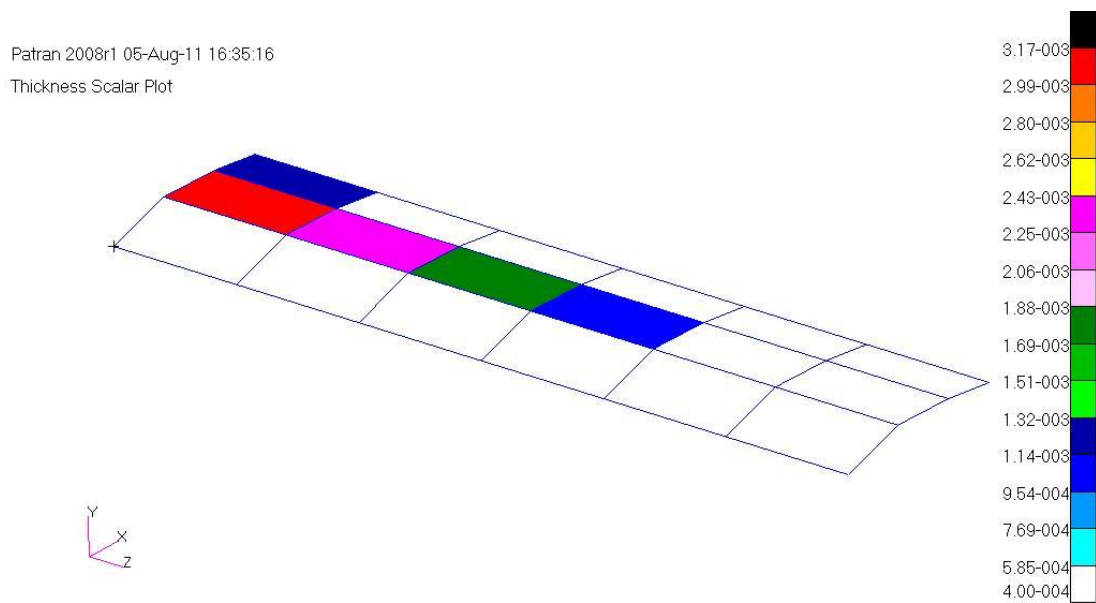


Figure 4.38: Thickness Scalar Plot of Upper Skin Panels in the Optimized Wing Torque Box - Coarse Mesh Beam/Membrane-R Model

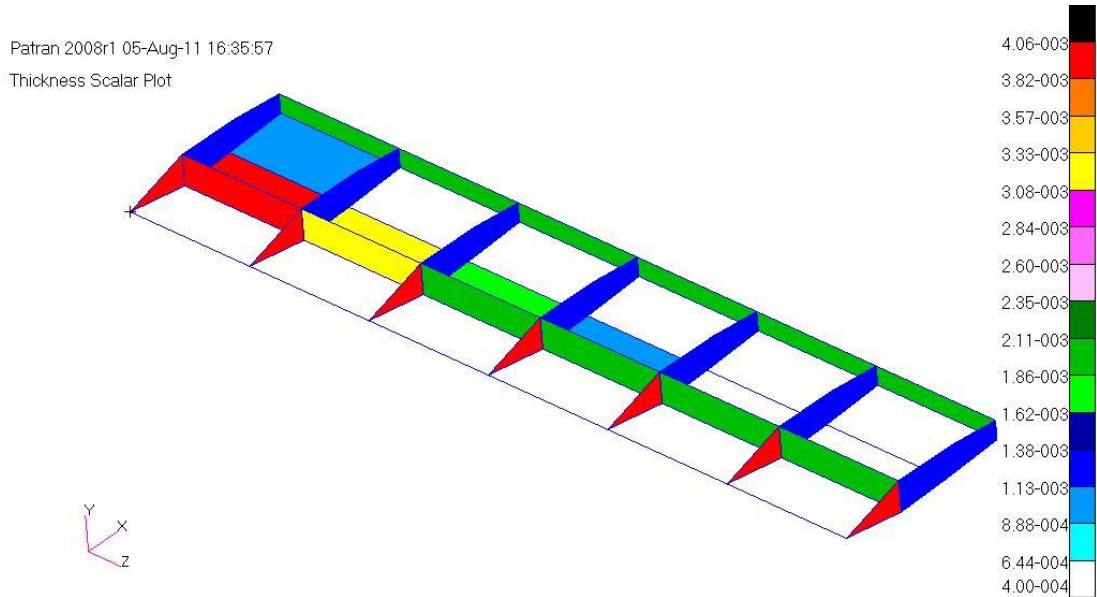


Figure 4.39: Thickness Scalar Plot of Lower Skin, Spar Web and Rib Panels in the Optimized Wing Torque Box - Coarse Mesh Beam/Membrane-R Model

Tables 4.28 and 4.29 summarize the spar cap areas of the front and the rear spar in the optimized wing torque box for the coarse mesh model. In the beam/membrane - r model, it is assumed that the spar caps have rectangular cross-section.

Table 4.28: Cross Sectional Areas of the Front Spar of the Wing – Beam/Membrane-R Model

Front Spar Cross Sectional Area– Beam/Membrane-R Model			
	Spar Cap (Root to Tip)	Coarse Mesh Model	
		Continuous Area (m²)	Discrete Area (m²)
Upper Flange	Spar Cap 1	6.09E-04	6.09E-04
	Spar Cap 2	2.88E-04	2.88E-04
	Spar Cap 3	1.08E-04	1.14E-04
	Spar Cap 4	5.79E-05	6.05E-05
	Spar Cap 5	2.05E-05	2.54E-05
	Spar Cap 6	1.24E-05	1.26E-05
Lower Flange	Spar Cap 1	6.09E-04	6.09E-04
	Spar Cap 2	1.95E-04	1.98E-04
	Spar Cap 3	8.15E-05	8.18E-05
	Spar Cap 4	4.16E-05	4.47E-05
	Spar Cap 5	1.83E-05	2.04E-05
	Spar Cap 6	1.40E-05	1.62E-05

Table 4.29: Cross Sectional Areas of the Rear Spar of the Wing – Beam/Membrane-R Model

Rear Spar Cross Sectional Area– Beam/Membrane-R Model			
	Spar Cap (Root to Tip)	Coarse Mesh Model	
		Continuous Area (m²)	Discrete Area (m²)
Upper Flange	Spar Cap 1	3.44E-05	3.48E-05
	Spar Cap 2	2.18E-05	2.54E-05
	Spar Cap 3	1.83E-05	2.03E-05
	Spar Cap 4	1.52E-05	1.62E-05
	Spar Cap 5	1.39E-05	1.62E-05
	Spar Cap 6	1.15E-05	1.26E-05
Lower Flange	Spar Cap 1	4.42E-05	4.84E-05
	Spar Cap 2	2.98E-05	3.21E-05
	Spar Cap 3	2.44E-05	2.54E-05
	Spar Cap 4	1.87E-05	2.03E-05
	Spar Cap 5	1.57E-05	1.62E-05
	Spar Cap 6	1.41E-05	1.62E-05

Table 4.30 summarizes the upper middle skin thicknesses in the optimized wing torque box for coarse mesh model.

Table 4.30: Thicknesses of the Upper Middle Skin of the Wing - Beam/Membrane-R Model

Upper Middle Skin Thicknesses – Beam/Membrane-R Model			
	Thickness (Root to Tip)	Coarse Mesh Model	
		Continuous Thickness (m)	Discrete Thickness (m)
Upper Middle Skin	Bay 1	2.72E-03	3.17E-03
	Bay 2	2.13E-03	2.28E-03
	Bay 3	1.70E-03	1.80E-03
	Bay 4	8.16E-04	1.02E-03
	Bay 5	3.00E-04	4.00E-04
	Bay 6	3.00E-04	4.00E-04

Comparison of the upper skin thickness and spar flange areas of the rod/membrane - r and beam/membrane - r models show that skins thicknesses of both models are nearly equal to each other. However, in most bays, beam/membrane - r model has slightly higher spar flange areas than the rod/membrane - r model. Thus, it can be concluded that the difference in the final optimized masses of the wing structure of the rod/membrane - r and beam/membrane - r models is mainly due to the differences in the flange areas.

4.9.1.7 Summary of the Optimization Results of the Wing Torque Box Modeled with Different Element Combinations

In order to examine the effect of using different element types in the finite element models used in the structural optimization, and the effect of mesh size on the optimized masses, final optimized masses of the wing torque boxes are tabulated in two tables for the coarse and the fine mesh cases. Tables 4.31 and 4.32 summarize the initial and optimized masses for all finite element models used in the optimization study for both coarse and fine mesh cases.

Table 4.31: Optimized Masses of the Wing Structure - Coarse Mesh Results – Coarse Mesh

Optimized Mass (kg) Results of FE Wing Torque Box Models – Coarse Mesh			
Models	Initial	Continuous	Discrete
Rod-Shell	65.38	41.09	46.77
Beam-Shell	65.38	38.28	42.97
Rod-Shell R	65.38	38.88	43.57
Beam-Shell R	65.38	38.29	42.11
Rod-Membrane R	65.38	39.01	44.07
Beam-Membrane R	65.38	37.77	42.84

Table 4.32: Optimized Masses of the Wing Structure - Fine Mesh Results

Optimization Mass (kg) Results of FE Wing Torque Box Models – Fine Mesh			
Models	Initial	Continuous	Discrete
Rod-Shell	66.67	51.50	58.61
Beam-Shell	66.67	50.25	58.02
Rod-Shell R	66.67	50.12	58.23
Beam-Shell R	66.67	52.13	59.70

It should be noted that in the discrete optimization, MSC Nastran is allowed to select the first round-up dimensions among a list of standard thicknesses and flange areas. Therefore, masses determined by the discrete optimization are higher than the masses determined by the continuous optimization. On the other hand, for each 1D and 2D element combination shown in Tables 4.31 and 4.32, the optimized mass of the wing torque box obtained using the fine mesh model in the optimization process, is higher than the optimized mass of the wing torque box obtained using the coarse mesh model. It should be noted that although the stresses at the centers of the domains of the bays are lower for the fine mesh models, maximum stresses of the fine mesh models in the domains of each bay are higher than the maximum stresses obtained by the coarse mesh models in the optimization process. For the coarse mesh case, the stresses at the element centers of the shell and bar elements are used in the stress constraint equations. Therefore, for the coarse mesh case, stresses at the element centers correspond to the mid bay locations. However, for the fine mesh case, stress constraints are written with respect to the maximum stress in the domains of each bay. Therefore, fine mesh models have higher stresses because maximum stress in a bay is at the inboard end of the bay. Thus, approximately there is 10 kg difference between the optimized masses of the wing torque boxes obtained by the coarse and fine mesh finite element models in the optimization process. However, the effect of local buckling and maximum deflection constraints should also be checked to confirm this conclusion.

Results of the optimization study shows that optimized wing masses, determined by the use of the different finite element models in the optimization process, are very close to each other with only slight favorable overall mass on behalf of models which have spar flanges and stringers meshed with beam elements.

As an example result, Figure 4.40 shows the effect of using different finite element types on the optimized thicknesses of upper mid skin for all six finite element models used in wing torque box structural optimization. As it can be seen from Figure 4.40, the thicknesses decrease along the wing span from root to tip, as expected.

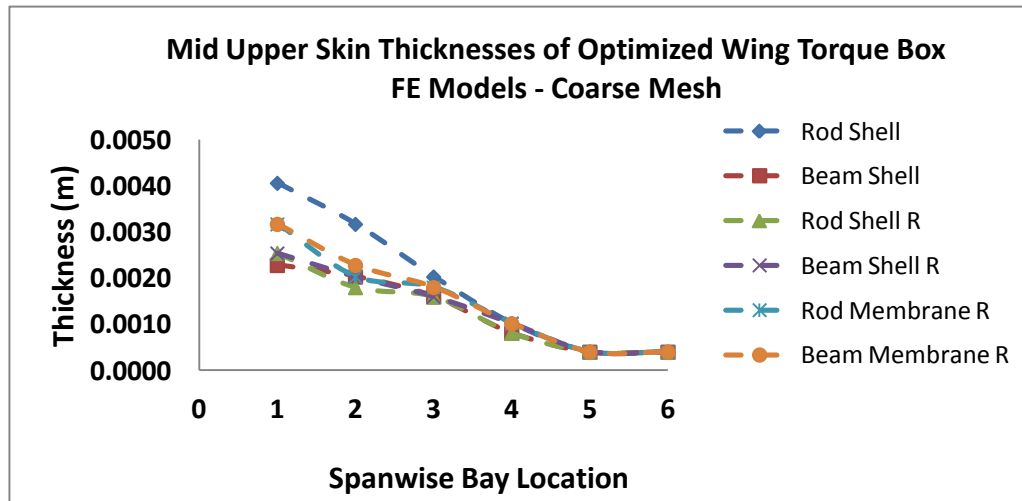


Figure 4.40: Variation of Upper Middle Skin Thickness of the Optimized Wing Torque Boxes - Coarse Mesh Models

Figure 4.41 shows the effect of using different finite element types on the optimized cross sectional areas of front spar upper-flange for all six finite element models used in wing torque box structural optimization.

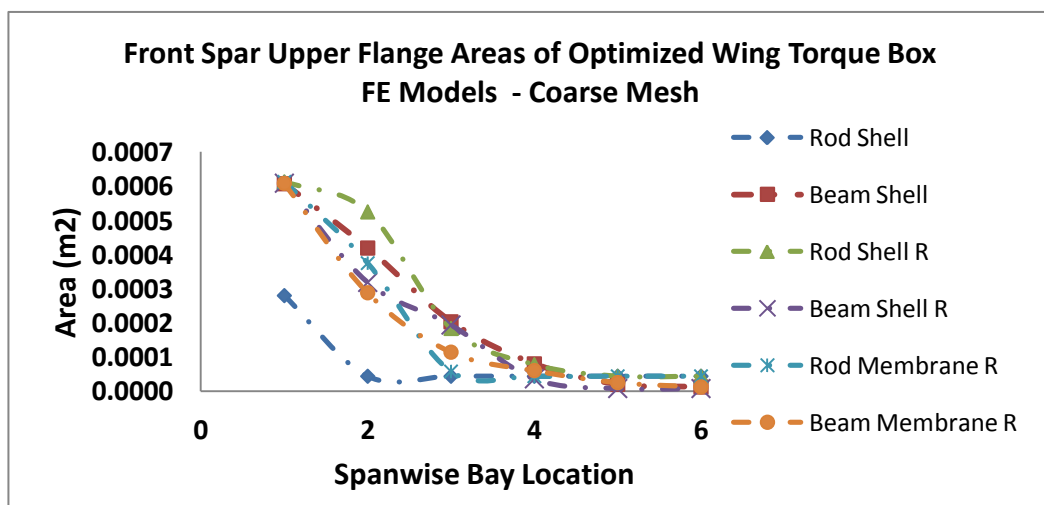


Figure 4.41: Variation Upper -Flange Cap Areas of the Front Spar in the Optimized Wing Torque Boxes - Coarse Mesh Models

4.9.2 The Effect of Design Constraints on Optimum Wing Torque Box Configurations

The effect of design constraints on optimum wing configurations is evaluated by relaxing certain constraints such as deflection and local buckling. In this section one of the wing torque box configurations (Rod/Shell Model) is optimized for minimum mass while considering the effect of each constraint individually on the optimum wing mass.

4.9.2.1 Optimization of the Wing Torque Box with Stress Constraints Only – Rod/Shell Model

Rod-Shell model of the wing is optimized using the Von Mises and axial stress constraints only, for both coarse and fine mesh models. For both mesh sizes, hard convergence achieved and feasible discrete designs are obtained. Table 4.33 gives the optimized mass results for coarse and fine meshes.

Table 4.33: Optimized Masses of the Wing - Rod/Shell Model under Stresses Constraints Only

Optimized Mass (kg) Results of the Wing			
Models	Initial	Continuous	Discrete
Rod-Shell / Coarse Mesh	65.38	17.95	21.10
Rod-Shell / Fine Mesh	66.67	26.84	30.37

As it can be seen from Table 4.33 above, optimization of wing torque box under stresses constraint only results in optimized masses which are significantly small when compared to the results in Tables 4.31 and 4.32 which give optimized masses for the rod/shell model with the local buckling and tip deflection constraints included. The main reason for the large difference is due to relaxing the local buckling and tip deflection constraints in the optimization problem. To decide on which constraint has more significant effect on the final optimized masses of the

wing, in the next section the optimization problem is solved using the combination of stress and tip displacement constraints only. Table 4.33 also shows that optimized masses determined by the use of fine mesh finite element models in the optimization process are higher than the optimized masses determined by the use of coarse mesh finite element models in the optimization process. Since for the particular optimization problem only stress constraints are used, with confidence it can be concluded that higher maximum stress of the fine mesh models in the domains of each bay is the main reason for the higher optimized mass obtained by the use of fine mesh model in the optimization process.

Figure 4.42 and 4.43 show the history of the objective function with respect to the design cycle for the coarse mesh and the fine mesh models. The objective function is defined as minimizing total weight of the wing torque box subject to stress constraints only.

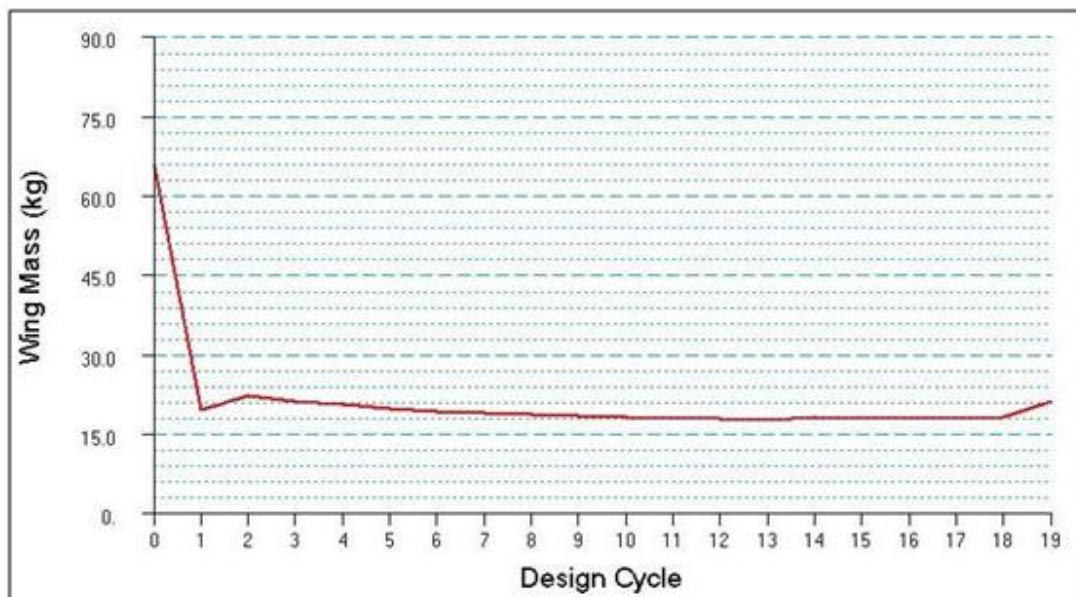


Figure 4.42: Variation of the Mass of the Wing With Design Iterations – Rod/Shell Coarse Mesh Model under Stress Constraints Only

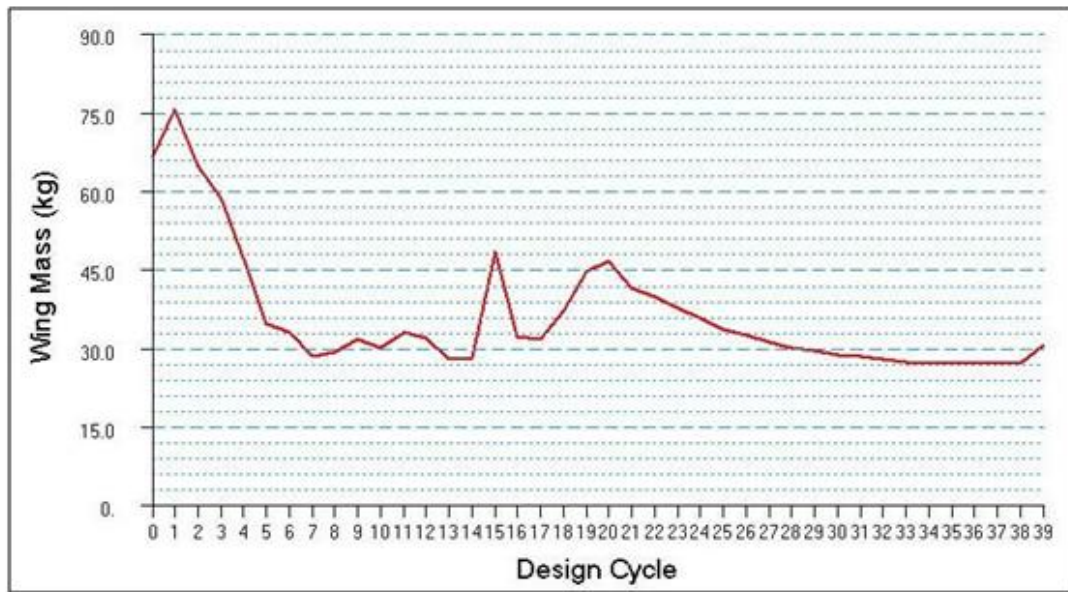


Figure 4.43: Variation of the Mass of the Wing With Design Iterations – Rod/Shell Fine Mesh Model under Stress Constraints Only

For both coarse and fine mesh models, Figures 4.44 - 4.47 show the thickness scalar plots, of the upper skin, lower skin, spar webs and ribs, in the optimized wing torque box which is modeled with rod/shell element combination. It must be noted that these scalar plots refer to discrete optimization solution results.

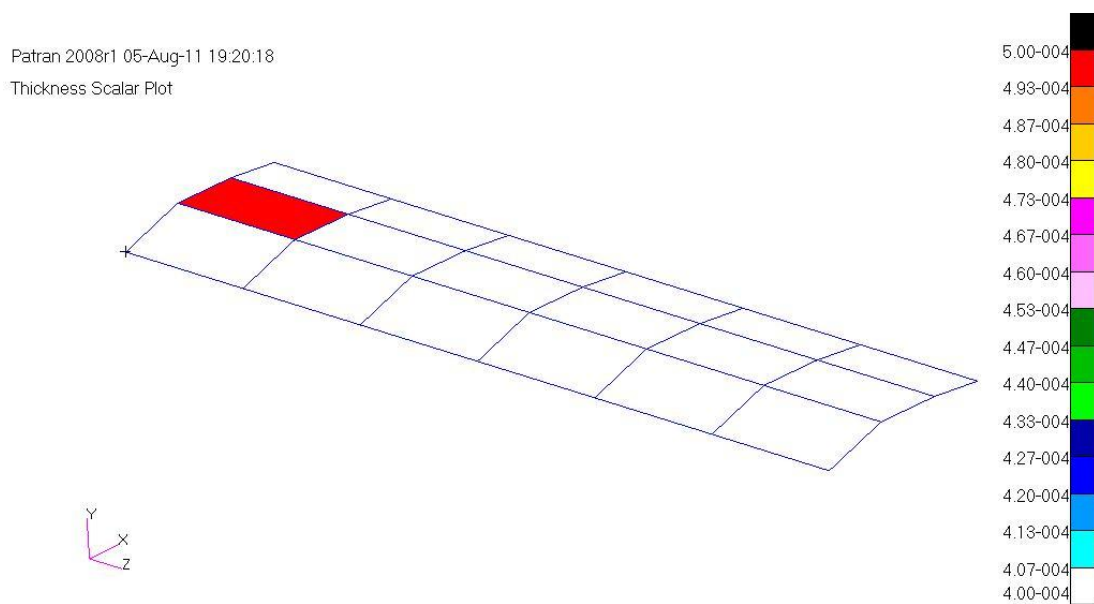


Figure 4.44: Thickness Scalar Plots of Upper Skin Panels in the Optimized Wing Rod/Shell for Coarse Mesh Model under Stresses Constraints

Patran 2008r1 05-Aug-11 19:26:22
Thickness Scalar Plot

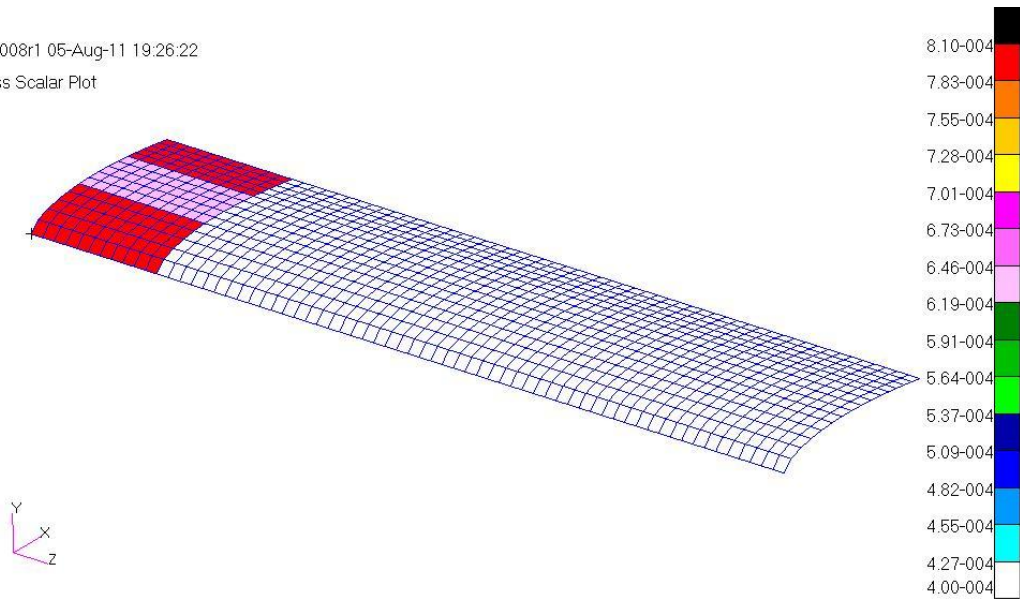


Figure 4.45: Thickness Scalar Plots of Upper Skin Panels in the Optimized Wing Rod/Shell for Fine Mesh Model under Stresses Constraints

Patran 2008r1 05-Aug-11 19:20:51
Thickness Scalar Plot

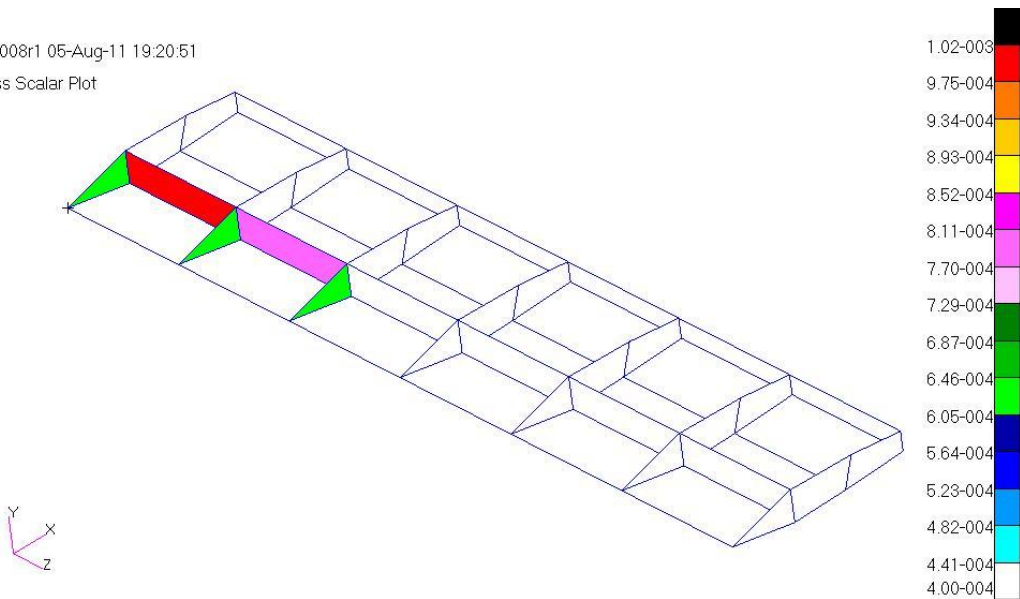


Figure 4.46: Thickness Scalar Plots of Interior Panels in the Optimized Wing Rod/Shell for Coarse Mesh Model under Stresses Constraints

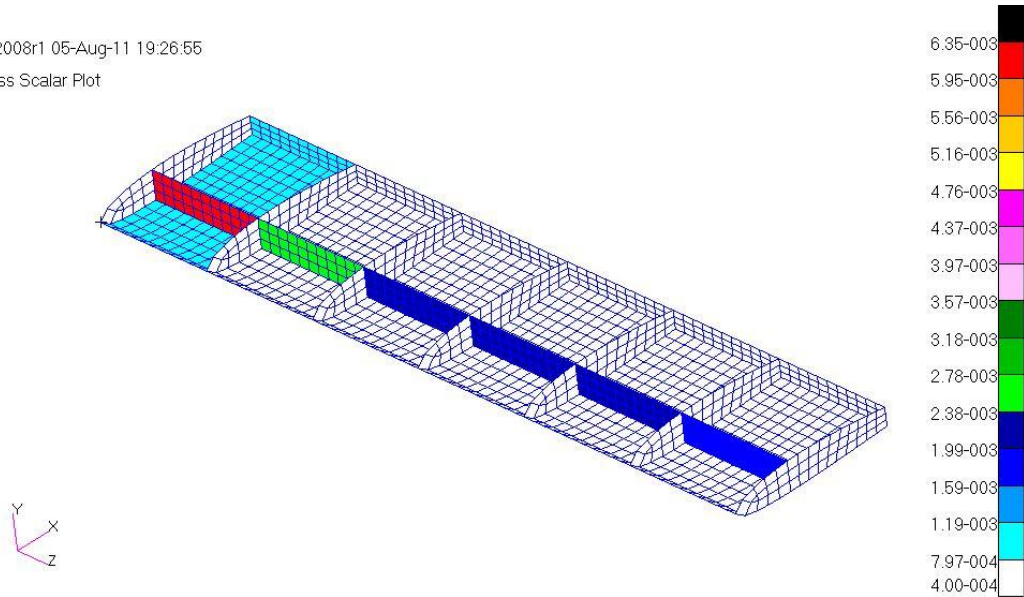


Figure 4.47: Thickness Scalar Plots of Upper Skin Panels in the Optimized Wing – Rod/Shell Fine Mesh Model under Stress Constraint Only

Figures 4.48 and 4.49 give the variation of front spar upper flange areas and upper middle skin thicknesses along the span of wing for both coarse and fine mesh.

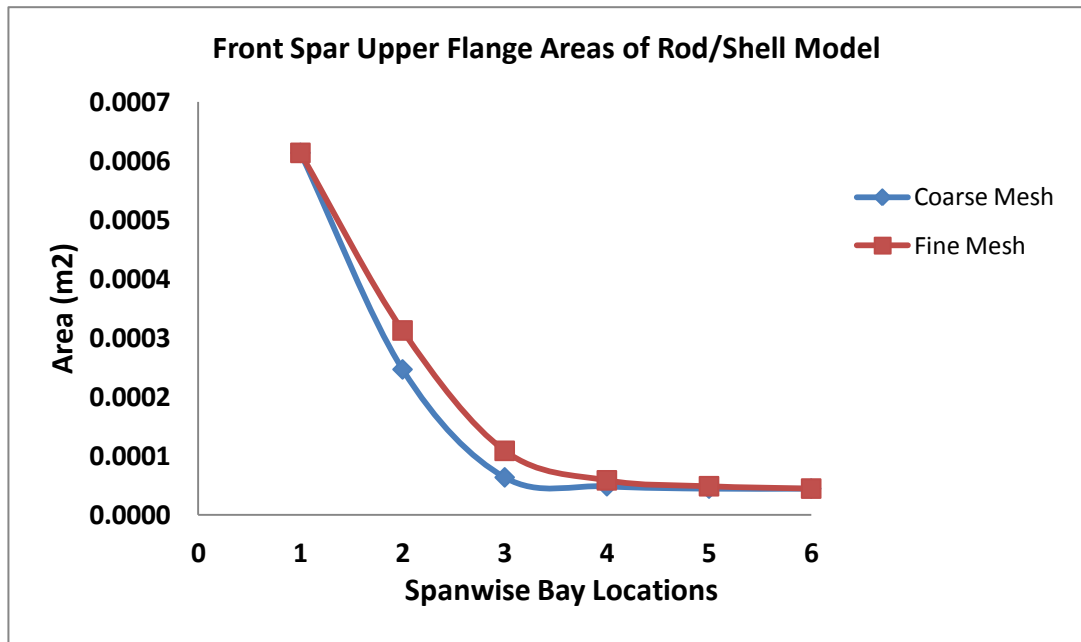


Figure 4.48: Variation of the Front Spar Upper Flange Areas of the Wing - Rod Shell Model under Stress Constraint Only

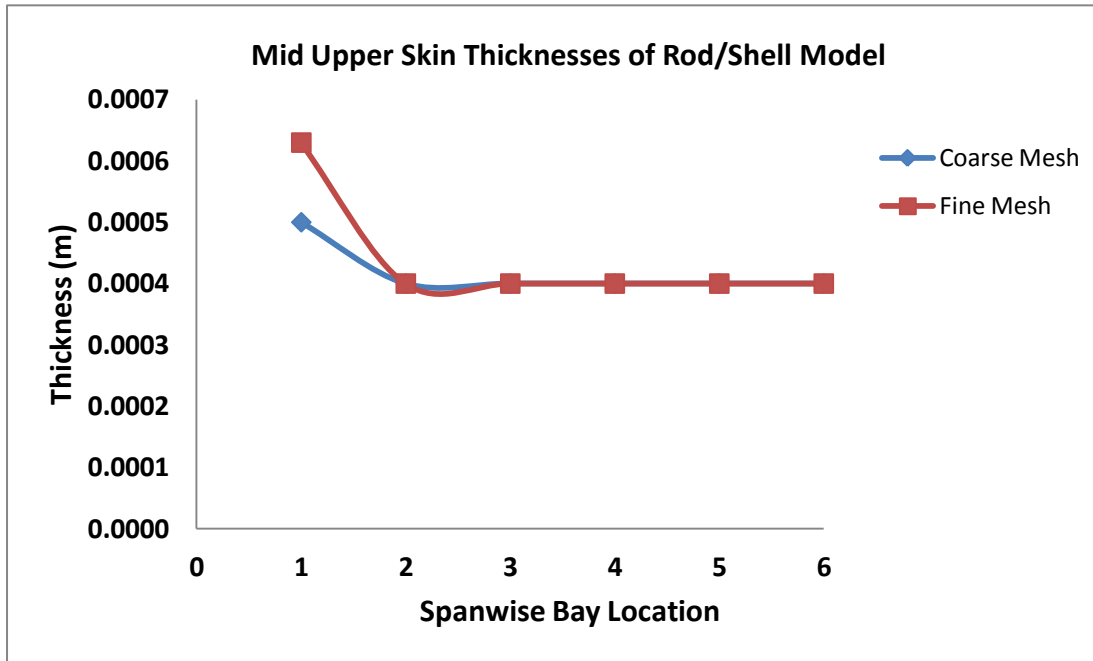


Figure 4.49: Variation of the Upper Middle Skin Thicknesses of the Wing – Rod/Shell Model under Stress Constraint Only

Optimization conducted using the finite element model with fine mesh gives higher flange areas and skin thicknesses compared to the coarse mesh model. Higher thickness and flange areas of the optimized wing obtained by the use of fine mesh finite element model in the optimization process, account for the higher optimized mass.

4.9.2.2 Optimization of the Wing Torque Box with Stress and Tip Displacement Constraints – Rod/Shell Model

Rod-Shell model of the wing is optimized using the Von Mises stress, axial stress and tip displacement constraints, for both coarse and fine meshes. For both mesh sizes, hard convergence achieved and feasible discrete designs are obtained. Table 4.36 gives the optimized masses for the coarse and the fine meshes.

Table 4.34: Optimized Masses of the Wing – Rod/Shell Model under Stress and Displacement Constraints

Optimized Mass (kg) Results of the Wing			
Models	Initial	Continuous	Discrete
Rod-Shell / Coarse Mesh	65.38	31.94	37.63
Rod-Shell / Fine Mesh	66.67	34.63	38.57

As it can be seen from Table 4.34, by introducing the displacement constraint besides the stress constraint, the difference between the optimized masses determined by the coarse mesh and the fine mesh models become less when it is compared to the results under stress constraint only. Compared to the results of the optimization problem with stress constraints only, for the combined stress and displacement constraint problem, the increase of the optimized mass of the coarse mesh model is much higher than the increase of the optimized mass of the fine mesh model. This result is an indication that displacement constraint is a more stringent constraint for the coarse mesh model compared to the fine mesh model.

Figure 4.50 and 4.51 show the history of the objective function with respect to the design cycle for the coarse and the fine mesh models. The objective function is defined as minimizing total weight of the wing torque box subject to stress and displacement constraints only.

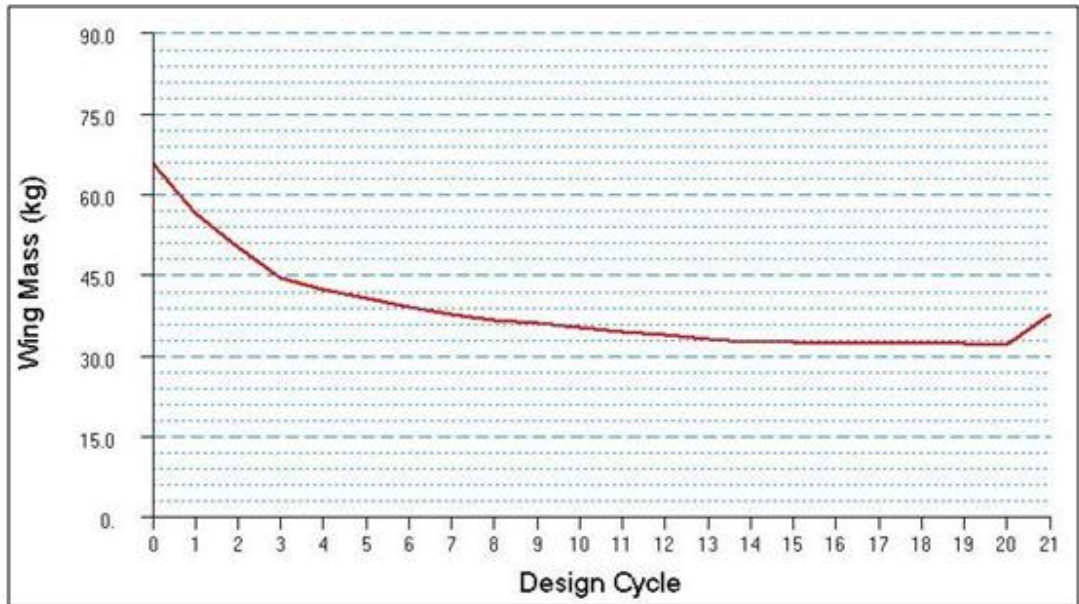


Figure 4.50: Variation of the Mass of Wing With the Design Cycles – Rod/Shell Coarse Mesh Model under Stress and Displacement Constraints

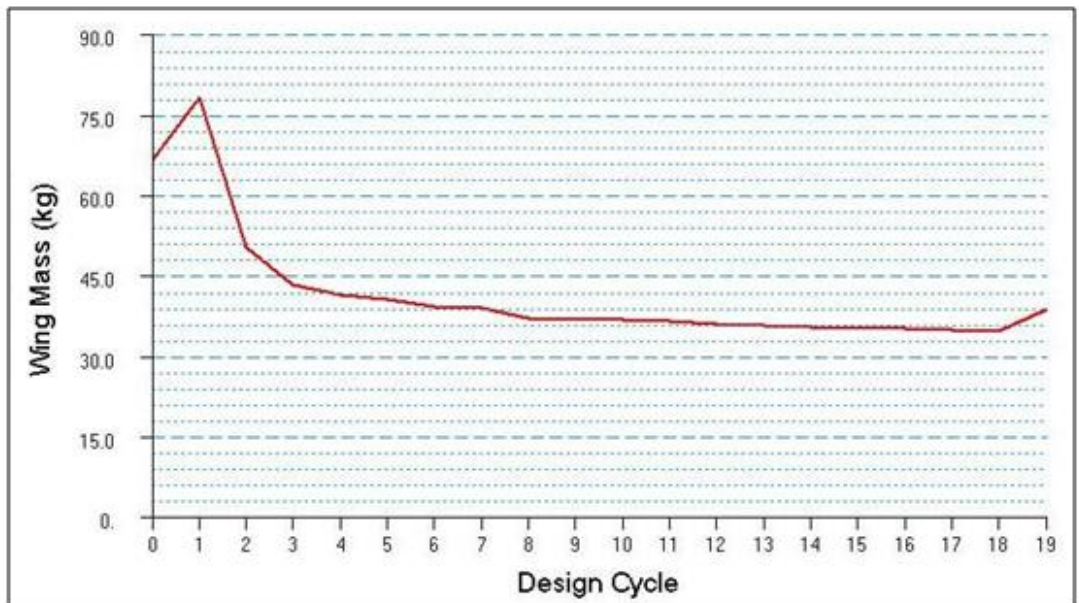


Figure 4.51: Variation of the Mass of the Wing With the Design Cycle – Rod/Shell Fine Mesh Model under Stress and Displacement Constraints

Figures 4.52 - 4.55 show the thickness scalar plots of the upper skin panels and interior panels in the optimized wing torque box, for the coarse and the fine mesh models.

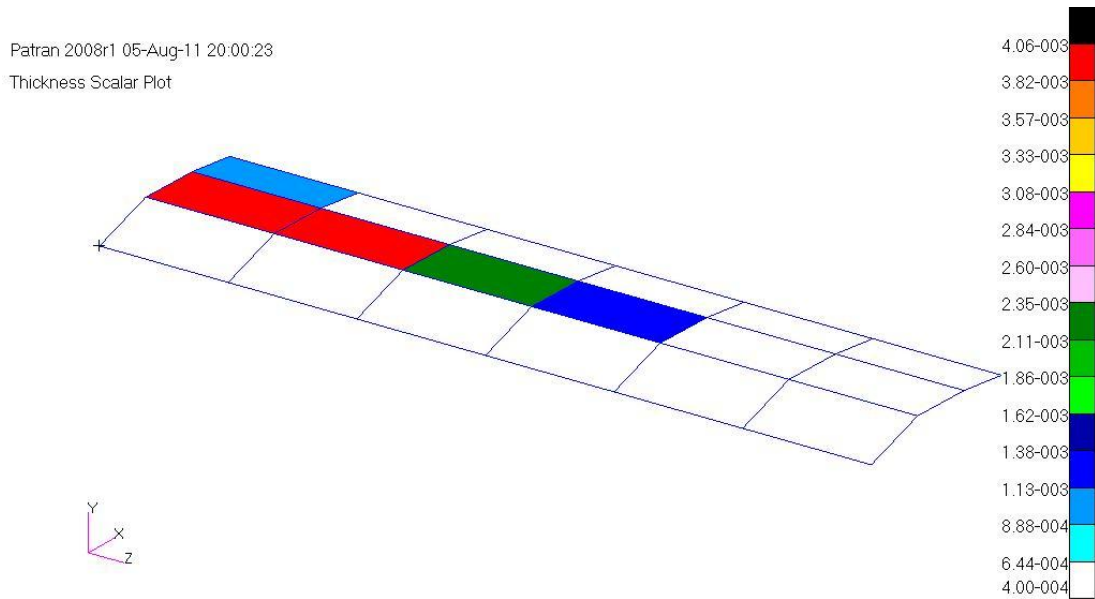


Figure 4.52: Thickness Scalar Plots of the Upper Skin Panels in the Optimized Wing
– Rod/Shell Coarse Mesh Model under Stress and Displacement Constraints

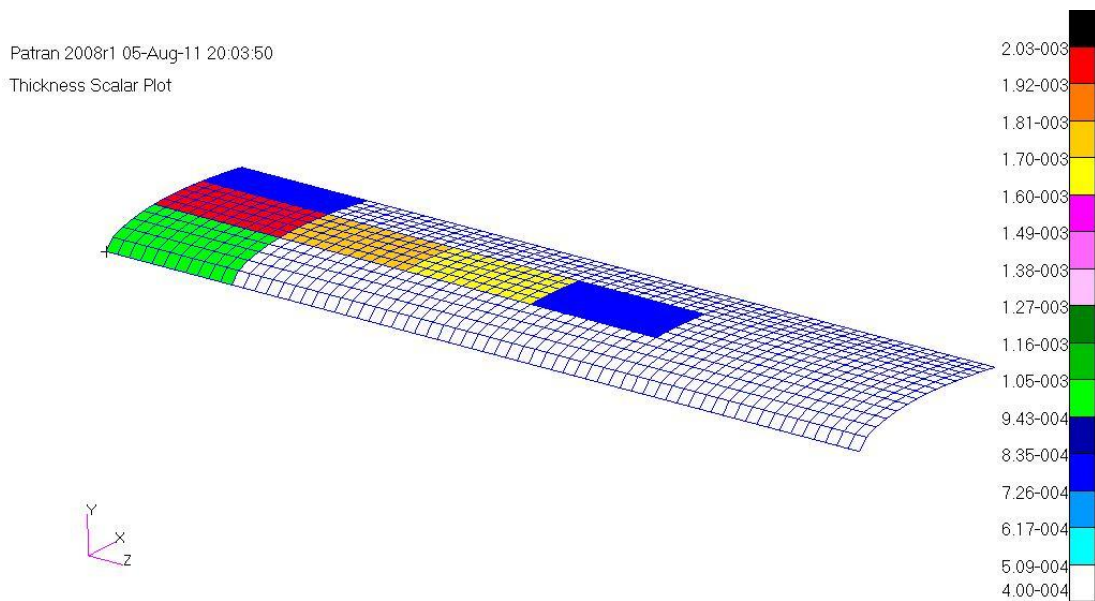


Figure 4.53: Thickness Scalar Plots of the Upper Skin Panels in the Optimized Wing
– Rod/Shell Fine Mesh Model under Stress and Displacement Constraints

Patran 2008r1 05-Aug-11 20:00:53
Thickness Scalar Plot

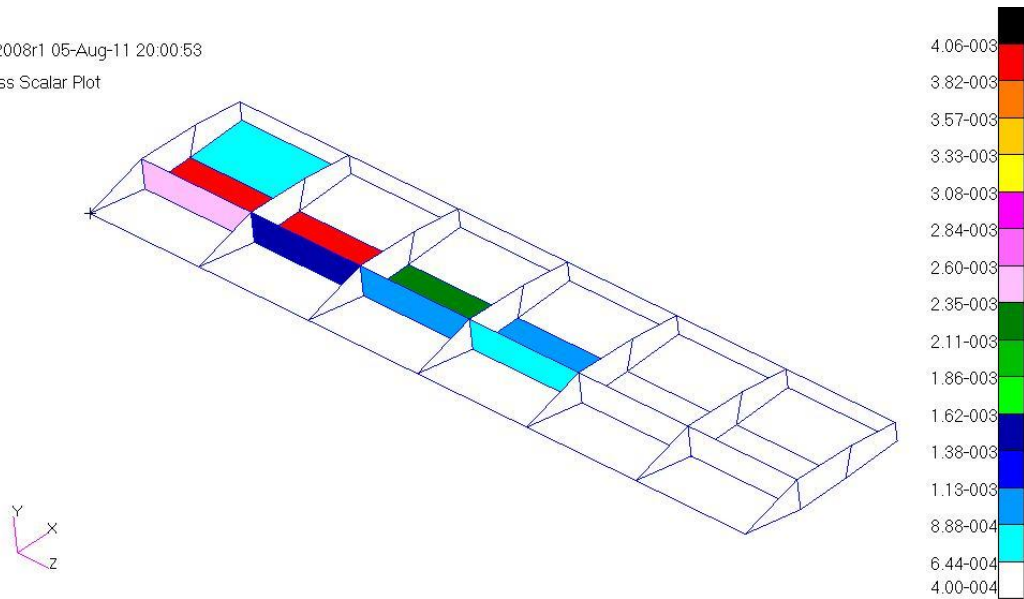


Figure 4.54: Thickness Scalar Plots of Interior Panels in the Optimized Wing – Rod/Shell Coarse Mesh Model under Stress and Displacement Constraints

Patran 2008r1 05-Aug-11 20:04:21
Thickness Scalar Plot

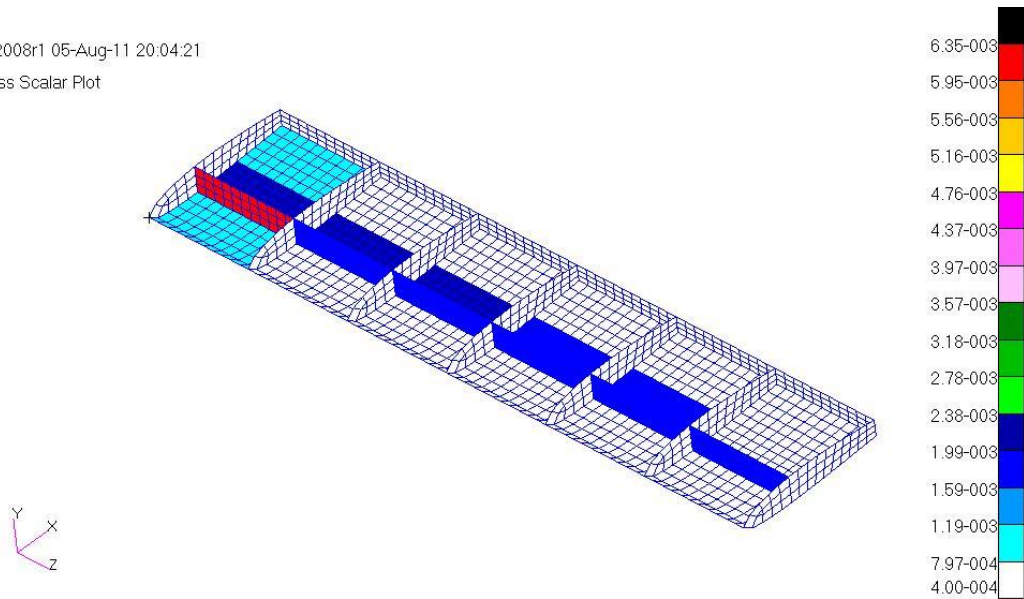


Figure 4.55: Thickness Scalar Plots of Interior Panels in the Optimized Wing – Rod/Shell Fine Mesh Model under Stress and Displacement Constraints

Figures 4.56 and 4.57 give the variation of the front spar upper flange area and upper middle skin thicknesses with the span-wise bay locations for both coarse and fine mesh models.

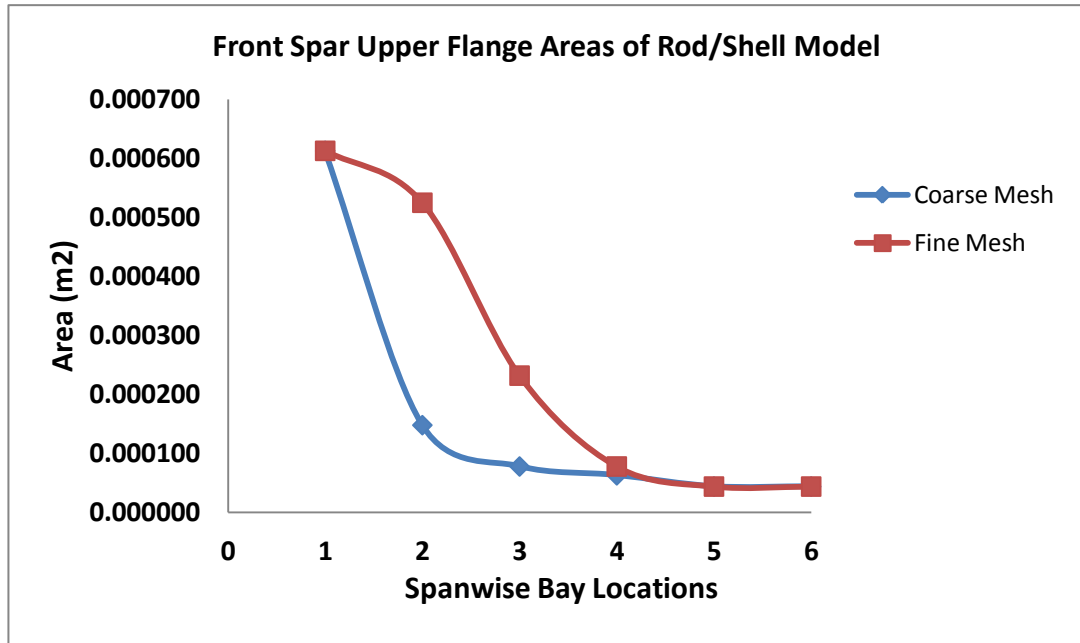


Figure 4.56: Variation of the Front Spar Upper Flange Areas of the Wing – Rod/Shell Model under Stress and Displacement Constraints

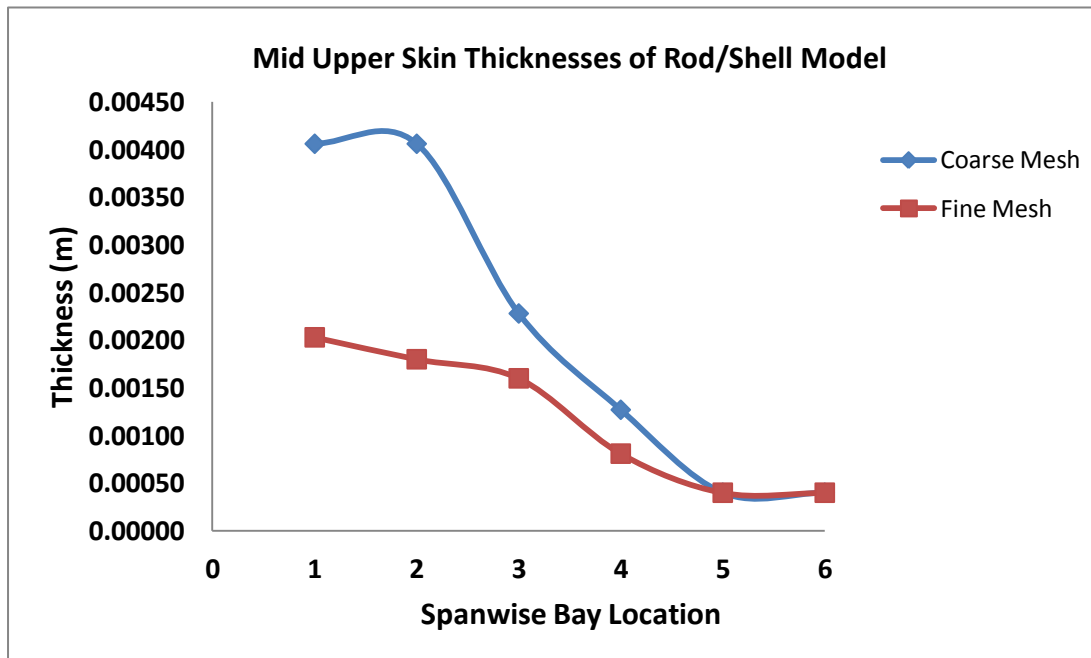


Figure 4.57: Variation of the Upper Middle Skin Thicknesses of the Wing – Rod/Shell Model under Stress and Displacement Constraints

Figures 4.56 and 4.57 show that the thickness of upper middle skin for the coarse mesh model is higher than the thickness determined by the use of the fine mesh model in the optimization process. It is seen that in order to satisfy the displacement constraint, upper middle skin thickness of the coarse mesh model has increased, and has become higher than the skin thickness of the fine mesh model.

4.9.2.3 Wing Rod/Shell Model Optimization with Stress and Buckling Constraints

Rod-Shell model of the wing is optimized using the Von Mises stress, axial stress and buckling constraints, for both coarse and fine meshes models. For both mesh sizes, hard convergence achieved and feasible discrete designs are obtained. Table 4.35 gives the optimized mass results for the coarse and the fine meshes.

Table 4.35: Optimized Masses of the Wing – Rod/Shell Model under Stress and Buckling Constraints

Optimized Mass (kg) Results of the Wing			
Models	Initial	Continuous	Discrete
Rod-Shell / Coarse Mesh	65.38	30.20	34.76
Rod-Shell / Fine Mesh	66.67	45.51	51.72

Table 4.35 shows that for the fine mesh case, buckling constraint besides stress constraint results in higher optimized mass compared to the optimized mass obtained under stress and displacement constraints. This result shows that local buckling is a much more stringent constraint than the deflection constraint for this particular problem. However, for the coarse mesh model, optimization using the stress and deflection constraints results in slightly higher mass than the optimization under stress and buckling constraints. This result is an indication of the significant effect of the mesh size on the optimum mass configurations. Since results of fine mesh finite element models are more reliable, it can be concluded that coarse mesh finite model

underestimates the effect of local buckling constraint on the optimum mass configuration.

Figure 4.58 and 4.59 show the history of the objective function of the coarse and the fine mesh model with respect to the design cycle. The objective function is defined as minimizing total weight of the wing torque box subject to stress and buckling constraints only.

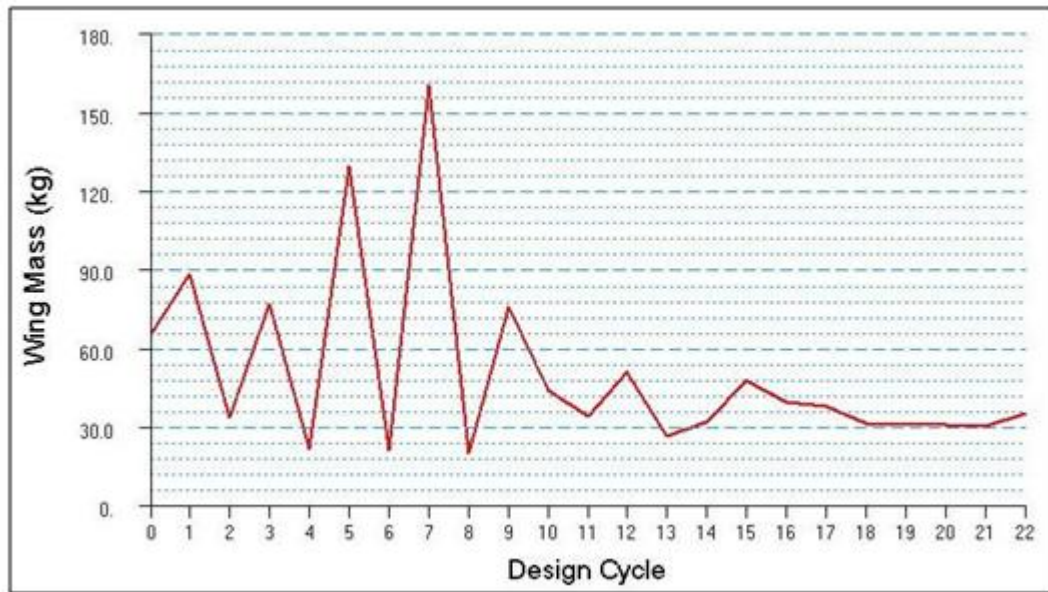


Figure 4.58: Variation of the Mass of Wing With the Design Cycles – Rod/Shell Coarse Mesh Model under Stress and Buckling Constraints

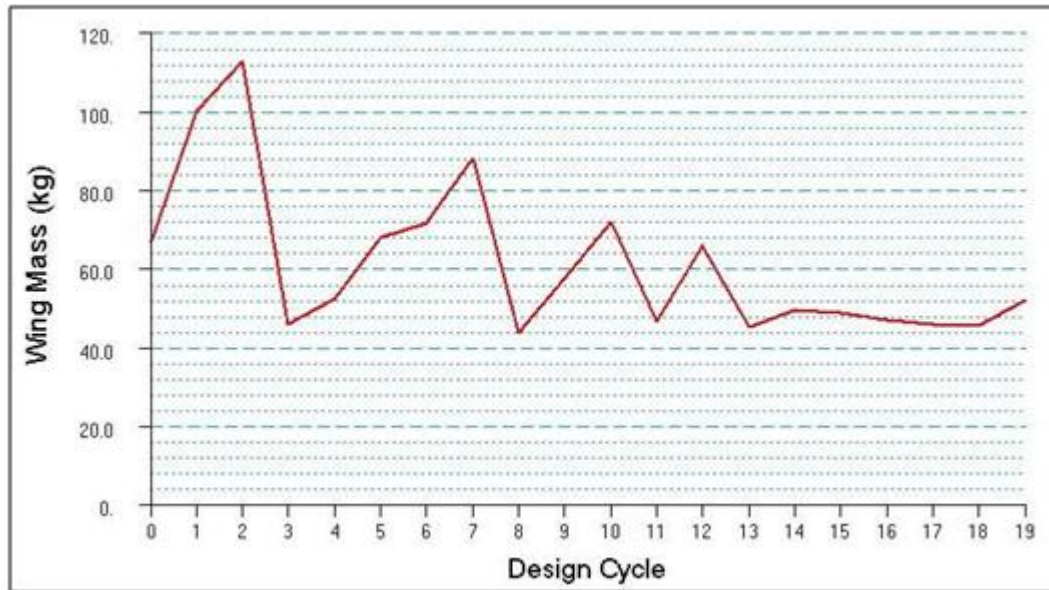


Figure 4.59: Variation of the Mass of Wing With the Design Cycles – Rod/Shell Fine Mesh Model under Stress and Buckling Constraints

For both coarse and fine mesh models, Figures 4.60 - 4.63 show the thickness scalar plots, of the upper skin, lower skin, spar webs and ribs, in the optimized wing torque box which is modeled with rod/shell element combination. It must be noted that these scalar plots refer to discrete optimization solution results.

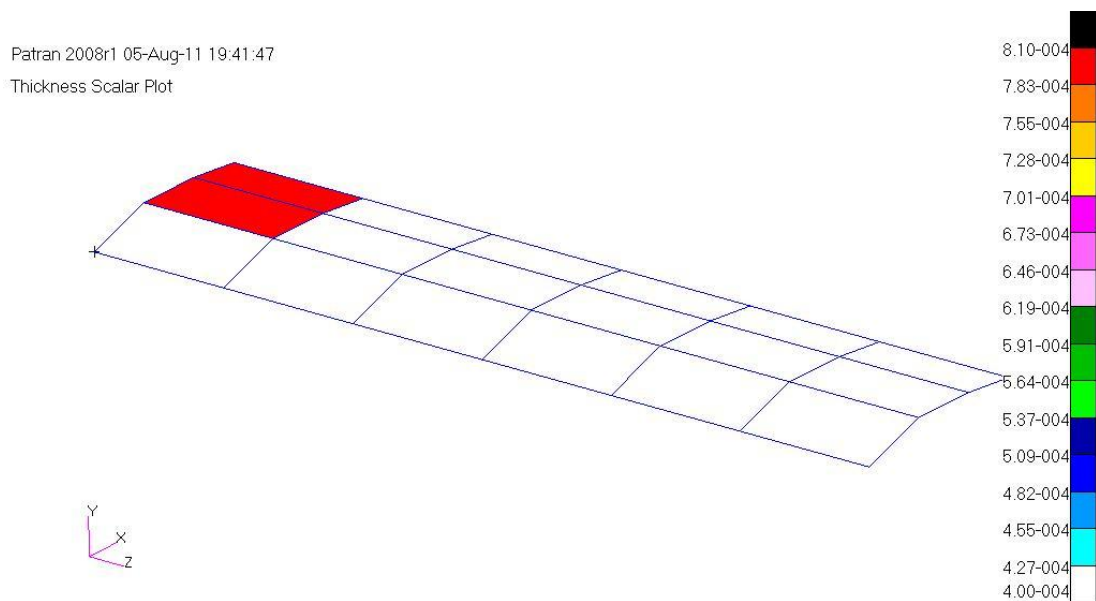


Figure 4.60: Thickness Scalar Plots of the Upper Skin Panels in the Optimized Wing – Rod/Shell Coarse Mesh Model under Stress and Buckling Constraints

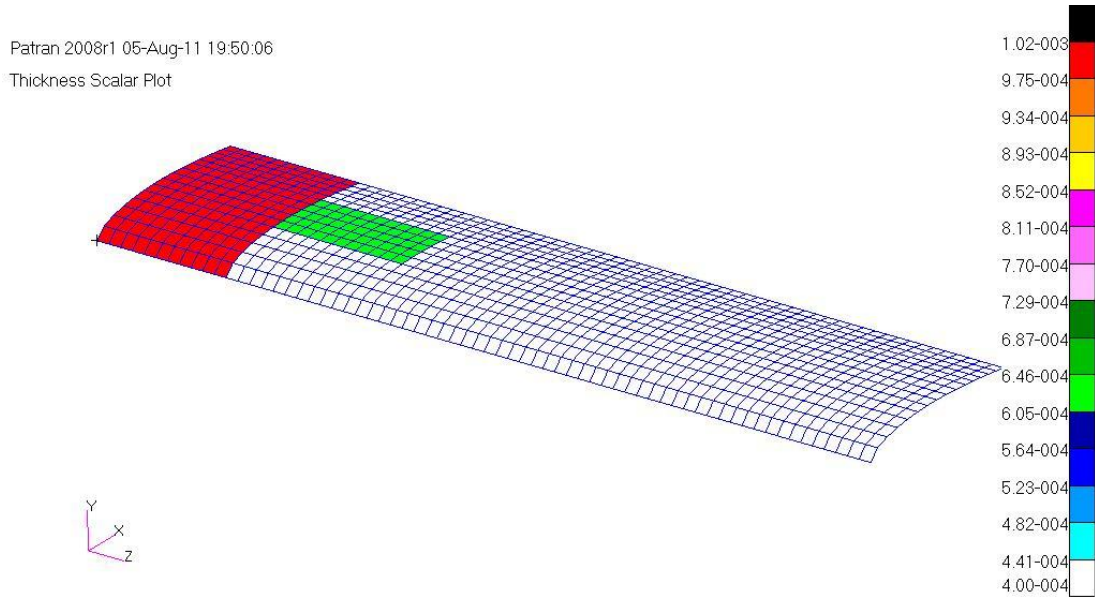


Figure 4.61: Thickness Scalar Plots of the Upper Skin Panels in the Optimized Wing
– Rod/Shell Fine Mesh Model under Stress and Buckling Constraints

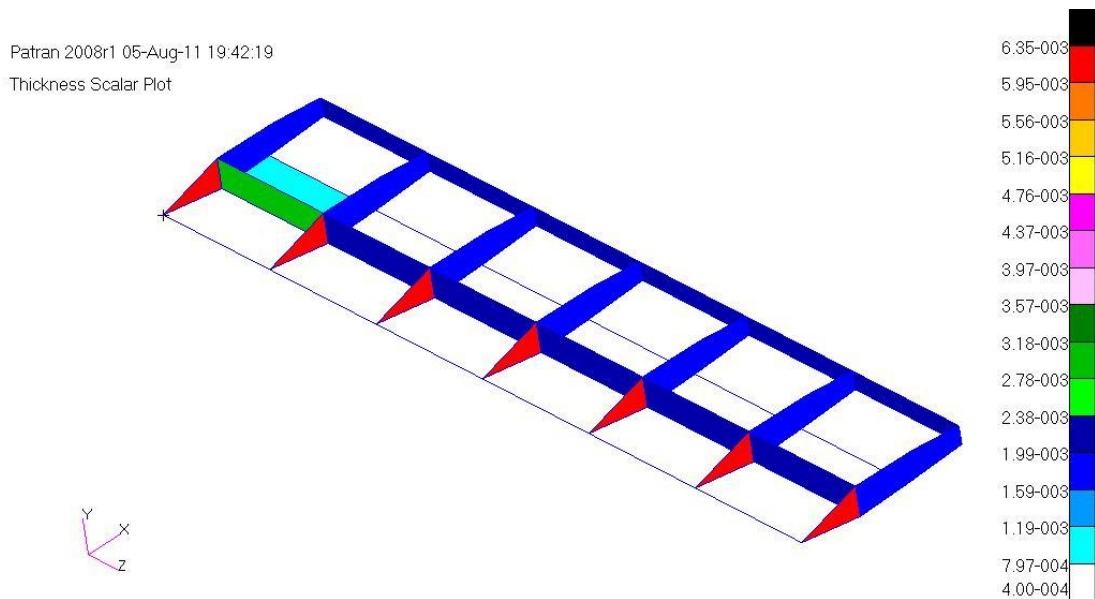


Figure 4.62: Thickness Scalar Plots of Interior Panels in the Optimized Wing
Rod/Shell for Coarse Mesh Model under Stress and Buckling Constraints

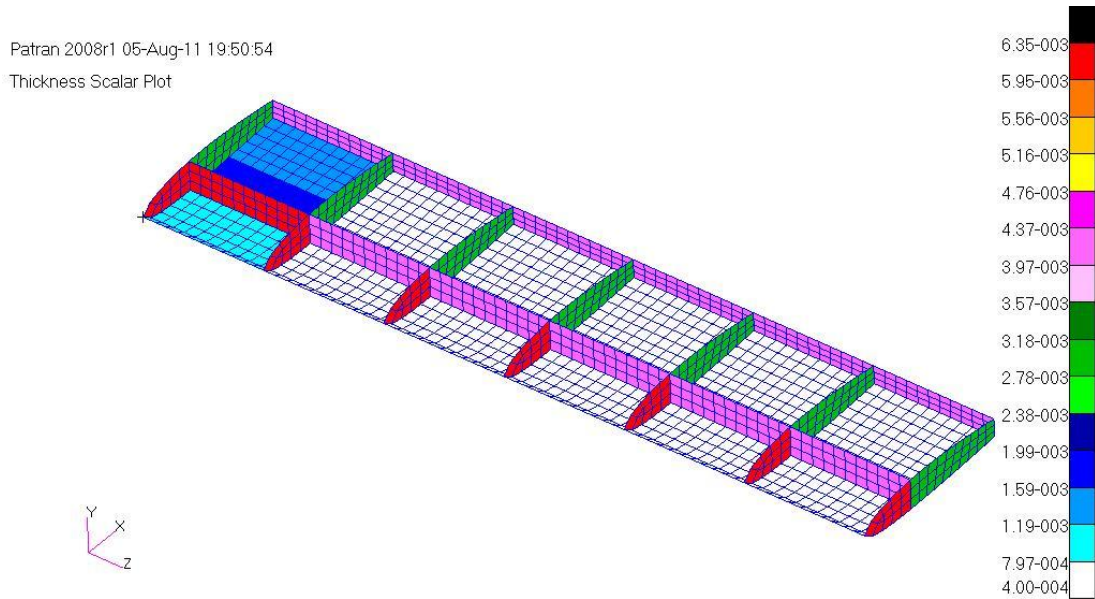


Figure 4.63: Thickness Scalar Plots of Interior Panels in the Optimized Wing Rod/Shell for Fine Mesh Model under Stress and Buckling Constraints

Figure 4.64 and 4.65 give the variation of the front spar upper flange area and upper middle skin thicknesses with the span-wise bay locations for both coarse and fine mesh models.

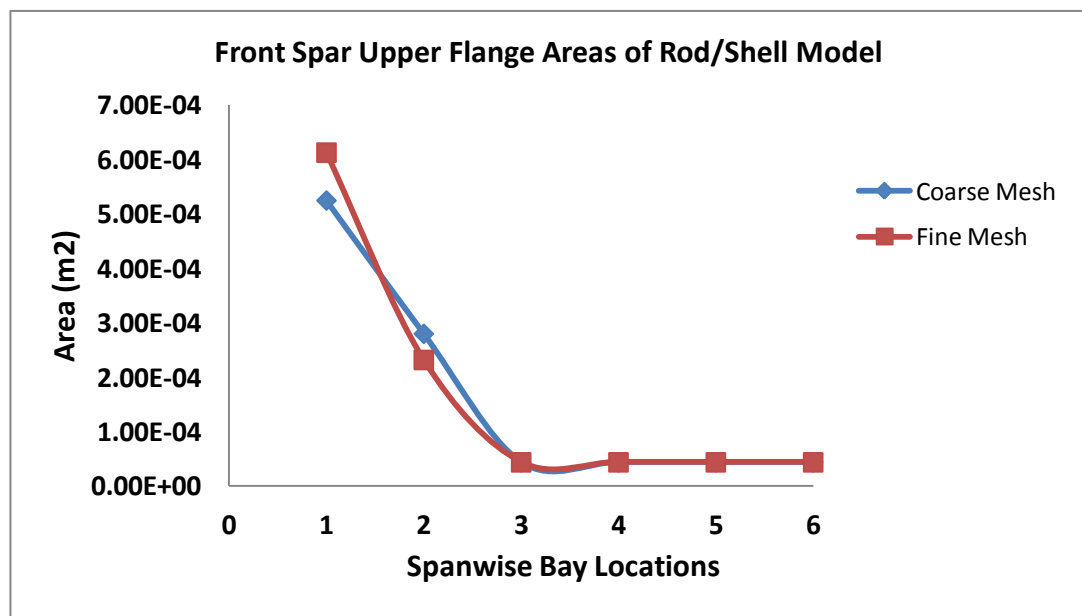


Figure 4.64: Variation of the Upper Flange Areas of the Front Spar of the Wing - Rod/Shell Model under Stress and Buckling Constraints

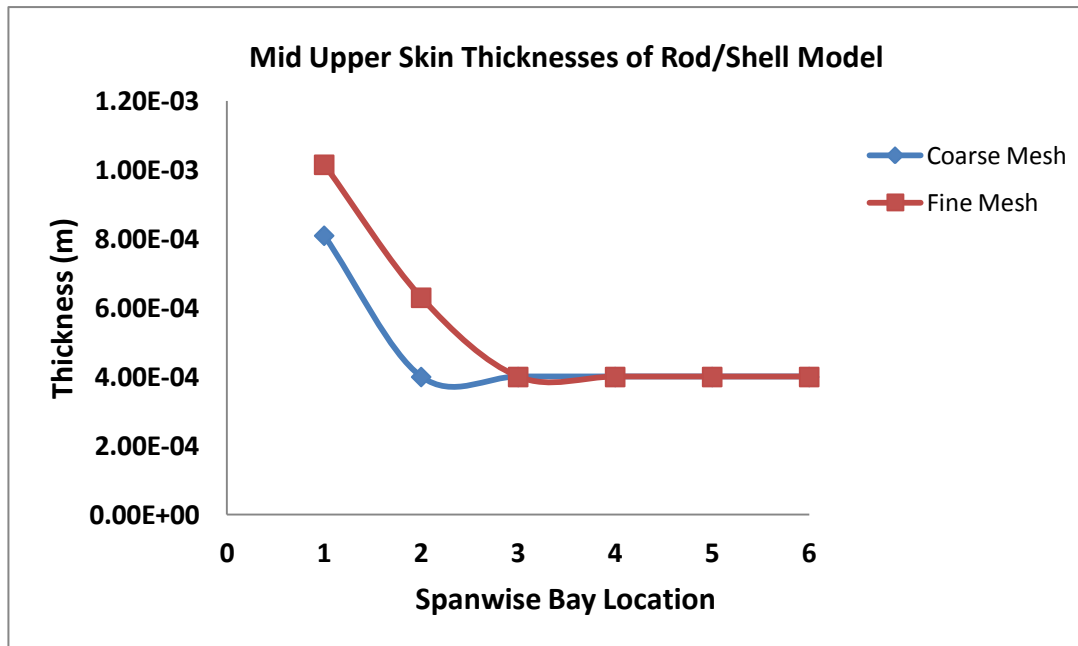


Figure 4.65: Variation of the Upper Middle Skin Thickness of the Wing – Rod/Shell Model under Stress and Buckling Constraints

It is noted that in general thicknesses and spar flange areas in the optimized configurations are close to each other in the outboard bays for the coarse and the fine mesh models. However, in the inboard bays the differences between thicknesses and the spar flange areas determined by the use of the coarse and fine mesh models in the optimization process are higher. This observation makes sense because in the inboard bays loads are higher, and the difference between the maximum stresses predicted by the coarse and the fine mesh finite element models are higher in the inboard bays compared to the outboard bays.

4.9.3 Wing Torque Box Optimization Study with Shear Panel and Membrane Elements

The wing torque box is optimized using rod/shear and rod/membrane element combinations under the loading condition of lift force only. Figure 4.66 shows the loading acting on the wing structure. Again single element is used to create the coarse mesh model for optimization purposes. The wing torque box models are optimized considering all constraints which include the Von Mises and axial stress

constraints, tip displacement, local buckling and side constraints. In the case of shear panels a shear stress value of 188 MPa for upper limit and -188 MPa for lower limit is defined as the constraint.

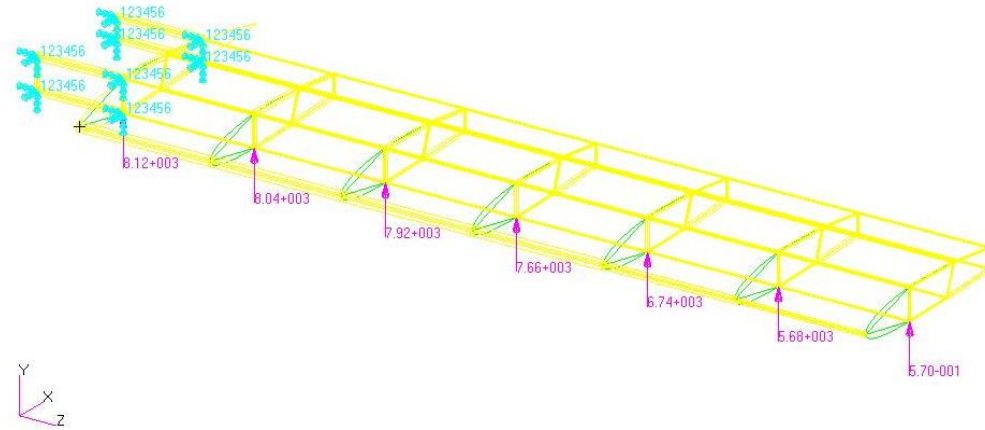


Figure 4.66: Lift Force Load Distribution and Boundary Conditions Acting on the Wing - Rod/Shear Panel Model

4.9.3.1 Wing Torque Box Optimization Study using Rod/Shear Panel Elements

Rod/shear panel model of the wing structure is optimized while considering the constraints defined previously in section 4.9.3. Hard convergence is achieved to a best compromise infeasible design but no feasible discrete design could be obtained. Table 4.36 shows the optimized mass of the wing structure modeled with rod/shear panel element combination.

Table 4.36: Optimized Mass (kg) of the Wing Structure – Rod/Shear Panel Model

Model	Initial	Continuous	Discrete
Rod/Shear Panel	85.87	139.22	148.46

From Table 4.36, it is obvious that the initial mass of the rod/shear panel model is larger than the initial mass of previous optimized models which is about 65.38 kg for the coarse mesh model. The reason for the higher initial mass of the rod/shear panel model is due to the definition of additional rod elements surrounding the shear panel

elements. As described in chapter 3 section 3.7.3, every shear panel must be surrounded on all four sides by normal stress carrying elements such as rod elements to carry the end loads in the equivalent areas. Therefore, these rod elements account for the higher initial mass of the wing rod/shear panel model.

The reason for infeasible design is due to the violation of some constraints. The maximum constraint value, which is the percent violation of the constraint, is greater than the default value which is 0.5 %. In order to check which constraint is causing such problem, the model is optimized again by relaxing some constraints and checking the results again. It is found that, displacement constraint which is defined with an upper limit of 20 cm causes problem. Therefore, a new upper limit for the displacement constraint is defined with a maximum value of 30 cm, and the model is optimized again. Table 4.37 shows the optimized mass of the wing rod/shear panel model under the new tip displacement constraint. In this case, hard convergence is achieved as well as hard and soft feasible discrete design.

Table 4.37: Optimized Mass (kg) of Wing Structure – Rod/Shear Panel Model with the 30 cm Tip Displacement Constraint

Model	Initial	Continuous	Discrete
Rod/Shear Panel	85.87	108.83	118.51

Figure 4.67 and 4.68 show the histories of the objective function of coarse mesh rod/shear panel model with respect to the design cycle under the 20 cm and the modified 30 cm tip displacement constraints. Again, the objective function is defined as minimizing the total mass of the wing torque box.

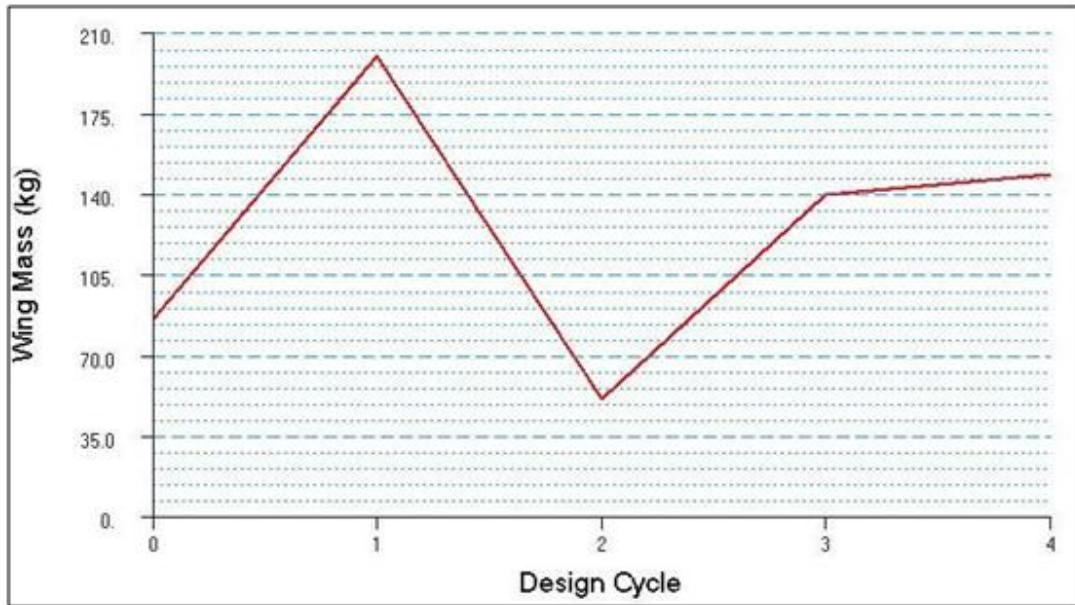


Figure 4.67: Variation of the Mass of Wing With the Design Cycle for the 20 cm Tip Displacement Constraint – Rod/Shear Panel Coarse Mesh Model

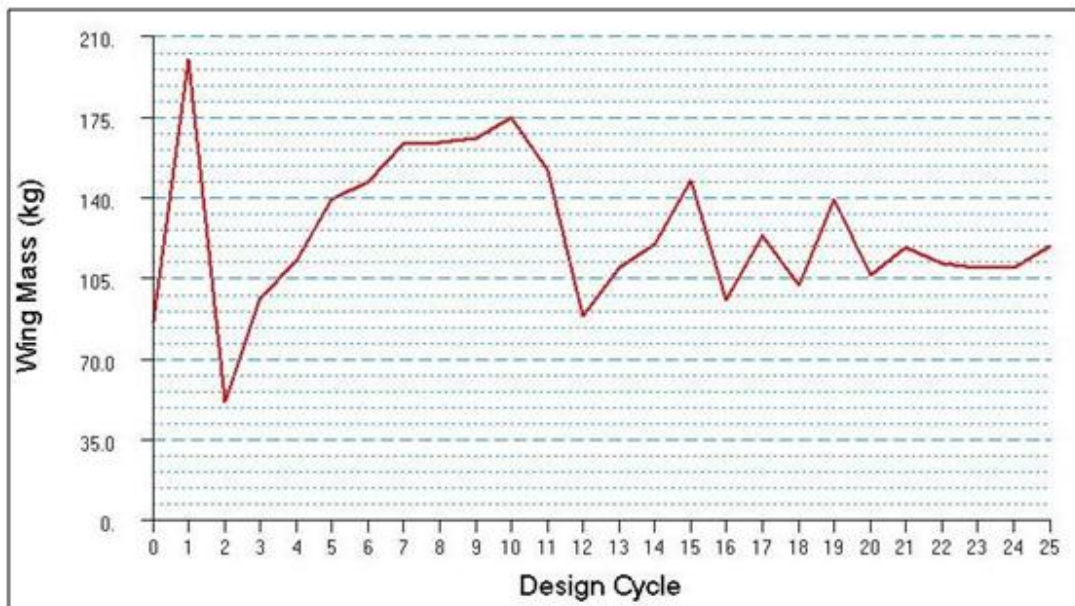


Figure 4.68: Variation of the Mass of Wing With the Design Cycle for the 30 cm Modified Displacement Constraint – Rod/Shear Panel Coarse Mesh Model

Figure 4.67 shows that in case of 20 cm tip displacement constraint no hard convergence is achieved as well as and in that case no hard and soft feasible discrete designs will be obtained. On the other hand, Figure 4.68 shows that after the

displacement constraint is modified to the new value of 30 cm, a converged solution is achieved with an optimized wing mass of 119.90 kg. At this point it should be noted that the fact that the tip displacement constraint is modified to 30 cm does not mean that in the optimized wing configuration the tip displacement is 30 cm. However, by increasing the tip displacement constraint from 20 cm to 30 cm, the optimizer got around where it was stuck and both hard and soft convergences could be obtained.

Figures 4.69 - 4.72 show the thickness scalar plots of the upper skin panels and interior panels in the optimized wing torque box, for the coarse and the fine mesh models. Figure 4.69 and 4.70 show the thickness plots for the 20 cm tip displacement case, and Figures 4.71 and 4.72 show the thickness plots for the 30 cm tip displacement plot.

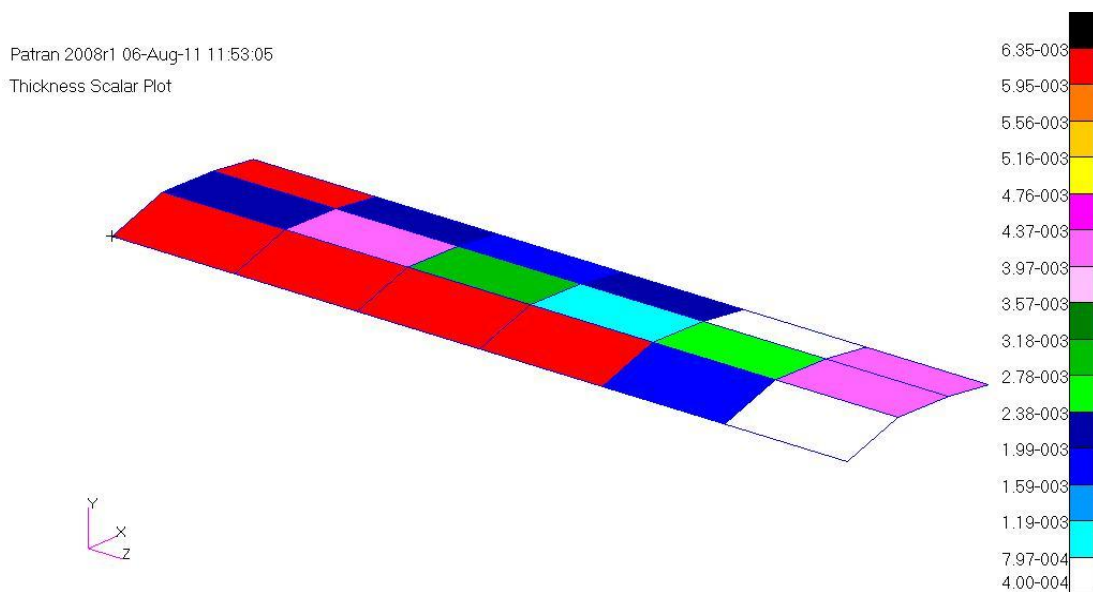


Figure 4.69: Thickness Scalar Plots of the Upper Skin Panels in the Optimized Wing – Rod/Shear Panel Coarse Mesh Model- 20 cm Tip Deflection Constraint

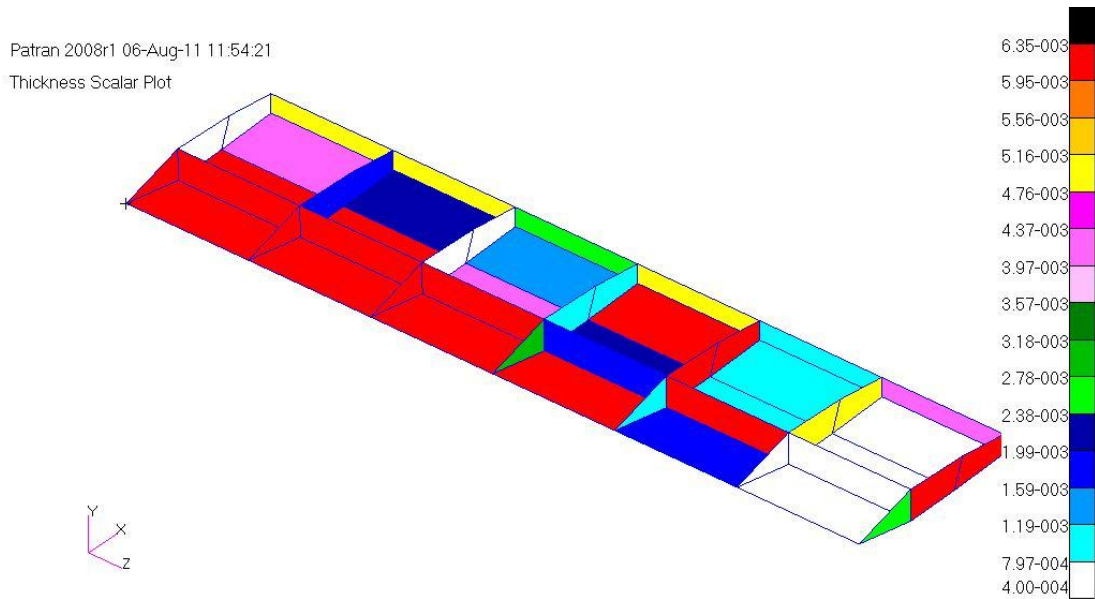


Figure 4.70: Thickness Scalar Plots of the Interior Panels in the Optimized Wing - Rod/Shear Panel Coarse Mesh Model-20 cm Tip Deflection Constraint

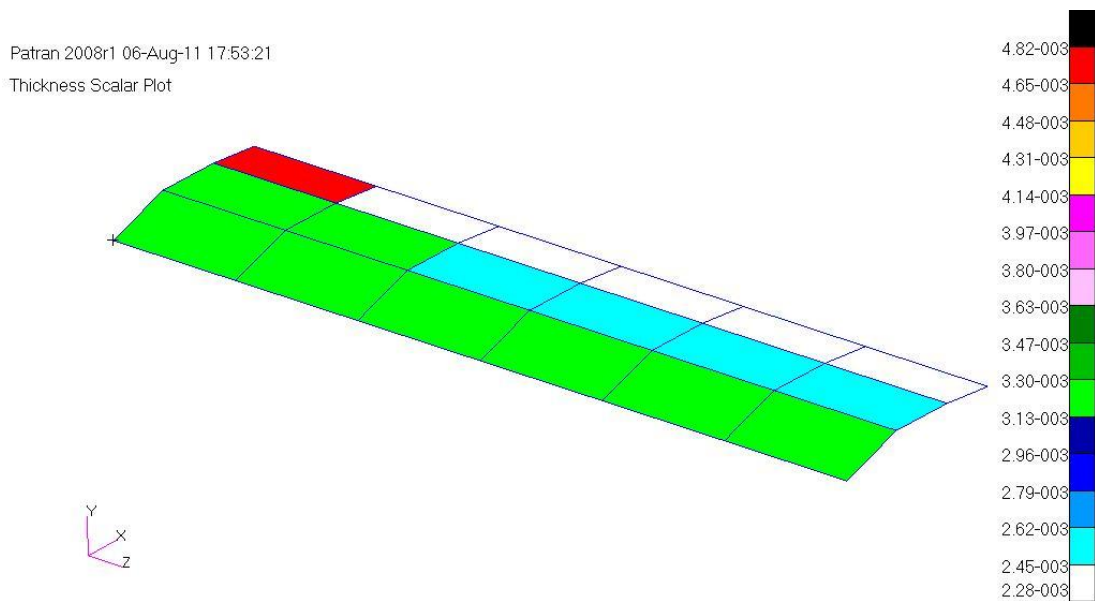


Figure 4.71: Thickness Scalar Plots of the Upper Skin Panels in the Optimized Wing – Rod/Shear Panel Coarse Mesh Model with the Modified 30 cm Displacement Constraint

Patran 2008r1 06-Aug-11 17:54:14
Thickness Scalar Plot

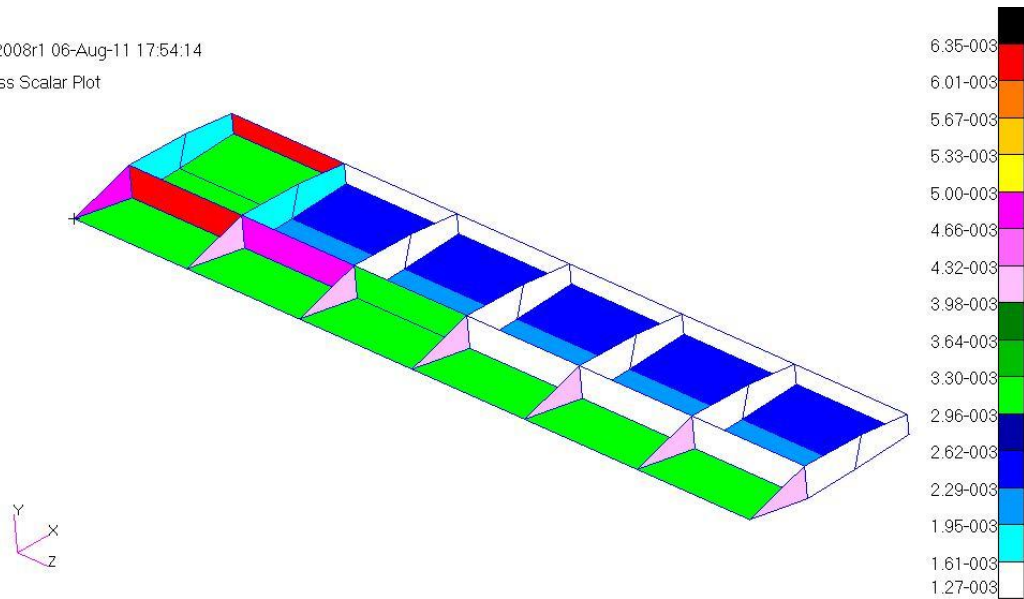


Figure 4.72: Thickness Scalar Plots of Interior Panels in the Optimized Wing Rod/Shear Panel Coarse Mesh Model with Modified 30 cm Displacement Constraint

Figures 4.69 and 4.70 show that since convergence could not be achieved, the side constraints forcing the thickness of the skin panels to decrease gradually from wing root to wing tip, are also not satisfied. On the other hand, Figures 4.71 and 4.72 show that thicknesses decrease from wing root to the wing tip.

Table 4.38 and 4.39 summarize the spar cap areas of the front spar in the optimized wing torque box for the coarse mesh model.

Table 4.38: Cross Sectional Areas of the Front Spar of the Wing for the 20 cm Tip
Displacement Constraint- Rod/Shear Panel Model

Front Spar Cross Sectional Area – Rod /Shear Panel Model			
	Spar Cap (Root to Tip)	Coarse Mesh Model	
		Continuous Area (m²)	Discrete Area (m²)
Upper Flange	Bay 1	3.98E-04	4.15E-04
	Bay 2	1.04E-04	1.08E-04
	Bay 3	1.65E-04	1.84E-04
	Bay 4	4.25E-05	4.40E-05
	Bay 5	5.54E-05	5.80E-05
	Bay 6	3.80E-05	4.40E-05
Lower Flange	Bay 1	2.61E-04	2.80E-04
	Bay 2	1.46E-04	1.48E-04
	Bay 3	3.02E-04	3.12E-04
	Bay 4	3.81E-05	4.40E-05
	Bay 5	3.80E-05	4.40E-05
	Bay 6	3.80E-05	4.40E-05

Table 4.39: Cross Sectional Areas of the Front Spar of the Wing for the 30 cm Tip
Displacement Constraint- Rod/Shear Panel Model

Front Spar Cross Sectional Area – Rod /Shear Panel Model			
	Spar Cap (Root to Tip)	Coarse Mesh Model	
		Continuous Area (m²)	Discrete Area (m²)
Upper Flange	Bay 1	6.43E-05	6.70E-05
	Bay 2	5.83E-05	6.30E-05
	Bay 3	5.30E-05	5.80E-05
	Bay 4	4.79E-05	4.80E-05
	Bay 5	4.29E-05	4.40E-05
	Bay 6	3.80E-05	4.40E-05
Lower Flange	Bay 1	6.44E-05	6.70E-05
	Bay 2	5.91E-05	6.30E-05
	Bay 3	5.30E-05	5.80E-05
	Bay 4	4.79E-05	4.80E-05
	Bay 5	4.29E-05	4.40E-05
	Bay 6	3.80E-05	4.40E-05

Table 4.38 shows that for the 20 cm tip displacement constraint case, spar flange areas do not show a gradual decrease from wing tip to the wing root. On the other hand, Table 4.39 shows that spar caps areas decrease from the wing root to the wing tip, as expected.

It should be noted that Table 4.39 reflects the results of a converged solution in which the tip displacement constraint is modified to a new value in order to overcome maximum violation constraint. Figure 4.73 illustrates the variations of front upper spar caps areas of wing rod/shear panel model.

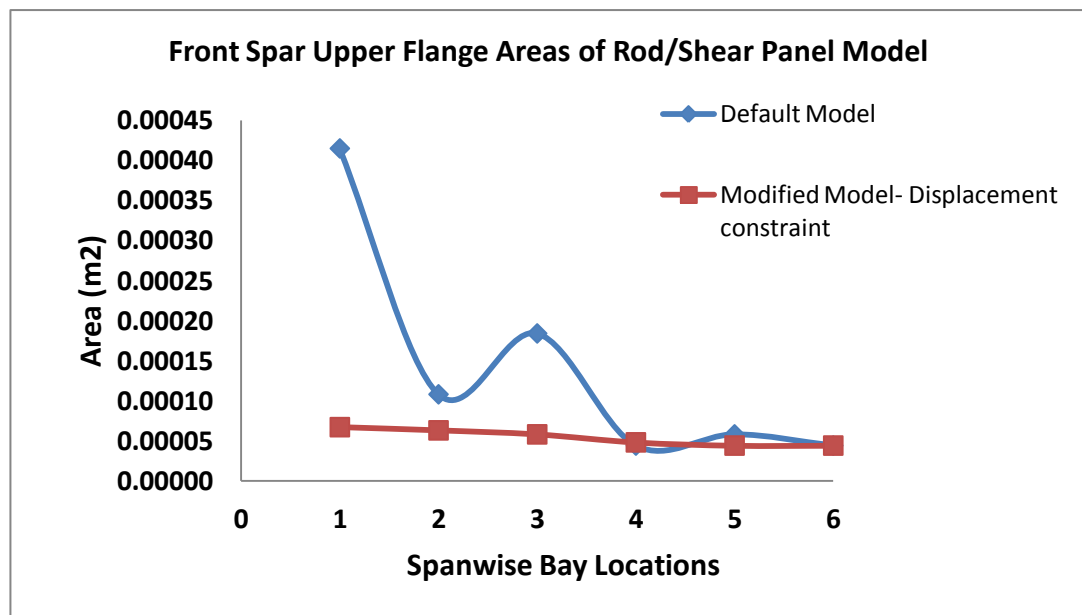


Figure 4.73: Variation of Front Upper Spar Caps Area of Wing Rod/Shear Panel Model

4.9.3.2 Wing Torque Box Optimization Study using Rod/Membrane Elements

Wing structure which is modeled with rod/membrane element combinations is optimized subject to Von Mises stress, axial stress, buckling and side constraint and the 30 cm tip displacement constraint. Thus, comparison of the rod/membrane model with the rod/shear panel model can be made. For the rod/membrane model both soft and hard convergences are achieved Table 4.40 gives the optimized mass of wing torque box.

Table 4.40: Optimized Mass (kg) of Wing Structure – Rod/Membrane Model with the 30 cm Tip Displacement Constraints

Model	Initial	Continuous	Discrete
Rod-Membrane	65.38	32.22	36.91

Figure 4.74 shows the history of the objective function with respect to the design cycle for the coarse mesh rod/membrane model.

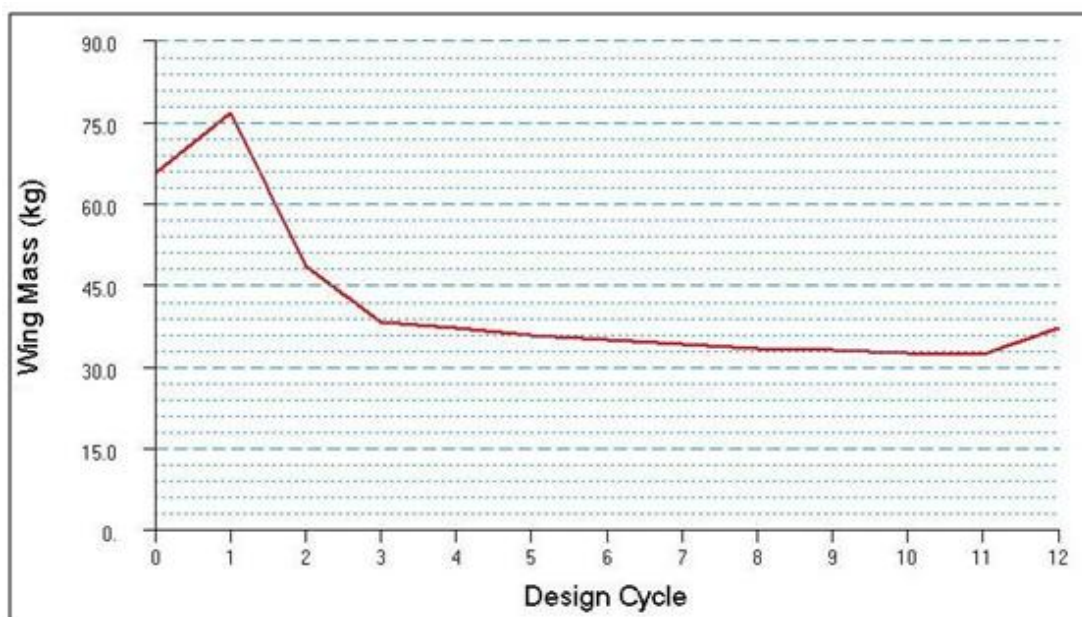


Figure 4.74: Variation of the Mass of Wing With the Design Cycle - Rod/Membrane Coarse Mesh Model

Figures 4.75 - 4.76 show the thickness scalar plots of the upper skin panels and interior panels in the optimized wing torque box, for the coarse mesh rod/membrane model. Figure 4.75 and 4.76 show that discrete thickness reduction from wing root to wing tip is achieved, as expected.

Patran 2008r1 06-Aug-11 18:18:06
Thickness Scalar Plot

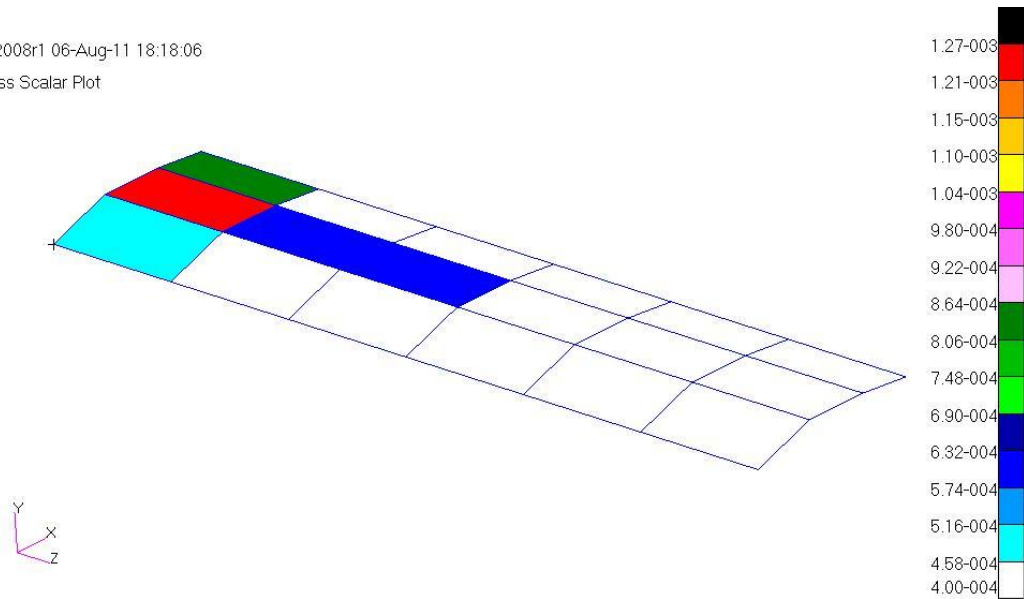


Figure 4.75: Thickness Scalar Plot of the Upper Skin Panels in the Optimized Wing Structure – Rod/Membrane Coarse Mesh Model

Patran 2008r1 06-Aug-11 18:18:30
Thickness Scalar Plot

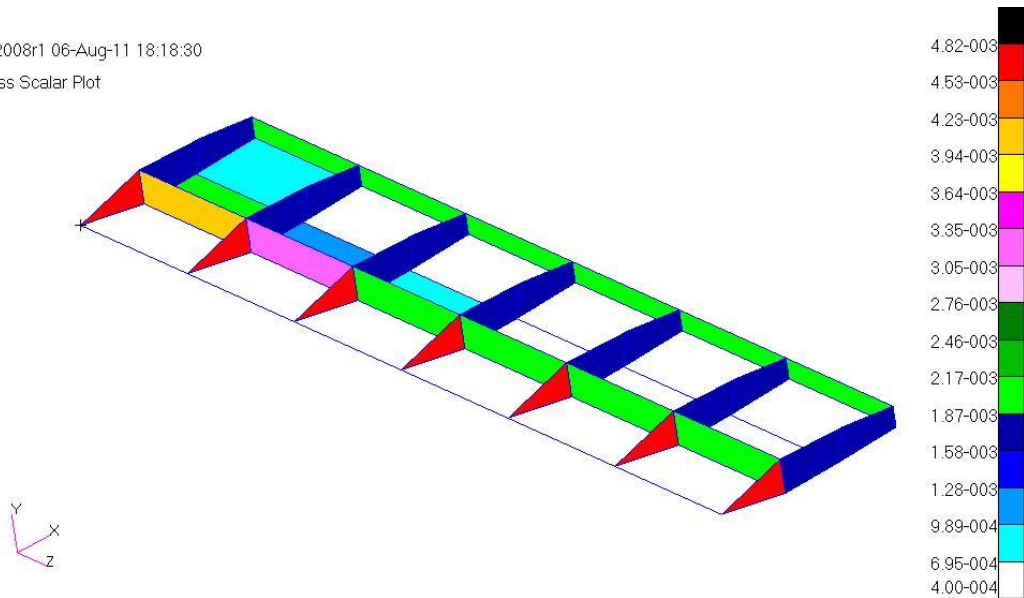


Figure 4.76: Thickness Scalar Plot of Interior Panels in the Optimized Wing Structure - Rod/Membrane Coarse Mesh Model

Table 4.41: Cross Sectional Areas of the Front Spar of the Wing- Rod/Membrane Model

Front Spar Cross Sectional Area – Rod /Membrane Model			
	Spar Cap (Root to Tip)	Coarse Mesh Model	
		Continuous Area (m ²)	Discrete Area (m ²)
Upper Flange	Bay 1	6.13E-04	6.13E-04
	Bay 2	3.84E-04	3.90E-04
	Bay 3	1.15E-04	1.16E-04
	Bay 4	3.80E-05	4.40E-05
	Bay 5	3.80E-05	4.40E-05
	Bay 6	3.80E-05	4.40E-05
Lower Flange	Bay 1	6.13E-04	6.13E-04
	Bay 2	1.74E-04	1.84E-04
	Bay 3	7.85E-05	8.80E-05
	Bay 4	3.80E-05	4.40E-05
	Bay 5	3.80E-05	4.40E-05
	Bay 6	3.80E-05	4.40E-05

Table 4.41 shows that spar caps area decreases from the root to the tip of the wing, as expected. Figure 4.77 shows the variation of the upper flange area of the front spar of the wing structure which is modeled with the rod/membrane element combinations.

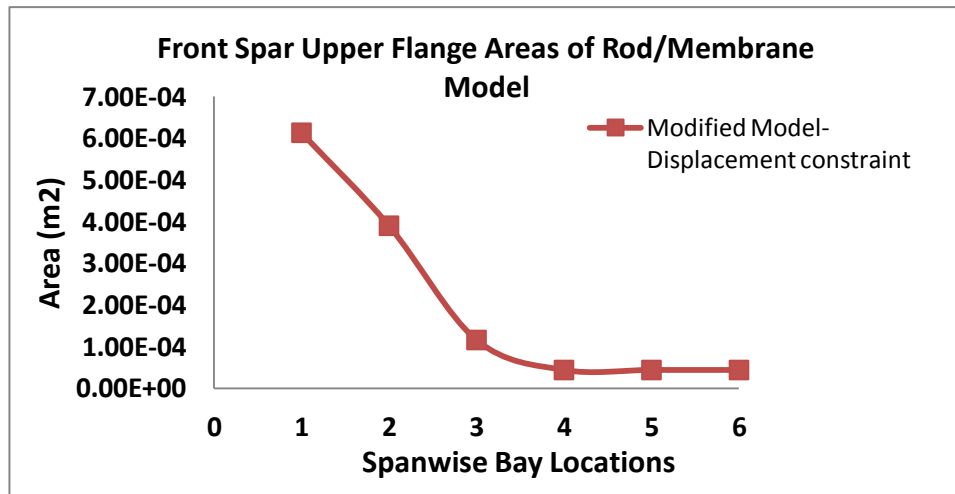


Figure 4.77: Variation of the Upper Flange Area of the Front Spar of the Wing - Rod/Membrane Model

4.9.3.3 Results and Discussions on the Use of Shear and Membrane Elements in the Optimization

Table 4.42 summaries the optimized masses calculated by using rod/shear panel and rod/membrane models under the line lift load only.

Table 4.42: Summary of Optimized Masses of the Wing Torque Box for the Rod/Shear and the Rod/Membrane Models

Model	Initial	Continuous	Discrete
Rod-Shear Panel	85.87	108.83	118.51
Rod-Membrane	65.38	32.22	36.91

Figures 4.78 and 4.79 give comparisons of the upper-flange area of the front spar and the upper middle skin thicknesses for the rod/shear and rod /membrane finite element models, respectively.

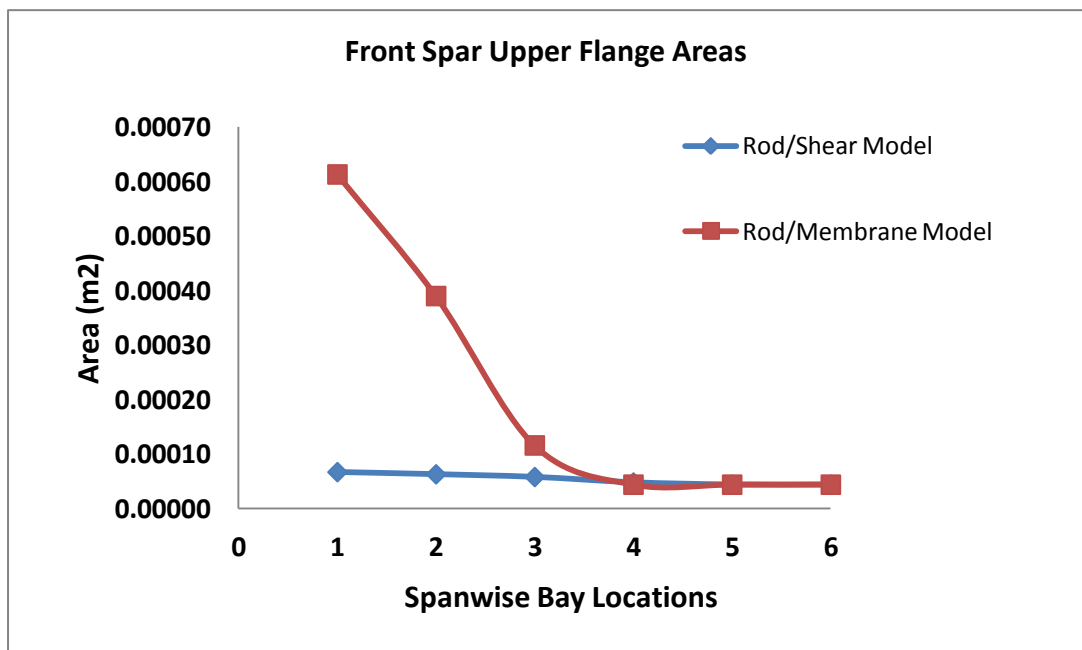


Figure 4.78: Comparison of the Upper Flange Area of the Front Spar of the Wing - Rod/Shear Panel and Rod/Membrane Model

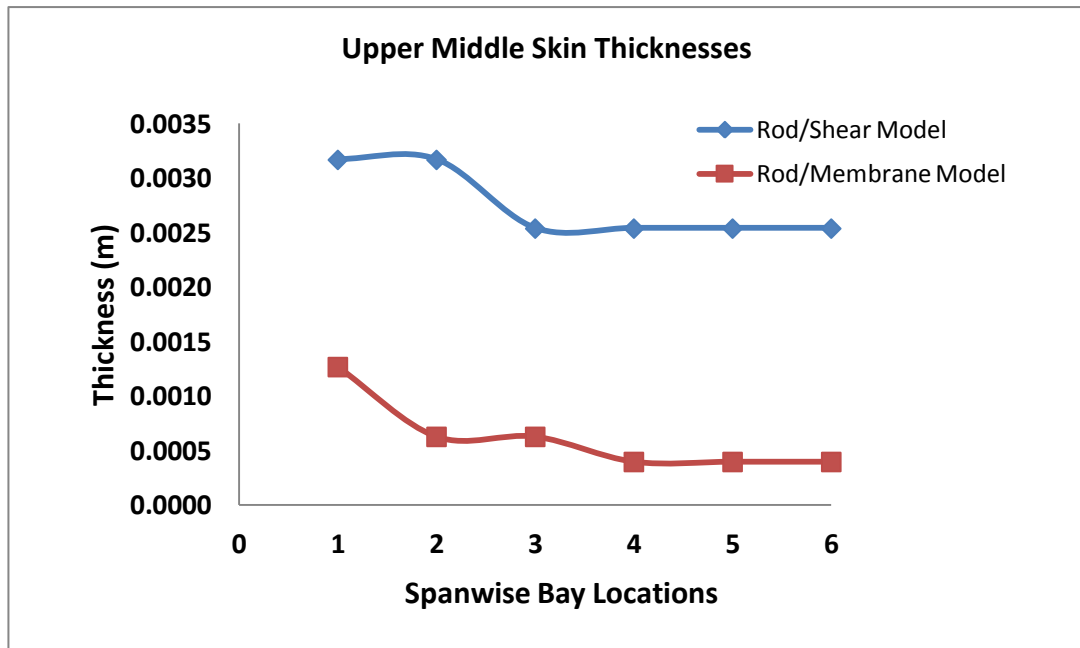


Figure 4.79: Comparison of Upper Middle Skin Thicknesses of the Wing Rod/Shear Panel and the Rod/Membrane Model

From Table 4.42 it is obvious that rod/shear panel model results in a heavier wing mass configuration when compared to the rod/membrane model. The initial mass of the rod/shear panel model is larger and it is due to the fact that, in order to model shear panels as described in chapter 3, section 3.7.3 every shear panel must be surrounded on all four sides by normal stress carrying elements, such as rod elements to carry end loads in the equivalent areas. So in this case, these side rod elements cause an extra mass on the initial mass of the wing rod/shear panel model. From Table 4.42, it is seen that this extra mass is approximately 20 kg. As an example, the final discrete optimized mass of the wing rod/shear panel under distributed lift force only is around 118.5 kg with an extra mass of 20 kg included inside it and if the extra mass is subtracted from the final mass, the optimized mass will be around 98.5 kg which is still very high compared to the optimized mass of the rod/membrane model which has discrete optimized mass of 36.91 kg.

By examining the thickness scalar plots of rod/shear model in Figures 4.71 – 4.72 and rod/membrane model in Figures 4.75 – 4.76, it becomes clear why the rod/shear panel model has higher optimized mass. It is seen that rod/shear panel model has higher skin thicknesses compared to the rod/membrane model. Although the spar flange areas of the rod/shear panel model are less than the spar flange areas of the

rod/membrane model, higher skin thickness accounts for the higher mass of the optimized wing structure which is modeled with the rod/shear panel element combination. It should be noted that in the rod/shear panel model, shear buckling is considered in the buckling constraint equations. However, for the rod/membrane model combined shear and compression buckling equation is used. In the combined shear and compression buckling, shear stress ratio is raised to power two, whereas in the shear buckling, shear stress ratio is used as is. Therefore, the main difference for the higher thickness of the upper skin panel of the rod/shear panel model could be due to the buckling constraint. However, this preliminary conclusion has to be checked by conducting further optimization studies by relaxing constraints one by one and checking the resulting optimized wing configurations. In this thesis, for the rod/shear panel and rod/membrane models, which are under line lift load only, this is not done and left as a future work.

4.10 Comparison of Minimum Wing Torque Box Mass Determined by the Analytical and Finite Element Optimization Solution

The minimum wing torque box mass that is found using two different idealization approaches as described in chapter two is compared to the final optimized mass of the wing torque box found using different models created by different finite element types. Table 4.43 gives the mass of the wing torque box found using analytical solution by the first and second idealization approaches. The first idealization assumes that spar caps and stiffeners carry only axial stress, and panels and webs carry shear stress only. The second idealization assumes that spar caps and stiffeners carry only axial loads but thin walled panels and webs carry axial stress and shear stress.

Table 4.43: Mass (kg) of the Wing Torque Box Obtained By Using the First and Second Idealization in the Analytical Solution – Point A

Idealization	Continuous (kg)	Discrete (kg)
1 st Idealization	62.90	67.69
2 nd Idealization	52.18	57.61

Tables 4.44 and 4.45 review the optimized masses for all finite element models used in the optimization study for both coarse and fine mesh sizes.

Table 4.44: Review of Mass (kg) Optimization Results of the Wing Torque Box Models – Coarse Mesh

Models	Continuous (kg)	Discrete (kg)
Rod-Shell	41.09	46.77
Beam-Shell	38.28	42.97
Rod-Shell R	38.88	43.57
Beam-Shell R	38.29	42.11
Rod-Membrane R	39.01	44.07
Beam-Membrane R	37.77	42.84

Table 4.45: Review of Mass (kg) Optimization Results of the Wing Torque Box Models – Fine Mesh

Models	Continuous (kg)	Discrete (kg)
Rod-Shell	51.50	58.61
Beam-Shell	50.25	58.02
Rod-Shell R	50.12	58.23
Beam-Shell R	52.13	59.70

Tables 4.44 and 4.45 give the masses of the final configuration wing structures which are also optimized iteratively based on the simplified method of analysis using the structural idealizations 1 and 2. Based on the results of optimized mass configurations given in Tables 4.44 and 4.45, the following conclusions can be drawn:

The initial mass of the fine mesh finite element models is slightly higher than the initial mass of the coarse mesh finite element models, because cambered surfaces of the wing is approximated better with the fine mesh.

Optimized masses obtained with the fine mesh finite element models are higher than the optimized masses obtained with the coarse mesh finite element models. It should be noted that although the stresses at the centers of the domains of bays are lower for

the fine mesh models, the maximum stresses in the domains of each bay are higher in the fine mesh finite element models. In the optimization solution, maximum stresses in the domains are used in the stress constraint equations.

Therefore, when fine mesh finite element models are used in the optimization process, optimized masses turn out to be higher than the optimized masses obtained by the use of coarse mesh finite element models in the optimization process. Since the round-up method is used in the discrete optimization, optimized masses determined by the discrete variable optimization are higher than the optimized masses determined by the continuous optimization. It should be noted that in the round-up method, Nastran selects the first round-up dimensions among a list of standard thickness and flange areas.

Results of the optimization study shows that optimized wing masses, determined by the use of the different finite element models in the optimization process, are very close to each other with only slight favorable overall mass on behalf of models which have spar flanges and stringers meshed with beam elements.

The mass of the wing configuration designed by the simplified method using the second structural idealization is very close to the optimized masses determined by the use of fine mesh finite element models in the optimization process. However, as it is discussed in the analysis section, simplified method of analysis using the second structural idealization is more comparable to the structural analysis performed by the coarse mesh finite element models. From Table 4.43 it is seen that mass of the wing configuration designed by the simplified method using the second structural idealization has approximately 10 kg mass penalty compared to the optimized masses determined by the coarse mesh finite element models.

Based on the results presented, it can be concluded that with the simplified methods, preliminary sizing of the wing configurations can be performed with enough confidence as long as the simplified method based designs are also optimized iteratively, which is what is practiced in the design phase of this study.

CHAPTER 5

CONCLUSION AND RECOMMENDATIONS

5.1 Conclusions

In this thesis, a comprehensive study on the effect of using different structural idealizations on the design, analysis and optimization of thin walled semi-monocoque wing structures in the preliminary design phase is performed.

The wing structures are designed using two different structural idealizations that are typically used in the preliminary design phase, and the finite element analysis of one of the designed wing configurations is performed using six different one and two dimensional element pairs which are typically used to model the sub-elements of semi-monocoque wing structures. The effect of using different finite element types on the analysis results of the wing structure, which is designed by the simplified method using two different idealization approaches, is investigated. Comparisons are also made between the analysis results of the finite element solution and the simplified method, and the applicability of the simplified method in the preliminary design phase is investigated for the wing configuration studied in the thesis. During the analysis study, depending on the mesh size used, conclusions are also inferred with regard to the deficiency of certain element types in handling the true external load acting on the wing structure.

Designs performed using the first and the second structural idealizations showed that the use of second structural idealization results in approximately 10 kg lighter mass in the final configuration compared to the use of first idealization during the design analysis. It is concluded that the mass of the spar flanges and the stringers account for the higher mass of the final configuration wing structure, which is designed using the first structural idealization.

Finite element analysis of the wing structure with different element types showed that the distributed line lift and pitching moment loading, which is used as the external load in the current study, necessitates the use of revised membrane elements in the wing ribs, because with the standard membrane elements in the wing ribs, the distributed pitching moment cannot be handled accurately. It is also concluded that in order to handle the distributed pitching moment accurately, single elements must be used between the rib stations in the finite element models with revised membrane elements. Moreover, the finite element analysis of the wing structure with different element types showed that away from any structural discontinuity, stresses predicted by the fine mesh finite element models are less than the stresses predicted by the coarse mesh finite element models at the identical locations on the wing structure. However, since fine mesh finite element models capture the stress gradients better, the maximum stresses predicted by the fine mesh models are usually higher than the maximum stresses predicted by the coarse mesh models.

In general, stresses predicted by the finite element models with beam elements are slightly lower than the stresses predicted by the finite element models with rod elements. Flexibility introduced by the beam elements is considered to be the main reason for the slightly lower stresses predicted by the finite element models which have flanges and stringers modeled with beam elements compared to the finite element models which have flanges and stringers modeled with rod elements.

Maximum Von Mises stresses determined by the finite element models with the standard shell elements are slightly higher than the maximum Von Mises stresses determined by the finite element models with the shell elements with drilling degrees of freedom. The reduction of the maximum Von Mises stress in finite element models with shell elements having drilling degrees of freedom is attributed to the additional flexibility introduced through the inclusion of drilling degrees of freedom. However, the use shell elements with drilling degrees of freedom does not have a major effect on the stresses obtained by the coarse and the fine mesh finite element models away from any structural discontinuity.

Finite element analysis by the fine mesh finite element models showed that stresses predicted by the simplified method, using the second structural idealization, are consistently higher than the stresses predicted by the fine mesh finite element models. On the other hand, stresses determined by the coarse mesh finite element models and the simplified method agree with each other closely in most of the bays which are away from the restraint end and the free edge boundary at the wing tip. Since the coarse mesh finite element models behave more stiff compared to fine mesh finite element models, it is concluded that simplified method based on unsymmetric beam theory can be best simulated by the coarse mesh finite element models. It is also observed that axial stresses determined by the coarse mesh finite element models and the simplified method of analysis agree better than the Von Mises stresses.

Structural optimization results showed that optimized wing masses, determined by the use of different finite element models in the optimization process, are very close to each other with only slight favorable overall mass on behalf of models using beam elements in the axial members. It is also observed that in the continuous optimization solution, in general, the use of shell elements with drilling degrees of freedom results in slightly lower optimum masses compared to the use of shell elements without drilling degrees of freedom. However, differences are negligible from an engineering point of view.

Optimized masses obtained with the fine mesh finite element models are higher than the optimized masses obtained with the coarse mesh finite element models. It should be noted that although the stresses at the centers of the domains of bays are lower for the fine mesh models, the maximum stresses in the domains of each bay are higher in the fine mesh finite element models. In the optimization solution, maximum stresses in the domains are used in the stress constraint equations. Therefore, when fine mesh finite element models are used in the optimization process, optimized masses turn out to be higher than the optimized masses obtained by the use of coarse mesh finite element models in the optimization process.

The mass of the wing configuration designed by the simplified method using the second structural idealization is very close to the optimized masses determined by the finite element based optimization process performed by MSC Nastran. Based on the preliminary results presented in the current study, it can be concluded that with the simplified methods, preliminary sizing of the wing configurations can be performed with enough confidence as long as the simplified method based designs are also optimized.

5.2 Recommendations for Future Works

For the future work the finite element analysis and optimization parts can be extended such that the true distributed aerodynamic loading obtained from the CFD analysis of the wing can be used as the external load. Multi-disciplinary optimization problems can be defined in MSC.NASTRAN[®] and the wing torque box analyzed can be optimized in all aspects. For instance, more design constraints can be added to the optimization problem such as constraints on fundamental frequency or aeroelastic constraints such as flutter speed.

Further work can be performed to demonstrate the application of shape optimization which can be done separately or it can be combined with element property optimization.

In the shape optimization, spars/stiffeners and ribs locations can be assigned as design variables and by allowing the optimizer to make slight changes on the position of these sub-elements in order to get better optimum solutions.

REFERENCES

- [1] Stephen A. Bunis, P.E., Wing Structural Design Project, Naval Postgraduate School, March 1994.
- [2] Ampofo, J. and Ferguson, F. Optimal Design of an Aircraft Wing Structures: A Computer Aided Design Method, Vol. 14, pp. 471-480. Automation Congress, 2002, Proceedings of the 5th Biannual World.
- [3] Vaughan, R.E., Daniel M.F., The Correct use of Finite Element Models for Stress Analysis of Aircraft Annual Forum Proceedings, Vol. 60, Part 1, pp. 140-192, American Helicopter Society, 2004.
- [4] Singiresu S. Rao, Engineering Optimization: Theory and Practice, Fourth Edition, 2009 by John Wiley & Sons, Inc.
- [5] Wasiutynski, Z., and Brandt, A., The Present State of Knowledge in the Field of Optimum Design of Structures, Applied Mechanics Reviews, Vol. 16, No.5, 1963, pp. 341-350
- [6] Gerard, G., Optimum Structural Design Concepts for Aerospace Vehicles, Journal of Spacecraft, Vol.3, No.1, 1966, pp. 5-18
- [7] Ashley, H., On Making Things the Best-Aeronautical Uses of Optimization, Journal of Aircraft, Vol. 19, No.1, 1982, pp. 5-28
- [8] Butler, R., The Optimization of Wing Structures, Aircraft Engineering and Aerospace Technology, Vol.70, No. 1, 1998, pp. 4-8.

- [9] MSC Inc., MSC Nastran 2004 Design Sensitivity and Optimization User's Guide, 2004
- [10] T. Miki, M. Kondo, F. Mizuguchi and Y. Ogino, Optimization Trial Analysis of A Journal/Thrust Bearing Structure. Mitsubishi Heavy Industries, Ltd and Ryoyu System Engineering, Ltd. Kobe, Japan
- [11] Xiaoming Yu, Erwin H. Johnson, and Shenghua Zhang. Discrete Optimization in MSC Nastran. MSC Software Corporation, Costa Mesa, CA 92626, September 2000
- [12] FAA Federal Aviation Regulations (FARS, CFR 14), FARS PART 23 Appendix A, A.23.1 General, http://www.flightsimaviation.com/data/FARS/part_23appA.html, last visited on 18/03/2010
- [13] ESDU 95010, Computer program for estimation of span-wise loading of wings with camber and twist in subsonic attached flow, <http://www.esdu.com>, last visited on 12/01/2009
- [14] Eastman N. Jacobs and Albert Sherman, Airfoil Section Characteristics As Affected By Variations of Reynolds Number, Report No. 586
- [15] Ira H. Abbott and Albert E. Von Doenhoff, Theory of Wing Sections Including a Summary of Airfoil Data, 1949, 1959, Dover Publications, INC. NEW YORK.
- [16] Bruhn, E.F., Analysis and Design of Flight Vehicle Structures, Tri-State Offset Company, USA, 1973, Chapter A3, pp. A3.12-A3.14, Chapter A5, pp. A5.10-A5.11,
- [17] Megson, T.H.G., Aircraft Structures for Engineering Students, Second edition, John Wiley and Sons, New York, USA, 1990
- [18] ASM Aerospace Specification Metals Inc.
<http://asm.matweb.com/search/SpecificMaterial.asp?bassnum=MA2024T3>, last visited on 10/06/2011

- [19] Y.C. Fung, An Introduction to the Theory of Elasticity, Dover Publications, 1994
- [20] Schaeffer, H.G., MSC.Nastran Primer for Linear Static Analysis, MSC Software Corporation, Santa Ana, California 2001, p.184—191, pp.289-306
- [21] William R. Spillers · Keith M. MacBain, Structural Optimization, Springer Dordrecht Heidelberg London New York, 2009
- [22] Vanderplaats R&D, DOT Optimization Software
<https://www.vrand.com/contact.html>, last visited on 13/07/2011
- [23] MSC.NASTRAN® 2005 r3, “Design Sensitivity and Optimization User’s Guide”, MSC Software Corp., 2003
- [24] Lee, K.H. and Park, G.J., “Discrete Post Process of the Constrained Size Optimization Using Orthogonal Arrays”, AIAA-96-3987-CP, 6th AIAA/NASA/ISSMO Symposium on Multidisciplinary Analysis and Optimization, Bellevue, WA, September 4-6, 1996
- [25] MD NASTRAN INPUT,
http://www.aero.polimi.it/~lanz/bacheca/downloads/cost/aa10_11/MD_Nastran_Inpt.pdf, last visited on 22/03/2010
- [26] Capital Aluminum Extrusions Ltd., <http://www.capalex.co.uk>, last visited on 10/06/2011
- [27] Aircraft Spruce and Specialty Co., <http://www.aircraftspruce.com>, last visited on 10/06/2011
- [28] Performance Metals Australia, <http://www.performancemetalsaustralia.com.au>, last visited on 14/06/2011

[29] MIL-HDBK-5H: Military Handbook Metallic Materials and Elements for Aerospace Vehicle Structures, Department of Defense, USA, December 1998

APPENDIX A

SAMPLE CALCULATION FOR THE SECOND IDEALIZATION CASE OF THE ANALYTICAL SOLUTION OF WING TORQUE BOX DESIGN

The sample calculation enclosed in this section is carried out for the second idealization case of designing the wing torque box which is related to Chapter 2, section 2.5 and subsections 2.5.1 – 2.5.5. The sample calculation is performed at rib 4 which is located at 50 % of wing span, at point - A.

The forces values acting at bay 4 are:

- 1- The shear force, $VZ(4) = 908.67 \text{ N}$
- 2- The bending moment $MX(4) = 120.33 \text{ N.m}$
- 3- The pitching moment $MY(4) = - 20.81 \text{ N.m}$

The moment of inertia results at bay 4:

$$I_{xx}(4) = 3.48 \times 10^{-5} \text{ m}^4, \quad I_{zx}(4) = 7.32 \times 10^{-5} \text{ m}^4, \quad I_{zz}(4) = 2.4 \times 10^{-3} \text{ m}^4$$

The axial stresses are calculated using the unsymmetrical bending formula as defined in Eqn. (A.1)

$$\sigma_Y = \frac{P}{A} + \left(\frac{M_X I_Z + M_Z I_{XZ}}{I_X I_Z - I_{XZ}^2} \right) Z - \left(\frac{M_Z I_X + M_X I_{XZ}}{I_X I_Z - I_{XZ}^2} \right) X \quad (\text{A.1})$$

The axial stresses results acting on spar caps and stiffeners at bay 4 as it is described in Figure A.1 are:

$$\sigma_1 = -41.7 \text{ MPa}, \quad \sigma_2 = -30.1 \text{ MPa}, \quad \sigma_3 = -81.3 \text{ MPa}, \quad \sigma_4 = 25.9 \text{ MPa}$$

$$\sigma_5 = -34.4 \text{ MPa}, \quad \sigma_6 = 29.9 \text{ MPa}$$

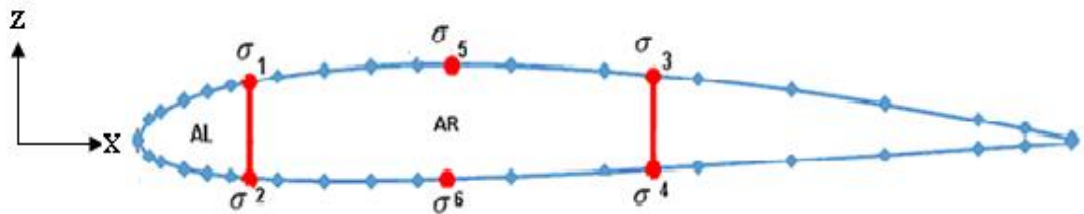


Figure A.1: Axial Stresses Acting On Spar Caps & Stiffeners

The axial stresses results acting on skins and spar webs at bay 4 as it is described in Figure A.2 are:

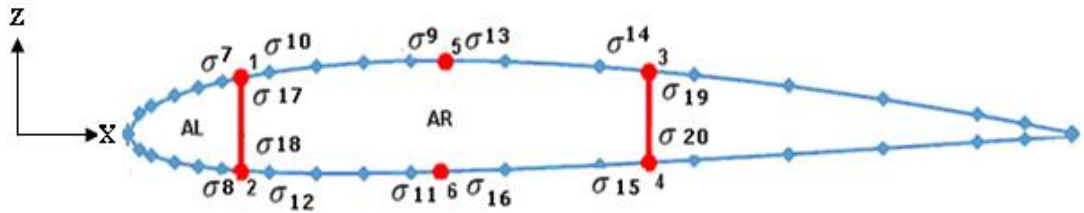


Figure A.2: Axial Stresses Acting on Skins and Spar webs of 2nd Idealization

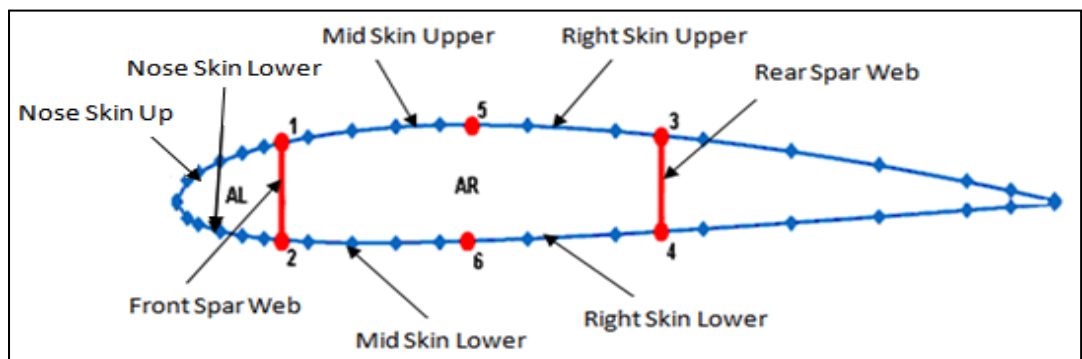


Figure A.3: Wing Skins and Spar Webs Definition

The axial stresses carried out by panels are calculated at the middle of each panel. The nose skin upper, nose skin lower, mid skin upper, mid skin lower, right skin upper and right skin lower stresses are calculated and their values are as an example:

$$\begin{aligned}\sigma_{\text{nose skin upper}} &= -20.8 \text{ MPa}, & \sigma_{\text{nose skin lower}} &= 15.0 \text{ MPa}, \\ \sigma_{\text{mid skin upper}} &= -40.0 \text{ MPa}, & \sigma_{\text{mid skin lower}} &= 21.4 \text{ MPa}, \\ \sigma_{\text{right skin upper}} &= -32.8 \text{ MPa} & \sigma_{\text{right skin lower}} &= 23.6 \text{ MPa}\end{aligned}$$

The values of the 14 stresses acting on each panel as it can be seen from Figure A.2 and Figure A.3 are calculated first, then the average value of each pair of stresses acting on each panel is used while calculating Von Mises stresses. The followings are the values of the 14 stresses acting on each panel.

$$\begin{aligned}\sigma_7 &= -41.7 \text{ MPa}, & \sigma_8 &= 30.1 \text{ MPa}, & \sigma_9 &= -34.4 \text{ MPa}, & \sigma_{10} &= -41.7 \text{ MPa} \\ \sigma_{11} &= 29.9 \text{ MPa}, & \sigma_{12} &= 30.1 \text{ MPa}, & \sigma_{13} &= -34.4 \text{ MPa}, & \sigma_{14} &= -18.3 \text{ MPa} \\ \sigma_{15} &= 25.9 \text{ MPa}, & \sigma_{16} &= 29.9 \text{ MPa}, & \sigma_{17} &= -41.7 \text{ MPa}, & \sigma_{18} &= 25.9 \text{ MPa} \\ \sigma_{19} &= -18.3 \text{ MPa}, & \sigma_{20} &= 25.9 \text{ MPa}\end{aligned}$$

The average values acting on each panel are tabulated in Table A.1 below:

Table A.1: Average Axial Stress Acting on Skins and Spar Webs Panels (MPa)

Bay Number	Nose Skin Up	Nose Skin-L	Mid- Up Skin	Mid-L Skin	Right-Up Skin	Right-L Skin	F-Spar Web	R-Spar Web
Bay - 4	-20.85	15.05	-38.10	30.00	-26.40	27.90	-5.78	3.79

The Von Mises stresses are calculated using Eqn. (A.2)

$$\sigma_{\text{VonMises}} = \sqrt{\sigma_x^2 + 3\tau_{xy}^2} \quad (\text{A.2})$$

$$\text{where } \tau = \frac{q}{t}$$

So in order to calculate Von Mises stress, it is needed to calculate shear flows and then shear stresses acting on each panel.

The shear flow acting on each panel, thicknesses and curvature lengths are described in Figure A.4. Since the shear flows are changing along the curvature length, two shear flows are defined just at the start point of a curvature and at the end point as shown in Figure A.4.

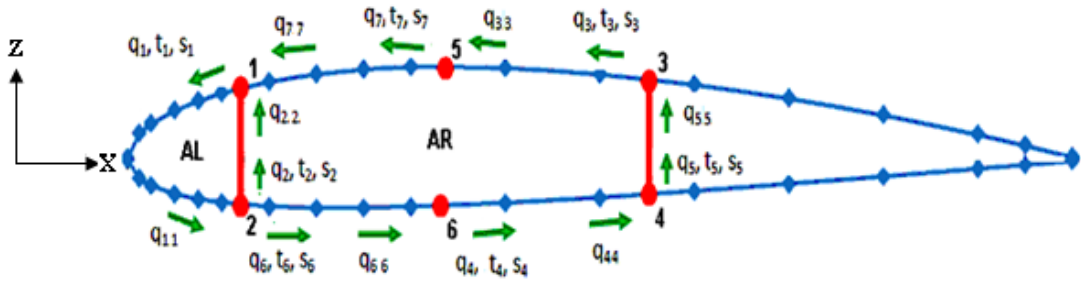


Figure A.4 : Shear Flow (q), Thickness (t), and Curvature Length (s) in 2nd Structural Idealization

The shear flows are calculated using the shear flow equality at a joint driven from the unsymmetrical bending formula as

$$q(s) = q_0 + \frac{(V_Z I_{XZ}) Q_Z}{I_{AA}} - \frac{(V_Z I_{ZZ}) Q_X}{I_{AA}} \quad (\text{A.3})$$

where $I_{AA} = I_X I_Z - I_{XZ}^2$

Additionally, the equality equation of twist angle between left and right boxes is used.

$$\theta_{Right} = \theta_{Left} \Rightarrow \frac{1}{2ARG} \sum \left(\frac{q_r s_r}{t_r} \right) = \frac{1}{2ALG} \sum \left(\frac{q_l s_l}{t_l} \right) \quad (\text{A.4})$$

Finally, the external equilibrium of moments around a point is used.

$$\sum M_{Y,external} = \sum M_{Y,shear\ flow} \Rightarrow M_Y + V_Z L = \sum 2Aq \quad (A.5)$$

where L is the moment arm.

The values of shear flows acting on each panel are as follows:

$$q_1 = -8190 \text{ N/m} \quad q_{11} = -15110 \text{ N/m}$$

$$q_2 = 4620 \text{ N/m} \quad q_{22} = 46850 \text{ N/m}$$

$$q_3 = 17040 \text{ N/m} \quad q_{33} = -5020 \text{ N/m}$$

$$q_4 = 11990 \text{ N/m} \quad q_{44} = 21800 \text{ N/m}$$

$$q_5 = 25920 \text{ N/m} \quad q_{55} = 24460 \text{ N/m}$$

$$q_6 = -12820 \text{ N/m} \quad q_{66} = 5930 \text{ N/m}$$

$$q_7 = -15900 \text{ N/m} \quad q_{77} = -43230 \text{ N/m}$$

The Von Mises stresses are calculated using Eqn. (A.2)

The results of Von Mises stresses calculated at the upper and lower skins are as follows:

$$\sigma_{\text{Von Mises mid skin upper}} = 39.8 \text{ MPa} , \quad \sigma_{\text{Von Mises mid skin lower}} = 56.1 \text{ MPa},$$

$$\sigma_{\text{Von Mises right skin upper}} = 59.1 \text{ MPa} \quad \sigma_{\text{Von Mises right skin lower}} = 33.1 \text{ MPa}$$

In the same manner the rest of Von Mises stress are calculated for other panels.

Flange areas calculation procedure

The areas of flanges are obtained while satisfying the ultimate stress value of 322 MPa. Eqn. (A.1) is used to calculate axial stress and in the case the value of stress is larger than the ultimate stress; the area of the flange is allowed to increase by an increment value of 1.001.

Table A.2 summarizes flange areas obtained for bay 4 and the rest of the bays of the wing torque box.

Table A.2: Flange Areas Determined Using the 2nd Idealization - Point A

FLANGE AREAS (in mm²) at Point A							
Root	Station	Spar Cap 1	Spar Cap 2	Spar Cap 3	Spar Cap 4	Stiffener 1	Stiffener 2
	1	38.92	38.50	38.57	38.23	38.77	38.42
	2	38.69	38.34	38.38	38.04	38.61	38.23
	3	38.54	38.08	38.11	38.00	38.34	38.00
	4	38.00	38.00	38.00	38.00	38.00	38.00
	5	38.00	38.00	38.00	38.00	38.00	38.00
Tip	6	38.00	38.00	38.00	38.00	38.00	38.00

These values are rounded up to the standard values. Table A.3 shows the final standard flange areas values.

Table A.3: Standard Flange Areas Determined Using the 2nd Idealization - Point A

FLANGE AREAS (in mm²) at Point A							
Root	Station	Spar Cap 1	Spar Cap 2	Spar Cap 3	Spar Cap 4	Stiffener 1	Stiffener 2
	1	44	44	44	44	44	44
	2	44	44	44	44	44	44
	3	44	44	44	44	44	44
	4	44	44	44	44	44	44
	5	44	44	44	44	44	44
Tip	6	44	44	44	44	44	44

Thin panels thickness calculation:

The thicknesses of the thin panels of the wing torque box are calculated while satisfying strength and buckling constraints.

Strength check:

Since the skin panels are allowed to carry axial stress and shear stress, Von Mises stress acting on each panel which is a function of axial stress and shear stress is used as strength check.

While calculating the axial stress carried by skin panels, it is already a check for strength since the value of axial stress is calculated while satisfying the ultimate stress value of 322. In the case the value of stress is larger than the ultimate stress; the thickness of the skin is allowed to increase by an increment value of 1.05.

For the shear stress, the thickness of the panel is calculated while the panel is satisfying maximum shear stress value of 188.67 MPa. In the case the value of stress is larger than the maximum shear stress; the thickness of the skin is allowed to increase by an increment value of 1.05. And as a last check, the overall value of Von Mises stress calculated by Eqn. (A.2) is checked while satisfying the ultimate stress value of 322 MPa and in the case the value of Von Mises stress is larger than the ultimate stress; the thickness of the skin is allowed to increase by an increment value of 1.05. It must be noted here that the average value of axial stress acting on each panel and the maximum shear flow acting on each panel is used while calculating Von Mises stress and carrying the final strength check.

Buckling check:

The thicknesses of the panel are calculated to satisfy combined buckling equations (A.6) and (A.7) respectively under compression/shear loading and bending/shear loading.

$$R_S^2 + R_C \leq 1 \Rightarrow \left(\frac{\tau}{K_S E \left(\frac{t}{b}\right)^2} \right)^2 + \left(\frac{\sigma_{Compression}}{K_C E \left(\frac{t}{b}\right)^2} \right) \leq 1 \quad (\text{A.6})$$

$$R_S^2 + R_b^2 \leq 1 \Rightarrow \left(\frac{\tau}{K_S E \left(\frac{t}{b}\right)^2} \right)^2 + \left(\frac{\sigma_{Compression}}{K_b E \left(\frac{t}{b}\right)^2} \right)^2 \leq 1 \quad (\text{A.7})$$

The value of K_C , K_b and K_S are defined as axial compressive buckling coefficient, bending buckling coefficient and shear buckling coefficient respectively and they are

dependent on supports condition and on (a/b) aspect ratio in which “b” is the plate width length and “a” is the length. The value of K_C , K_b and K_s are read from Figures A.5 – A.7.

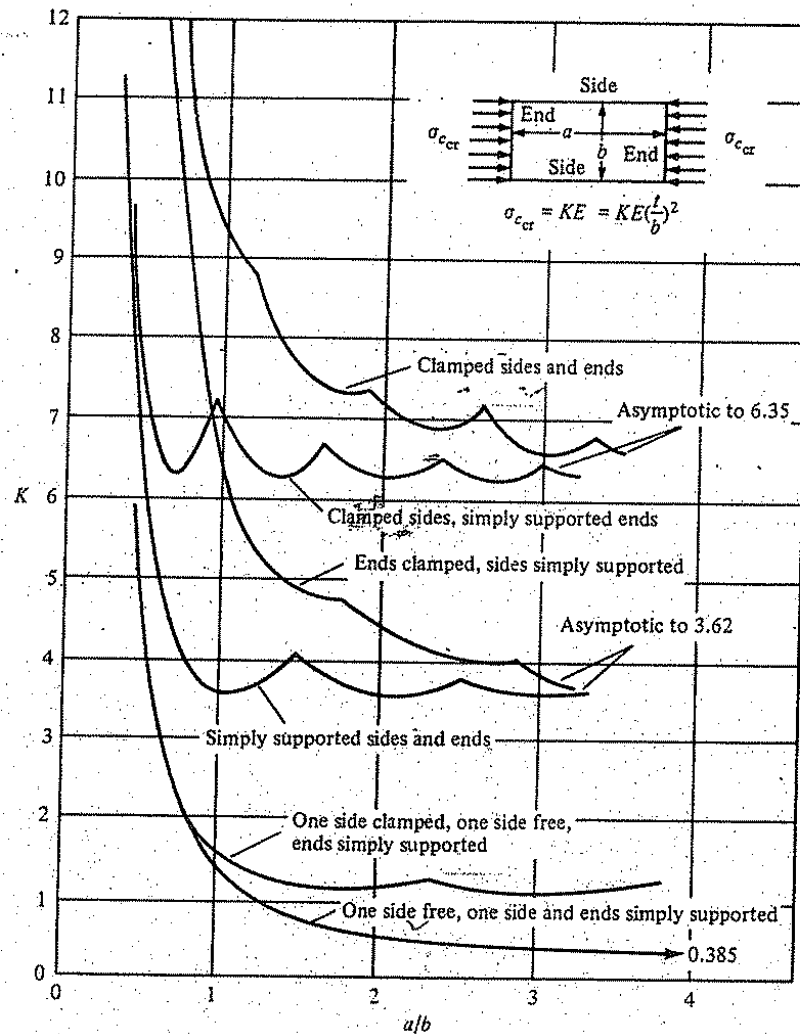


Figure A.5: Compressive Buckling Coefficient K_c Graph

The equation of compressive buckling coefficient K_c is formularized by means of curve fitting with the help of Microsoft Excel to be used while solving buckling equations.

$$K_c = -1.8939 \cdot x^6 + 16.69 \cdot x^5 - 55.609 \cdot x^4 + 84.987 \cdot x^3 - 54.093 \cdot x^2 + 3.4296 \cdot x + 10.144; \quad x \leq 2.7$$

$$K_c = 3.62; \quad x > 2.7$$

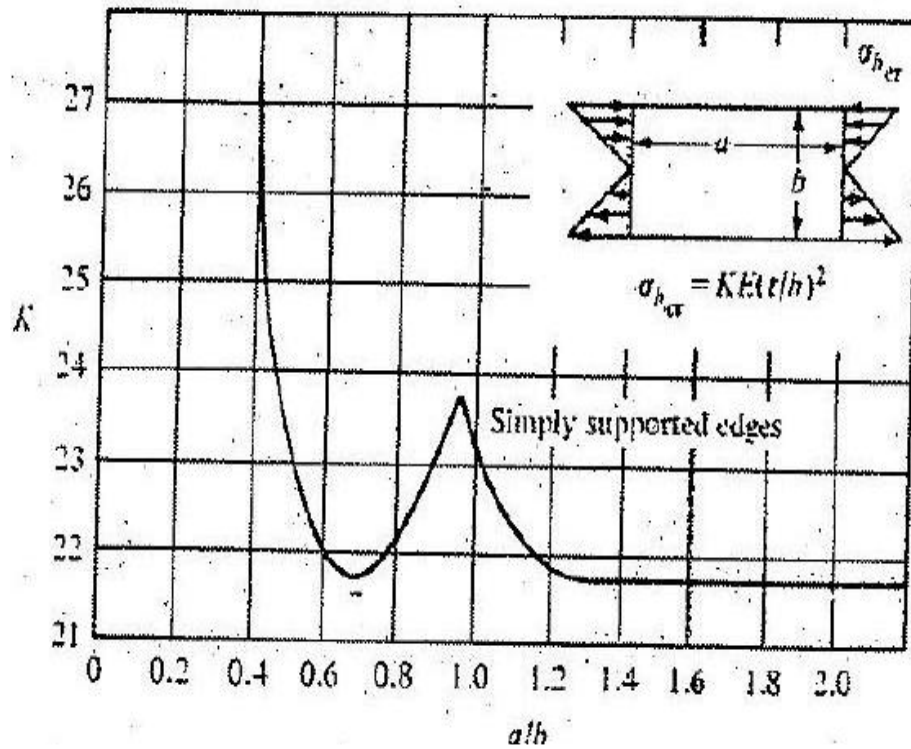


Figure A.6: Bending Buckling Coefficient K_b Graph

The equation of bending buckling coefficient K_b is formularized by means of curve fitting with the help of Microsoft Excel to be used while solving buckling equations.

$$K_b = -231.72 \cdot x^6 + 1471.7 \cdot x^5 - 3586.3 \cdot x^4 + 4285.9 \cdot x^3 - 2623.1 \cdot x^2 + 762.95 \cdot x - 56.102; \quad \text{for } x \leq 1.3$$

$$K_b = 21.8; \quad \text{for } x > 1.3$$

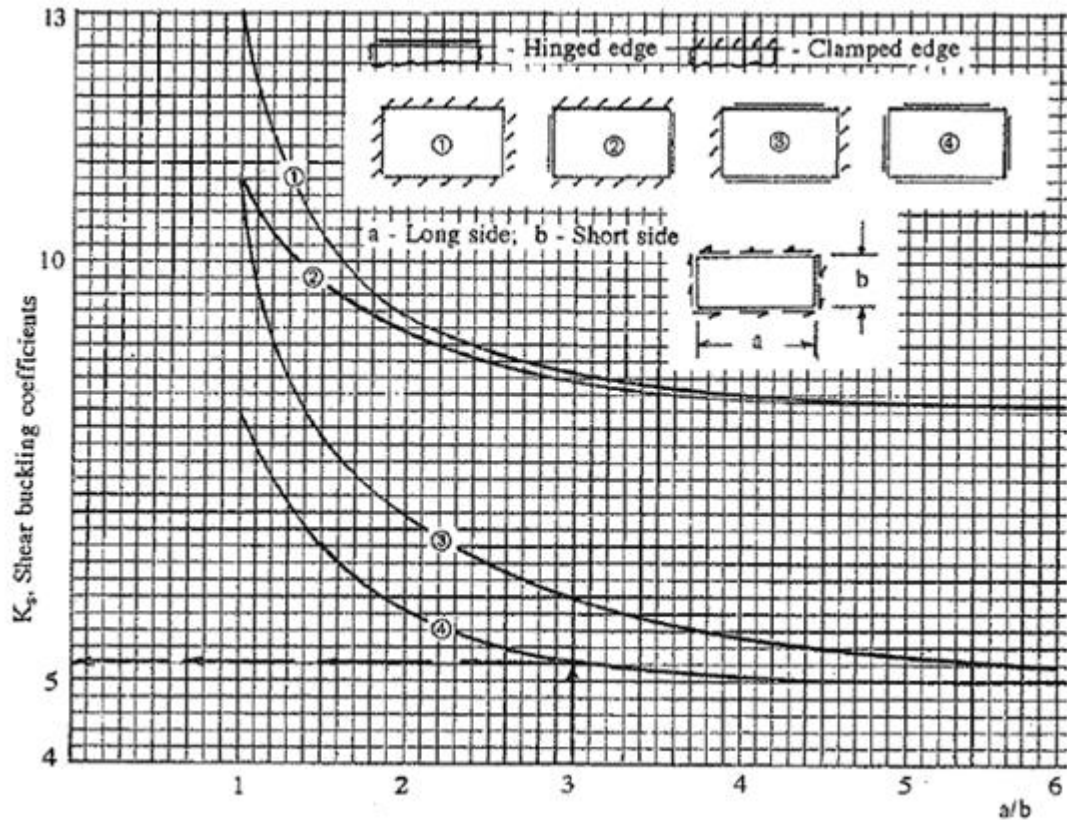


Figure A.7: Shear Buckling Coefficient K_s Graph

The equation of shear buckling coefficient K_s is formularized by means of curve fitting with the help of Microsoft Excel to be used while solving buckling equations.

$$K_s = -0.0234*x^5 + 0.3669*x^4 - 2.3717*x^3 + 8.0599*x^2 - 14.757*x + 16.925; \text{ for } x \leq 4.4$$

$$K_s = 6.0; \text{ for } x > 4.4$$

It must be noted while solving for thicknesses of skins and spar webs under buckling constraints, the average shear flow and axial stresses acting on each panel are used in the Eqn. (A.6) and (A.7).

As an example, the thickness of mid skin upper that is found while satisfying strength check is 0.0003 m and the thickness found while satisfying compressive

buckling equation is 0.0008 m. So the maximum thickness is chosen as mid skin upper thickness that satisfies both constraints as 0.0008 m and then this value was rounded up to standard thickness value of 0.001 m as mid upper skin thickness.

Deciding on thickness of ribs

The thickness of the ribs is calculated while satisfying buckling constraints.

Buckling check:

The thicknesses of ribs are calculated while satisfying buckling constraint defined by Eqn. (A.8). Figure A.8 shows the nose rib and mid rib shear flows, thicknesses and curvature lengths.

$$\tau_{critical} = K_S E \left(\frac{t}{b}\right)^2 \tag{A.8}$$

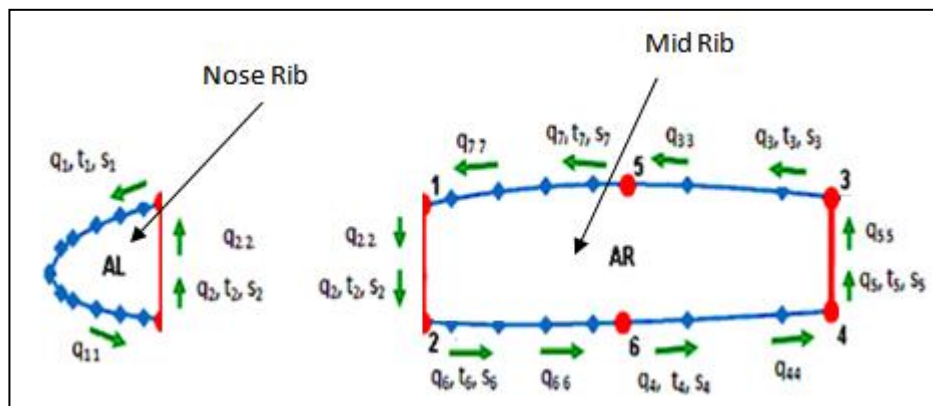


Figure A.8: Nose and Middle Rib Shear Flows, Thicknesses and Curvature Length Definitions

Actually the process of analysis the ribs is usually faced by two major difficulties. The first difficulty is related to the fact that, the shear flow is not constant along the curvature of the rib; it is changing with chord wise distance as well as the rib flange loads. The second difficulty is the shape of the rib; it is quite unconventional for buckling analysis. Thus, two assumptions are made. The first assumption is the average shear flow is used on each panel, and in that way the rib is assumed to be under uniform shear stress of an average value. The second assumption approximates

the ribs curvatures by straight lines creating almost a triangular shape for nose rib and rectangular shape for middle rib. It must also be noted that, the ribs will be under the effect of the shear flows generated on each skin attached to the rib and in that case there will be different shear flows on each side of the rib and their effect is taken into account while calculating the net average shear flows acting on each rib.

As an example, the thickness of nose rib at bay 4 that is found while satisfying buckling constraint is 0.00067 m. and then this value was rounded up to standard thickness value of 0.0008 m as nose rib thickness.

APPENDIX B

ORGANIZATION OF THE NASTRAN BDF INPUT FILE

The Nastran input file is arranged in five sections as it shown in Figure B.1 [25]

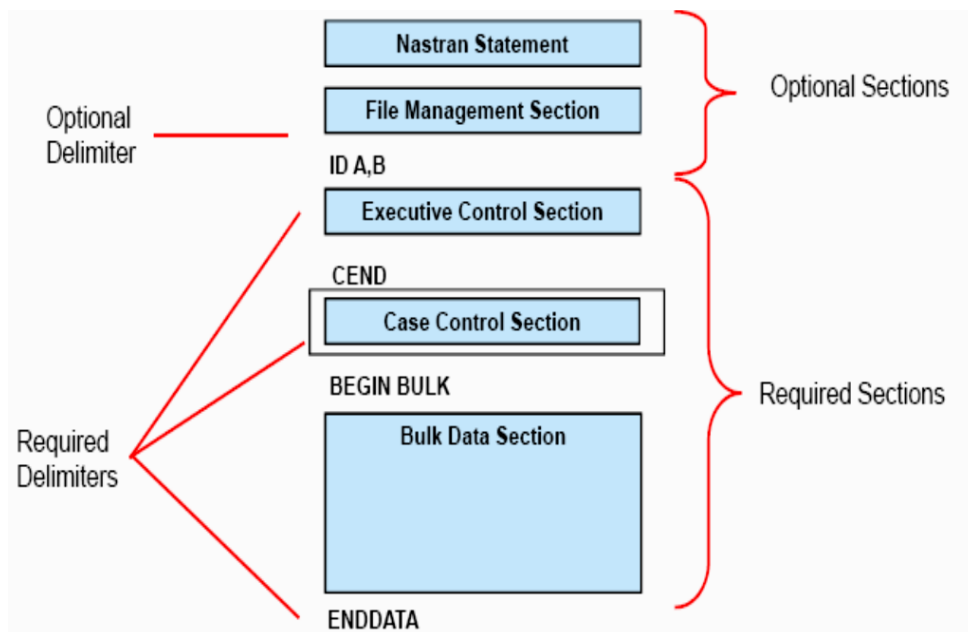


Figure B.1: Organization of Nastran Input File

NASTRAN INPUT FILE SECTIONS

1. Nastran Statement – Used to modify system defaults. Not needed in most runs.
2. File Management Section – Allocates files, controls restarts and database operations
3. Executive Control Section – Solution type, time allowed, program modifications, and system diagnostics.

4. Case Control Section – Requests Output and selects Bulk Data items such as loadings and boundary conditions to be used
5. Bulk Data Section – Model definition, loadings, and boundary conditions

NASTRAN INPUT FILE DELIMITERS

1. The delimiters are ID A,B First statement in Executive Control Section (optional)
2. CEND End of Executive Control Section, beginning of Case Control Section
3. BEGIN BULK End of Case Control Section, beginning of Bulk Data Section
4. ENDDATA Last entry in the input file

BULK DATA SECTION

1. The Bulk Data Section contains all data necessary for describing a structural model
2. Each item described in the Bulk Data section is called an Entry
3. The Bulk Data entries are not required to be input in any order

APPENDIX C

SAMPLE BDF-FILE FOR WING TORQUE BOX OPTIMIZATION

Nastran Statement Section A \$ sign is used in the beginning of comments.

**\$ NASTRAN input file created by the Patran 2008r1 input file translator
\$ on December 11, 2010 at 21:36:40.
\$ Direct Text Input for Nastran System Cell Section**

File Management Section

\$ Direct Text Input for File Management Section

.....

.....

Executive Control Section

**\$ Design Sensitivity and Optimization Analysis
SOL 200
\$ Direct Text Input for Executive Control
CEND**

Case Control Section

TITLE = MSC.Nastran job created on 10-Dec-10 at 20:14:15

ECHO= SORT,PUNCH (NEWBULK) command provides initial bulkdata written in f06-file and final (optimized) bulk data in pch-file.

ECHO = SORT,PUNCH (NEWBULK)

The DESOBJ command is used in the subcase information section to select a single response definition as the objective function of an optimization. The DESOBJ command also indicates if this response is to be minimized or maximized.

DESOBJ(MIN) = 1 , indicates that the objective function is given in DRESP1 card with number 1 and MIN indicates the response to be minimized. This card is in the design response section of the design model.

Linear Static Analysis is performed in the optimization.

ANALYSIS = STATICS

Applied Load Case Definition

\$ Direct Text Input for Global Case Control Data

SUBCASE 1

\$ Subcase name : Default

SUBTITLE=Default

SPC = 2

LOAD = 2

DISPLACEMENT(PRINT,PUNCH,SORT1,REAL)=ALL

SPCFORCES(PRINT,PUNCH,SORT1,REAL)=ALL

STRESS(PRINT,PUNCH,SORT1,REAL,VONMISES,BILIN)=ALL

DESSUB = 22

Bulk Data Section

\$ Direct Text Input for this Subcase

BEGIN BULK

Parameters definition to control the output of analysis

PARAM POST -1

PARAM PRTMAXIM YES

PARAM NASPRT 1

Analysis Model Description and Bulk data entries

In this section assigned properties of the elements are defined here and as an example wing nose thicknesses are modeled using shell Property with CQUAD4 elements.

The thickness is defined as 0.0048 m. The upper front Spar flange is modeled using Rod property with CROD element. The cross sectional area is defined as 4.4-5 m²

```

$ Direct Text Input for Bulk Data
$ Elements and Element Properties for region: NO1S
PSHELL 1 1 .0048 1 1
$ Pset: "NO1S" will be imported as: "pshell.1"
CQUAD4 36 1 1 3 6 4
CQUAD4 42 1 2 1 4 5
.....
.....

```

```

$ Elements and Element Properties for region : FS1U
PROD 58 1 4.4-5
$ Pset: "FS1U" will be imported as: "prod.001 18"
CROD 72 58 2 5
.....
.....

```

In this section element assigned properties are defined here and as an example wing nose thicknesses are modeled using shell Property with CQUAD4 elements. The thickness is defined as 0.0048 m. The upper front Spar flange is modeled using Rod property with CROD element. The cross sectional area is defined as 4.4-5 m²

Material Definition and Properties

```

$ Referenced Material Records
$ Material Record : Aluminum_2024-T3
$ Description of Material : Date: 10-Dec-10 Time: 18:37:37
MAT1 1 7.31+10 2.8+10 .3 2768.

```

Nodes definition using Grid

```

$ Nodes of the Entire Model
GRID 1 0. 0. 0.
GRID 2 .381 .116891 0.
GRID 3 .381 -.064313 0.
GRID 4 0. 0. .762
.....
.....

```

Loads and Boundary Conditions Definitions

\$ Loads for Load Case : Default

SPCADD 2 1
LOAD 2 1. 1. 1 1. 3 1. 4
1. 5 1. 6 1. 7 1. 8
1. 9 1. 10 1. 11 1. 12
1. 13

\$ Displacement Constraints of Load Set : Displacement

SPC1 1 123456 2 3 46 47 72 73
76 77

\$ Distributed Loads of Load Set : Load1

FORCE 1 3 3084.29 0. 1. 0.
FORCE 1 6 3073.06 0. 1. 0.
MOMENT 3 3 143.551 0. 0. -1.
MOMENT 3 6 143.206 0. 0. -1.

.....
.....

Design Variables Definitions

Design variables are defined. "DESVAR" card includes the number, name, initial value, upper bound and lower bound information of a design variable and it can be related to discrete design variable set. As an example the number 2 by the end of DESVAR 57 card relates the design variable value to a set of discrete values to be chosen from the standard areas which are defined using the statements starting with ddval (discrete design values), and the number 2 relates this list to the design variable card 57 in this example.

\$...DESIGN VARIABLE DEFINITION

\$ MIDR1_Thickness

DESVAR 1 MIDR1_Th.001 3.-4 .00635 .001 1

.....
.....

\$ FS1L_Area

DESVAR 57 FS1L_Are4.4-5 3.8-5 6.13-4 .001 2

.....
.....

\$STANDARD THICKNESS

ddval 1 3.-4 .4-3 .5-3 .63-3 .81-3 1.016-3 1.27-3

.....

.....

\$STANDARD AREA

ddval 2 38-6 44-6 48-6 58-6 63-6 67-6 73-6

.....

.....

Definition of Design Variable to Analysis Model Parameter Relations

Design variables are related to element properties in the analysis model during the optimization. DVPREL1 card is used to relate a design variable to an element property in analysis model.

**\$...DEFINITION OF DESIGN VARIABLE TO ANALYSIS MODEL
PARAMETER RELATIONS**

**DVPREL1 57 PROD 58 A
58 1.**

.....

.....

As an example, the thickness value on a PSHELL card is related to the design variable 20 as follow, where the ID number of the design variable is 1 (**DVPREL1 1**) , the type of the property and its ID is defined as **PSHELL 1** and the property name is defined as **T**. The real value **1.** defines the coefficient in the relationship equation between a connectivity property and design variables.

**DVPREL1 1 PSHELL 1 T
20 1.**

.....

.....

Structural Response Identification

\$...STRUCTURAL RESPONSE IDENTIFICATION

DRESP1 defines first level response or set of responses. These responses are available directly from MSC Nastran analysis. Structural weight, displacements at grid points, element stresses, and so on, are all examples of type-1 responses. Each **DRESP1** card must have a unique ID.

As an example the ID number of **DRESP1** is **1** in the card entry below and **MinWeigh** is the name of the response defined by the user and **WEIGHT** defines the type of response.

DRESP1 1 MinWeigh WEIGHT

DCONADD collect the **DCONSTR** (design constraints) entries into a master set using the **DCONADD** entry. **22** refers to ID number of **DCONADD**, the set of numbers **1 2 3 4 6** refers to **DCONSTR**

\$ DCONADD22

DCONADD 22 1 2 3 4 6

As an example here, the displacement **DRESP1** is defined in the same manner as mentioned before with some extra information like the number **2** in the last entry line is the constraint region identifier, in this special case it refers to displacement in Y direction. The last entry number **19** is one of the response attributes.

\$ Displacement

DRESP1 2 DIS2 DISP 2 19

20 21 68

.....

In the case of dealing with stresses, the extra information is related to the type of stresses which are assigned. For instance, the maximum Von Mises stress in ELEM 1 is identified by ID **9**. The numbers **1 2 3 4 5** refer to ELEM ID number. In the same manner the rest of entries related to axial, shear and normal stress are defined.

\$ STRESS VON

DRESP1 3 STR3 STRESS ELEM 9 1

2 3 4 5

DRESP1 4 STR4 STRESS ELEM 11 8

.....

\$ AXIAL

DRESP1 5 STR5 STRESS PROD 2 58

.....

\$ SHEAR

DRESP1 6 STR6 STRESS ELEM 5 1

2 3 4

```

DRESP1 7 STR7 STRESS ELEM 7 8
.....
.....

```

```

$ STRESS NORMAL-Y
DRESP1 8 STR8 STRESS ELEM 4 1
  2 3 4 5 .....

```

```

DRESP1 9 STR9 STRESS ELEM 6 8
.....
.....

```

Equation Definition

Equation 100, where **100** is the equation ID number, defines the relation between the FS1L and FS2L (Front Spar Lower Flange Cross Sectional Areas at Bay 1 and 2 respectively) and it is used as second type response. The **DRESP2** is defined in the same manner as **DRESP1**, the number **10** refer to design response ID and **B1** is the label defined by the user for the equation. The equation relates the two design variable FS1L and FS2L by **DESVAR**, **57** and **58** are ID number of the design variables.

```

$FRONT SPAR
DRESP2 10 B1 100
  DESVAR 57 59
$ FRONT SPAR
DEQATN 100 B1(FS1L,FS2L) = FS1L - FS2L
.....
.....

```

Another example of an equation definition is the following equation that defines local buckling of nose skin at bay 1 (**NO1S**). As described previously, **DRESP2** is defined in the same manner. **DEQATN 1** defines the first part of combined buckling equation under compression and **DEQATN 2** defines the second part under shear stress. **DEQATN 3** defines the overall local buckling equation under combined compression and shear loads. The equation **BK1** relates the design variable **NO1S** by **DESVAR**, where **20** is the ID number of the design variable. Also **BK1** relates the response stress (**STR9**) by **DRESP1 9**. As a reminder the combined buckling equation under compression and shear stress is defined as:

$$R_C + R_S^2 \leq 1 \Rightarrow \left(\frac{\sigma_{compression}}{K_C E \left(\frac{t}{b}\right)^2} \right) + \left(\frac{\tau}{K_S E \left(\frac{t}{b}\right)^2} \right)^2 \leq 1 \quad (C.1)$$

So by referring to eqn. C.1 the set of equations are being written.

```

DRESP2 100 BK1 1
DESVAR 20
DRESP1 9
DEQATN 1 BK1(STR9,NO1S)= STR9*0.4**2 /
(3.65*7.31e10*NO1S**2)

```

Here **STR9** is the compression stress related to design variable **NO1S**, **b** is the nose skin plate width with a value of **0.4 m**, **Kc** is the compression buckling coefficient with a value of **3.65**, the modulus of elasticity **E** value is **7.31e10** and the thickness of the plate is related to the design variable **NO1S** that defines the thickness.

In the same way the second part of the local buckling equation is defined. **STR7** here refers to shear stress label which is defined by **DRESP1 7**.

```

DRESP2 101 BS1 2
DESVAR 20
DRESP1 7
DEQATN 2 BS1(NO1S,STR7)=
STR7**2*0.4*0.4*0.4*0.4 / (5.9**2*7.31e10**2*
NO1S**2*NO1S**2)

```

The third part define overall local buckling equation under combined compression and shear loads by relating the first two parts to each other by the use of **DRESP2 100 101**. The eqns. **BK1** and **BS1** were subtracted from each other in order to count for compression stress since the output of the stress will be with a minus (-) sign.

```

DRESP2 102 BT1 3
DRESP2 100 101
DEQATN 3 BT1(BK1,BS1)= BK1 - BS1

```

Design Constraints Definition

The design constraints are defined with upper and lower limits and they are related to design responses using **DCONSTR** identification number. As an example, the

number 1 in **DCONSTR 1** card, is the related design response number. So by looking to **DCONSTR 1 2** card, 0.2 defines the upper limit of the displacement constraint, **DCONSTR 3 5, -3.22+8 3.22+8** are the lower and upper limits of axial stress and **DCONSTR 6 239, 1.01** is the upper limit for buckling constraint.

```

$ ...CONSTRAINTS
DCONSTR 1 2 .2
DCONSTR 2 3 3.22+8
DCONSTR 2 4 3.22+8
DCONSTR 3 5 -3.22+8 3.22+8
DCONSTR 4 10 .1e-10
.....
.....
DCONSTR 6 239 1.01

```

Optimization Control Section

Here maximum iteration number, number of fully stressed design cycles, discrete optimization method, convergence criteria and move limits on approximate optimization are defined by using “**DOPTPRM**”. The maximum number of specified design cycles is defined by **DESMAX** and the maximum number of fully stressed design cycles is specified by **FSDMAX**.

P1 and **P2** are some of the design cycle print controls, **P1** controls the frequency of the output and **P2** provides a “first level” control of which design quantities are printed. **P1 = 0** is the default value and it gives the output for initial and optimal designs and **P1 = n** gives the output for every n-th design cycle. **P2** can take different values depending on which output is needed, **P2 = 0** gives no output, **P2 = 1** gives the output of the objective function and design variables and **P2 = 2** outputs the designed properties, for more details refer to Reference [9].

METHOD defines optimization method, so the value 1 refers to the modified method of feasible directions for both MSCADS and DOT, the parameter that permits the specification of the optimization code to be used is defined by **OPTCOD**, **MSCADS** is the default for shape and sizing optimization while the familiar DOT code is available as an option. The parameters **CONV1**, **CONV2**,

CONVDV and **CONVPR** are used to test for overall design cycle convergence. These parameters are used in connection with tests for both hard and soft convergence for more details refer to Reference [9]. **DELP**, **DPMIN**, **DELX** and **DXMIN** define move limits on the approximate optimization. They can be changed from their defaults by modifying **DELP** and **DPMIN** for properties, and **DELX** and **DXMIN** for design variables. **CT** is used to define the threshold above which a constraint is considered active while **CTMIN** is used to identify violated constraints. **DISCOD** and **DISBEG** control the discrete variable processing. The **DISBEG** parameter specifies at which mathematical programming design cycle you want to start performing discrete optimization. The default value of 0 performs discrete optimization only after the continuous optimization process is complete. The **DISCOD** parameter selects from one of the four discrete optimization alternative methods. The value of 3 performs Round – Up discrete optimization.

\$...OPTIMIZATION CONTROL

```
DOPTPRM DESMAX 200  FSDMAX 0  P1  1  P2  1
METHOD 1  OPTCOD MSCADS CONV1 .001  CONV2 1.-20
CONVDV .001  CONVPR .01  DELP .2  DELX .5
DPMIN .01  DXMIN .05  CT -.03  GMAX .005
CTMIN .003  DISCOD 3  DISBEG 0
```

End Data

\$ Referenced Coordinate Frames

ENDDATA f5560e60

APPENDIX D

EXAMPLES OF VARIATIONS OF SOME OF THE DESIGN VARIABLES AND THE MAXIMUM CONSTRAINT WITH THE DESIGN ITERATIONS

The history of some of the design variables of a wing torque box modeled by rod/shell elements with coarse mesh are given in Figures D.1 – D.9 .The model is optimized under the aerodynamic distributed lift and pitching moment loads while including Von Mises and axial stress constraints, tip displacement, local buckling and side constraints too.

Figure D.1 shows the history of front upper spar cap area at bay 4 until an optimum design is reached.

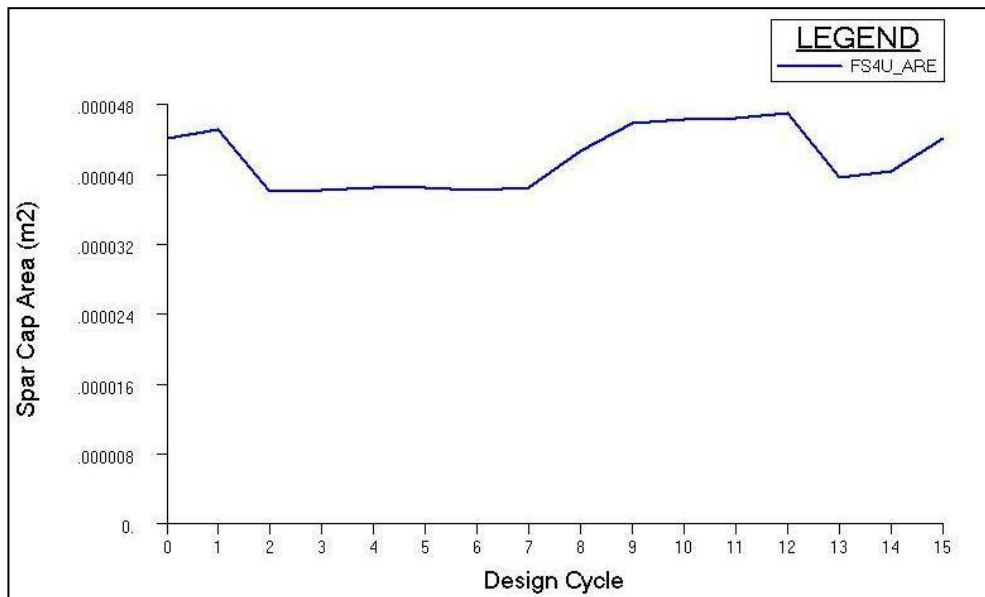


Figure D.1: History of Front Upper Spar Cap Area at Bay 4

Figure D.2 shows the history of front upper spar cap area at bay 4 until an optimum design is reached.

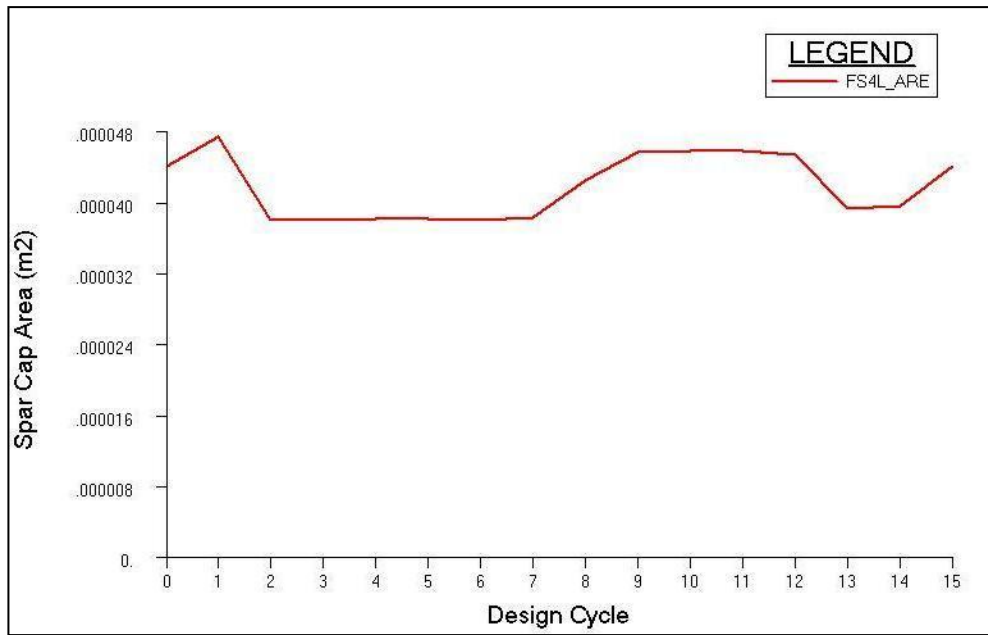


Figure D.2: History of Front Lower Spar Cap Area at Bay 4

Figure D.3 shows the history of rear upper spar cap area at bay 3 until an optimum design is reached.

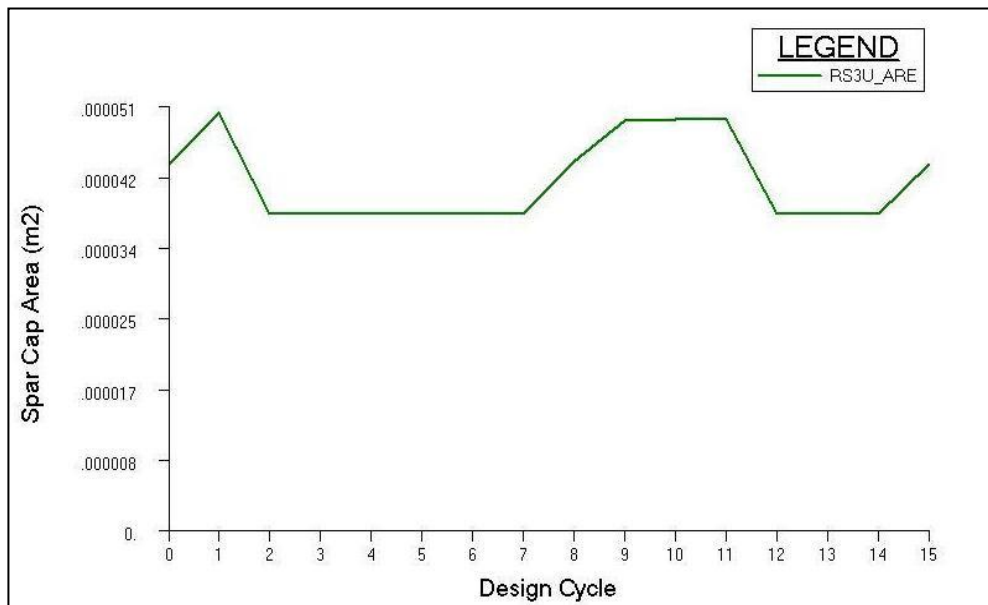


Figure D.3: History of Rear Front Spar Cap Area at Bay 3

Figure D.4 shows the history of rear lower spar cap area at bay 3 until an optimum design is reached.

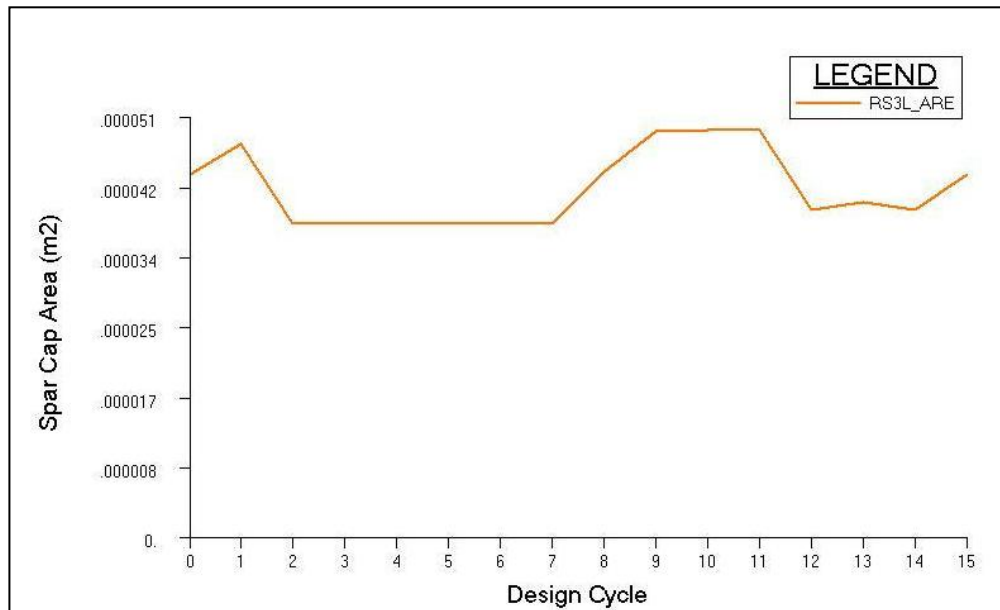


Figure D.4: History of Rear Lower Spar Cap Area at Bay 3

Figure D.5 shows the history of nose skin thickness at bay 2 until an optimum design is reached.

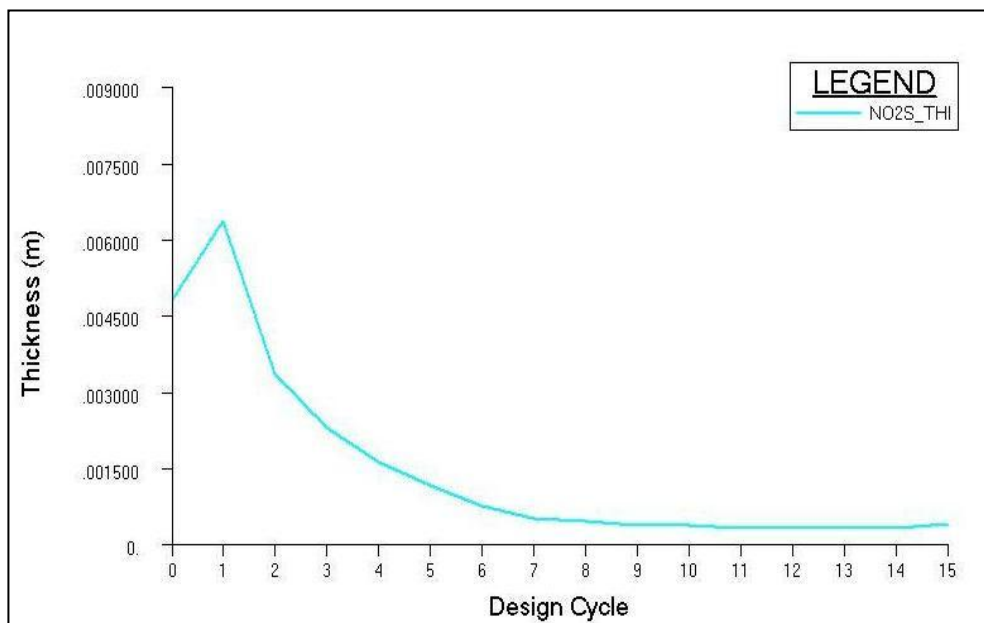


Figure D.5: History of Nose Skin Thickness at Bay 2

Figure D.6 shows the history of right upper skin at bay 2 until an optimum design is reached.

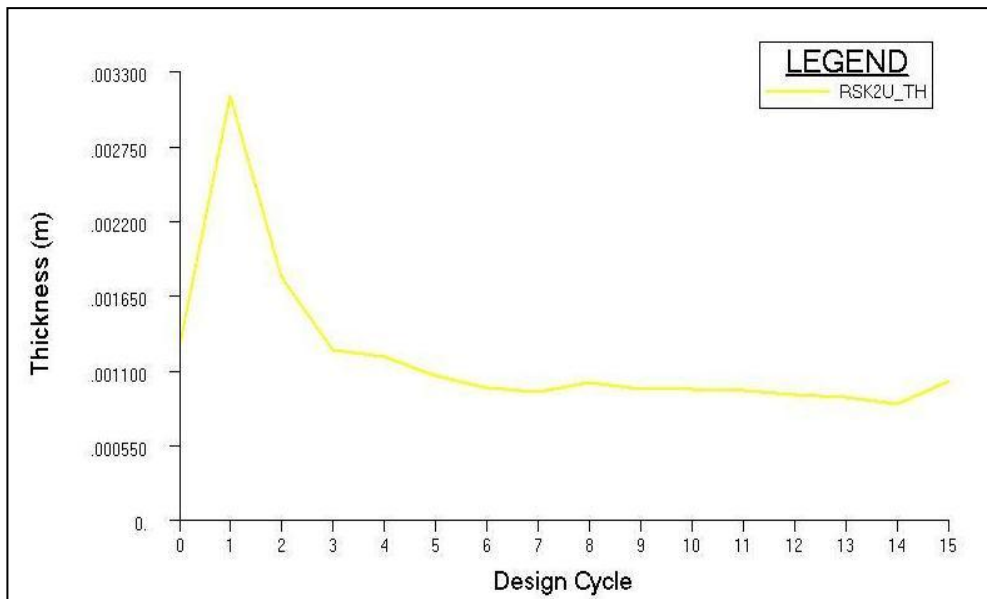


Figure D.6: History of Right Upper Skin Thickness at Bay 2

Figure D.7 shows the history of nose skin thickness at bay 2 until an optimum design is reached.

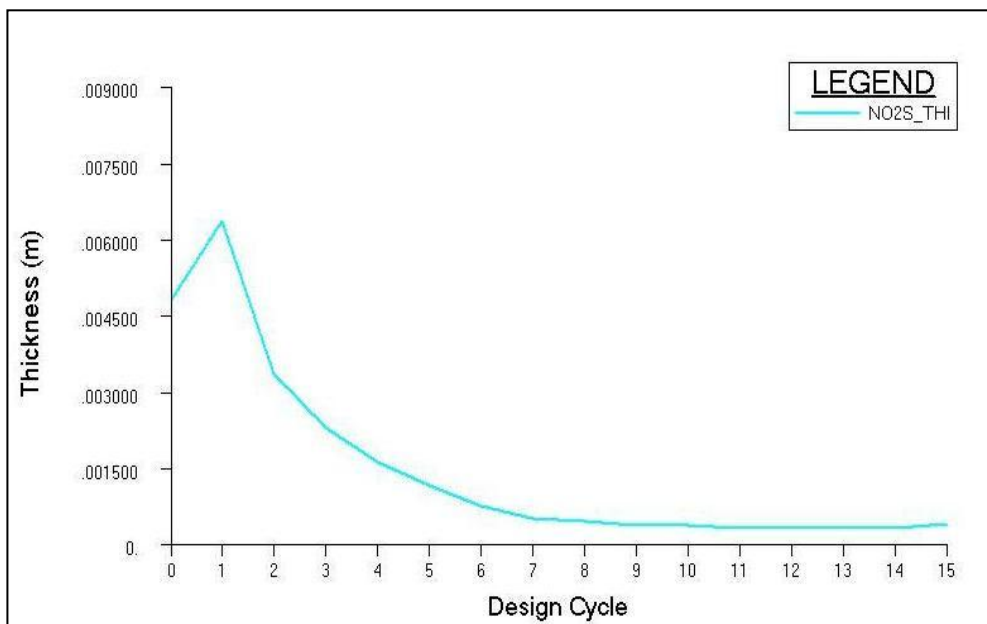


Figure D.7: History of Nose Skin Thickness at Bay 2

Figure D.8 shows the history of middle upper skin thickness at bay 4 until an optimum design is reached.

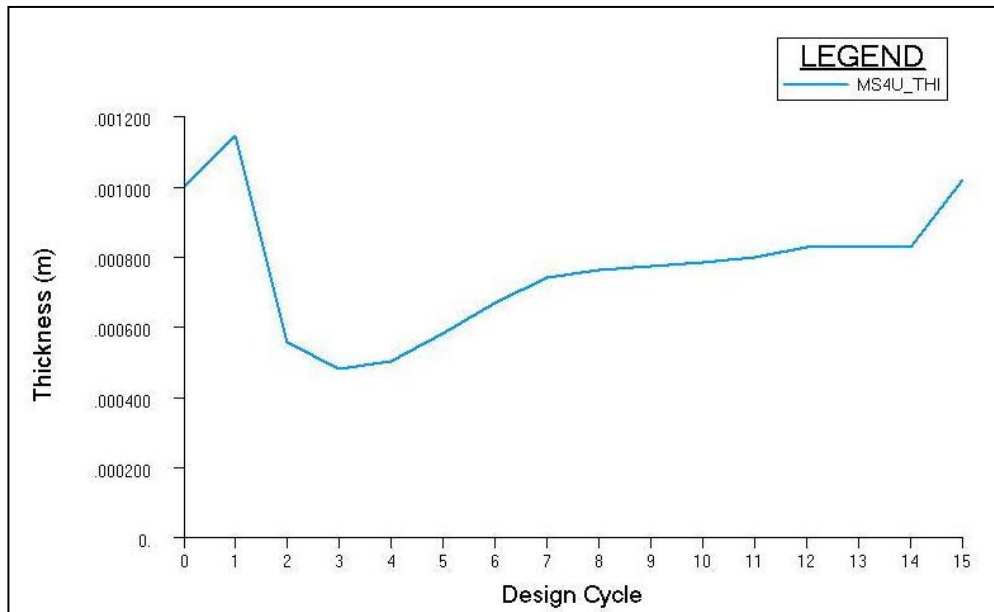


Figure D.8: History of Middle Upper Skin Thickness at Bay 4

Figure D.9 shows the history of rear spar web thickness at bay 3 until an optimum design is reached.

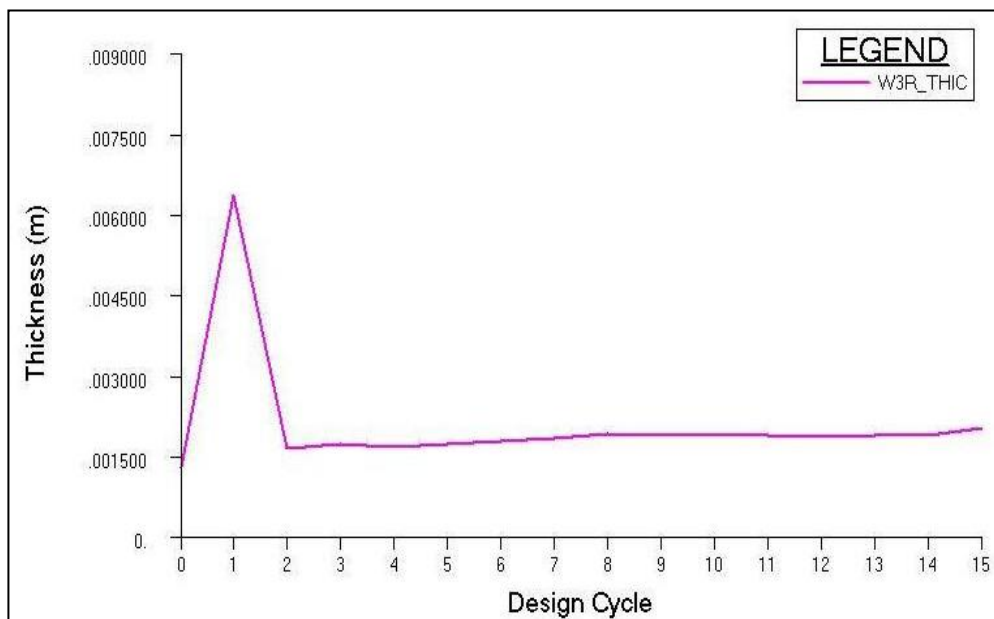


Figure D.9: History of Rear Spar Web Thickness at Bay 3

It observed from Figure D.1 – D.9, design variable value decreased compared to its initial value and this observation is in accordance with the variation of the objective function with the design cycle as shown in Figure D.10.

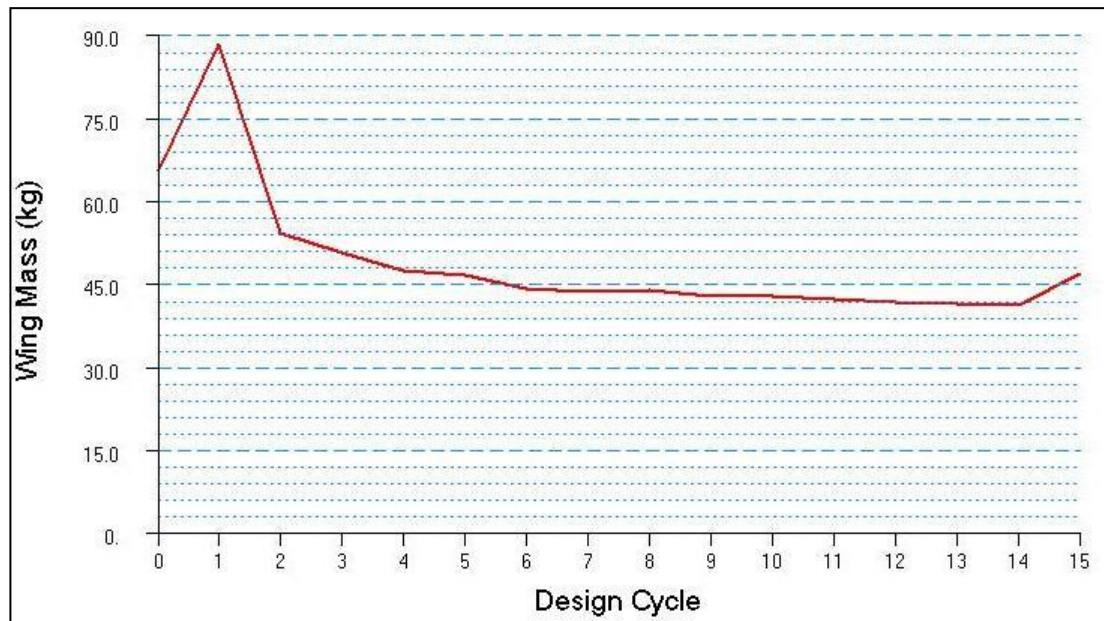


Figure D.10: Variation of the Mass of Wing with Respect to Design Cycles - Coarse Mesh Rod/Shell Model

APPENDIX E

STANDARD THICKNESSES AND FLANGE AREAS VALUES

Table E.1 summarizes the standard thicknesses and standard flange areas made of aluminum sheet metals and are used in aerospace industries while manufacturing aircraft wings, fuselages, spar and stiffeners. These values are obtained from different sources, for more information it can be referred to references [16, 26, 27, 28, 29].

Table E.1: Standard Thicknesses and Flange Areas

Standard Thicknesses and Flanges Areas			
Sheet Thicknesses (mm)	Flange Areas (mm ²)		
0.3	38	133	430
0.4	44	137	444
0.5	48	148	525
0.63	58	151	573
0.81	63	153	592
1.016	73	161	613
1.27	78	184	
1.6	88	195	
1.8	94	213	
2.03	98	232	
2.28	104	246	
2.54	108	280	
3.17	112	312	
4.06	116	375	
4.82	118	390	
6.35	131	415	